

# Flexible High Power Electronics Solutions for Hydro-Power Applications

Présentée le 18 août 2023

Faculté des sciences et techniques de l'ingénieur  
Laboratoire d'électronique de puissance  
Programme doctoral en génie électrique

pour l'obtention du grade de Docteur ès Sciences

par

**Philippe Alexandre BONTEMPS**

Acceptée sur proposition du jury

Prof. F. Rachidi-Haeri, président du jury  
Prof. D. Dujic, directeur de thèse  
Prof. G. Papafotiou, rapporteur  
Dr A. Schwery, rapporteur  
Dr E. Vagnoni, rapporteuse



*Dedicated to all of those who helped make this work happen.*

*"The real question is not whether machines think but whether men do."*

B.F. Skinner



# Abstract

The current global energy landscape is characterized by an increasing demand for affordable and sustainable energy sources, leading to an ever increasing integration of intermittent renewable energy resources into the grid. The intermittent nature of these sources has led to a growing interest in energy storage technologies, which can help to smooth out fluctuations in supply and demand and improve the overall stability and resilience of the grid. Pumped hydro storage power plants are a proven technology for energy storage, with the ability to store large amounts of energy for long periods of time. However, their conventional fixed speed operation lacks the required flexibility to follow the fluctuations in energy production resulting from intermittent renewable energy sources. By utilizing the energy stored in pumped hydro storage facilities in a more flexible manner, we can reduce our reliance on fossil fuels and increase the use of renewable energy sources, helping to mitigate climate change and improve the sustainability of our energy systems as well as techno-economical performances of these systems. This flexibility can be achieved through variable speed operation.

This thesis focuses on the use of the modular multilevel matrix converter in pumped hydro storage power plants to enable variable speed operation through the so-called converter fed synchronous machine configuration. The advantages of this variable speed configuration lie in its increased operating range and flexibility. The ratings of typical pumped hydro storage power plant units are within the ten to hundreds of MW combined with voltages in the tens of kV range. Achieving such ratings on the converter side requires emerging converter topologies such as the modular multilevel converter. Among this family of converters, the matrix topology outperforms the other topologies due to its better current sharing, which is further demonstrated in this thesis.

Being a modular converter topology, due to its series connection of cells with individual energy storage elements, raises control challenges as to keep the energy within the converter balanced through all the cells. A proven method for the validation of the control structure and algorithm is the so-called real-time hardware-in-the-loop tests, which are widely used in industry. This thesis demonstrates how this complex converter topology can be divided into multiple sub-circuits, which can be deployed on various small scale real-time simulators to build a real-time hardware-in-the-loop platform. This platform is used throughout this thesis to generate high fidelity results regarding control validation and system optimization.

With the hardware-in-the-loop platform developed, this thesis provides an in-depth analysis of the three main control loops, namely the internal energy balancing, grid side current control and machine side current control. The currently existing energy control algorithms are brought into a common reference frame to allow a thorough mathematical comparison revealing major differences in the execution of the given task. The hardware-in-the-loop platform serves as tool to validate the mathematical findings, which allow multi-dimensional performance analysis. Being a grid connected storage facility, grid code requirements have to be followed, which is demonstrated under various scenarios in this thesis.

In a pumped hydro storage facility, losses do not only have the economical impact by generating less profit, they are also wasting water, a valuable resource. Exploiting all degrees of freedom of the synchronous generator to minimize the losses of the overall system is another part of this thesis. The evaluation of all system losses, together with their implementation on the hardware-in-the-loop platform, is explained and allows for a very fast real-time optimization of the whole system.

**Keywords** matrix modular multilevel converter, ac-ac converter, pumped hydro storage, real-time simulations, hardware-in-the-loop, converter control



# Résumé

Le mixe énergétique mondial actuel se caractérise par une demande croissante de sources d'énergie abordables et durables, conduisant à une intégration toujours plus importante de sources d'énergie renouvelable à caractère intermittent dans le réseau électrique. La nature irrégulière de ces sources a suscité un intérêt croissant pour les technologies de stockage d'énergie, qui peuvent aider à lisser les fluctuations de l'offre et de la demande et ainsi améliorer la stabilité et la résilience globale du réseau. Les centrales hydroélectriques de pompage-turbinage sont une technologie éprouvée pour le stockage d'énergie, avec la capacité de stocker de grandes quantités d'énergie sur de longues périodes. Cependant, leur fonctionnement conventionnel, à vitesse fixe, manque la flexibilité requise pour suivre les fluctuations de production d'énergie provenant des sources intermittentes d'énergie renouvelable. En utilisant l'énergie stockée dans les installations de stockage hydroélectrique de manière plus flexible, il est possible de réduire la dépendance aux combustibles fossiles et d'augmenter l'utilisation de sources d'énergie renouvelable, contribuant ainsi à atténuer le changement climatique et à améliorer la durabilité de nos systèmes énergétiques. Cette flexibilité peut être obtenue grâce à une opération à vitesse variable des centrales hydroélectriques.

Cette thèse se concentre sur l'utilisation du convertisseur matrice multiniveaux modulaire dans les centrales hydroélectriques de pompage-turbinage pour permettre une opération à vitesse variable grâce à la configuration de la machine synchrone alimentée par convertisseur. Les avantages de cette configuration à vitesse variable résident dans sa plage de fonctionnement et sa flexibilité. Les puissances nominales des unités typiques des centrales hydroélectriques de pompage-turbinage se situent dans la plage des dizaines à plusieurs centaines de MW combinées à des tensions dans la plage des dizaines de kV. Pour atteindre de telles puissances nominales du côté du convertisseur, des topologies de convertisseur émergentes telles que le convertisseur multiniveaux modulaire sont nécessaires. Parmi cette famille de convertisseurs, la version matricielle surpasse les autres topologies en raison de sa meilleure répartition du courant, ce qui est également démontré dans cette thèse.

Étant une topologie de convertisseur modulaire, en raison de sa connexion en série de cellules avec des éléments de stockage d'énergie individuels, cela soulève des défis de contrôle pour maintenir l'énergie à l'intérieur du convertisseur équilibrée à travers toutes les cellules. Une méthode établie pour la validation de la structure de contrôle et de l'algorithme est celle du hardware-in-the-loop en temps réel, largement utilisée dans l'industrie. Cette thèse démontre comment cette topologie de convertisseur complexe peut être divisée en plusieurs sous-circuits, qui peuvent être implémentés sur divers petits simulateurs temps réel pour construire une plateforme hardware-in-the-loop en temps réel. Cette plateforme est utilisée tout au long de cette thèse pour générer des résultats de haute fidélité en ce qui concerne la validation de la commande et l'optimisation du système.

Avec la plateforme hardware-in-the-loop en temps réel développée, cette thèse fournit une analyse approfondie des trois boucles de contrôle principales, à savoir l'équilibrage interne de l'énergie, le contrôle du courant côté réseau et le contrôle du courant côté machine. Les algorithmes de contrôle de l'énergie existants sont mis dans le même référentiel pour permettre une comparaison mathématique approfondie révélant les principales différences dans l'exécution de la tâche donnée. La plateforme hardware-in-the-loop sert d'outil pour valider les résultats mathématiques, permettant une analyse de performance multidimensionnelle. Étant une installation de stockage connectée au réseau, les exigences du code du réseau doivent être respectées, ce qui est démontré dans cette thèse sous différents scénarios.

Dans une installation de stockage hydroélectriques de pompage-turbinage, les pertes ont non seule-

ment un impact économique en générant moins de profits, mais elles constituent également un gaspillage d'eau, une ressource précieuse. Exploiter tous les degrés de liberté du générateur synchrone pour minimiser les pertes de l'ensemble du système est un autre aspect de cette thèse. L'évaluation de toutes les pertes du système, ainsi que leur mise en œuvre sur la plateforme hardware-in-the-loop, est expliquée et permet une optimisation en temps réel très rapide de l'ensemble du système.

**Keywords** convertisseur matrice multiniveaux modulaire, convertisseur ac-ac, stockage hydroélectrique de pompage-turbinage, simulations en temps réel, hardware-in-the-loop, contrôle du convertisseur.

# Resumé

Déi aktuell global Energiesituatioun zeechent sech duerch eng ëmmer gréisser Nofro no bezuelbaren an nohaltegen Energiequellen aus, wat zu enger ëmmer gréisserer Integratioun vu sougenannte stochasteschen erneierbaren Energieressourcen an d'Netz féiert. Déi variabel Natur vun dese Quellen huet zu engem wuessenden Interessi un Energiespäichertechnologïe gefouert, déi derbäi hëllef kënnen, Schwankungen an der Versuergung an an der Demande auszegläichen an déi allgemeng Stabilitéit a Widderstandsfäegkeet vum Netz ze verbesseren. Duerch hir Fäegkeet grouss Quantitéiten un Energie iwwer länger Zäit ze späicheren, hu sech Pompspäicherkraaftwierker als Technologie fir d'Späichere vun Energie bewäert. Allerdéngs feelt hirem konventionellen Operatiounssystem mat fixer Dréizuel déi néideg Flexibilitéit, fir op d'Schwankungen an der Energieproduktioun, déi stochastesch erneierbar Energiequelle mat sech bréngen, ze reagéieren. Andeems mir d'Energie, déi a Pompspäicheranlage gespäichert ass, op eng méi flexibel Manéier notzen, kënnen mir eis Ofhängegkeet vu fossille Brennstoffer reduzéieren a méi erneierbar Energiequelle verwenden, fir esou dozou bäizedroen, de Klimawandel ofzebremsen an d'Nohaltegkeet vun eisen Energiesystemer esouwéi d'technesch-wirtschaftlech Leeschtunge vun dese Systemer ze verbesseren. Dës Flexibilitéit kann duerch variabel Operatiounssystemer, déi also eng verstellbar Dréizuel hunn, erreecht ginn.

Dës Dissertatioun konzentréiert sech op d'Verwendung vum Modulare Multilevel Matrix-Konverter a Pompspäicherkraaftwierker, deen, duerch déi Konverter gespeiste Synchronmaschinn-Konfiguratioun (converter fed synchronous machine configuration), de variablen Operatiounssystem erméiglecht. D'Virdeeler vun dëser variabler Dréizuelekonfiguratioun leien am erweiderten Operatiounsberäich an an der gréisserer Flexibilitéit. D'Leeschtung vun typeschen Unitéite vu Pompspäicherkraaftwierker läit tëschent zéng bis honnerte MW a Kombinatioun mat enger Spannung am zweestellige kV-Beräich. Fir dës Leeschtung och säitens vum Konverter ze errechen, brauch et modernste Konvertertopologïe wéi de Modulare Multilevel-Konverter. Ënnerhalb vun dëser Famill vu Konverteren, erbréngt de Matrix-Modell déi beschte Leeschtung am Verglach zu aneren Topologien opgrond vu senger besserer Stroumopdeeling, wat am Laf vun dëser Dissertatioun och nogewise gëtt.

Vu datt et sech, wéinst senger Reieschaltung vun Zelle mat individuellen Energiespäicherelementer, ëm eng modular Konvertertopologie handelt, bréngt dës gewëssen Erausforderunge bei der Steuerung mat sech. D'Energie ënnerhalb vum Konverter soll nämlech gläichméisseg iwwer all d'Zelle verdeelt sinn. Eng Method, déi sech fir d'Validatioun vun der Steuerungsstruktur an dem Algorithmus bewäert huet, sinn déi sougenannten Echtzäit „Hardware-in-the-Loop“-Tester, déi an der Industrie wäit verbreet sinn. Dës Dissertatioun weist, wéi dës komplex Konvertertopologie a verschidden ofgezweigte Schaltkreesser opgedeelt ka ginn, déi esou a méi klengem Mooss op verschiddenen Echtzäitsimulatoren agesat kënnen ginn, fir eng Echtzäit „Hardware-in-the-Loop“-Plattform ze kreéieren. Dës Plattform gëtt am Laf vun dëser Dissertatioun benotzt, fir besonnesch zouverlässeg Resultater betreffend der Steuerungsvalidatioun a Systemoptimiséierung ze generéieren.

An engem nächste Schrëtt analyséiert dës Dissertatioun am Detail déi dräi Haaptsteierkreesser: den internen Energie-Ausgläichsystem, d'Stroumsteuerung säitens vum Netz an d'Stroumsteuerung säitens der Maschinn. Déi aktuell Energiesteierungsalgorithmé ginn an e gemeinsaamt Referenzsystem gewandelt, fir e grëndleche mathematesche Verglach ze erméiglechen, dee grouss Ënnerscheeder an der Ausféierung vun der Aufgabestellung opweist. D'„Hardware-in-the-Loop“-Plattform déngt als Tool, fir déi mathematesch Erkenntnisser ze validéieren, déi eng multidimensional Performanceanalyse erlaben. Bei enger Späicheranlag, déi mam Netz verbonnen ass, mussen d'Netzuschloss-Reglementatioune respektéiert ginn, wat dës Dissertatioun unhand vu verschiddenen Zenarien demonstréiert.

An engem Pompspäicherkraaftwierk hu Verloschter, doduerch datt manner Gewënn generéiert gëtt, net nëmmen e wirtschaftlechen Impakt, mee se verschwenden och Waasser, eng wäertvoll Ressource. Och d'Ausnotze vun alle méigleche Fräiheeten, déi Synchrongeneratore bidden, fir d'Verloschter am gesamte System ze minimiséieren, gëtt an dëser Dissertatioun thematiséiert. D'Auswäertung vun alle Systemverloschter, zesumme mat der Ëmsetzung an der „Hardware-in-the-Loop“-Plattform, gëtt erkläert an erlaabt eng besonnesch séier Echtzäit-Optimiséierung vum ganze System.

**Keywords** Modulare Multilevel Matrix-Konverter, ac-ac Konverter, Pompspäicherkraaftwierker, Echtzäitsimulatiounen, hardware-in-the-loop, Konverter Steuerung

# Acknowledgments

*"If you have everything under control, you're not moving fast enough."*

Mario Andretti

Following my Master's thesis in the Power Electronics Laboratory (PEL), I was given the opportunity to continue and pursue a PhD degree. I would like to express my deepest appreciation and admiration to Prof. Dražen Dujić, who not only provided me with unwavering support throughout my four-year research journey, but also played a crucial role in shaping my perspectives on a range of non-scientific matters. His guidance and mentorship extended beyond the realm of academia, and I am truly grateful for his holistic approach to my personal and professional development.

I was extremely delighted to have Prof. Georgios Papafotiou from TU Eindhoven, Dr. Alexander Schwery from GE Renewable Energy and Dr. Elena Vagnoni from EPFL as the jury members. Their effort to read my work and be part of the examining process is highly appreciated. Also, I would like to thank Prof. Farhad Rachidi-Haeri, who gladly accepted the role of jury president.

Many thanks to Yanick for his meticulous proofreading of this document and to Lara for the amazing translation of the abstract into my native tongue (Luxembourgish).

In my opinion, a PhD can be compared in some ways to professional cycling, even though there is one person getting most of the glory, there is a whole team behind making sure to offer support in all situations. In my case, this team would be the PEL members, thus I would like to thank each one of them for making my PhD experience the unique one it was. From all the friendships created during my stay at PEL, I would like to thank in particular: Stefan for his guidance and never-ending support in all matters; Daniel, for his support regarding hydro machinery; Gabriele for his effort of both, maintaining the coffee breaks and not getting dropped; Chengmin (Chefmin), Max and *maybe* Changhwan for making running a fun activity; Nikolina, Xiaotong, Jules, Emilien, Marko and Andrea for being susceptible to all break-calls.

Furthermore, there have been a few friends that I would like to thank in particular for their support throughout this journey. Michael, Olivier and Cathia, for always freeing up time when I was back home, and for joining me in some challenging activities. Joé, for showing me how a PhD is supposed to be done. Marie, for being a consistent training partner and an excellent baker. Casper, for all the trash-TV evenings. Melik, for all the countless hours spent online and offline. Maurice (Moe), Sophie (Sophocle), Marielle, Julien (Jules), for the many bottles of wine and the great times spent together. The members of the *rushteam* triathlon club, for creating a fantastic training atmosphere, combining laughter and competitiveness, which helped me stay fit. The people from the *Malley-squad*, for ensuring that the next party was literally just a doorstep away.

It goes without saying that I am most thankful to my family for their unconditional love and support without which, this work would not have been possible. My niece Julie, even though she will not be able to read this. My brothers, Mathieu and Nicolas, for reminding me that I have yet to learn some things. My sister, Sylvie, who made me discover my love for dinosaurs. My parents, Brigitte and Romain, for their continuous support in every decision I make.

Finally, my biggest gratitude goes to my love, Lena! For the past four years she has been my biggest supporter and source of strength. Moreover, I am grateful for the wonderful bond I share with her family and the support they have provided. I eagerly anticipate embarking on the next chapter of my life in Sachseln with her by my side.

Lausanne, June 2023

Philippe Bontemps





# List of Abbreviations

2LVL	Two-Level
B2B	Back-to-Back
CFSM	Converter Fed Synchronous Machine
DFIM	Doubly Fed Induction Machine
DSOGI	Double Second-Order Generalized Integrator
DSP	Digital Signal Processor
ESR	Equivalent Series Resistance
FB	Full Bridge
FC	Frequency Converter
FEM	Finite Element Modeling
FLL	Frequency Lock Loop
FOL	Fiber Optical Link
FSFC	Full Size Frequency Converter
HB	Half Bridge
HIL	Hardware-In-The-Loop
HV	High Voltage
HVdc	High Voltage dc
IARC	Instantaneous Active and Reactive Control
IGBT	Insulated Gate Bipolar Transistors
IGCT	Integrated Gate-Commutated Thyristor
IM	Induction Machine
IMMC	Indirect Modular Multilevel Converter
LHP	Left Half-Plane
LVRT	Low Voltage Ride Through
M3C	Matrix Modular Multilevel Converter
ML	Multi-Link

MLDL	Multi-Link Device-Link
MMC	Modular Multilevel Converter
MOSFET	Metal–Oxide–Semiconductor Field-Effect Transistor
MV	Medium Voltage
NPC	Neutral Point Clamped
P-HIL	Power-Hardware-In-The-Loop
PDV	Pump Discharge Valve
PEL	Power Electronics Laboratory
PHSP	Pumped Hydro Storage Power Plant
PLL	Phase-Locked Loop
PSC	Phase Shifted Carrier
PV	Photo-Voltaic
PWM	Pulse-Width Modulation
RES	Renewable Energy Sources
RT	Real-Time
SM	Synchronous Machine
SVD	Singular Value Decomposition
VC	Virtual Capacitor
VR	Virtual Resistor
VS	Variable Speed
VSD	Variable Speed Drive

# Contents

<b>Abstract</b>	<b>i</b>
<b>Résumé</b>	<b>iii</b>
<b>Resumé</b>	<b>v</b>
<b>Acknowledgments</b>	<b>vii</b>
<b>List of Abbreviations</b>	<b>ix</b>
<b>1 Introduction</b>	<b>1</b>
1.1 Background	1
1.2 Fixed Speed Pumped Hydro Storage Power Plants	2
1.3 Change in the Energy Market	4
1.4 Flexible Operation of Pumped Hydro Storage Power Plants	5
1.4.1 Flexibility through hydraulic short circuit	5
1.4.2 Flexibility through high power electronics converters	7
1.5 Evolution of power converters for Medium Voltage (MV) Variable Speed Drive (VSD) applications	9
1.6 Objectives and contributions of the thesis	10
1.7 Outline of the thesis	12
1.8 List of publications	13
<b>2 The Modular Multilevel Converter in Pumped Hydro Storage Power Plants</b>	<b>15</b>
2.1 Variable Speed Pumped Hydro Storage Power Plants (PHSPs)	15
2.1.1 Doubly Fed Induction Machine	15
2.1.2 Converter Fed Synchronous Machine	18
2.2 Frequency converters for PHSPs using Converter Fed Synchronous Machine (CFSM)	19
2.2.1 Conventional NPC topologies	20
2.2.2 Modular Multilevel Converter (MMC) topology	21
2.3 The Matrix Modular Multilevel Converter (M3C)	26
2.3.1 M3C modeling	26
2.3.2 Control structure of the M3C	30
2.4 PHSP research platforms	31
2.4.1 Power-Hardware-In-The-Loop (P-HIL) research platform	32
2.4.2 Real-Time (RT)-Hardware-In-The-Loop (HIL) research platform	33
2.5 Summary	34
<b>3 Advantages of Variable Speed Drive Units</b>	<b>35</b>
3.1 Conventional PHSP operation	35
3.1.1 Start-up	35
3.1.2 Speed reversal	36
3.2 <i>Z'Mutt</i> power plant station	37
3.3 Operation of <i>Z'Mutt</i> U1 with a Frequency Converter (FC)	40
	xi

3.3.1	Modeling of the unit	41
3.3.2	Simulation results	42
3.4	Summary	44
<b>4</b>	<b>Hardware-in-the-Loop Test Platform</b>	<b>45</b>
4.1	RT-HIL hardware	45
4.1.1	Industrial control platform	45
4.1.2	Real-time simulation platform	47
4.2	Real-time modeling of the M <sub>3</sub> C	49
4.2.1	Branch modeling	49
4.2.2	Splitting of the M <sub>3</sub> C model	50
4.3	Validation of the model	53
4.3.1	Mathematical verification	53
4.3.2	Tuning of the VC	57
4.3.3	RT-HIL simulation verification	58
4.4	Summary	62
<b>5</b>	<b>Performance Comparison of Energy Balancing Algorithms for M<sub>3</sub>C</b>	<b>63</b>
5.1	Energy balancing requirements	63
5.2	Existing energy balancing control methods	66
5.2.1	Method 1: double $\alpha\beta 0$ transformation	67
5.2.2	Method 2: Null space vector projection	70
5.2.3	Method 3: Direct arm energy control	73
5.3	Performance comparison	76
5.3.1	Power reference comparison	76
5.3.2	Circulating currents comparison	78
5.4	HIL simulation results	80
5.5	Summary	84
<b>6</b>	<b>Grid Code Compliant Behavior of CFM in PHSP</b>	<b>87</b>
6.1	M <sub>3</sub> C control algorithms	87
6.1.1	Grid code requirements	88
6.1.2	Grid side control	89
6.1.3	Machine current control	89
6.1.4	M <sub>3</sub> C energy balancing	91
6.2	RT-HIL simulation results	93
6.2.1	Power reference change	93
6.2.2	Grid frequency deviation	95
6.2.3	Low voltage ride through	95
6.2.4	Single phase to ground fault	97
6.2.5	Voltage swell	97
6.3	Summary	99
<b>7</b>	<b>PHSP Variable Speed Drive Loss Minimization</b>	<b>101</b>
7.1	System description	101
7.2	Loss calculation of the M <sub>3</sub> C using sub-cycle averaged model	103

7.3	Synchronous machine loss determination and implementation	107
7.4	Optimal trajectory	111
7.5	RT-HIL experimental results	114
7.6	Summary	117
<b>8</b>	<b>Summary, Overall Conclusions and Future Works</b>	<b>119</b>
8.1	Summary and contributions	119
8.2	Future work	121
8.2.1	Operation with one faulty cell or faulty branch	121
8.2.2	M <sub>3</sub> C design optimization	122
8.2.3	Building the hardware	122
8.2.4	Integration in the P-HIL	122



# 1

## Introduction

### 1.1 Background

Power shortage, a term that is, unfortunately, more than ever present in the everyday life in 2023 due to an increasing energy demand while conventional power plants are being phased out from the grid to achieve EU climate objectives [1], [2]. Having enough installed capacity to cover the energy demand is a necessary but not sufficient condition to avoid power shortages. Only if the energy production is able to follow the demand curve, such power shortages can be avoided. While increasing the installed capacity of energy storage systems can resolve the issue at hand, the economically and ecologically more interesting solution is to invest into existing energy storage systems to increase their flexibility using power electronics.

Three major categories of energy power plants, each with its advantages and disadvantages, and designed for a specific role within the energy market, can be distinguished. The first one includes big thermal power plants, such as nuclear and coal, with the advantage of having a constant power output at a high efficiency and providing inertia to the grid. However, the major disadvantages of these power plants are the very long start-up times and their constant power output (base load) which is unable to follow the energy demand curve throughout the day. Additionally the ecological impact of coal power plants make it an unpopular option in future energy scenarios. The second category regroups the more flexible power plants, such as gas and hydropower, accounting for the fast energy variations between the demand and production from the first category of power plants. With a proper combination of power plants from these two categories, the energy demand can accurately be followed by the production. The third category includes all the stochastic energy generation sources, such as wind and solar. While the former one has the advantage of adding inertia to the grid, the main disadvantage of this category is the intermittent and stochastic energy production.

As seen in **Fig. 1.1**, the conventional thermal power plants, e.g. nuclear and coal, still hold the highest share of production in the EU while the Renewable Energy Sources (RES) account for 38.8% of the electricity production, as of 2022 [3]. Within the RES, wind turbines and hydropower plants are the biggest producers with 36.8% and 35.1%, respectively. The total net electricity generation for the given year in the EU was 2664TWh [4].

With the goal of the EU to be climate-neutral by 2050, and the objective of the Paris Agreement to limit the increase in temperature to 1.5°C above pre-industrial levels, greenhouse emitting power plants, such as coal, are being decommissioned and replaced by RES such as wind and solar [2], [5]. This translates into covering for the 35.6% of the electricity demand currently generated by fossil fuel power plants using mainly renewable energies.

Simply increasing the share of RES alone cannot be considered, as this generates grid stability problems

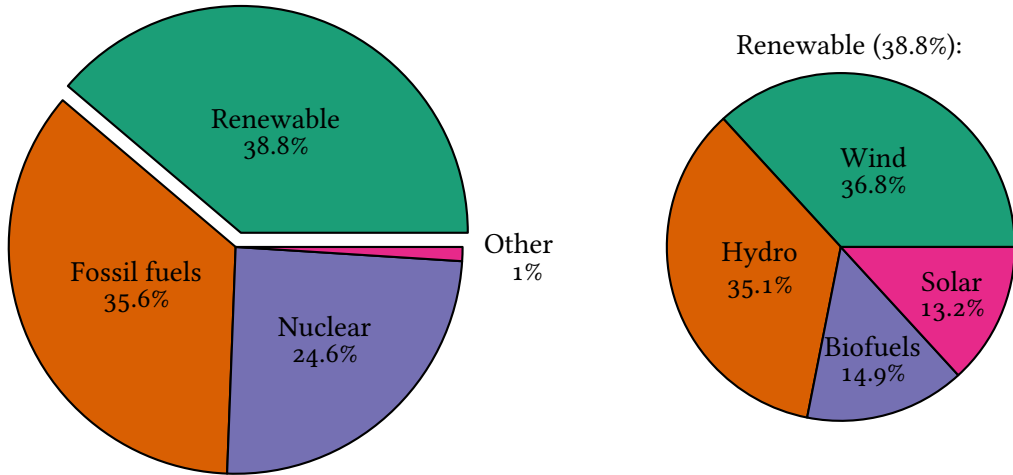


**Fig. 1.1** Source of electricity production in the EU in 2022. The right side shows the shares of the different types of RES covering 38.8% of the overall electricity demand [3].

leading to power system failures due to the highly intermittent nature of these sources. To maintain grid stability, it is required to develop large-scale grid-connected energy storage systems that are able to act as a buffer and compensate for the difference between electricity production and consumption.

While the battery technology is progressing rapidly, as of today, Pumped Hydro Storage Power Plant (PHSP) represent over 90% of the grid connected storage capacity on a worldwide as well as EU scale [6]. Most of these PHSP, which for the majority were build several decades ago, are operated as fixed-speed units and offer only limited flexibility, as they were developed for the power system of that time. Thus, to remain relevant on the power market and react to the fast changing energy generation of RES, a higher share of PHSP need to mitigate to variable speed.

## 1.2 Fixed Speed Pumped Hydro Storage Power Plants

Three main types of hydroelectric plants can be differentiated, namely run-of-river, storage and PHSP. From the previously mentioned types of hydroelectric power plants, the PHSPs are the most flexible one, as they allow for both, energy production and energy storage. A PHSP is generally constituted of an upper and lower reservoir between which the water flows through a pump/turbine connected to a generator, a representation of which is shown in **Fig. 1.2**. In pumping operation, the water is transferred through the hydraulic pump from the lower reservoir to the higher reservoir, thus the installation is absorbing energy from the grid and storing it as potential energy. The turbine operating mode is the exact opposite, where the potential energy of the water is used to spin the turbine together with the generator, thus injecting energy into the grid. The storage capacity of a PHSP is defined by the height difference between the reservoirs (hydraulic head) and the capacity of the reservoirs. The first installation was commissioned in 1890, making it the oldest and largest of all grid connected storage technologies [7]–[9]. It took, however, nearly another century for the society to recognize the potential of this storage technology which finally led in 1960 to a significant increase in the number of installations. PHSP have a very long storage time and very high storage capacity, and with a round trip efficiency typically between 70 and 85% [10].

Typical start-up times of big thermal power plants exceed 12 h, which is the reason why they



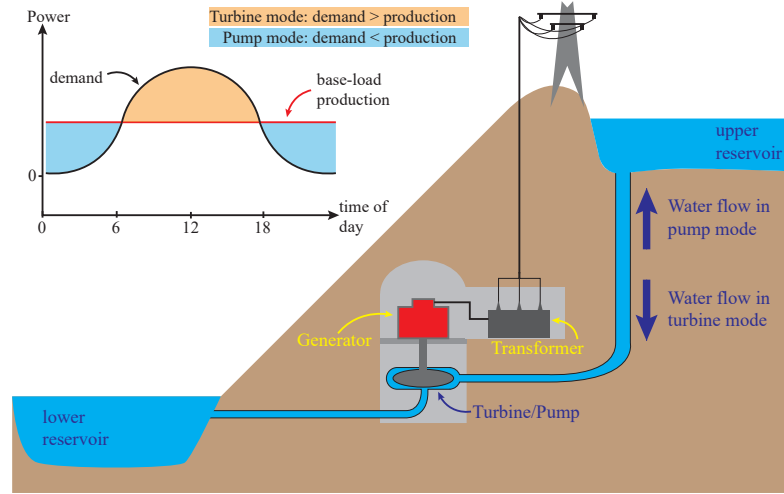


**Fig. 1.2** Simplified representation of a conventional fixed speed PHSP including an illustration of the operating mode depending on the energy demand and base-load production of conventional thermal power plants.

are generally run constantly throughout day and night. The deviation between this base energy production and the demand can be in part covered by PHSP. As illustrated on graph in **Fig. 1.2**, the energy demand during the day outweighs the night time demand, thus PHSP generally operate in turbine mode during the day and pump mode throughout the night, requiring two power reversal in a typical day. Whenever the energy demand is lower than expected, the excess energy generated by the conventional thermal power plants is offered on the market at a low price, which avoids switching them off. This constitutes the business case of a PHSP, pumping when the energy prices are low and releasing the energy when the demand and the prices are high.

Conventionally, the generator is a Synchronous Machine (SM) connected through a transformer directly to the grid. This setup is called a fixed speed PHSP, as the direct connection to the 50 Hz grid together with the fixed number of pole pairs of the SM defines the rotational speed. The hydraulic pump/turbine used in an installation is highly dependent on the hydraulic head of the installation, as seen in **Fig. 1.3**:

- Pelton turbine: used for high head installations ranging from 250 to 1000 m.
- Francis turbine: used for medium head installations ranging from 40 to 600 m.
- Kaplan turbine: used for low head installations ranging from 10 to 70 m.

Due to the concentrated water beam coming from the nostril, the Pelton turbine can only be used only in turbine mode. Combining two hydraulic units, shaft connected, to one single SM, including a Pelton turbine and an additional pump creates the so-called ternary system, allowing for a pump and turbine operation without change in rotational direction of the shaft. This setup features several advantages such as the fast pump start-up using the turbine to drive the shaft, as well as fast transitions between the operation modes. Drawbacks include the higher investment cost due to the high number of components, higher maintenance complexity and increased ventilation losses in pump mode due to the freely spinning turbine [11].

For the two other types of turbines, namely the Francis and Kaplan types, the operation as both turbine and pump is possible with one single hydraulic unit. However, the reversible pump-turbine

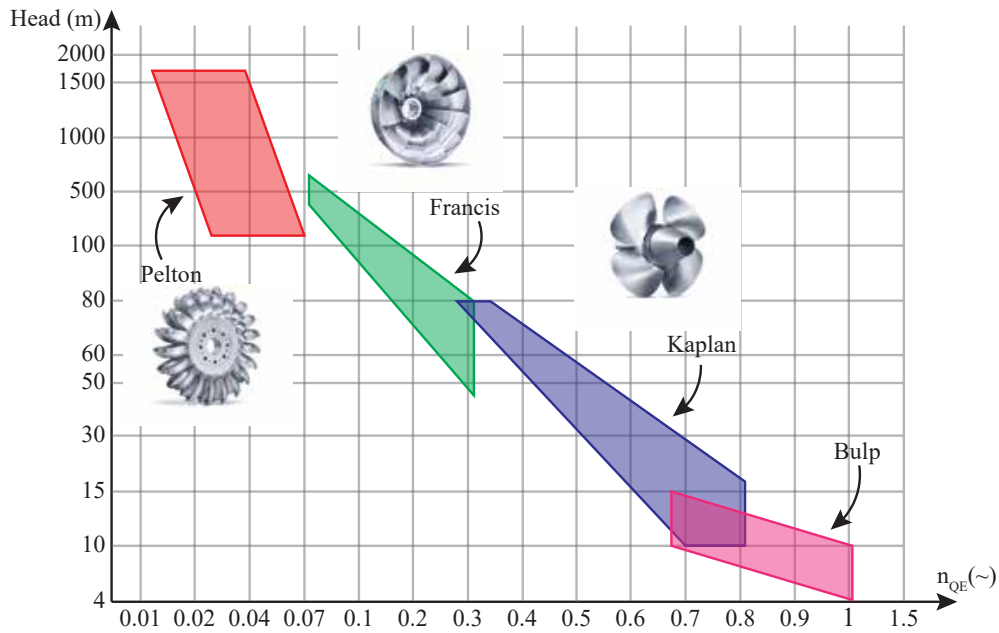


**Fig. 1.3** Type of turbine depending on the specific speed of the hydraulic machinery and the head of the installation.

requires a change in the shafts rotational direction to change between pump and turbine operation. A single reversible Francis type pump-turbine unit is the most common hydraulic system installed in PHSP [12], [13].

### 1.3 Change in the Energy Market

In recent years, RES such as wind and solar have seen a huge boom in their installed capacity. The two main elements contributing to this installation are on one hand the evolution of the power electronics converters achieving constantly higher reliability, efficiency and availability, and on the other hand economical subsidies that have increased the interest in RES. The two most common sources of renewable energy, excluding hydropower, are solar energy and wind energy, extracted using Photo-Voltaic (PV) and wind turbines respectively. Since 2012, the total installed wind energy capacity has more than doubled, reaching 236 GW in 2021 [14]. Additionally, the installed PV energy capacity has tripled in Europe between 2011 and 2020 to reach 161 GW [15]. In 2020, the share of RES installations in Europe represented nearly 50% of the total installed electricity capacity, compared to 34% in 2011 [15].

**Fig. 1.4** illustrates the installed capacity as well as the net produced electricity of a given energy source in Europe for 2020. While the installed capacity of RES represent nearly 50% of the total installed electricity capacity, it accounts for only around 33% of the produced net electricity, without including biofuels. This illustrates the difference between RES compared to, for example, the 11% of nuclear power which account for nearly one fourth of the overall electricity production.

For solar and wind energy, the energy production cannot be controlled, as they depend on the current weather situation. Their ever increasing share in the energy production requires energy storage

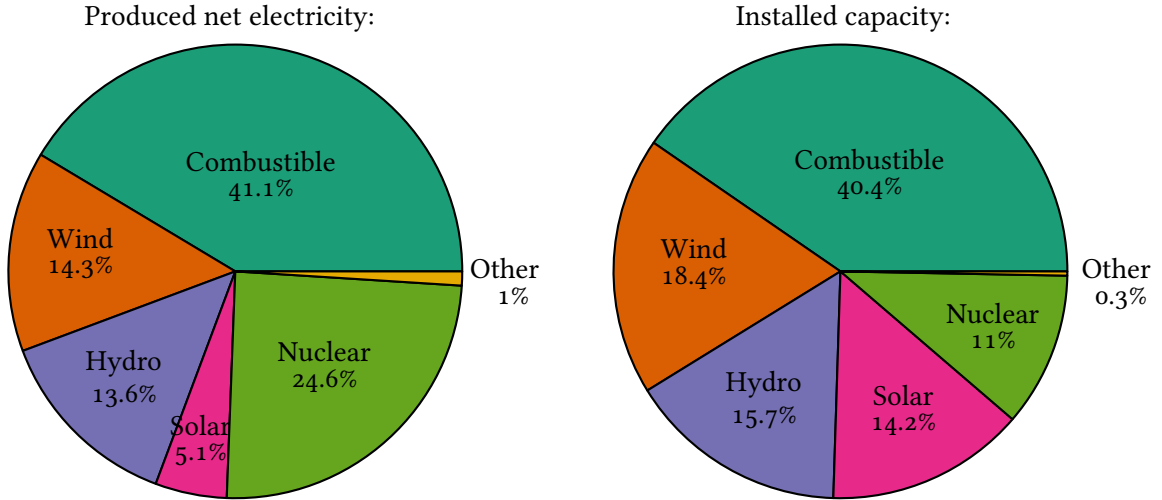


**Fig. 1.4** The left side shows the net electricity production from a given source in Europe in 2020. The right side shows the installed capacity in Europe of the given source for the same year. [4], [16].

solutions able to store these vast amounts of energy and release them when the demand is high. Several of these solutions are already present in the form of e.g. PHSP, compressed air storage, batteries and flywheels, to name a few. Currently PHSP is by far the most dominant grid connected storage system in terms of installed capacitance and battery storage projects start to emerge as their technology matures and their development cost is reduced [17]. Their high share of installed capacity makes it worthwhile to analyze the performance of PHSPs in the changing energy market.

The energy market has to provide the right incentives to make sure that the power plants contribute to ensure reliability and availability of the energy supply to the consumers. The highly intermittent nature of the RES creates a less predictable production, thus creating a high variation in the energy price throughout the day, to which the PHSP needs to be able to react as to stay profitable. PHSPs realize their profit through the difference in energy prices between the times where the units operate in turbine mode and the times where it operates in pumping mode, thus a faster reaction to the energy market price translates into higher profits.

## 1.4 Flexible Operation of Pumped Hydro Storage Power Plants

Flexible operation of the PHSP is defined by the ability of the PHSP to react to changes in energy production and demand as well as to provide ancillary services to the grid. Previously mentioned fixed speed units operated as a single unit in either pump or turbine mode do not fulfill these requirements. Two possibilities increasing the flexibility of PHSP are presented below, the first one relying on the hydraulic short circuit operation and the second one relying on the use of a power electronics Frequency Converter (FC), presenting a mechanic and an electric solution.

### 1.4.1 Flexibility through hydraulic short circuit

While it is possible for fixed speed units to operate at variable power when in turbine mode, in pump mode the power consumed from the grid is fixed and defined by the hydraulic head of the installation. To achieve flexibility in power consumption when in pumping mode, the so-called hydraulic short

circuit operation can be used [11], [18]. **Fig. 1.5** illustrates the hydraulic short circuit operation mode using two configurations as an example. Having the goal of enabling variable power consumption from the grid, means that the pumping power remains greater than the turbine power, and the overall water flow is from the lower to the upper reservoir. However, instead of only pumping from the lower to the upper reservoirs, part of the water is also fed to the turbine. While the pump unit is still consuming the fixed power defined by the hydraulic head, due to the flexible power generation from the turbine, the total power consumed from the grid becomes variable as it is the difference between the pumping and generating power.

By increasing the amount of water transferred between the pump and the turbine, the overall electrical power consumption of the unit is reduced as the power generation of the turbine is increased. Increasing the flow to the upper reservoir will increase the power consumption and reaches a maximum when the turbine is entirely disconnected and all the water is pumped to the upper reservoir.

**Fig. 1.5(a)** illustrates the possibility of operating a ternary unit in hydraulic short circuit. A ternary unit is constituted by a single SM connected through the same shaft to a pump and a turbine. This simplifies the hydraulic short circuit operation as both water inlets and outlets are connected close to the unit itself. In addition to enabling a variable power consumption, this configuration allows for a very fast transition from pumping to turbine mode as no change of direction of the shaft is required. Start-up time of the unit in pump mode is significantly reduced, as the turbine can be used to drive the shaft. Finally, this configuration has the advantage of choosing an optimal pump and turbine separately, thus increasing their efficiency [19].

However, the initial investment cost of a ternary unit is very high due to the increased civil engineering cost and the increased shaft complexity. Additionally, ternary units have increased ventilation losses due to the turbine spinning freely in pumping mode.

**Fig. 1.5(b)** illustrates the hydraulic short circuit operation using two separated units. As displayed, this operation is only possible if both water inlets and outlets are connected and allow a water flow between two units. The principle remains the same as for the ternary unit, with the main difference that two SM that are connected to the same grid are used. As one SM is operating as a generator and the other one as a load, the difference of the consumed and produced energy is what can be observed from the grid.

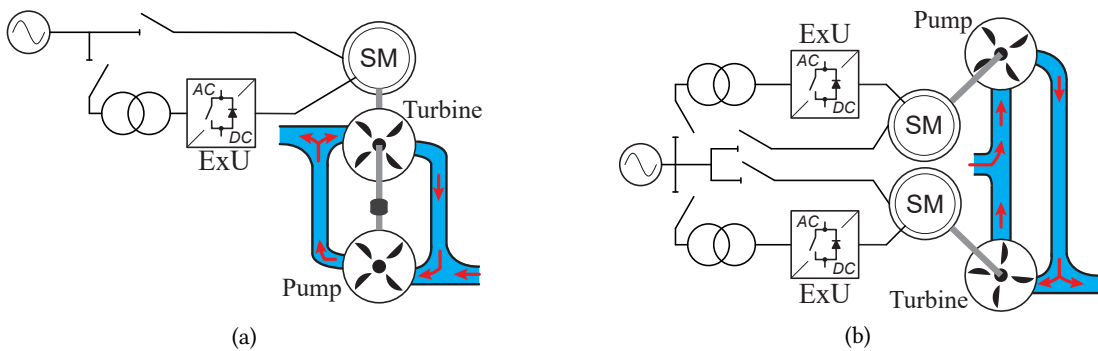


**Fig. 1.5** Simplified representation of two typical hydraulic short circuit configuration. One using a ternary unit as shown in (a) and the second one relying on two separate units shown in (b).

Even if the hydraulic short circuit operation with two separate machines allows for a variable pumping power consumption, this configuration does not demonstrate any of the other advantages of the ternary unit as the two units are separated.

The ternary unit demonstrates typical flexibility characteristics needed to react to the fast changes of the stochastic energy production of RES. However, the main disadvantages related to having both a turbine and a pump connected to the SM through the same shaft requires a special power plant layout to be considered in contrast to other variable speed options. Variable speed operation of the unit requires the use of a FC to enable variable frequency operation of the machine connected to a fixed frequency grid.

### 1.4.2 Flexibility through high power electronics converters

The use of Variable Speed Drive (VSD) started in 1990 in Japan and is becoming increasingly more popular as the share of RES requires a more flexible energy storage method allowing for fast power reversals. Being a well established technology, the advantages of VSD in PHSP are well known and presented in various papers [12], [20]–[25]. However, as of today, the share of VSD represent only around 0.9% of the installed hydropower capacity [26]. Two distinct types of advantages can be distinguished compared to fixed speed installations, on one hand the additional grid service that can be provided, and on the other hand the advantages for the hydraulic installation. From a grid services point of view the advantages are:

- Instantaneous response to fast variation in power demand using the energy stored in the rotating mass of the rotor connected to the turbine.
- Variable power consumption while in pumping mode, allowing to contribute to the grid frequency control.
- Black start-ups as well as faster regular start-ups without necessarily dewatering the chamber.
- Fast power reversal transitions, allowing for a fast reaction to significant changes in the energy demand and reducing the loss of water.

Furthermore, additional benefits on the hydraulic machinery is achieved through the implementation

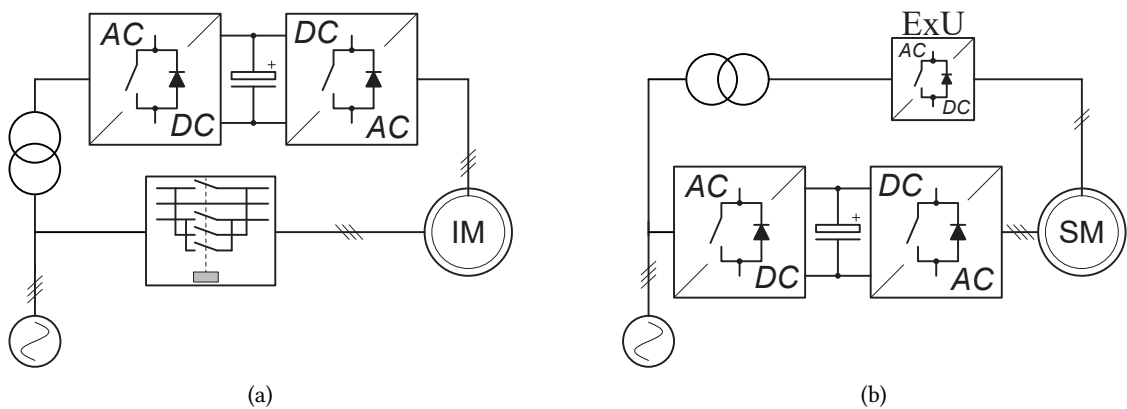


**Fig. 1.6** Simplified representation of two typical variable speed drive configurations used in PHSP, (a) DFIM and (b) CFMSM.

of VSD:

- Operation at the highest hydraulic efficiency by considering the variation in the hydraulic head.
- Extension of the operating range considering the differences between the minimum and maximum head.
- Reduced hydraulic stress, increasing the availability of the hydraulic unit as well as increasing the machinery lifetime.

Two main configurations of VSD PHSP exist, namely the Doubly Fed Induction Machine (DFIM) and the Converter Fed Synchronous Machine (CFSM) [27]. While the two configurations have distinct features, they both share the need of a power electronics converter, allowing for the variation of the machine mechanical speed to the fixed grid frequency of 50 Hz. An illustration of both configurations can be seen in **Fig. 1.6**. For the CFSM, depending on the type of FC, up to two additional transformers are required to match the voltage between the FC and the grid as well as the stator of the machine.

**Tab. 1.1** Variable speed PHSP in the range of hundreds of MW currently in operation or under construction, arranged by individual power rating. Only two installations are based on Converter Fed Synchronous Machine (CFSM) and currently in operation: Grimsel 2 being a retrofit and Malta 2 comprising new machines and converters.

Name	Country	Type	Turbine power [MW]	No. of units	Total power [MW]
Kazunogawa	Japan	DFIM	460	2	920
Okawachi	Japan	DFIM	395	2	790
Frades 2	Portugal	DFIM	390	2	780
Okukiyotsu 2	Japan	DFIM	340	1	340
Snowy II (2026)	Australia	DFIM	333	3	1000
Omarugawa	Japan	DFIM	330	3	990
Okutataragi	Japan	DFIM	320	2	640
Omarugawa	Japan	DFIM	310	1	310
Shiobara	Japan	DFIM	309	1	309
Fengning	China	DFIM	300	2	600
Goldisthal	Germany	DFIM	265	2	530
Linth-Limmern	Switzerland	DFIM	250	4	1000
Tehri	India	DFIM	250	4	1000
Kaprun Limberg III (2025)	Austria	DFIM	240	2	480
Kyogoku	Japan	DFIM	230	2	460
Avče	Slovenia	DFIM	180	1	180
Nant de Drance	Switzerland	DFIM	150	6	900
Takami 2	Japan	DFIM	103	1	103
Hatta	UAE	DFIM	125	2	250
Grimsel 2	Switzerland	CFSM	100	1	100
Kühtai (2026)	Austria	CFSM	95	2	190
Tauernmoos (2025)	Austria	CFSM	85	2	170
Malta 2	Austria	CFSM	80	2	160

The simplified illustration on **Fig. 1.6** shows in each case a Back-to-Back (B2B) connection of two ac/dc stages with a common capacitance connecting the machine to the grid. This illustration should indicate that an ac/ac conversion is required between the machine and the grid, but should, by no means, indicate that the converter topologies are limited to the illustrated one. For the DFIM configuration, as shown in **Fig. 1.6** (a), this converter is installed on the rotor side and controls the slip frequency of the machine. On the SM, as shown in **Fig. 1.6** (b), the converter is processing the full stator power. Additionally this configuration requires an excitation unit, labeled ExU on the figure, on the rotor side generating the magnetic flux.

**Tab. 1.1** shows all the existing VSD PHSPs in the range of hundreds of MW that are currently operational or under construction in the world.

## 1.5 Evolution of power converters for Medium Voltage (MV) VSD applications

The electric motor was invented in 1834 by Moritz Hermann Jacobi and throughout the 20th century it gained in popularity for various applications [28]. Today, it constitutes the biggest consumer of electrical energy, accounting for 70% of the overall electrical energy consumption [29]. However, it required the development of power semiconductor devices in the late 1950's to allow variable speed operation, and with the advancement in power electronics came the increased popularity of VSD.

Large scale deployment of power electronics started with the invention of the thyristors by General Electric in 1957 [30]. The first high speed train using a dc drive with diode rectifiers began its operation in 1964 and the first electric car using an Induction Machine (IM) and a thyristor inverter was launched the same year [31], [32]. **Fig. 1.7** (a) shows the layout of the thyristor inverter. The development of power Metal–Oxide–Semiconductor Field-Effect Transistors (MOSFETs) in the 1970's allowed the development of the V/f control method and later the field oriented or vector control technique to improve the performance of ac drives [33], [34]. **Fig. 1.7** (b) shows the inverter using series connection of IGBT semiconductor devices. It is, however, only in 2001 that the MMC topology was introduced which then, years later, found its first deployment in High Voltage dc (HVdc) applications [35], [36]. The advantages of this topology that will be further explored in **Chap. 2**, make it suitable for machine applications.

In parallel to the inverters, another type of converters started to emerge, namely the family of the matrix converters. They differentiate themselves from the previously introduced converters as they have the ability to transform the input terminal ac voltage directly to an output ac voltage with a different frequency and amplitude. **Fig. 1.7** (d) shows the cycloconverter, which is a naturally commutated converter as the thyristors are turned off only with the correct polarity, which depends on the input ac voltages. It required the invention of the bi-directional switch to allow switching on and off independently of external voltages for the matrix converter, as shown in **Fig. 1.7** (e), to be invented. The development of this converter started in 1980's, where it was first called by its current name, matrix converter. Firstly used for wind power applications, the M3C as shown in **Fig. 1.7** (f) was presented with two cells in 2001 [37].

Due to its advantages over the other converter topologies shown in **Fig. 1.7**, the M3C presents itself as good alternative for high power ac applications, which will be covered in **Chap. 2** [38]. PHSPs applications fall within this set of applications, thus the deployment of the M3C in these applications

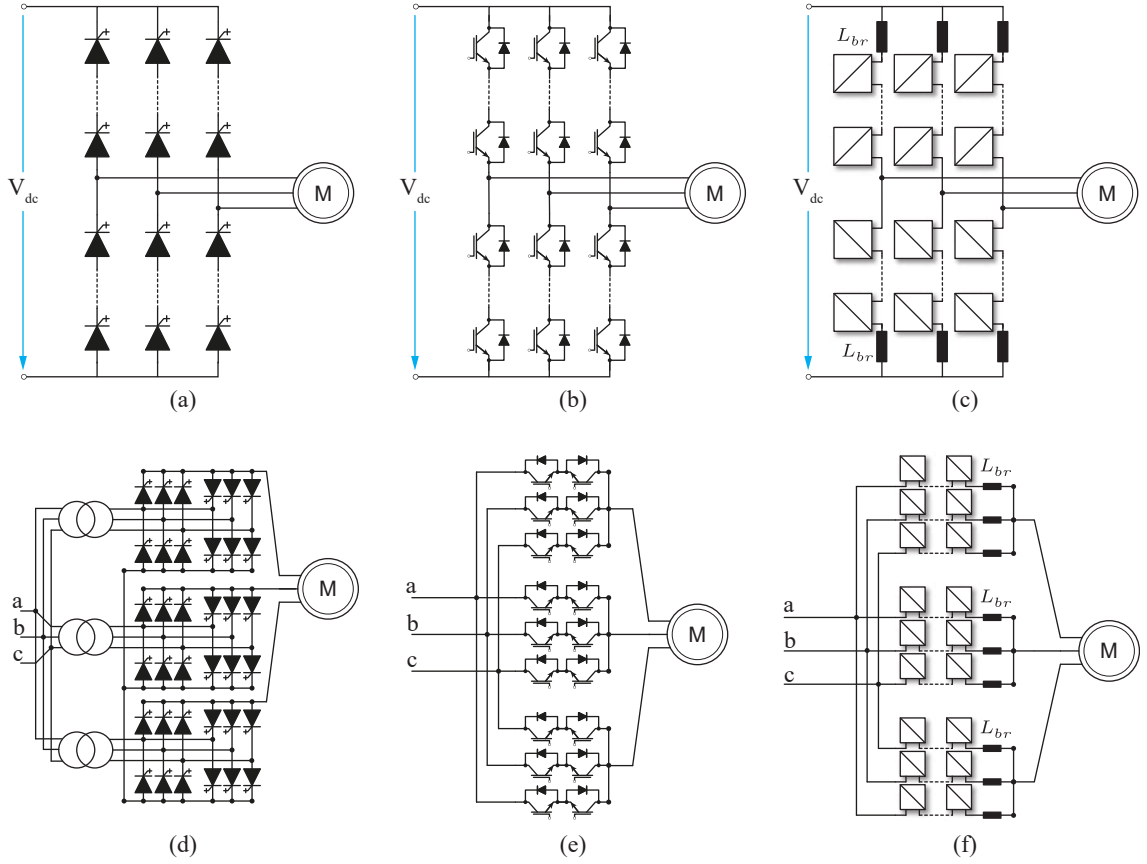


**Fig. 1.7** Development of converters for machine applications. (a)-(c) depicts converters performing a dc-ac conversion, (a) shows the thyristor inverter, (b) shows the IGBT inverter and (c) the Modular Multilevel Converter (MMC) inverter. (d)-(f) illustrates converters doing a direct ac-to-ac conversion, changing both the amplitude and frequency of the input voltage. (d) shows the cycloconverter, requiring, as illustrated three phase shift transformers, (b) shows the matrix converter using bi-directional switches and (f) shows the Matrix Modular Multilevel Converter (M3C) based on a series connection of Full Bridge (FB) cells.

is worth to be further analyzed. The relevance of this topic is demonstrated by the fact that in 2022 the first PHSP with a CFM and using a M3C has been commissioned [39]. Further details about this world's first installation will be covered in **Chap. 2**.

## 1.6 Objectives and contributions of the thesis

The main objectives and contributions of this thesis are:

- The inaccessibility of converters fulfilling the ratings needed for PHSP, together with the complexity of MMC topology, require a thorough verification process of the control structure before the deployment in the field. This thesis includes the development of a Real-Time (RT)-Hardware-In-The-Loop (HIL) platform using small scale simulators where the hardware part includes the whole control structure of the M3C based on the industrial controllers from ABB, the AC800PEC. Throughout this thesis, this research platform is used for the validation of all control related developments.



- The final verification step regarding control structure and algorithm is the RT-HIL verifications. On this platform, the power elements of the M3C together with the grid and applications are modeled on RT computers, while the control structure is implemented as for the final prototype. However, topologies such as the M3C rely on the use of a series connection of FB cells, which requires a high number of switches, thus resulting in a high number of switching states. For RT computers which rely on the usage of state-space matrices, modeling such a complex system with such a high number of state space matrices is impossible. To enable RT simulations on small scale simulators that rely on the usage of state-space matrix computation, a significant reduction in switching states needs to be achieved without altering the functionalities of the initial model. This thesis demonstrates the usage of Virtual Capacitor (VC) and Virtual Resistor (VR) to modify the implementation of the M3C model and reduce the number of state space matrices. The achieved reduction allows for a complex system, such as the M3C, to be deployed on small scale simulators, such as the PLEXIM RT Box 1.
- In addition to conventional converter control algorithms, the MMC requires a control layer to regulate the so-called circulating currents to enable the balancing of the energy among the branches of the converter, thus allowing its correct functioning. Three different approaches to the energy balancing control challenge exist in the literature, and this thesis covers theoretical gaps that still exist in the theory of the M3C. While all three methods achieve the required goal, they rely on different mathematical transformations and are not sharing a common reference frame. Thus, all three methods differentiate each other in matter of performance, implementation simplicity and understandability. This thesis converts all methods to the same reference frame and performs a thorough theoretical comparison, highlighting the reasons for their various performances. The implementation of the RT-HIL platform allows for an experimental validation of the theoretical findings.
- Aid in development of a 600 kVA M3C prototype by development of the control hardware structure as well as the control software. The validation of this control structure, as well as control algorithms including the grid code complying behavior and the SM control, is done on the RT-HIL system.
- Recent developments in the energy market require large scale grid storage methods such as PHSPs to increase their flexibility to allow a fast reaction to the difference in energy demand and production due to the large scale integration of RES. This thesis demonstrates how the M3C can be deployed as to achieve the required flexibility to ensure the profitability of PHSPs on the changing energy market. This thesis includes HIL results illustrating the increased transient performance and grid compliant behavior of PHSP using a M3C.
- Reacting to fast changing power references from the grid leads to an increase of start-stop transients of Variable Speed (VS) PHSP units. This involves an increased interest in an efficiency optimization of these transients to reduce power and water losses. Additionally, pumping at variable speed involves steady-state operation at speeds which differ from the nominal speed of the SM. This thesis includes an efficiency optimization of both steady-state and start-stop transients on the RT-HIL platform.
- To evaluate the losses and perform an efficiency optimization of the system, both the M3C as well as SM losses need to be determined. This thesis describes a method to implement the all M3C losses on the RT-HIL platform, including semiconductor switching and conduction

losses, in a computational efficient way without modeling individual switches. Additionally the measurement process to determine all SM losses as well as the implementation on the RT-HIL is included within the thesis.

## 1.7 Outline of the thesis

The thesis is organized into eight chapters:

- **Chapter 2** introduces the various VSD options for PHSP with their respective advantages and disadvantages, followed by a description of the two biggest existing CFSM PHSP installations. Basic operating principles of conventional Neutral Point Clamped (NPC) converter topologies are described and the impact of emerging topologies such as the MMC is discussed. A comparison of the two topologies within the MMC family, namely the Indirect Modular Multilevel Converter (IMMC) and M3C depicting the advantages and inconveniences of each of them is included. Finally, a thorough description of the M3C operating principle and a description of the existing control loops is covered.
- **Chapter 3** illustrates the advantages of VSD operation of PHSPs with a special focus on the benefits for the hydraulic machinery, the power plant operator and the additional grid services that emerge from the CFSM implementation. These advantages are mostly independent of the converter topology and for this reason, this chapter does not focus on a specific converter topology, but rather illustrates the advantages of the CFSM in PHSP.
- **Chapter 4** focuses on the RT-HIL implementation of the M3C. Modeling challenges arising from a complex system like the M3C, including multiple switches, are developed and solved. The final model is optimized to an extend of being able to run in RT on small scale simulators such as the PLECS RT Box 1. This chapter includes a description of the hardware included in the HIL and illustrated the interconnection between the elements. Finally, a thorough analysis of the simulation results is conducted, to prove their validity and to make sure the modified model behaves equivalent to the initial one.
- **Chapter 5** comprehensively compares the three existing control methods for balancing the energy among the branches of the M3C. Only three different methods can be found in the literature, and these three are thoroughly explained in order to fill any theoretical gaps that exist. As they are developed in different reference frames, a theoretical comparison is only possible if all the methods are brought in the same reference frame, which is included in this chapter. After the theoretical development, all the findings are verified by HIL simulations.
- **Chapter 6** depicts the advantages of the CFSM configuration in PHSP using a M3C. Compliance with existing grid code requirements is proven and the given converter control is explained. Proper operation of the M3C for hydraulic transients that might be encountered is proven using the previously described HIL.
- **Chapter 7** covers the optimal operation of the PHSP exploring all degrees of freedom, namely the SM excitation current as well as the SM stator current components. The determination of the SM losses depending on its operating point is done using experimental results executed on a 500 kW SM installed in the Power Electronics Laboratory (PEL). Before the validation of the optimal operation is conducted on the RT-HIL platform, the loss computation of all the

elements is added into the RT model, which is further described in this chapter.

- **Chapter 8** concludes the work and provides an outlook for future work.

## 1.8 List of publications

Journal papers:

- J1. **P. Bontemps**, D. Biner, C. Münch-Alligné, *et al.*, “Online loss calculation and optimization of a m3c driven externally excited sm,” *IEEE Transactions on Industrial Electronics*, 2023
- J2. M. Utvić, **P. Bontemps**, and D. Dujic, “Direct arm energy control of the modular multilevel matrix converter,” *IEEE Access*, vol. 11, pp. 1793–1805, 2023
- J3. **P. Bontemps**, S. Milovanovic, and D. Dujic, “Performance analysis of energy balancing methods for matrix modular multilevel converters,” *IEEE Transactions on Power Electronics*, pp. 1–15, 2022
- J4. **P. Bontemps**, S. Milovanovic, and D. Dujic, “Distributed real-time model of the m3c for hil systems using small-scale simulators,” *IEEE Open Journal of Power Electronics*, vol. 2, pp. 603–613, 2021

Conference papers:

- C1. **P. Bontemps**, S. Milovanovic, and D. Dujic, “Virtual capacitor concept for partitioning of large converter systems for rt-hil simulations,” in *2022 International Power Electronics Conference (IPEC-Himeji 2022- ECCE Asia)*, 2022, pp. 1801–1808
- C2. **P. Bontemps** and D. Dujic, “Flexible operation of variable speed direct-mmc in hydropower applications,” in *PCIM Europe 2022; International Exhibition and Conference for Power Electronics, Intelligent Motion, Renewable Energy and Energy Management*, 2022, pp. 1–9
- C3. **P. Bontemps**, N. Hugo, and D. Dujic, “Flexibility enhancements in pumped hydro storage power plants through variable speed drives,” in *IECON 2020 The 46th Annual Conference of the IEEE Industrial Electronics Society*, 2020, pp. 1820–1825

Other publications, not directly related to the scope of the thesis:

- O1. D. Biner, **P. Bontemps**, D. Dujic, *et al.*, “Discretization uncertainties of flow and fatigue damage simulations of a reversible francis pump-turbine at off-design operation in turbine mode,” in *Advances in Hydroinformatics*, P. Gourbesville and G. Caignaert, Eds., Singapore: Springer Nature Singapore, 2022, pp. 649–670



# 2

## The Modular Multilevel Converter in Pumped Hydro Storage Power Plants

*This chapter covers the details of the various variable speed drive configurations available for pumped hydro storage power plants while pointing out the differences, inconveniences and advantages of each implementation. Additionally, the modular multilevel converter topology is explained in detail and its differences compared to conventional converter topologies are pointed out. Within the family of modular multilevel converters, the two main topologies allowing for an ac-to-ac conversion, namely the indirect modular multilevel converter and the matrix modular multilevel converter are illustrated, explained and compared. Finally, the working principles and control structure of the matrix modular multilevel converter are presented.*

### 2.1 Variable Speed PHSPs

As pointed out in the introduction, PHSPs conventionally operate at fixed speed with a direct connection to the grid. However, nowadays they require more flexibility as to remain competitive. Being a well established technology deployed for decades leads to a multitude of installations reaching 50 years of operation, where replacement of some parts, due to aging, is required. This constitutes a perfect time to modernize the installation and convert the fixed speed unit into a VSD [40]. Independently of the chosen implementation, the variable speed operation of a PHSP has significant advantages over fixed speed units:

- Regulating power consumption when in pumping mode by varying the rotational speed of the hydraulic machinery.
- Higher efficiency due to optimal choice of rotational speed depending on the current available hydraulic head.
- Reducing water loss during transients as well as reducing wear and tear due to the operation at optimal speed.
- Better dynamic responses in case of grid disturbances, thus increasing grid stability.

#### 2.1.1 Doubly Fed Induction Machine

Among the two VSD configurations for PHSPs introduced in **Chap. 1**, the DFIM, as shown in **Fig. 2.1**, is currently significantly more popular than the CFM. The reason being that the FC is connected to the rotor of the DFIM, thus only required to be rated at the rotor power. Any variation from the synchronous speed creates the so-called slip, which is directly proportional to the rotor power.

Thus the higher the speed variation, the higher the rotor power and in turn also the rating of the FC. Typically, in steady state operation, a VSD PHSP does not exceed a speed variation of  $\pm 10\%$  as any further deviation from the synchronous speed exceeds the stability limits of the hydraulic machinery. In pumping mode, a speed variation of  $\pm 10\%$  translates to a  $\pm 30\%$  power variation as for the same hydraulic head, a reduced speed impacts the water flow through the pump and impacts the shaft torque proportionally to the speed [41].

The slip is defined as being the difference between the stator frequency and the mechanical speed, usually expressed in relation to the synchronous speed.

$$s = \frac{\omega_m - \omega_s}{\omega_s} \quad (2.1)$$

Three main operating regime, which are illustrated in **Fig. 2.2**, can be differentiated for a DFIM:

- Subsynchronous operation:  $\omega_m < \omega_s \rightarrow s > 0$
- Synchronous operation:  $\omega_m = \omega_s \rightarrow s = 0$
- Supersynchronous operation:  $\omega_m > \omega_s \rightarrow s < 0$

It is well known that with the slip  $s$  defined above, the rotor power can be expressed as [42]:

$$P_r = -sP_s \quad (2.2)$$

With the expression above, it is straightforward to conclude that the FC connected to the rotor has the requirement of a bidirectional power flow. Additionally, with the maximum allowed deviation from the rated synchronous speed, the minimum required power rating of the converter can be determined. With typical power levels of PHSP units ranging from a few MW up to 460 MW, as in the Kazunogawa pumped storage power plant in Japan, the power requirements of the FC remain below 100 MW [43]. Within this power requirement range, conventional FC, which have the benefit of being commercially available and a proven technology, can be considered. It yields that, due to the current state of the power electronics FC, this topology is significantly more popular than the CFSM [44]–[46].

Nevertheless, even being the dominant variable speed configuration for PHSP, the DFIM does not come without drawbacks. While the reduced power FC allows the use of conventional topologies and industrial available products, it is also the cause of some disadvantages of this configuration. In

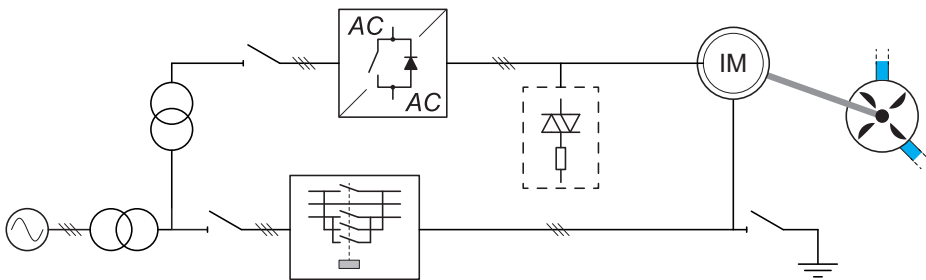


**Fig. 2.1** Details of the DFIM installation. The rotor of the DFIM is connected to a FC, whereas the stator is connected through switchgear to the grid. The crowbar for Low Voltage Ride Through (LVRT) protection is directly connected to the rotor.

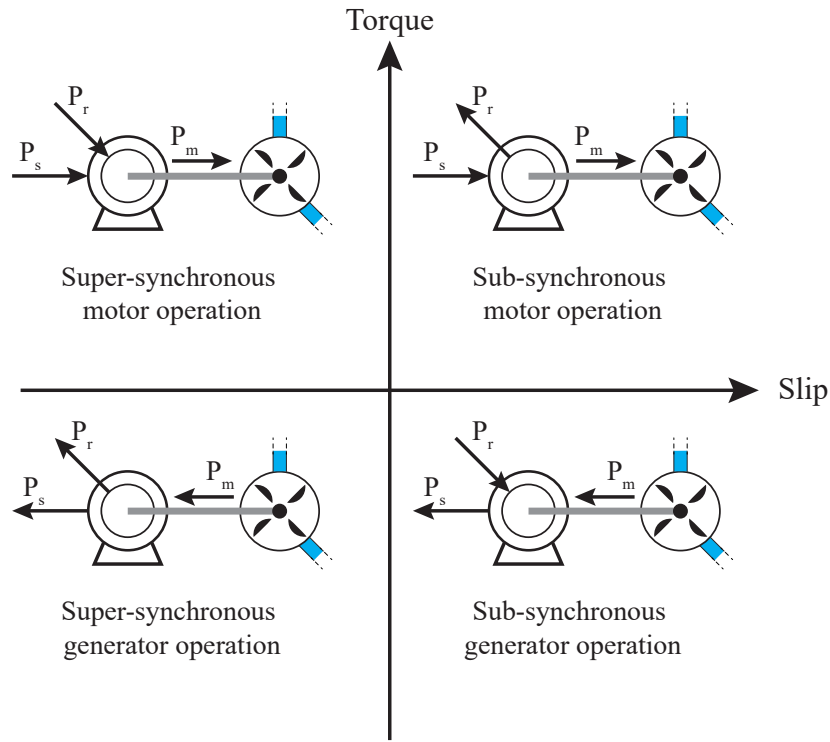


**Fig. 2.2** Power flows for the various operation modes of the DFIM.

addition, the direct connection of the machine stator to the grid requires additional considerations. The main disadvantages of this topology are listed below:

- Limited start-up torque, leading not only to higher starting time in pumping mode, but also increasing the time to transition between turbine and pump mode. Furthermore, dewatering of the chamber, which requires not only additional de-watering system, but leads also to an increase in time of the starting sequence.
- Additional protections schemes are required for the case of a LVRT grid fault. As the machine stator flux does not follow the fast variation of the stator voltage, the rotor voltage is required to rise significantly to avoid a sudden peak in the rotor current. The FC is usually not dimensioned for such a high voltage and to avoid a loss of control, an additional protection device, a so-called crowbar, has to be installed on the rotor. As the crowbar protects the converter from high current, it has to be rated for these high currents that might occur during a LVRT. They are usually build using thyristors.
- In addition to the above mentioned drawbacks related to the FC, it is to be noted that the machine design is rendered difficult by the wound rotor and the slip rings, which also include additional maintenance.
- With the stator directly connected to the grid, a complex synchronization procedure needs to be implemented and requires additional equipment to connect to the grid.
- Phase reversal equipment is required to allow bi-directional rotation of the DFIM. As this

switchgear is connected to the stator of the machine, it requires the same voltage and current ratings.

Despite the disadvantages listed above, the feasibility of this solution considering the FC as well as the coverage of the whole acceptable speed variation make it the most popular VSD configuration for PHSPs. Recent advances in power electronics semiconductor technologies and converter topologies allow for ever increasing FC power ratings, thus allowing to consider CFSM and eliminate the above mentioned drawbacks of the DFIM configuration [47].

### 2.1.2 Converter Fed Synchronous Machine

By inserting a FC between the stator of a SM and the grid, as shown in Fig. 2.3, the SM becomes totally decoupled from the grid in terms of frequency. Due to its connection to the machine stator, the FC is required to be rated at the full machine power, which for typical PHSP is in the range of tens to hundreds of MW. It is only through the development of the power electronics FC that this configuration can be made feasible, which is the reason for its unavailability at this time, despite its numerous advantages:

- Possibility to achieve full torque over the whole feasible speed range, allowing for very rapid start-ups and speed reversals without requiring dewatering of the pump.
- Ability to perform black starts, thus contributing to restoration of the power grid following a blackout.
- Ability to provide reactive power to the grid in case of a LVRT, helping to restore the voltage.
- As a SM is used, retrofitting an existing power plant can be considered, thus saving the cost of the development of a new machine. Additionally, compared to the DFIM, the SM is lighter and has a less complex design, which makes it the cheaper option even when a new machine is required.
- In case of a new SM, the nominal frequency can be chosen and the SM does not need to be designed for reactive power supply.

As mentioned in the introduction, the change in the energy market requires the storage facilities such as the PHSPs to operate in a more flexible manner. Multiple start-ups, stops as well as speed reversals are expected throughout the day. Compared to the more popular DFIM configuration, the CFSM does not require dewatering of the pump for any of this transients. Adding the fact of the

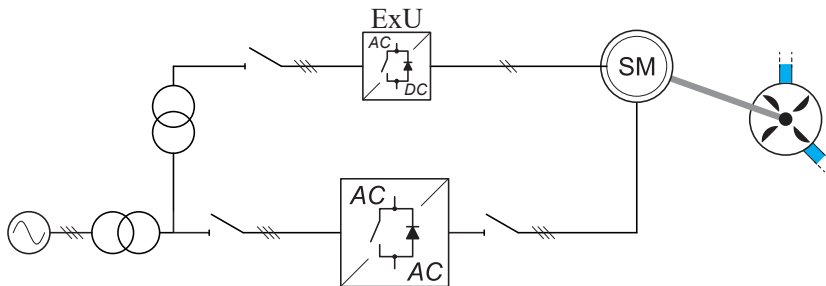


**Fig. 2.3** Details of the CFSM installation. For a separately excited SM, two FC are required. One excitation unit connected to the rotor winding and another FC connected to the stator winding.



available maximum torque over the full speed range, the transition times will be significantly reduced compared to the DFIM configuration. These advantages result in a significant time saving, which ultimately translates in a higher profit margin of the installation.

Even if the CFSM configuration eliminates the disadvantages created by the reduced converter ratings of the DFIM, it has the disadvantage of requiring a FC rated at the full power of the unit. The cost related to the FC are higher and the increased amount of processed power leads to additional losses compared to the DFIM configuration. Additionally, the FC might introduce additional stress on the stator winding insulation due to the high  $dV/dt$ . Without replacing the SM, the FC is designed with a limited  $dV/dt$ , usually achieved through the addition of a filter between the FC and the SM. For cases involving the design of a new SM, the insulation of the machine can be designed considering the converters  $dV/dt$ , thus not requiring any filtering at the output of the FC.

Besides, while the totally decoupled machine and grid allows for an optimal operation of the SM, increasing the flexibility of the overall installation, it has the disadvantage of having effectively decoupled the machine inertia from the grid, which reduces its stability. In case of grid faults, the converter needs to assure that grid code requirements are fulfilled, leading to an increase in control complexity of the system. However, taking the example of the LVRT, where the CFSM requires a more complex control structure, the DFIM requires a crowbar on the rotor to reduce the machine flux and limit the rotor current through the converter, translating into additional material and design costs.

## 2.2 Frequency converters for PHSPs using CFSM

Power ratings of PHSP units go up to 500 MW, however for the converter ratings, not only the power, but also the nominal stator voltage of the SM has to be considered. While multiple smaller rated units exist, their ratings allow for conventional and commercially available converters, thus the focus lies on the larger PHSP units. **Tab. 2.1** provides typical nominal characteristics of SM deployed in large PHSPs.

Europe currently counts two PHSPs installations with units exceeding 80 MW equipped as CFSM. The larger and older one, being in the Grimsel 2 power plant located in Switzerland, where one of its four 100 MVA units was retrofitted in 2013 with two parallel connected 50 MW FC [48]. Each of the FCs is a B2B monolithic multilevel converter based on Integrated Gate-Commutated Thyristors (IGCTs) semiconductor technology, an illustration of which is shown in **Fig. 2.4**. This setup allows for a power variation in pumping mode from 60 MW to full nominal power of 100 MW. Additionally, the whole FC can be bypassed, which then connects the SM directly to the grid and allows for a higher overall efficiency when operated in generating mode.

The more recent installation equipped with two 80 MW CFSM is the Galgenbichl power station located in Austria, which was commissioned in 2021 [49]–[52]. Pictures of the installation are shown

**Tab. 2.1** Typical synchronous machine ratings in PHSP applications.

Power	$P = 80 \text{ MW to } 500 \text{ MW}$
Stator voltage (line-to-line)	$V_{LL} = 6 \text{ kV to } 30 \text{ kV}$
Stator current (RMS)	$I_{RMS} = 2 \text{ kA to } 8 \text{ kA}$

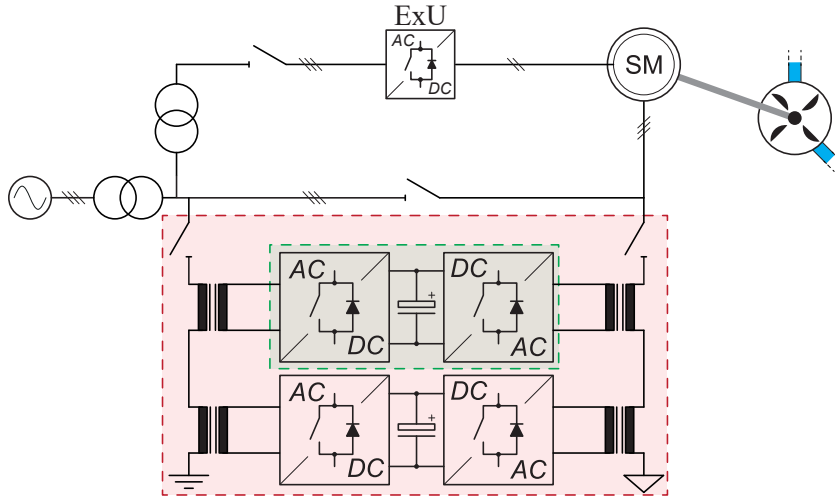


**Fig. 2.4** Illustration of CFSM operational at the the Grimsel 2 power plant. The retrofit converter installed on the SM is highlighted in red. The FC consists of two parallel connected units, one of which is highlighted in green.

in **Fig. 2.5**. The difference to the Grimsel 2 power plant unit is that this project was not a retrofit project, but included the design of two new SMs, allowing for additional degrees of freedom in the implementation, such as the nominal frequency of the SM. Instead of using a monolithic multilevel converter, the choice was made to use the MMC topology, and rather than having a B2B configuration, the M<sub>3</sub>C, a direct ac to ac conversion without common dc terminals, is implemented.

### 2.2.1 Conventional NPC topologies

Considering power and voltage rating of large PHSP, currently available semiconductor devices in combination with conventional monolithic converters do not match the requirements. Taking the example of the Grimsel 2 installation shown in **Fig. 2.4**, two 50 MW FC are operated in parallel. The project was a retrofit including the existing high voltage SM. With the available converter having a lower voltage rating, additional input and output transformers were required as to match the grid voltage to the converter rating and the output of the converter to the machine rated voltage. The parallel connection of two units is required as to increase the current rating of the installation to the

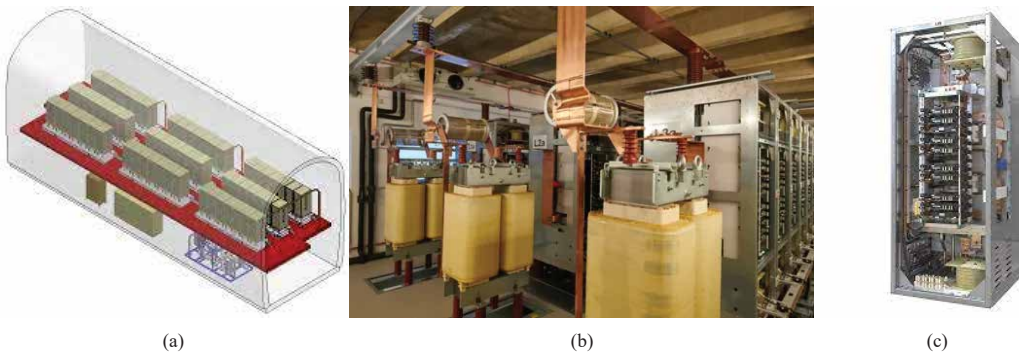


**Fig. 2.5** Galgenbichl Malta 2 SFC light from Hitachi energy [51], [52].

requirements of the SM stator.

For monolithic converters, such as the one shown in **Fig. 2.6** or the one used in Grimsel 2, the series connection of power semiconductor devices allows for a higher voltage blocking capability. However, this series connection requires additional considerations to operate properly. Static voltage balancing among all the semiconductors is achieved through passive circuits connected to each semiconductor. Dynamic voltage balancing requires switching events of series connected switches to occur simultaneously, adding complexity to the gate driver circuit. Furthermore, the series connection of switches does not add voltage levels to the output waveform, and thus high filtering requirements remain.

With the increased number of semiconductor devices comes an increased likelihood of a failure. The failure of a single semiconductor should, however, not alter the proper operation of the converter, which requires special design consideration. Assuming redundancy of the switches, a short circuit failure mode is required for the converter to continue operation after a fault. This prohibits for example the use of cheaper IGBT modules and requires the more expensive press-pack IGBTs [53].

### 2.2.2 MMC topology

With the intention of being used for HVdc applications, the MMC as shown in **Fig. 2.7** (a) was first introduced in 2001 [35], [36], [54]. As shown in **Fig. 2.7**, the principle of the MMC relies on the series connection of cells, each with its own energy storage element. The advantage over conventional monolithic converters lies in the fact that the semiconductors of each cell are required to block only the cell capacitance voltage. For High Voltage (HV) or MV applications, multiple cells are connected in series achieving the required voltage rating similarly to the series connection of switches in monolithic converters. However, due to the distributed capacitances in each cell, the number of voltage levels of the output waveform of the MMC is proportional to the amount of cells in the converter. Thus, while increasing converter voltage rating, the increased number of cells also reduces the ac filtering requirements, as the high number of voltage levels approaches the fundamental waveform. Similar to monolithic converters, the current rating of MMC is achieved through paralleling of either semiconductors within the cells, cells, legs or whole converters [55].

**Fig. 2.8** depicts a selection of cells used in the MMC. For a single stage MMC, the most common implementation is the HB cell, as this topology has the least number of power switches while fulfilling

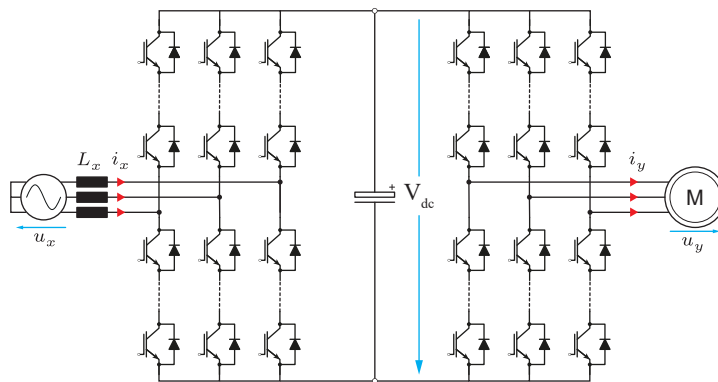


**Fig. 2.6** Illustration of a conventional monolithic 2 level converter in a B2B configuration.

the converter requirements. If negative cell voltage is required by the operation, the FB cell becomes the most popular choice. It is possible to also use two different types of cells within the same branch, resulting in the so-called hybrid MMC [56], [57]. The other types of cells are less common and for this reason will not be further analyzed within this thesis.

Conventional converter topologies, such as the Two-Level (2LVL) shown in **Fig. 2.6**, require for continuous operation that the input power matches the output power and the losses. This will be referred to as total energy control, meaning that the control algorithm ensures that the capacitor remains charged to the required voltage by forcing the input power to match the sum of output powers and the losses. Although not having a centralized capacitance, this total energy controller is required in the MMC topology to ensure that the overall energy within the converter remains constant.

In addition to the total energy controller, the MMC requires energy control layers on the branch and on the cell level. As the cells in the MMC include their own energy storage element, this control layer needs to ensure equal energy distribution among the cells. This equal cell energy distribution requires an additional branch current component to be controlled by the controller. Besides, the control needs to ensure that this balancing current does not influence the operation of the converter and thus is not present on either terminal of the converter. This is the reason for their names, the circulating currents, as they remain circulating within the converter. The final branch current expression takes the following expression:

$$i_{br}(t) = \frac{i_{ac}(t)}{2} + \frac{i_{dc}}{3} + i_{cc}(t) \quad (2.3)$$

Independent of the cell topology, for the mathematical development of the governing equations, the branch can be considered as a controlled voltage source with a resistive and an inductive element as shown in **Fig. 2.9**. The development is done for a single leg and divided into the upper branch  $V_p$  and lower branch  $V_n$  equations:

$$u_p(t) = \frac{U_{dc}}{2} - u_x(t) - u_{cm}(t) - R_{br}i_{br}(t) - L_{br}\frac{\partial i_{br}(t)}{\partial t} \quad (2.4)$$

$$u_n(t) = \frac{U_{dc}}{2} + u_x(t) + u_{cm}(t) - R_{br}i_{br}(t) - L_{br}\frac{\partial i_{br}(t)}{\partial t} \quad (2.5)$$

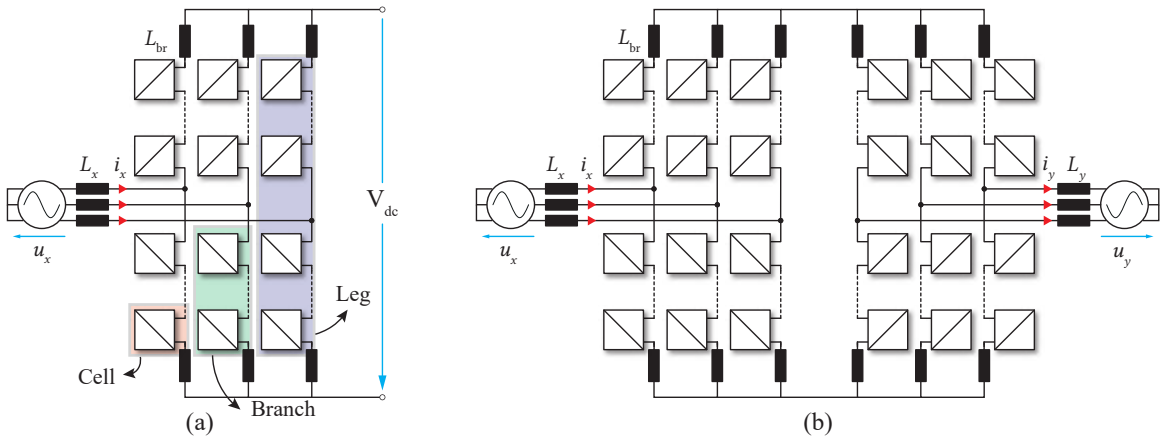


**Fig. 2.7** Illustration of the MMC in (a) and a B2B connection of two MMC called IMMC in (b).

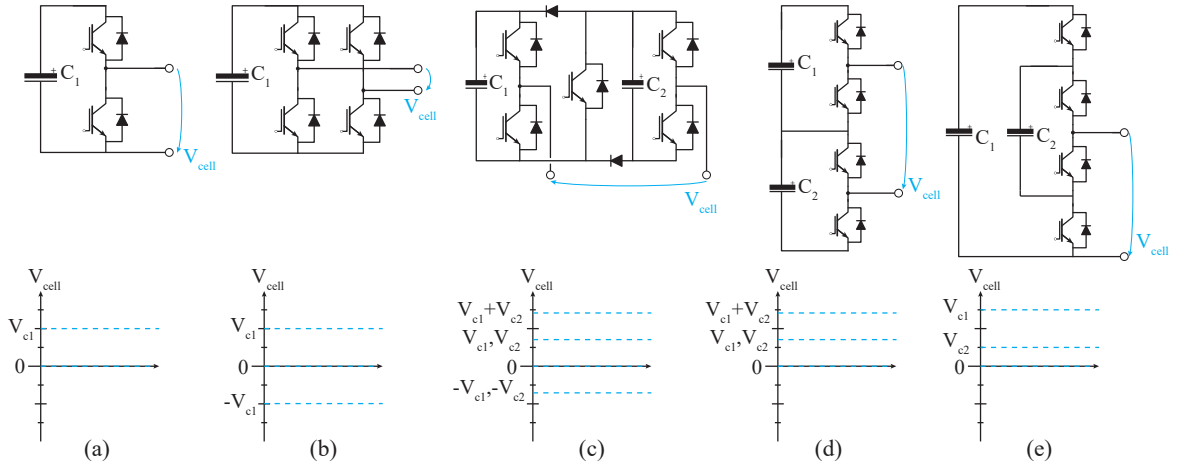


**Fig. 2.8** Some of the proposed cell topologies used for the MMC. (a) shows the Half Bridge (HB) cell, (b) the FB cell, (c) the double clamped cell, (d) the cascaded HB cell and (e) the flying capacitor cell.

The normally low branch inductance, through which the circulating currents are controlled, results in a small voltage component controlling these currents. Compared to the terminal voltages that the branches must generate, this component can be neglected and is thus not shown in (2.4) and (2.5).

From (2.4) and (2.5), it can be seen that the branch voltages contain both, dc voltage as well as ac voltage components. The branch voltage is generated by the cells of the given branch and its amplitude is defined by the cell capacitance voltage as well as the number cells that are inserted. The so-called insertion index, defining the percentage of cells per branch that are actively contributing to the branch voltage (inserted), is used to express the instantaneous branch voltage. This results in the following expression of the branch voltage:

$$u_{br} = \sum_{i=1}^{N_{cell}} n_{SM,i} U_{cell,i} = \underbrace{\left( \frac{1}{N_{cell}} \sum_{i=1}^{N_{cell}} n_{SM,i} \right)}_{m(t)} u_{br\Sigma} \quad (2.6)$$

Where  $u_{br\Sigma}$  defines the total branch voltage and  $m(t)$  is the previously mentioned insertion index,

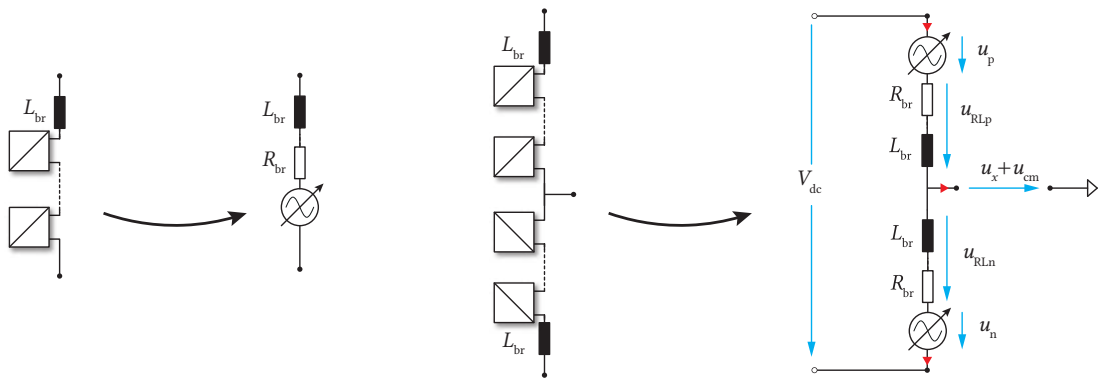


**Fig. 2.9** Equivalent model of the MMC branch and leg.

and the factor  $n_{SM}$  is defined by:

$$n_{SM} = \begin{cases} 1, & \text{if the cell is inserted} \\ 0, & \text{if the cell is bypassed.} \end{cases} \quad (2.7)$$

With the knowledge of the total branch voltage  $u_{br\Sigma}$  and the fact that this branch voltage is defined by both the number of cells per branch as well as the cell capacitor voltage, which is defined by the semiconductor voltage class, the total number of cells per branch can be defined.

Having cells which include their own energy storage element, the voltage scaling of this converter topology is straightforward by increasing the number of cells per branch. The number of cells required depends on the dc-link voltage ( $U_{dc}$ ), the ac terminal voltages ( $\hat{V}_{ac} + \hat{V}_{cm}$ ), the voltage component to control the circulating currents and enable energy balancing of the cells as well as possible cell redundancy ( $N_{re}$ ) within the branch. The final number of cells per branch is defined as:

$$N_{cell} = \frac{1}{U_{cell}} \left( \frac{U_{dc}}{2} + \hat{V}_{ac} + \hat{V}_{cm} \right) + N_{re} \quad (2.8)$$

Where  $N_{re}$  defines the amount of redundant cells per branch.

The number of cells per branch defines the number of possible output voltage levels, which in case of the MMC is defined by  $(2N_{cell} + 1)$  in case of non-symmetric switching between the upper and the lower branch, and  $(N_{cell} + 1)$  in case of symmetric switching, where  $N_{cell}$  defines the number of cells per branch. Choosing a lower semiconductor voltage class results in a higher number of cells per branch, thus also a higher number of output voltage levels, which reduces the size or even eliminates the requirements of a filter on the ac output voltage. Whereas the advantage of the higher voltage class semiconductors, thus lower cell number per branch consists of the lower risk of a cell failing, as well as the reduced amount of control boards and connections.

Current scaling of the MMC occurs in the same way as for conventional converters creating parallel paths to share the current, thus increasing the maximum converter current rating without changing semiconductor devices [55], [58], [59]. This parallel connection can occur at various levels with the same effect on the ac terminal currents as shown in **Fig. 2.10**. The four stages where this parallel connection can occur is at the semiconductor level shown in **Fig. 2.10** (a), at the cell level as shown in **Fig. 2.10** (b), at the branch level **Fig. 2.10** (c) or at the converter level **Fig. 2.10** (d).

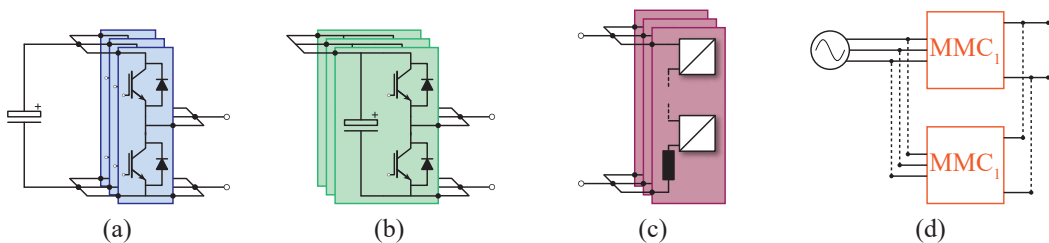


**Fig. 2.10** Simplified illustration of the current scaling possibilities of the MMC. (a) showing a parallel connection of switches connected to a common capacitance. (b) illustrating a parallel connection of cells, (c) showing the parallel connection at the branch level and (d) at the converter level.

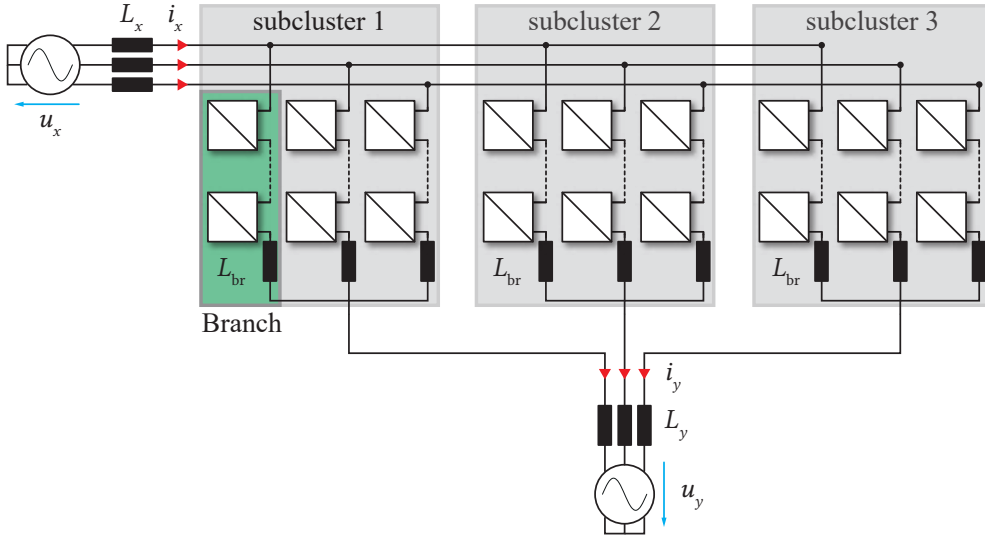


**Fig. 2.11** Illustration of the M3C with the three subclusters, highlighted in gray, each containing three branches, highlighted in green, and  $N$  cells per branch. The input ac system uses the subscript  $x$  and the output ac systems the subscript  $y$ .

To achieve three phase ac to three phase ac conversion using the MMC requires a B2B connection, as seen on **Fig. 2.7** (b). Similar to conventional converters, the rectifier MMC regulates the dc-link voltage and the inverter MMC controls the connected three phase ac load. The intermediate dc terminals present in the B2B connection decouples the load from the grid and thus eliminates all restrictions on the load frequency. As will be seen in the following section, this statement does not hold for the M3C topology. This characteristics make the IMMC a good fit for retrofit applications where the existing 50 Hz SM does not require replacement.

The MMC as shown in **Fig. 2.7** (a) is also able to generate a single phase ac voltage instead of the shown dc voltage. This configuration is interesting for the usage in railway interties which operate at 16.7 Hz. However, a few conditions have to be considered for this three phase to single phase ac conversion to be possible:

- Different input and output frequency.
- Ability of the cell to generate negative terminal voltage.

To allow a three phase ac to ac conversion requires the addition of a set of three branches connected to the three phase input system. This addition creates a third terminal on the previously defined dc side, transforming the MMC into the M3C as seen in **Fig. 2.11**. This topology, similarly to conventional matrix converters, enables a three phase ac to ac conversion.

Comparing both topologies, the IMMC from **Fig. 2.7** (b) and the M3C in **Fig. 2.11**, some of the operational differences can be pointed out prior to a mathematical development. Each of the input and output terminals is connected to three branches in the M3C compared to two for the IMMC, thus a better current distribution leading to lower current stresses on the semiconductors within the branches can be expected in the M3C. The M3C is connected between two three phase ac systems, thus no dc current is flowing within the branches, in contrast to the MMC, where one terminal is a dc terminal. This leads to advantages in the branch inductor design, as a more compact design can be

achieved in the M<sub>3</sub>C using an iron core inductor, which is unpopular in the MMC due to its reduced efficiency and core saturation.

## 2.3 The M<sub>3</sub>C

While the IMMC has the advantage of being compatible for retrofit applications in existing PHSP installation, the M<sub>3</sub>C, as illustrated in **Fig. 2.11**, is the more interesting topology for installations where the SM will be replaced. The advantages of the M<sub>3</sub>C for VSD applications have been presented in [60]–[62]. Thus, when designing a VSD for PHSP together with the design of the machine, the M<sub>3</sub>C is the favorable option. This is demonstrated by the Galgenbich installation, where the choice of the new SM was made considering the M<sub>3</sub>C as a drive topology [39]. A SM designed to be operated with a FC, thus not directly connected to the grid, allows for weight and cost saving as well as increased efficiency [63].

### 2.3.1 M<sub>3</sub>C modeling

Similar to the MMC, the expression of the voltage and the current can be developed and generalized for all branches of the M<sub>3</sub>C. The naming convention adopted throughout this thesis is the following:

Input ac system:	$i_x(t), u_x(t)$	where	$x \in [a, b, c]$
Output ac system:	$i_y(t), u_y(t)$	where	$y \in [1, 2, 3]$
M <sub>3</sub> C branches:	$i_{xy}(t), u_{xy}(t)$	where	$xy \in [a1, ..., c3]$

**Fig. 2.12** defines the current and voltage directions based on which the branch equations can be developed as (2.9) and (2.10). The branch currents expression, as seen in (2.10), has in addition to the input and output terminal currents a third component, which is the previously mentioned circulating current [64]. While the branch voltage expression also contains the component driving the circulating current, this voltage component is negligible with respect to  $u_x(t)$ ,  $u_y(t)$  and  $u_0(t)$  due to the normally low value of branch inductances.

$$u_{xy} = \left( \underbrace{u_{gx}(t) - L_x \frac{\partial i_x(t)}{\partial t}}_{u_x(t)} \right) - \left( \underbrace{u_{gy}(t) + L_y \frac{\partial i_y(t)}{\partial t}}_{u_y(t)} \right) - u_0(t) \quad (2.9)$$

$$i_{xy} = \frac{1}{3}i_x(t) + \frac{1}{3}i_y(t) + i_{\text{circ}_{xy}}(t) \quad (2.10)$$

The previously mentioned condition, that the cell used within the M<sub>3</sub>C is required to generate both positive and negative voltage, is determined by (2.9). Both  $u_x(t)$  and  $u_y(t)$  are sinusoidal waveforms with arbitrary frequency and amplitude centered around zero. Therefore, the generated branch voltage defined by the difference between those two terms can take both positive and negative values. As the HB cell commonly used for the MMC cannot be used in this topology, the most common cell topology used for the M<sub>3</sub>C is the FB cell, shown in **Fig. 2.13**. The right side table in **Fig. 2.13** shows all the allowed active switching sequences and the resulting terminal voltage of the FB cell. It is noteworthy that, besides the shown active switching states, there is the possibility of having all switching signals at low, in which case the terminal voltage is defined by the branch current direction.



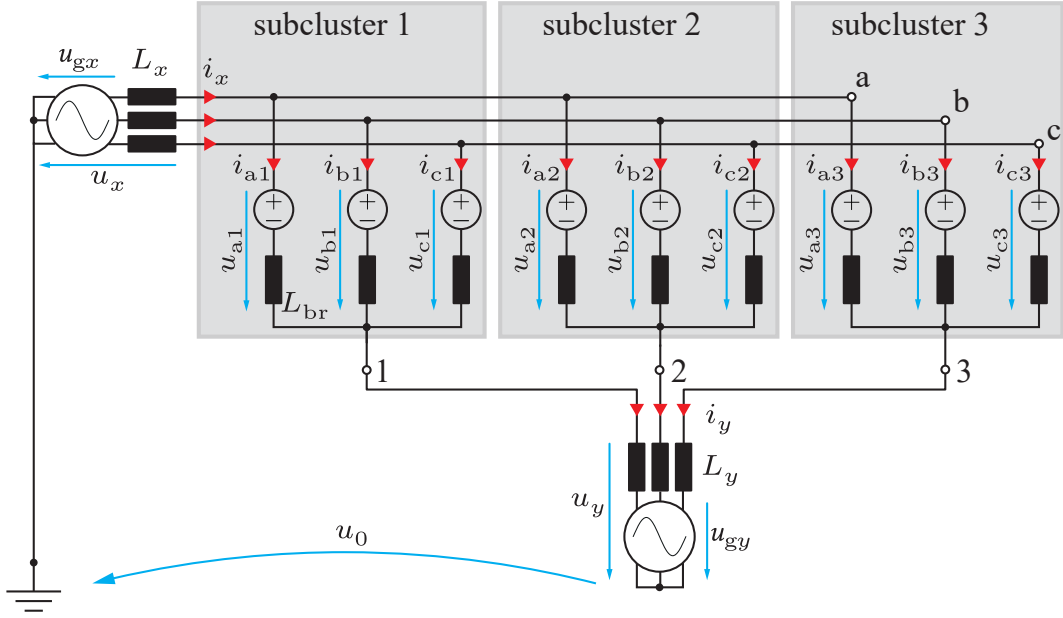


**Fig. 2.12** Illustration of the M3C using a controlled voltage source as equivalent model for the string of cells. Adopted current and voltage directions are used throughout the rest of this paper. Values associated with the input grid get the subscripts  $[a, b, c]$  and the ones associated with the output grid the subscripts  $[1, 2, 3]$ .

Similar to the IMMC, the required number of cells per branch for the M3C can be determined using (2.9) and considering the cell capacitance voltage as well as the number of redundant cells per branch,  $N_{re}$ .

$$N_{cell} = \frac{1}{u_{Cxyi}} (\hat{u}_x + \hat{u}_y + \hat{u}_0) + N_{re} \quad (2.11)$$

The number of cells per branch defines the number of possible output voltage levels. For the M3C, using FB cells, similar to the MMC case, the number of output voltages is defined by  $(N_{cell} + 1)$  or  $(2N_{cell} + 1)$  depending on the switching pattern, where  $N_{cell}$  defines the number of cells per branch. As for the MMC, depending on the choice of voltage class of the semiconductor, a different number of cells are connected in series as to match the design voltage requirements.

From (2.9), it can be seen that the branch voltages includes two ac voltage components. Similar to the development done for the MMC, the branch voltage is generated by the inserted cell terminal

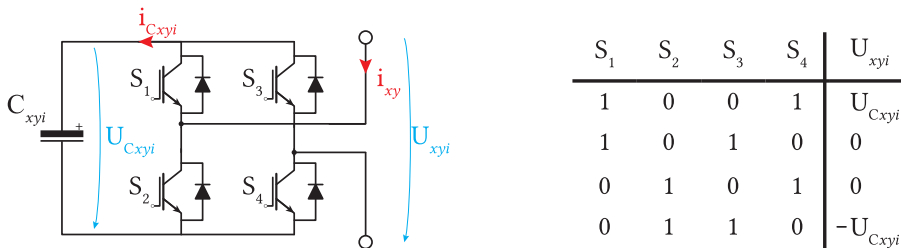


**Fig. 2.13** Details of the FB cell extracted from the branch  $xy$ ;  $i$  depicts the number of the cell within the branch.

**Tab. 2.2** Cell power variation depending on cell terminal voltage.

Switching state ( $n_{xyi}$ )	Branch current direction	Cell capacitance voltage variation
1	$i_{xy} > 0$	charging
1	$i_{xy} < 0$	discharging
0	$i_{xy} > 0$ or $i_{xy} < 0$	indifferent
-1	$i_{xy} > 0$	discharging
-1	$i_{xy} < 0$	charging
passive	$i_{xy} > 0$ or $i_{xy} < 0$	charging

voltages of the given branch, together with the cell capacitance voltage. Three distinct switching states of the typical FB cell used in the M3C can be defined:

$$n_{xyi} = \begin{cases} 1, & \text{if the cell is inserted with a positive terminal voltage} \\ 0, & \text{if the cell is bypassed} \\ -1, & \text{if the cell is inserted with a negative terminal voltage.} \end{cases} \quad (2.12)$$

With the switching state defined above, the cell capacitance current  $i_{Cxyi}$ , as shown in **Fig. 2.13**, can be defined as a function of the branch current  $i_{xy}$ :

$$i_{Cxyi} = n_{xyi} i_{xy} \quad (2.13)$$

Depending on the branch current direction and the cell switching state, the cell capacitance can either be discharged, charged, or remain uninfluenced. The variation of the cell capacitance voltage can be expressed as:

$$\frac{\partial u_{Cxyi}}{\partial t} = \frac{1}{C_{xyi}} i_{Cxyi} = \frac{1}{C_{xyi}} n_{xyi} i_{xy} = \frac{1}{C_{xyi}} \frac{u_{xyi}}{u_{Cxyi}} i_{xy} \quad (2.14)$$

From (2.14), the variation of the cell voltage can be expressed as a function of the switching state, as shown in **Tab. 2.2**. The passive state equals to all switches being off, thus the terminal voltage of the cell is dictated by the branch current direction.

The final branch voltage is the sum of all the cell terminal voltages of the given branch and can be expressed as:

$$u_{xy} = \sum_{i=1}^{N_{\text{cell}}} n_{xyi} u_{Cxyi} = \left( \frac{1}{N_{\text{cell}}} \sum_{i=1}^{N_{\text{cell}}} n_{xyi} \right) u_{Cxy} \quad (2.15)$$

Additionally, the variation of the overall branch capacitance voltage can be calculated by summing up the capacitance voltages of each cell within the branch and using (2.14):

$$\frac{\partial u_{Cxy}}{\partial t} = \sum_{i=1}^{N_{\text{cell}}} \frac{\partial u_{Cxyi}}{\partial t} = \frac{N_{\text{cell}}}{C_{xyi}} \frac{p_{xy}}{u_{Cxy}} \quad (2.16)$$

The branch power expression is obtained by the multiplication of (2.9) and (2.10):

$$\begin{aligned}
 p_{xy}(t) &= \left( u_x(t) - u_y(t) - u_0(t) \right) \left( \frac{1}{3} i_x(t) + \frac{1}{3} i_y(t) + i_{\text{circ}_{xy}}(t) \right) \\
 &= \frac{1}{3} \underbrace{u_x(t)i_x(t)}_{\substack{\omega_\Sigma=2\omega_x \\ \omega_\Delta=0}} - \frac{1}{3} \underbrace{u_y(t)i_x(t)}_{\substack{\omega_\Sigma=\omega_y+\omega_x \\ \omega_\Delta=\omega_y-\omega_x}} - \frac{1}{3} \underbrace{u_0(t)i_x(t)}_{\substack{\omega_\Sigma=\omega_0+\omega_x \\ \omega_\Delta=\omega_0-\omega_x}} + \frac{1}{3} \underbrace{u_x(t)i_y(t)}_{\substack{\omega_\Sigma=\omega_x+\omega_y \\ \omega_\Delta=\omega_x-\omega_y}} - \frac{1}{3} \underbrace{u_y(t)i_y(t)}_{\substack{\omega_\Sigma=2\omega_y \\ \omega_\Delta=0}} - \frac{1}{3} \underbrace{u_0(t)i_y(t)}_{\substack{\omega_\Sigma=\omega_0+\omega_y \\ \omega_\Delta=\omega_0-\omega_y}} \\
 &\quad + \underbrace{u_x(t)i_{\text{circ}_{xy}}(t)}_{\substack{\omega_\Sigma=\omega_x+\omega_{\text{circ}} \\ \omega_\Delta=\omega_x-\omega_{\text{circ}}}} - \underbrace{u_y(t)i_{\text{circ}_{xy}}(t)}_{\substack{\omega_\Sigma=\omega_y+\omega_{\text{circ}} \\ \omega_\Delta=\omega_y-\omega_{\text{circ}}}} - \underbrace{u_0(t)i_{\text{circ}_{xy}}(t)}_{\substack{\omega_\Sigma=\omega_0+\omega_{\text{circ}} \\ \omega_\Delta=\omega_0-\omega_{\text{circ}}}}
 \end{aligned} \tag{2.17}$$

The instantaneous branch power, expressed in (2.17), is proportional to the variation of the cell capacitance voltage. However, this expression includes oscillating terms with an oscillating frequency of  $\omega_\Sigma$  and  $\omega_\Delta$ . The energy being the integral of the power, the branch energy variation can be developed from (2.17):

$$e_{xy}(t) = \int p_{xy}(t) dt \tag{2.18}$$

(2.17), can be separated in two categories of terms, the first one being ac terms and the second one being the dc terms. The first category, if inserted into (2.18), does not alter the overall energy of the branch, but leads to energy oscillations. The sizing of the cell capacitance is done considering this oscillations, as they could cause over-voltages or under-voltages in case of a too low cell capacitance value. The second category of terms, if inserted into (2.18), results in an either ever increasing or decreasing energy component. Thus, if not compensated, they will eventually cause an over-voltage or under-voltage. The two existing dc terms within (2.17), resulting from the multiplication of  $u_x(t)i_x(t)$  and  $u_y(t)i_y(t)$ , should always cancel each other out. Similar to conventional topologies, the total energy controller is responsible to guarantee this cancellation of dc terms.

To avoid having uncompensated dc terms in the branch power expression, the terminal frequencies of the M3C are required to be different. To prove this, an analysis of (2.17) is required, but a few simplifications can be done beforehand. As the circulating currents are internal to the converter, they can be assumed zero for this analysis. Furthermore, with a properly working total energy controller, the  $\omega_\Delta = 0$  parts of  $u_x(t)i_x(t)$  and  $u_y(t)i_y(t)$  cancel each other out. This leads to the simplified expression:

$$\begin{aligned}
 p_{xy}(t) &= \frac{1}{3} \underbrace{u_x(t)i_x(t)}_{\omega_\Sigma=2\omega_x} - \frac{1}{3} \underbrace{u_y(t)i_x(t)}_{\substack{\omega_\Sigma=\omega_y+\omega_x \\ \omega_\Delta=\omega_y-\omega_x}} - \frac{1}{3} \underbrace{u_0(t)i_x(t)}_{\substack{\omega_\Sigma=\omega_0+\omega_x \\ \omega_\Delta=\omega_0-\omega_x}} + \frac{1}{3} \underbrace{u_x(t)i_y(t)}_{\substack{\omega_\Sigma=\omega_x+\omega_y \\ \omega_\Delta=\omega_x-\omega_y}} - \frac{1}{3} \underbrace{u_y(t)i_y(t)}_{\omega_\Sigma=2\omega_y} - \frac{1}{3} \underbrace{u_0(t)i_y(t)}_{\substack{\omega_\Sigma=\omega_0+\omega_y \\ \omega_\Delta=\omega_0-\omega_y}}
 \end{aligned} \tag{2.19}$$

Looking at (2.19), the terms  $u_y(t)i_x(t)$  and  $u_x(t)i_y(t)$  generate an oscillating power at the frequencies defined by the sum and the difference of the input and output terminal voltage. In order to avoid a dc component, it is thus straightforward that both frequencies are required to be different. If both frequencies approach each other, this oscillation occurs at a very low frequency, namely the difference of the two frequencies, which requires a high capacitance value to buffer the energy without exceeding the voltage limits. For this reason, the M3C is used in applications where input and output frequency differ, and the exact frequency difference is dependent on converter design choices and chosen control methods [38].

It is noteworthy that the circulating currents can be used as to eliminate the dc power term and thus avoid any energy divergence within the branches as has been demonstrated in [65]–[67]. However, this increases the current requirements on the semiconductor devices and still requires oversizing of the cell capacitance. For this reason, the IMMC is the favorable option in this case which includes retrofit applications, where the existing SM is not replaced. The equal input and output frequency operation of the M3C is not further covered in this thesis.

### 2.3.2 Control structure of the M3C

The control scheme on a branch and on a converter level is shown in **Fig. 2.14**. The converter level control includes the total energy controller, grid current control, as well as machine control and is highlighted in red in **Fig. 2.14**. The total energy controller ensures, as the name suggests, that the overall energy within the converter remains constant by regulating the input power (what is considered input power depends on the status of the application). When the machine is in speed control, the overall energy controller regulates the grid power to match the overall converter energy requirements. In a PHSP, usually the grid operator provides a power reference to be followed by the power plant, thus the grid side power reference is fixed and the total energy controllers regulates the reference power of the machine. For any converter topology, the overall stored energy is required to remain constant, making this control layer identical for all FC, and it will be further covered in **Chap. 6** of this thesis.

The lower level control differentiates the branches within the converter and controls their respective energy. It is highlighted in blue in **Fig. 2.14**. While being a level below the total energy controller, this layer still does not differentiate between the cells of a given branch and acts simply on the branch average energy. This control layer is specific to the MMC family due to their distributed energy storage elements within the cells that constitute the branch of the converter. As this control layer results from the characteristics of the respective topology, it should not interfere on an application level as the application should not be able to differentiate the converter families. For this reason, the entity controlled in this layer should be internal to the converter, which for the MMC are the circulating currents. The average branch energy, which is the reference that each controller receives in this layer, is calculated based on the total stored energy which, in turn, is regulated by the total energy controller. The branch balancing power reference is then generated for each branch based on its deviation from the average branch power reference. To make sure that the terminals remain uninfluenced by this control layer, the current reference has to be modified before generating the corresponding branch voltage reference. This control layer is further developed and analyzed in **Chap. 5** of this thesis.

An even lower control layer, which is not shown on **Fig. 2.14**, involves the distribution of the energy among the cells of the same branch. This control layer requires knowledge of the respective modulation scheme, measure of the respective cell energy as well as a measure of the branch current and is covered in the literature [68]–[70]. For the developed control structure used in the RT-HIL system at PEL, which will be further explained in **Chap. 4**, the employed Pulse-Width Modulation (PWM) scheme is based on Phase Shifted Carrier (PSC). Based on all the previously described control layers and once the total number of cells that are required to be inserted in a given branch is determined, this control layer defines which cells are inserted. If the branch current is positive, inserting a cell into the branch results in the cells capacitance voltage to increase, thus also increase the energy within the inserted cell. On the other hand, inserting a cell when the branch current is negative will reduce

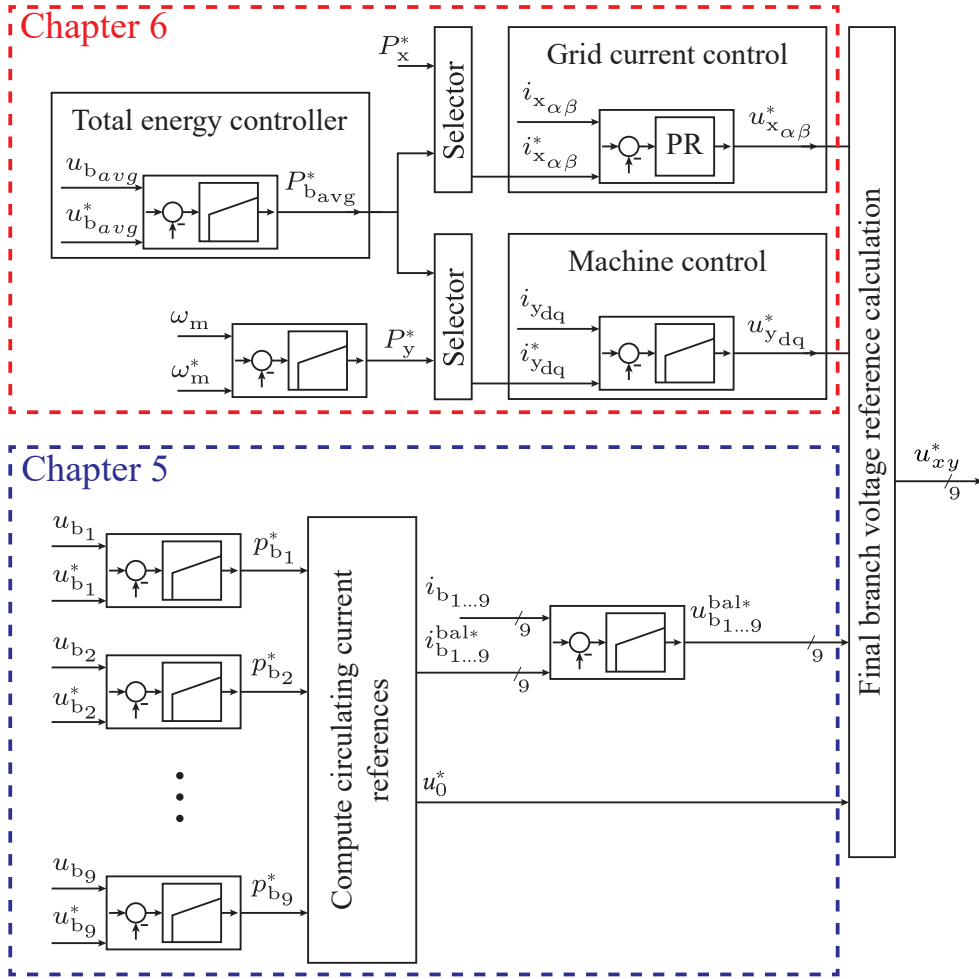


**Fig. 2.14** Overview of the M3C control structure. The top part, encircled in red, illustrates in a simplified manner the terminal current control of the M3C including SM and grid current control. The lower part, encircled in blue, shows the control structure of the circulating currents used to balance the energy among the branches of the M3C.

the energy within that cell by reducing its capacitance voltage. From there it is straightforward that during a positive branch current, the cells with the lowest energy are inserted, while for a negative branch current, the cells with the highest energy are inserted.

## 2.4 PHSP research platforms

Before the deployment in the field, hardware as well as software of the respective FC systems are required to be tested thoroughly. Especially for applications like PHSP, where the deployed FC is usually a single prototype, verification at various levels is mandatory to guarantee a successful commissioning. At the PEL, two research platforms for testing of the M3C exist, namely a Power-Hardware-In-The-Loop (P-HIL) and a RT-HIL. The RT-HIL allows a verification of the control structure and algorithms as well as to aid in the development of the involved hardware. The P-HIL, as the name

suggest, enables to test the hardware and the software of the converter as power is processed.

### 2.4.1 P-HIL research platform

**Fig. 2.15** shows a picture of the MV equipment included in the P-HIL research platform. Colored in dark blue is the 500 kW 6.3 kV SM, in light blue the 500 kW 6 kV IM and the industrial FC, the ACS 2000, driving the IM is on the far right of the picture. The shaft of the SM is connected to the IM and beneath the shaft is the torque measurement unit from Kistler, the CoMo Torque Type 4700.

**Fig. 2.16** illustrates the interconnection of the elements of the P-HIL. The whole platform is connected to the external 6 kV grid; however, as the power is circulating in the loop, this connection accounts

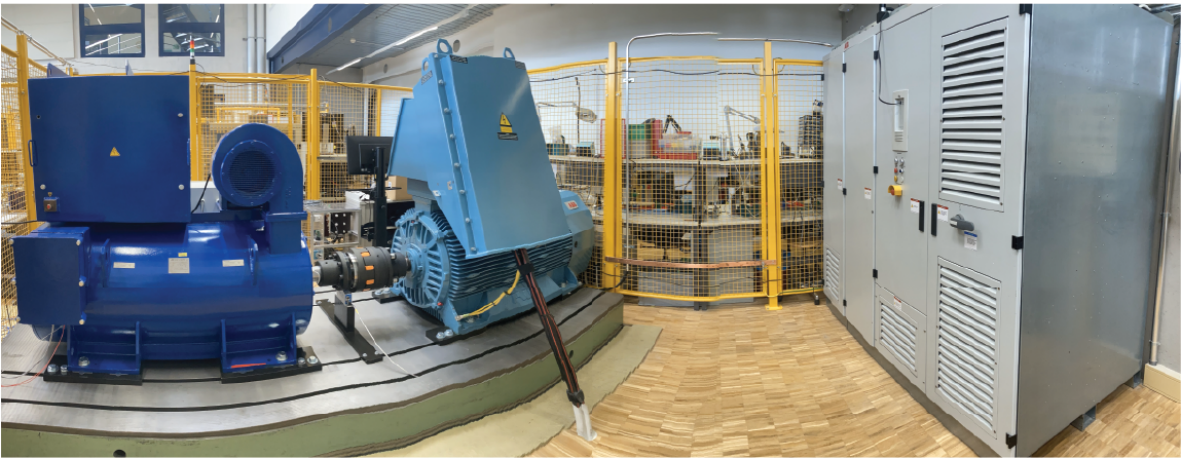


**Fig. 2.15** Picture of MV P-HIL research platform installed at PEL.

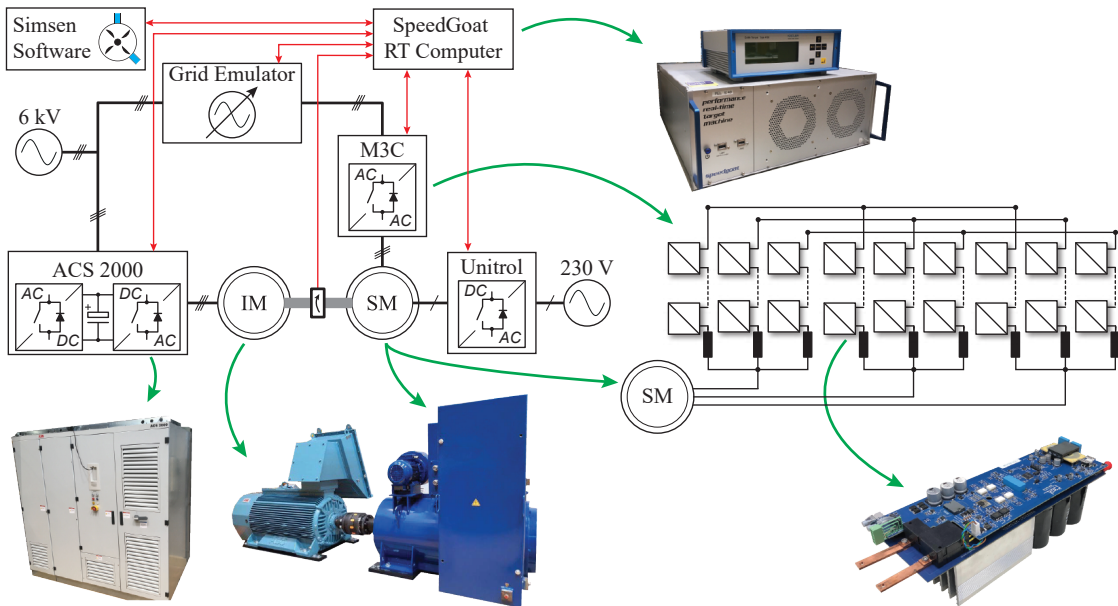


**Fig. 2.16** Overview of the interconnection of the elements of the P-HIL including the communication channels between the equipments and the SpeedGoat test supervision system.

only for the losses within the platform. This principle allows a full power testing of the FC with a significant reduction in grid power requirements. The ABB ACS2000 is an industrial available 5-level 1 MW drive, which is used in this platform to drive the IM. In general, high power PHSP rely on the SM for the generation, thus in most cases, the IM in the P-HIL emulates the prime mover of the PHSP. The SM will be driven by the M3C, once the development of this one is finalized. Additionally, a grid emulator connected to the M3C will allow to test various grid scenarios and analyses the response of the M3C as well as the behavior of the full system. The excitation of the SM is provided by the ABB Unitrol excitation system.

With the IM as prime mover, the here shown P-HIL has been developed with the aim to be testing the performance of the M3C in a CFSM installation. While an installation with an IM type generator could be emulated on this platform, the deployment of the industrial ACS2000 allows for less degrees of freedom in operation compared to the M3C which is being developed at PEL.

The SpeedGoat RT computer is used as a platform supervisor, where all the signals and references are assembled or generated. To emulate a realistic behavior of the prime move of a PHSP, the simsen software is running on an external pc and providing torque references to the IM. This software is usually used in PHSP as a digital twin to the installed unit in order to detect any anomaly within this unit by comparing theoretical behavior from simulation to actual measurements. However, for the P-HIL, this software will include the exact hydraulic model of the PHSP that is to be tested and will provide torque references to the ACS2000, which drives the IM to emulate the behavior of a pump/turbine. The communication between the SpeedGoat and the elements of the P-HIL is done using various industrial protocols such as RS232, Modbus and Profibus that are supported by the equipment.

Due to the power processing nature of the P-HIL platform, initial verification on hardware and software of the M3C are required before its deployment. For this reason, the RT-HIL platform is developed.

#### 2.4.2 RT-HIL research platform

Prior to the P-HIL tests, hardware and software around the control of the M3C have to be verified. While the software implementation can be verified using simple offline simulations, the controller hardware and control structure including the interconnection of the various control elements requires a RT simulation. The final step before starting P-HIL is usually the RT-HIL verification step. In a RT-HIL platform, the control structure includes all the elements as well as their interconnection in the same way as it will be for the final prototype. However, the power parts of the final platform, which include M3C, SM and grid, are implemented on RT computers and react upon changes coming from the controller. With a correct model of the power elements mentioned and the same signal exchange between the RT computers and the controllers, this platform allows for a validation of the control algorithm and control structure. If working properly, the controller should not be able to differentiate the RT-HIL from the actual converter, making this a very reliable test without risking of damaging high value equipment.

**Fig. 2.17** shows the difference between the P-HIL and the RT-HIL. The left side shows the interconnection of the elements used during the P-HIL as previously explained, and the right side shows the RT-HIL, where only the controller and control structure are kept, while the remaining elements are implemented on RT computers. This RT-HIL platform relies on the RT Box 1 from PLEXIM. The

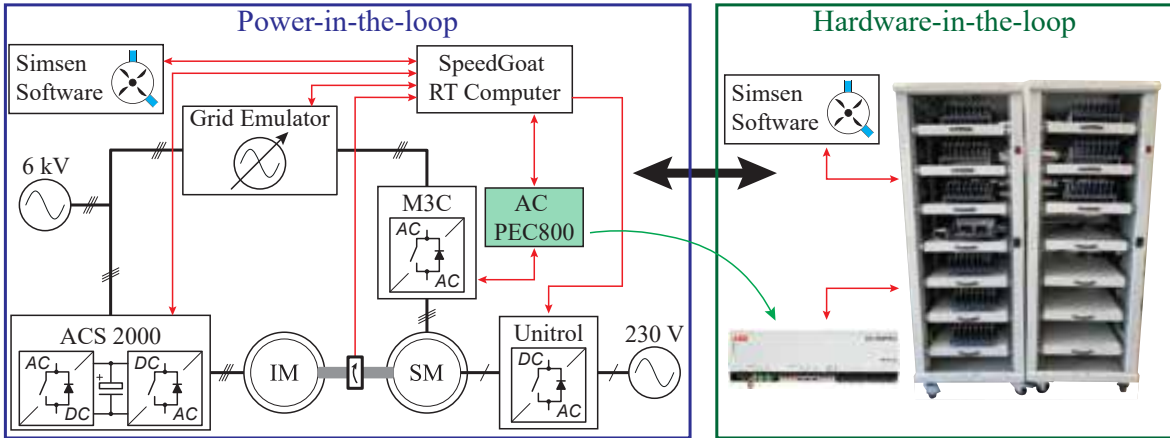


**Fig. 2.17** Illustration of the P-HIL as well as the RT-HIL testing platforms. The ABB PEC 800 controller is highlighted in green, as it is the main part of the control structure, which is equivalent among the two platforms.

RT-HIL research platform as shown in **Fig. 2.17** as well as the deployed models of the converter are further explained in **Chap. 4**.

In addition to the previously mentioned reasons, the RT-HIL setup is used to aid the development of the M3C prototype as the sizing of the elements such as the cell capacitance and branch inductance can be verified without requiring their production. Having a correctly working RT-HIL platform with the control structure defined, the sizing of the relevant converter elements can be verified through various scenarios that the converter might encounter without having to physically develop these elements.

## 2.5 Summary

This chapter presented the two main variable speed configuration for PHSP, namely DFIM and CFMSM. For each of the configurations, the basic operating principle as well as advantages and limitations have been presented. As the rating of the FC represents the main barrier for CFMSM configurations, current solutions, converter topologies, and the potential of emerging topologies are discussed.

Considering the high power ratings of typical PHSP together with the converter power requirement of a CFMSM configuration, the most promising solution is the MMC topology, relying on the series connection of lower rated cells. This chapter presented the existing configurations as well as the basic operating principle of the MMC. As the M3C configuration outperforms the IMMC for VSD PHSP applications, it is further analyzed within this chapter. Governing equations as well as general outline of the control structure are further analyzed. Finally, the two PHSP research platforms that are available at PEL, namely the P-HIL and the RT-HIL are described in detail.

As presented in this chapter, this technology achieves the typical ratings of PHSP in the hundreds of MW range. However, the main advantages in terms of flexible operation generated through CFMSM in PHSP are independent of the converter topology. Smaller units, which, due to their power level, can rely on the implementation of established industrial converters, still achieve all the benefits of VS operation, as will be demonstrated in the next chapter.



# 3

## Advantages of Variable Speed Drive Units

*The necessity of a large and flexible grid energy storage is demonstrated in **Chap. 1** and the possibility of pumped hydro storage power plants taking over this role is elaborated. This chapter covers the current operating modes of fixed speed pumped hydro storage power plants while pointing out the advantages regarding hydraulic machinery and power plant operator gained through variable speed operation. As these benefits are generally independent of the converter choice, this chapter is not limited to a single converter type. By taking as an example the Z'Mutt pumped hydro storage power plant located in Switzerland, the advantages of convert fed synchronous machines are demonstrated. Current operating conditions of the Z'Mutt power plant and transient characteristics are illustrated and compared to the potential converter fed synchronous machine operation.*

### 3.1 Conventional PHSP operation

As explained in **Chap. 1**, conventionally PHSP units operate at a fixed speed with a SM directly connected to the grid. Therefore the mechanical rotating frequency is fixed and defined by both, the number of poles of the SM as well as the grid frequency.

#### 3.1.1 Start-up

Reversible units in PHSP may encounter any of two start-ups that have to be differentiated, namely the pumping and turbine start. Generally, a start in pumping mode requires a connection to the grid, while a start in turbine mode requires power from the upper reservoir. The ternary units, presented in **Chap. 1**, may be started in pump mode using the shaft connected turbine driven by the water. However, here the focus lies on a single unit consisting of a single pump/turbine, thus the case of the ternary unit is disregarded.

The turbine start-up procedure generally involves the water from the upper reservoir of the PHSP as energy source, which is driving the turbine and spinning the rotor up to nominal speed. Once at nominal speed, the synchronization to the grid in terms of voltage amplitude and phase angle is achieved through the excitation system and is required prior to the connection to the grid.

The start-up of a fixed speed unit in turbine mode can be achieved with three distinct principles [71]. The first one relies on the use of an external motor or a shaft-connected turbine, as is the case for the ternary unit. The second principle, the so called synchronous start, evolves around starting the unit through a frequency converter or an adjacent unit of the power plant. The third method, called asynchronous start-up, enables, through short-circuit of the rotor, to start the SM in a similar fashion to an IM.

The first method relies on the connection of either a turbine or an auxiliary motor to the shaft of the main unit. As this unit or motor is only used during the start-up, its power requirement is only a fraction of the unit it is starting. While this method is very gentle on the electrical and mechanical system, it requires either an additional machine or turbine and is not very cost effective. In the case of a ternary unit, the power source is the upper reservoir, whereas for the auxiliary motor, the power is drawn from the grid.

The second method does not require any modification or any additional unit connected to the shaft of the main unit. However, it requires an available machine set operating in turbine mode and electrically connected to the pump with a low impedance. This allows for a synchronous start-up using the reservoir as energy source. The other possibility of synchronous starting the pump uses a frequency converter, which, similar to the starting motor in the first case, does not require to be rated at the full machine power. Once at nominal speed, and synchronized to the grid, the machine disconnects from the FC and connects to the grid. This method draws power from the grid, but due to the FC, there is no power surge on the grid side.

The asynchronous start-up requires a short-circuit of the SM rotor and is achieved either through a direct connection of the stator to the grid, or using either a series reactor or an auto-transformer. The direct connection to the grid is the most cost-effective starting method, as it only requires an additional resistance in the rotor circuit and the switchgear to short-circuit the rotor. However, the connection to the grid generates a load surge for the grid and a high inrush current in the machine, which needs to be accounted for during the design of the machine winding. While this starting method always relies on the grid as energy source, the inrush current can be limited by connecting either a reactor or an auto-transformer to the machine stator.

### 3.1.2 Speed reversal

Two distinct speed reversal scenarios occur in a reversible PHSP unit, namely from pump to turbine mode and vice versa. The first case has the advantage of the water acting in its favor, thus the guide vanes remain open throughout the process. However, the latter requires closing of the Pump Discharge Valve (PDV) to break the rotor through friction, followed by one of the start-ups in pumping mode explained previously. For either of the speed reversal transients, the configuration without FC, found in conventional PHSP units, requires a disconnection from the grid.

In the case of a pump-to-turbine transient, the disconnection from the grid remains from nominal pumping speed to nominal turbine speed. The breaking of the SM and the acceleration in turbine mode is managed by the water pressure through the regulation of the PDV. Once nominal turbine speed is achieved, synchronization to the grid is managed by the excitation system. Due to the water pressure pushing the shaft into turbine operation, this speed reversal occurs faster than the pump-to-turbine one.

For the pump-to-turbine transient, the disconnection from the grid occurs at full pumping speed. The PDV are closed and the water friction in the runner brings the SM shaft to a halt. Once stopped, either of the previously starting methods of the direct grid connected units mentioned above is used to accelerate the machine to full pumping speed.

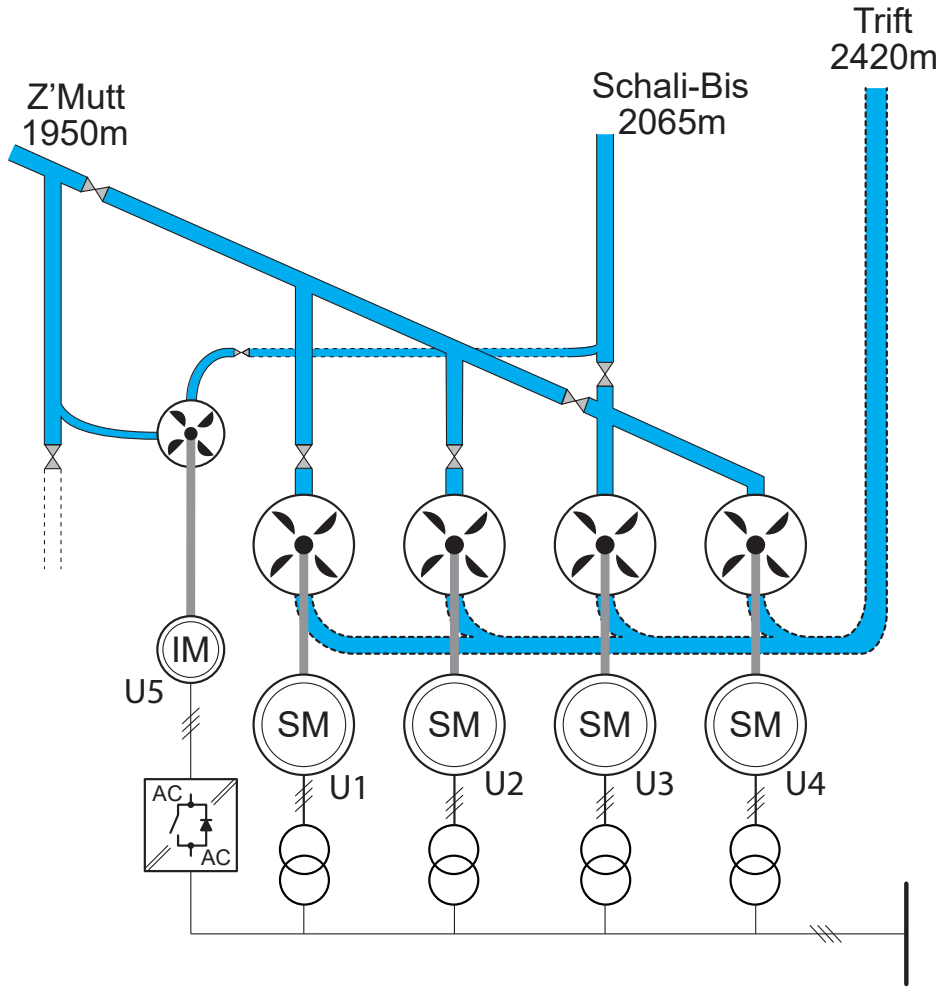


**Fig. 3.1** Layout of the Z'Mutt power plant station with five electric motors, four synchronous machine units (U1 to U4) producing a total power of 88 MW, and one induction machine bypass unit (U5) with a 3 MW power rating.

### 3.2 Z'Mutt power plant station

Z'Mutt is a pumping station with a total installed power of 91 MW and can discharge up to  $17.4\text{ m}^3/\text{s}$  of water. **Fig. 3.1** shows a simplified representation of the power plant station layout with a total of five units with three different power levels:

- Two pumps discharging  $5.5\text{ m}^3/\text{s}$  against 470 m head, with a 30 MW synchronous machine each (U1 and U2)
- Two pumps discharging  $3.2\text{ m}^3/\text{s}$  against 365 m head, with a 14 MW synchronous machine each (U3 and U4)
- One bypass pump discharging  $2\text{ m}^3/\text{s}$  against 90-130 m head, with a 3 MW induction machine (U5)

In summer, all five units are used as pumps, whereas in winter, both 14 MW (U3 and U4) turbines are

**Tab. 3.1** Nominal parameters of U<sub>1</sub>

Parameter	Value
Apparent Power	31.7 MVA
Voltage	10 kV
Current	1.83 kA
Torque	180.4 kNm
Field Current	341.71 A
Pole pairs	2
Frequency	50 Hz
Machine inertia	3300 kgm <sup>2</sup>
Pump inertia	300 kgm <sup>2</sup>

used as generators. As of today, the four main units of the power plant station don't have any flow control device other than the PDV. This PDV is either open or closed and does not allow any flow regulation, which means that for the fixed operating speed, the active power requirement from the grid is defined only by the water level of the upper and lower reservoirs. A total of three reservoirs are connected to the power plant station. The highest one, *Trift*, varying between 2424 m and 2419 m, the middle reservoir, *Schali-Bis*, varying between 2066 m and 2059 m and the compensating basin, *Z'Mutt*, varying between 1972 m and 1930 m.

The currently used start-up procedure of the synchronous motor consists of an asynchronous start, where the rotor is short-circuited until synchronous speed is nearly achieved. Afterwards, the excitation on the rotor is applied and the motor synchronizes to the grid.

In *Z'Mutt*, U<sub>1</sub> and U<sub>2</sub> are both started by a direct connection to the grid without any current limiting device. During the initial part of the asynchronous start-up, the stator is directly connected to the grid and the rotor is short circuited with an additional 1.6 Ω resistance. Operating as asynchronous machine, the produced electromagnetic torque is defined by the following equation [72]:

$$T_{em} = \frac{\frac{3}{2}n_p U_s^2 \frac{R_r}{s}}{\omega_s \left( \left( R_s + \frac{R_r}{s} \right)^2 + \omega_s^2 (L_{\gamma s} + L_{\gamma r})^2 \right)} \quad (3.1)$$

Where  $U_s$  defines the rms voltage on the stator,  $n_p$  the number of pole pairs and  $L_{\gamma s}$  and  $L_{\gamma r}$  are the stator and rotor leakage inductances.

This equation can be simplified for the two regions of interest, namely the starting torque (slip ( $s$ ) close to 1), assuming that  $(R_s + R_r) \ll \omega_s (L_{\gamma s} + L_{\gamma r})$ , and at pull-in torque (slip close to 0), assuming that  $\frac{R_r}{s} \gg \omega_s (L_{\gamma s} + L_{\gamma r}) \gg R_s$ , giving the two simplified expressions:

$$\begin{aligned} T_{em} &\approx \frac{\frac{3}{2}n_p U_s^2 R_r}{\omega_s^3 (L_{\gamma s} + L_{\gamma r})^2} && \text{for } s \text{ close to } 1 \\ T_{em} &\approx \frac{\frac{3}{2}n_p U_s^2 s}{\omega_s R_r} && \text{for } s \text{ close to } 0 \end{aligned} \quad (3.2)$$

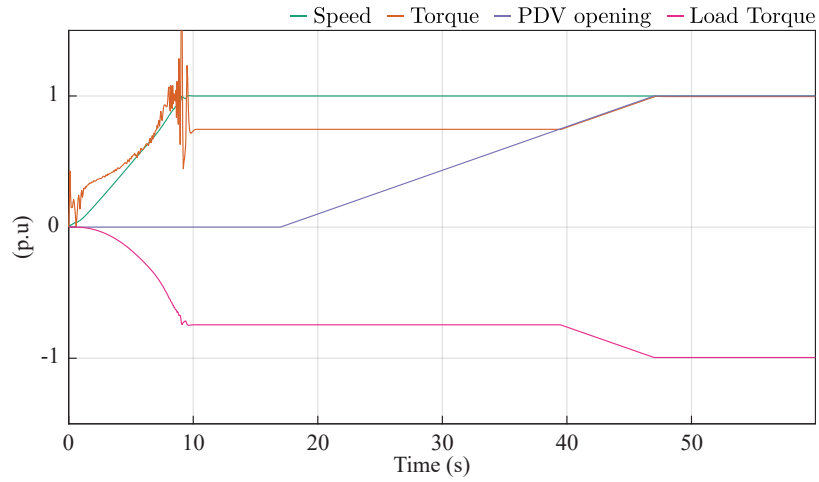


**Fig. 3.2** Simulation results showing the normalized variation of the speed, torque, PDV opening and load torque from standstill to nominal pumping operating point.

Increasing the start-up torque by adding an external resistance on the rotor comes with the trade-off of a reduced final torque near synchronous speed.

Simulations of the current start-up procedure at Z'Mutt are shown in **Fig. 3.2** - **Fig. 3.4**.

**Fig. 3.2** shows the variation of the measurements during the start-up procedure without Full Size Frequency Converter (FSFC), directly connecting U1 to the grid. The maximum torque produced by the machine is only marginally bigger than the load torque created by the head, for this reason the PDV must remain closed during the start-up of the machine, removing this torque component and allowing for a faster acceleration. This process of speeding up the machine to nominal speed takes currently about 10 seconds.

After the nominal speed of the machine is achieved, synchronization to the grid occurs before opening

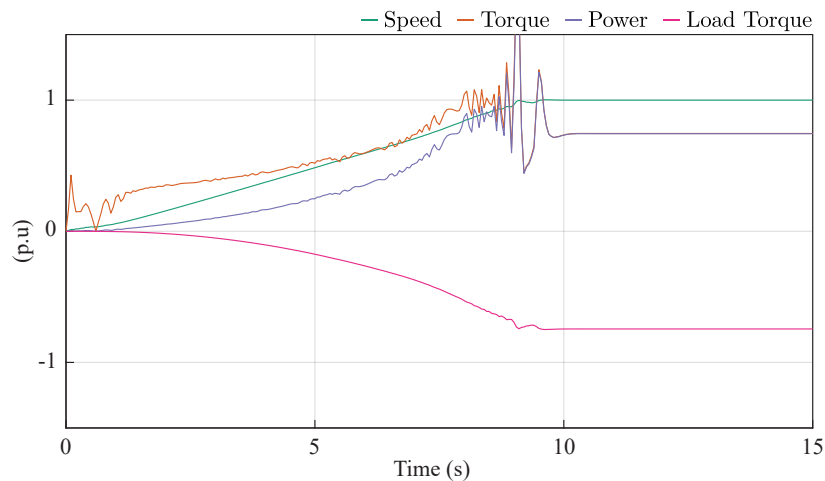


**Fig. 3.3** Simulation results showing the normalized variation of speed, torque, power and load torque during the speed up of the electric motor with a direct connection to the grid.

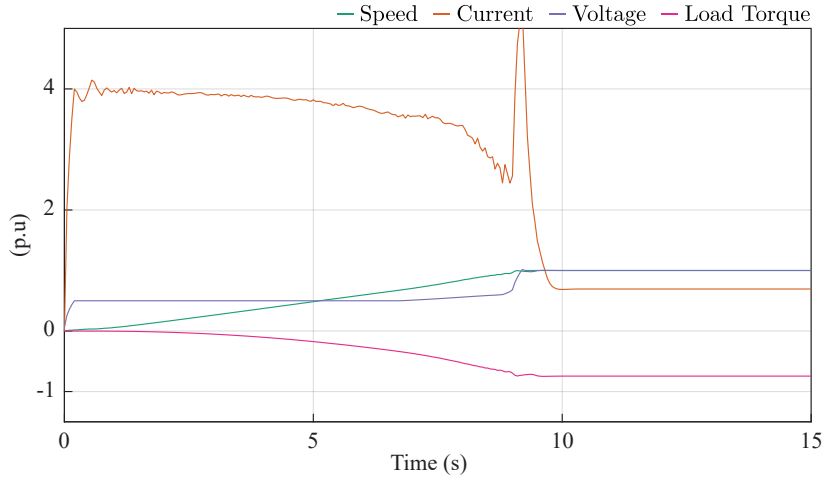


**Fig. 3.4** Simulation results showing the normalized variation of speed, stator current, stator voltage and load torque during the speed up of the electric motor with a direct connection to the grid.

the PDV. It takes currently about 6 seconds after the nominal speed of the machine has been achieved until the start of the opening of the PDV. The opening process of the PDV takes another 30 seconds, after which the full torque is delivered by the pump and the nominal discharge rate is achieved. Following the start-up process, the pump operates at a constant discharge and head, thus a constant power is delivered to the grid. The whole starting process to reach full power operation takes a total of approximately 46 seconds.

**Fig. 3.3** illustrates a detailed view of the speed-up process of the SM. The oscillations near full speed occurs due to the synchronization process. As the excitation current increases, pull-in torque increases proportionally; however, until the required pull-in torque is generated, the synchronization between rotor and stator is lost, generating these high torque ripples.

During the start-up process with a direct connection to the grid, a high inrush current is measured at the stator of the machine, as shown in **Fig. 3.4**. This current rises up to four times the nominal current of the machine, creating a voltage drop on the line connected to the stator.

### 3.3 Operation of *Z'Mutt U1* with a FC

The advantages of a CFSM have been present over the full operating range of a reversible PHSP and have been elaborated in **Chap. 2**. While variable speed operation in both pumping and turbine mode is possible, the dynamics of the transients differ for both operating regions.

In pumping mode, the PDVs are entirely opened, thus no flow regulation is occurring and the absorbed power reference is achieved through variation of the SM speed and torque. As the full regulation is occurring on the SM side, the dynamics of a power reference change is defined by the dynamics of the FC.

In turbine operation, however, the speed of the unit is controlled by the hydraulic machinery whereas the FC is following the power reference received by the grid operator. As the speed of the unit is controlled hydraulically, the dynamics of a power reference change are limited by its capability of

varying the unit's speed. Even if, in turbine mode, the FC enables variable speed operation, the dynamics are still defined by the hydraulic unit and thus slower than in pumping mode.

As the here simulated U1 of the *Z'Mutt* power plant operates only as a pump, the advantages of CFSM in pumping mode are discussed hereafter.

### 3.3.1 Modeling of the unit

To model the non electric parts consisting of the pump and the influence of the water on the pump, an equivalent model of those parameters is created. For the pump, this consists of a simple inertia that is added to the shaft, and with the assumption that there is no vibration on the shaft created by the pump, this is a valid model. The water acting on the pump can be modeled by a simple load torque applied to the shaft. This load torque, simulating the pressure of the water on the pump, can be determined by the following set of equations:

$$\begin{aligned} P_{shaft} &= \gamma Q g H = 25.26 \text{ MW} \\ T_{shaft} &= \frac{P_{shaft}}{\omega_{shaft}} = 161.44 \text{ kN m} \end{aligned} \quad (3.3)$$

Where  $\gamma$  is the water specific density ( $1000 \text{ kg/m}^3$ ),  $g$  is the gravitational acceleration ( $9.81 \text{ m/s}^2$ ),  $Q$  is the flow rate ( $5.5 \text{ m}^3/\text{s}$ ),  $H$  is the pump head (470 m) and  $\omega_{shaft}$  the speed of the shaft ( $157.08 \text{ rad/s}$ ).

With the assumption that the levels of the reservoirs remain unchanged, this torque remains constant throughout the start-up process of the pump. If the power reference changes during operation of the pump, the speed needs to be adapted to keep the produced torque at the shaft constant. The discharge of the pump following a change of speed varies linearly:

$$Q_{new} = \Omega_{new} \frac{Q_{old}}{\Omega_{old}} \quad (3.4)$$

As the water level in a reservoir does not remain constant throughout an entire pumping season, the variation of the load torque following a change in the water level needs to be defined. For *Z'Mutt*, the maximum variation for the upper and the lower reservoir is 5.09 m and 41.6 m respectively, which leads to a maximum and minimum head of 494.35 m and 447.66 m, giving a maximum load torque span of:

$$T_{shaft} \in [153.77 \quad 169.80] \text{ kNm} \quad (3.5)$$

During the start-up phase, the PDV remains closed to allow faster start-ups. As the pump is not dewatered, the torque seen on the shaft of the pump varies with the square of the speed, as defined in (3.6).

$$T_{shaft} = k_{F_w} \Omega_m^2 \quad (3.6)$$

Where  $k_{F_w}$  is the friction coefficient of the pump in the water turning with closed PDV. This coefficient is calculated using start-up measurements of the speed and torque from U1.

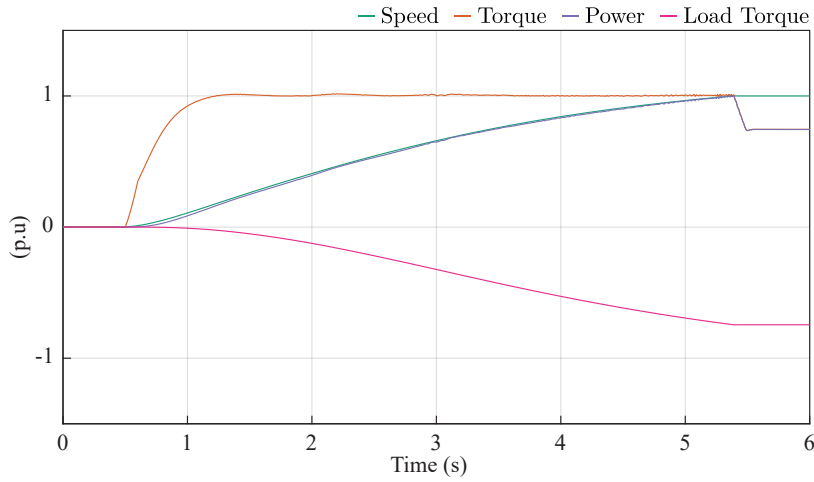


**Fig. 3.5** Simulation results showing the normalized variation of speed, torque, power and load torque during the speed up of the electric motor with a FSFC.

### 3.3.2 Simulation results

The friction coefficient with closed PDV is modeled as a load torque that varies proportionally to the square of the rotational speed of the pump, as expressed in (3.6), with a value of  $k_{F_w} = 0.06$  for the simulated unit. With the FC, full torque can be achieved at zero speed without exceeding the nominal ratings of the machine, thus not damaging the machine while having a fast start-up. Installing a FSFC will have an impact on the time needed to achieve nominal speed of the machine, but the opening time of the PDV remains the same. As there is no need to achieve nominal speed to synchronize, the PDV can start opening even if the machine is not at nominal speed, which can further accelerate the starting process.

The decrease in start-up time due to the installation of a FSFC on the machine can be seen on **Fig. 3.5**.

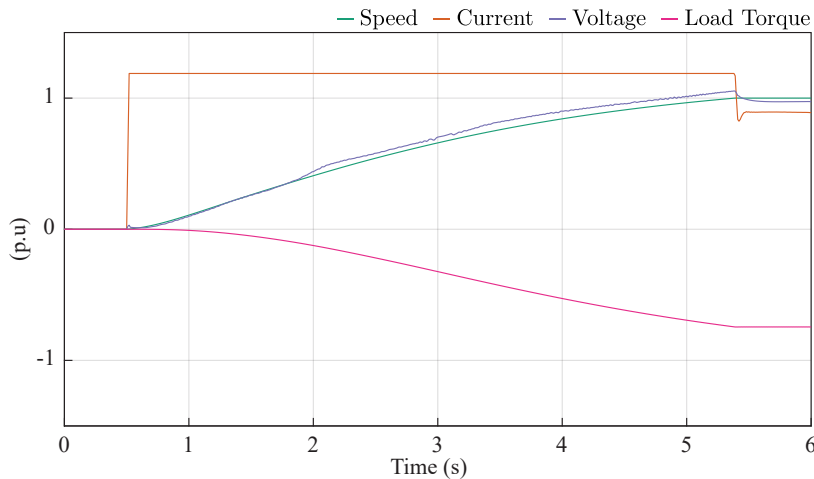


**Fig. 3.6** Simulation results showing the normalized variation of speed, stator current, stator voltage and load torque during the speed up of the electric motor with a FSFC.



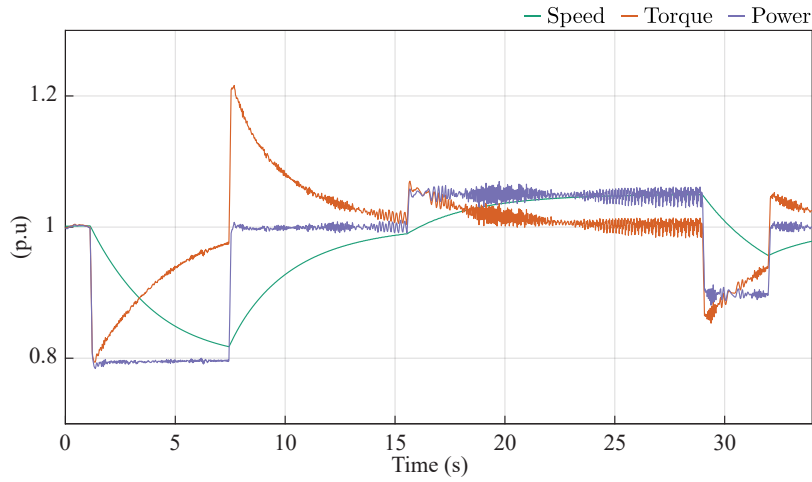


**Fig. 3.7** Variable speed pumping simulation results showing the normalized variation of speed, torque and power with a FSFC.

Nominal speed of the machine is reached within 5 seconds, due to the full torque applied from standstill, and as there is no need for synchronization, adding the 30 seconds of PDV opening, the whole start-up process takes 35 seconds. Comparing the start-up times up to the point where the PDV are being opened, the FSFC configuration generates over 60% time saving compared to the conventional start-up sequence. **Fig. 3.6** shows that during the whole acceleration of the machine, the stator current never exceeds the nominal current by more than 20%.

Once the PDVs are opened and water is being pumped, the lack of a flow control device means that the discharge of the pump is constant for a given speed, thus not allowing any dynamic power consumption from the grid when operated at a fixed speed. The behavior of the *Z'Mutt* SM equipped with a FC following a power reference change can be seen on **Fig. 3.7**. With the load torque remaining constant due to the constant head, a change of 20% in the power reference is done at the time instance

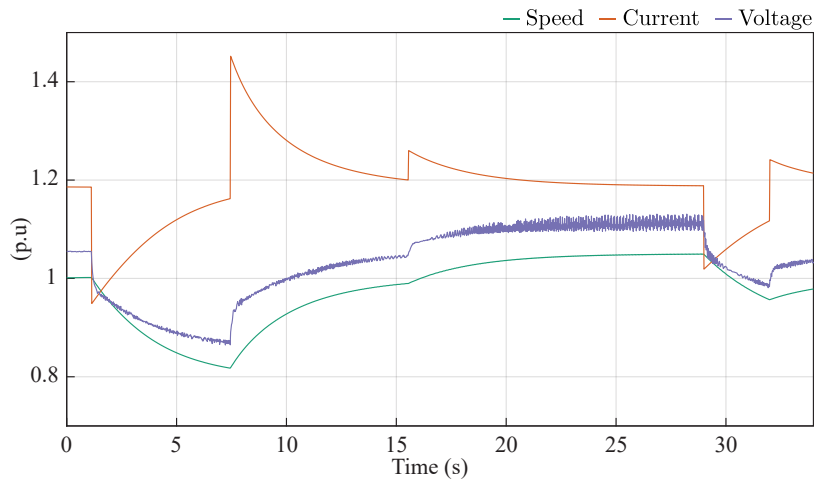


**Fig. 3.8** Variable speed pumping simulation results showing the normalized variation of speed, stator current and stator voltage with a FSFC.

$t = 1$  s, and the FC follows this reference within 0.12 seconds. The increase of the reference power from 80% of the nominal power to nominal power is tracked by the converter within the same response time as the falling power reference, under the condition that the nominal stator current can be increased above the rated value of the machine. Compared to the inrush current during the start-up without FC, which is 4 times the rated value for nearly 10 seconds, seen on **Fig. 3.2**, and because the machine has been designed to withstand that current, the 40% above nominal current for about 5 seconds seen on **Fig. 3.8** will not cause any damage to the machine.

### 3.4 Summary

This chapter demonstrates the benefits of the CFSM configuration for a PHSP, taking as an example the unit 1 from the *Z'Mutt* power plant. Currently, the power plant counts five units: four SMs as well as one newly installed smaller bypass unit relying on the use of an IM. Due to the relatively low power rating, U5 includes a industrial FC enabling variable speed operation. Commonly, the higher ratings of typical PHSP units require the use of a SM, thus this chapter analyses the benefits of operating either U1 or U2 as a CFSM. Being a SM, the previously presented results demonstrating the benefits of CFSM can be generalized for units at various power levels.

The fast response to a change in the grid power reference, as well as the faster start-up of the U1 without exceeding the nominal stator current, imply that the installation of a FSFC can contribute to the relevance of the power plant station on a evolving power market. The relatively low power of 30 MW eliminates the main drawback of the FSFC, as commercial equipment at such power ratings is available on the market.

While the power rating of the here analyzed U1 allows for the use of conventional and industrial available FC, this is not the case for units with higher power ratings. However, independent of the power rating of the FC, the complexity of the system and the cost involved calls for a very thorough verification process prior to the deployment in the field. This is especially true for high power units requiring emerging converter topologies such as the M3C, which is relying on a very complex control structure. The main advantage of this topology is a consequence of its distributed energy storage in each cell; however, this adds a control challenge to keep the energy among the cells balanced. A RT-HIL system is generally the last validation step prior to the deployment in the field, as it represents a relatively cost effective way of generating high fidelity results for the validation of the control structure and algorithms.

# 4

## Hardware-in-the-Loop Test Platform

*Hardware-in-the-loop systems are an essential tool to verify controllers and deployed control algorithms in a risk-free environment. The inaccessibility of the converters used in applications such as pumped hydro storage power plants, caused by their high ratings, can be mitigated by the development of a hardware-in-the-loop platform to perform the validation of the deployed control structures and algorithms. This chapter focuses on the real-time hardware-in-the-loop platform, using industrial controllers and small scale simulators, developed in the power electronics laboratory. The aim of which is to support the development of the matrix modular multilevel converter prototype and the development of the control platform and algorithms.*

### 4.1 RT-HIL hardware

Two main hardware parts can be distinguished on the RT-HIL platform. On one side, there is the control platform which corresponds to an industrial control platform, and on the other side, there are the RT computers emulating the designed power hardware. The interconnection between the RT computers and the controllers is achieved using interface boards. The industrial control platform used in the RT-HIL is based on ABB PEC800 controllers, of which two are used in a master-slave configuration. The RT computers deployed in the system are RT Box 1 from PLEXIM. **Fig. 4.2** illustrates the interconnection of the various hardware elements of the RT-HIL.

#### 4.1.1 Industrial control platform

The core of the control platform are the two ABB PEC800 controllers, with one acting as master and one as slave controller. The master controller handles the general state machine related to the application, thus all high-level signals are managed by this controller. The slave controller hosts the core control of the M3C, including Phase-Locked Loop (PLL), grid side and machine side current control, as well as internal energy balancing. Communication between the master and slave controller is achieved through Fiber Optical Link (FOL) using the ABB proprietary Multi-Link (ML) communication protocol.

The communication of the modulation index to the various cells of the system is achieved through FOL. Due to the limited FOL outputs of the slave controller and the high number of cells required in the M3C topology, the slave controller communicates the various current and voltage references to two Control HUBS (CHUB), which are mapping the modulation indexes and other relevant control software data to the various cells. With nine branches and eight cells per branch, a total of 72 FOL communication links between the cells and the control platform are required. Due to its limited 50 FOL outputs, the here tested M3C system requires two CHUB systems. As seen on the left part in **Fig. 4.2**, one CHUB feed the first six branches and the cells of the remaining three branches are

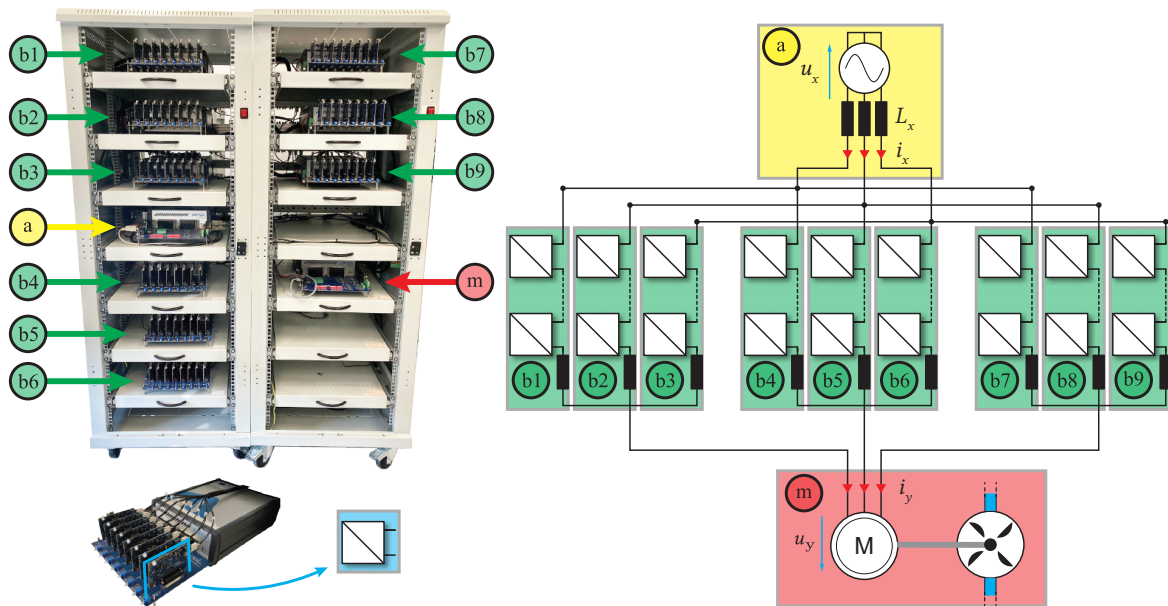


Fig. 4.1 RT-HIL division of the M3C onto multiple RT Boxes.

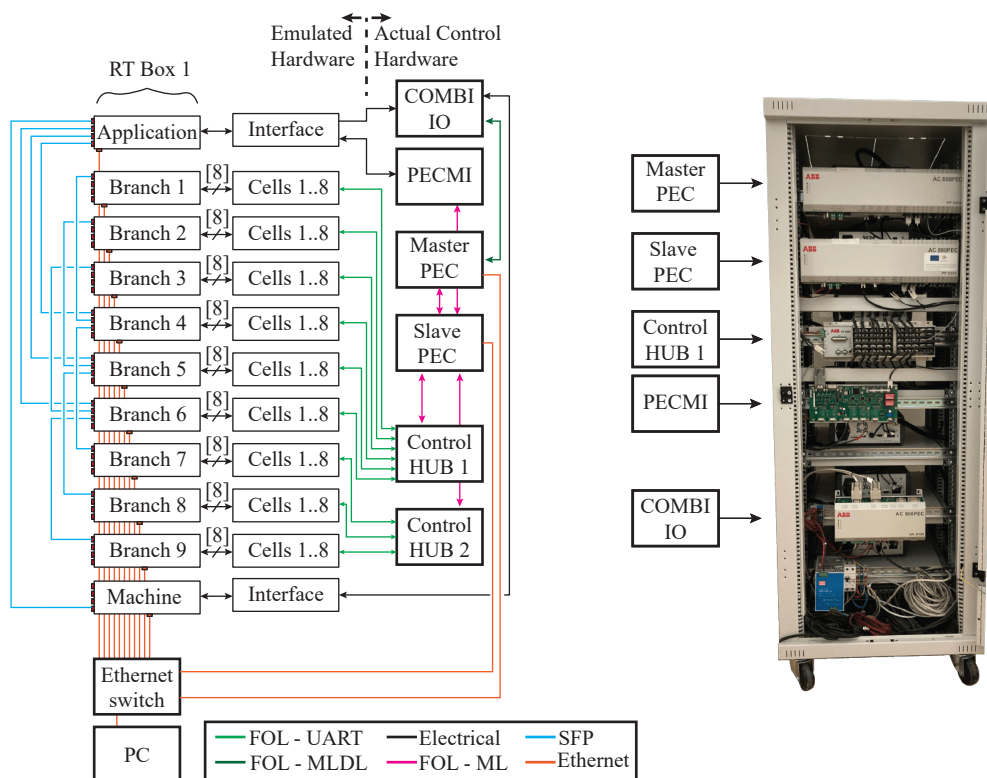


Fig. 4.2 RT-HIL structure showing the connection between the various hardware elements of the test platform on the left side and a picture of the industrial control platform on the right side. The type of connection between the devices is differentiated by the different colors.

getting their references through the second CHUB.

The CHUBs are receiving the measurements from the cells and communicating them upstream to the slave controller. To achieve proper operation of the M3C, its controllers do not require to receive all the individual cell voltages and currents. The CHUB converts the individual cell voltages and currents into the equivalent branch voltages and currents and communicates only these two values to the controller. The FOL UART protocol is used for the communication between the CHUB and the Digital Signal Processor (DSP) of the cells. The communication with the slave controller is done using the ABB proprietary ML protocol through FOL.

Being connected to the grid, the M3C requires several grid side measurement in order to allow a correct power exchange. The PECMI is the measurement unit of the control platform and measures grid side currents and voltages. Scaling of the various measurements to suit the controller inputs is done on the PECMI before being send using the ABB proprietary ML protocol through FOL to the slave controller.

The ABB PEC800 controllers are limited to FOL outputs, and are thus not suited to drive relays requiring 24 V signals. One example of such is during the passive charging process, where a charging resistor is required in the circuit to limit the inrush current to the M3C. In normal operation, this resistor should be bypassed, thus a relay is required to be operated. These tasks are taken over by the COMBI IO, which has, as the name suggest, multiple input and output ports using the 24 V logic, which can drive the coils of the relays in the system. The COMBI IO is connected directly to the master controller through FOL using the Multi-Link Device-Link (MLDL) protocol and translates the commands received from the master to its 24 V digital outputs connected to the given relay. The manual grounding switch, which should not be closed during operation, is blocked in its open position by the COMBI IO. Multiple other elements requiring 24 V signals are connected to the COMBI IO (i.e: doors, fans,...).

#### 4.1.2 Real-time simulation platform

**Fig. 4.3** shows the picture of the front side of the RT-HIL, where the Application RT Box is marked by the number 1, the nine Branch RT Boxes by the number 2, and the Machine RT Box the number 3. The scaling of the analog and digital inputs/outputs to fulfill the requirements of the PEC is achieved through the interface board connected to the Application RT Box. The aim of the Branch RT Boxes, each with its eight cell cards, is to emulate the behavior of the actual branch of the M3C prototype in order to ensure that, from a control perspective, RT-HIL system and prototype behave similarly.

The cell that is designed for the actual M3C prototype can be divided into two main parts. The power part, which includes i.e. power switches, capacitances, protection and power connectors. The control part includes the cell controller connected through FOL to the M3C slave controller through the CHUB. It is, among other things, responsible to generate the switching signals based on the received voltage and current references.

The RT-HIL test platform serves to verify the control structure of the M3C without the risk of damaging expensive hardware. For this reason, the previously mentioned power part of the M3C cell is implemented on RT computers, and the cell control part is kept the same on the RT-HIL and on the final prototype. As the whole control structure from master controller down to cell DSP and their interconnection is equivalent to the final prototype hardware, the RT-HIL provides a great platform for verifying the control structure and algorithms with a very high fidelity. In addition, compared to

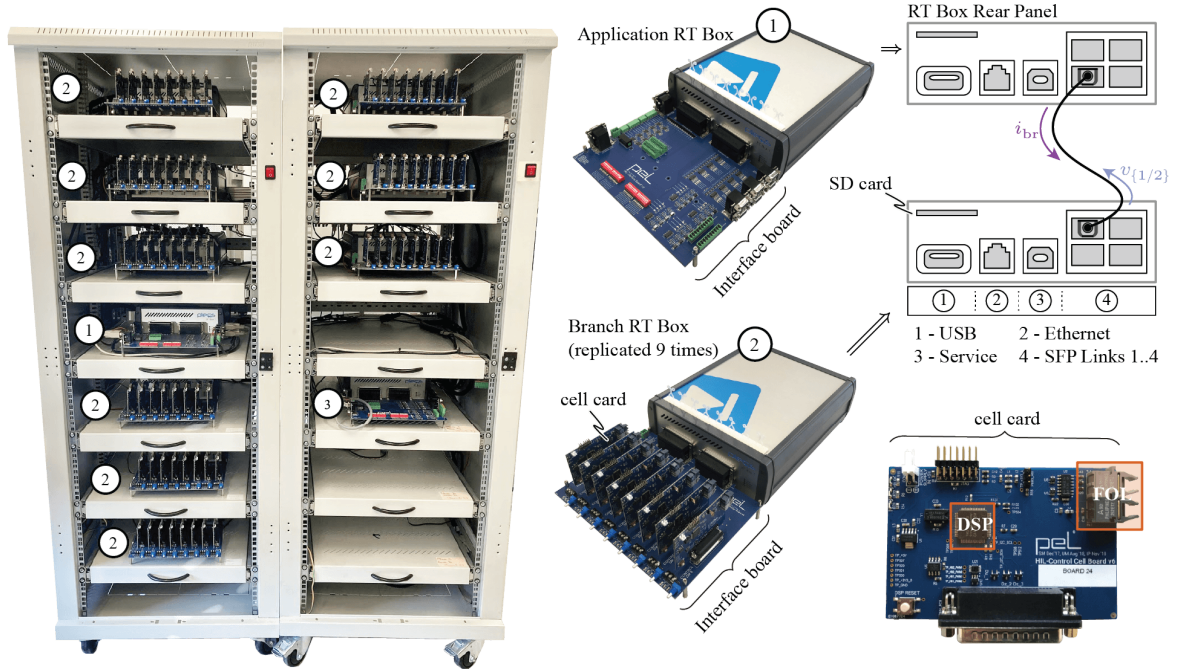


**Fig. 4.3** RT-HIL system used for model verification purpose. The left side shows a front picture of the RT-HIL reconfigured for the M3C, based on to the cabinet used in [73]. A zoomed picture of both the Application and Branch RT Box is shown in the middle labeled by 1 and 2, and their interconnection is shown on the top right. The Machine RT Box, labeled by 3, includes the same interface board as the Application RT Box. The logical circuit of the cells is implemented on the cell card shown on the bottom right.

the final prototype, it represents a relatively cheap and very low risk alternative to verify all possible control related scenarios that might occur.

On the RT-HIL system, the power part is modeled on the Branch RT Boxes and the logic part is implemented on the so called cell cards, each having a local cell control algorithm running on TI DSP. The cell cards are connected to the interface board [73] [74]. This interface board connected to the Branch RT Box allows for a connection of eight cell PCB cards as shown in **Fig. 4.3**. The cell card receives the voltage and current reference for the cell terminals through FOL and sends back both the measurement of the branch current and cell capacitance voltage, among other relevant exchanged data.

The Branch RT Box hosts the model of the series connection of several FB cells, representing the power stage of the cascaded connected cells which form the branch of the M3C. The limited number of digital input ports on the RT Box, namely 32, together with the requirement of four switching signals per cell that are generated by the DSP on the cell card, limits the number of cells per RT Box to 8. Through the analog outputs, the measurements of the branch current and the cell voltages is sent to each cell card, respectively. As shown in **Fig. 4.3**, the Branch RT Boxes communicate, through the SFP link, two voltage references for each branch to the Application RT Box, whereas the latter one sends the respective branch current to each Branch RT Box. The Machine RT Box receives the voltage measurements of the M3C machine side terminals from the Application RT Box and, in return, communicates the machine stator currents back to the Application RT Box. More details about the interconnection of the RT Boxes as well as the model running on them is illustrated hereafter.

## 4.2 Real-time modeling of the M3C

A RT-HIL system is necessary to verify proper operation of the converter control algorithm to avoid damaging high value equipment. The following section is dedicated to the modeling of the M3C on the RT-HIL. The RT-HIL system presented above requires development of suitable models that can support RT simulation requirements, even for a system as complex as the M3C, which must be distributed over several RT Boxes.

The RT Box is relying on the use of state space matrices, the number of which depends on the amount of switches in the system. Assuming a model with  $N$  ideal switches and each switch having two distinct states (conducting or blocking), the number of state space matrices is defined by  $2^N$ . The validity of a RT model lies in the capability of the simulator to select and load, among the pre-computed matrices, the one corresponding to the next state of the converter. Logically, the higher the number of matrices, and the larger these matrices are, the longer it takes for the simulator to select the correct matrix, potentially increasing the computational burden above the threshold for achieving accurate RT simulations.

Modeling of the M3C, without any simplifications, using FB cells and  $N$  cells per branch, the total number of state space matrices related to this model is equivalent to  $2^{9 \times 4 \times N}$ , which results in  $2^{288}$  matrices for the case of eight cells per branch, as implemented in this work. Such a high number of states renders M3C RT simulations impossible on the platform used in this work. Therefore, simplifications, which guarantee preservation of the model correctness are required and they are discussed here.

### 4.2.1 Branch modeling

The implementation of the nine single branches on the nine Branch RT Boxes is done using the sub-cycle averaged model of the series connected FB cells without any loss of generality, as explained in [75] and used in [73]. While the use of the sub-cycle averaged model does not interfere with the main purpose of the RT-HIL, being the verification of the control structure and algorithms, it makes the evaluation of the losses on the HIL more challenging, as will be seen in **Chap. 7**.

**Fig. 4.4** shows the model implemented on the Branch RT Box, and this model is equivalent for all of

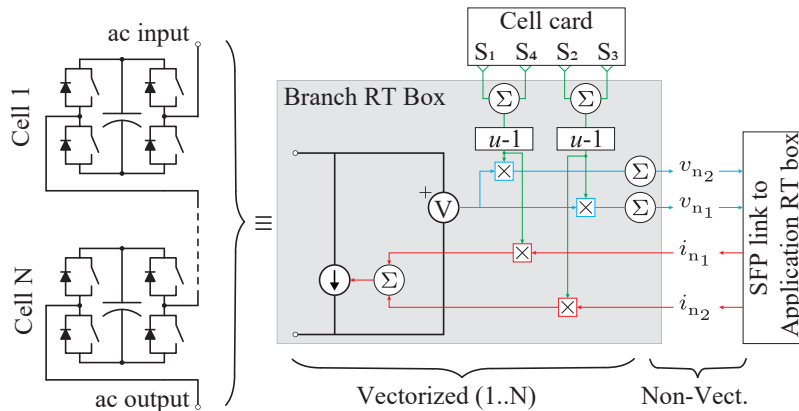


**Fig. 4.4** Sub-cycle average model of the series connected FB cells running on each Branch RT Box.



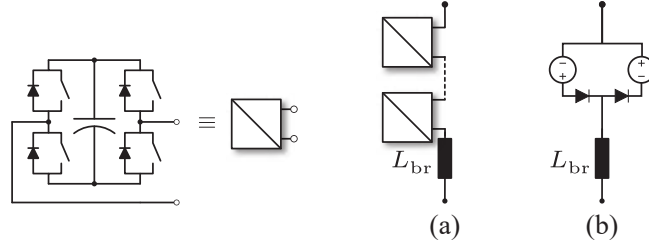


**Fig. 4.5** Equivalent branch model for (a) the real converter using a cascaded connection of full bridge cells (b) the RT model using two controlled voltage sources and two diodes.

the nine Branch RT Boxes. Four switching signals are generated by the local cell controller DSP and sampled by RT Box digital inputs. With a combination of the switching signals, the voltages  $v_{n_1}$  and  $v_{n_2}$ , where  $n \in [1, 2, \dots, 9]$  representing the number of the branch, is used in the M3C model illustrated in **Fig. 4.6**, which is further explained hereafter.

#### 4.2.2 Splitting of the M3C model

One of the challenges for RT simulations of converters made from series connection of identical cells is to find an equivalent branch model, which reduces the number of switches to a minimum, while not limiting the model to certain operating points. The idea of replacing a branch by a controlled voltage source, as used in [76] and [77], while working in steady state operation, it fails to model the blocking state of the converter correctly. While an extension of this model is proposed in [78], the increase in the number of switches makes it less suitable for RT applications. With two diodes and two controlled voltage sources, as shown in **Fig. 4.5(b)**, the model as proposed in [79] and [80] ensures correct simulation of both blocked and active states of the cell. The equivalent model of the converter using this branch simplification is shown in **Fig. 4.6**.

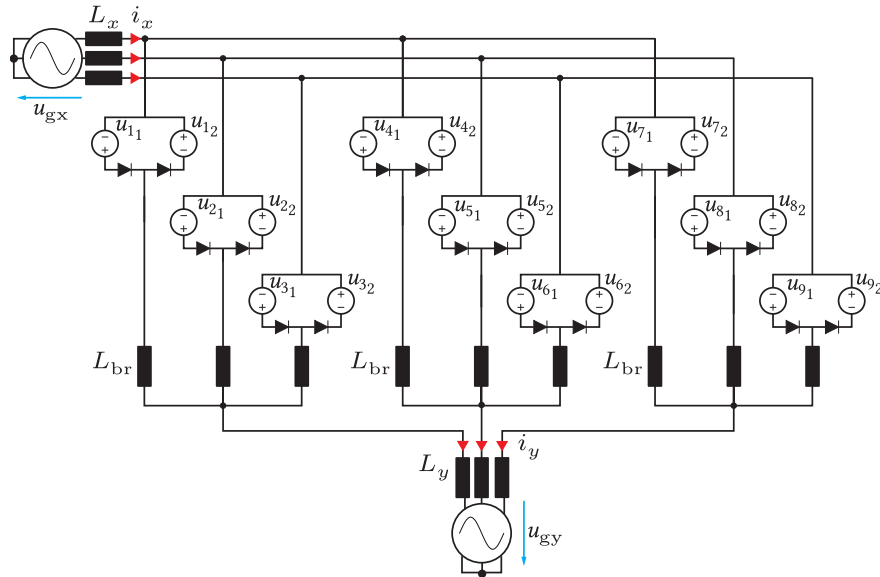


**Fig. 4.6** M3C model using a branch equivalent representation reducing the number of switches and making them independent from the number of cells per branch.



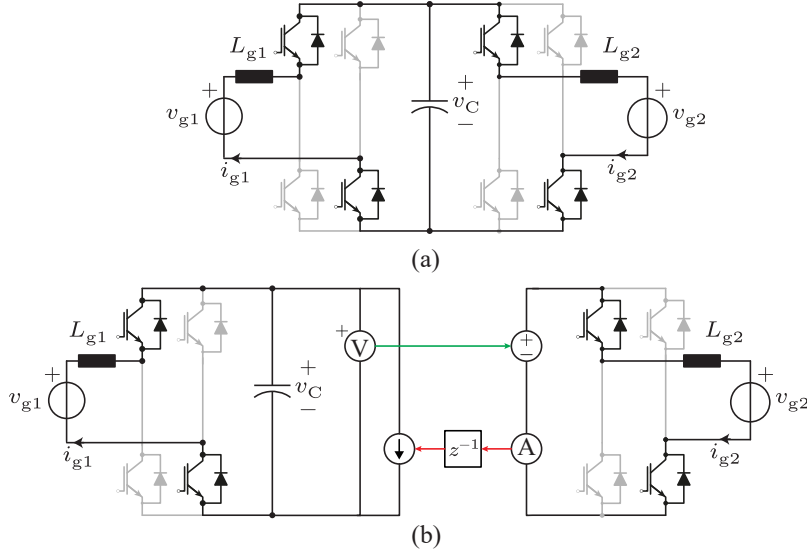


**Fig. 4.7** Example of circuit splitting, with (a) showing the initial circuit an arbitrary switching state and (b) the equivalent split circuit in the same switching state.

This simplification reduces the number of switches to two diodes per branch, independent of the number of cells. Thus, the number of state space matrices is significantly reduced from  $2^{288}$  to  $2^{18}$ . Nevertheless, the complexity of this model, due to the high number of state space matrices, makes it unsuitable for the implementation on the Application RT Box, to the point of not even being able to load this configuration onto the RT Box. Consequently, the already simplified model requires additional splitting to further reduce the number of state matrices to make it compatible with the RT Box and to reduce the simulation time step.

The branch model, as shown in **Fig. 4.6**, being simplified to the minimum while still being valid in all operating conditions, makes further simplification impossible without loss of generality. In order to further reduce the number of state space matrices, the dependency between the subclusters of the M3C shown in the **Fig. 4.6** has to be eliminated, which requires splitting of the model into multiple smaller circuits running in parallel. From the topology, as shown in **Fig. 4.6**, an available separation would be the one of the three subclusters into three parallel running circuits and replacing them with current sources in the original circuit. Such a separation allows to reduce the number of state space matrices from  $2^{18}$  to  $3 \times 2^6$ , which results in the reduction needed to allow an acceptable step size for the RT-HIL simulations.

The concept of splitting a circuit into smaller independent circuits and the resulting benefits are demonstrated on the circuit shown in **Fig. 4.7**, using two FB cells with a common capacitance in an arbitrary switching stage. The state space matrix defining the initial circuit is expressed as:

$$\underbrace{\frac{\partial}{\partial t} \begin{bmatrix} i_{g1} \\ v_c \\ i_{g2} \end{bmatrix}}_{\dot{x}} = \underbrace{\begin{bmatrix} 0 & -\frac{1}{L_{g1}} & 0 \\ \frac{1}{C} & 0 & \frac{1}{C} \\ 0 & \frac{1}{L_{g2}} & 0 \end{bmatrix}}_A \underbrace{\begin{bmatrix} i_{g1} \\ v_c \\ i_{g2} \end{bmatrix}}_x + \underbrace{\begin{bmatrix} \frac{1}{L_{g1}} & 0 \\ 0 & 0 \\ 0 & -\frac{1}{L_{g2}} \end{bmatrix}}_B \underbrace{\begin{bmatrix} v_{g1} \\ v_{g2} \end{bmatrix}}_u \quad (4.1)$$

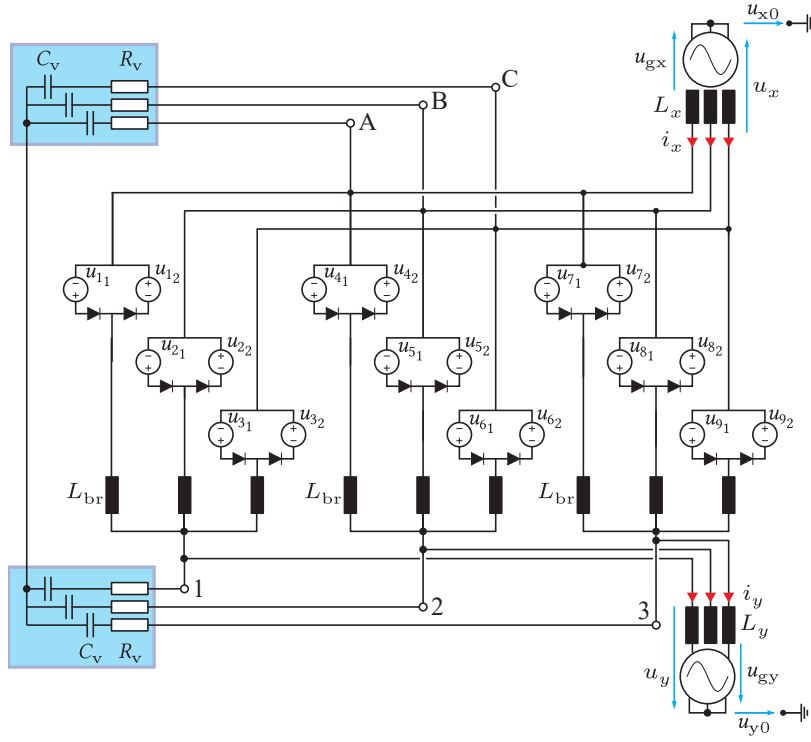


**Fig. 4.8** Extension of the M3C model using Virtual Capacitor and Virtual Resistor, highlighted in blue. This addition allows splitting of the model, resulting in further time step reduction while not changing its validity regarding the testing of the control scheme.

The total number of state space matrices that define such a circuit is calculated by  $N_{ss} = 2^{4+4}$ . An intuitive way of splitting this circuit is at the capacitance, resulting in two individual circuits with each having four switches, thus resulting in  $N_{ss} = 2 * 2^4$ . The resulting state space matrices of the split circuit in the same switching state, shown in **Fig. 4.7**, is:

$$\begin{aligned} \frac{\partial}{\partial t} \begin{bmatrix} i_{g1} \\ v_c \end{bmatrix} &= \underbrace{\begin{bmatrix} 0 & -\frac{1}{L_{g1}} \\ \frac{1}{C} & 0 \end{bmatrix}}_{A_1} \begin{bmatrix} i_{g1} \\ v_c \end{bmatrix} + \underbrace{\begin{bmatrix} \frac{1}{L_{g1}} & 0 \\ 0 & -\frac{1}{C} \end{bmatrix}}_{B_1} \begin{bmatrix} v_{g1} \\ i_s \end{bmatrix} \\ \frac{\partial i_{g2}}{\partial t} &= \underbrace{\begin{bmatrix} 0 \end{bmatrix}}_{A_2} \begin{bmatrix} i_{g2} \end{bmatrix} + \underbrace{\begin{bmatrix} \frac{1}{L_{g2}} & -\frac{1}{L_{g2}} \end{bmatrix}}_{B_2} \begin{bmatrix} v_s \\ v_{g2} \end{bmatrix} \end{aligned} \quad (4.2)$$

Assuming a small time-step, such that the following approximation holds:  $i_s = i_{g2}[k-1] \approx i_{g2}[k]$  and replacing  $v_s = v_c$ , it is obvious that the resulting state space matrix from the split circuit corresponds to the initial one.

Applying the same logic to the model of the M3C, as shown in **Fig. 4.6**, is not possible due to the absence of a centralized dc link. Nevertheless, this issue can be solved by the addition of artificial capacitances and resistances. As this addition exists only in the RT model, the added elements will be referred to as Virtual Resistor (VR) and Virtual Capacitor (VC), respectively. The RT-HIL platform is

all about processing virtual power, which allows the introduction of additional components to the circuit under the condition that the virtual circuit, which is introduced, does not affect the frequency components of interest to allow the validation of the controller. **Fig. 4.8** shows the addition of two sets, each consisting of three resistances and capacitances to the initial circuit shown in **Fig. 4.6**. The tuning of the VC and VR is presented afterwards.

### 4.3 Validation of the model

The goal of the addition of the VC and VR is to split two of the three subclusters from the rest of the system, in this case subclusters 1 and 2 were chosen. To prove the validity of this separation, the Kirchhoff voltage and current laws can be analyzed and compared to the initial equations resulting from **Fig. 4.6**. The following analysis of **Fig. 4.8** holds for any of the nine branches, where  $x$  denotes the input phase,  $x \in [a, b, c]$  and  $y$  the output phase,  $y \in [1, 2, 3]$ .

#### 4.3.1 Mathematical verification

The mathematical verification is relying on the branch current and voltage equations. Recalling the generalized branch voltage equation:

$$u_{xy} = u_x + u_{x0} - u_y - u_{y0} \quad (4.3)$$

From (4.3), combining  $u_{y0}$  and  $u_{x0}$ , the common mode voltage can be defined by  $u_0 = u_{y0} - u_{x0}$ .

The AC terminal currents from both the input and output terminals of **Fig. 4.6** can be defined by:

$$i_x = \sum_y i_{xy} \quad \text{for } x \in [a, b, c] \quad (4.4)$$

$$i_y = \sum_x i_{xy} \quad \text{for } y \in [1, 2, 3] \quad (4.5)$$

While it is obvious that (4.3) remains the same for the model with the virtual circuit shown in **Fig. 4.8**, (4.4) and (4.5) will be influenced by the current flowing through the virtual circuit,  $i_{vx}$  and  $i_{vy}$ .

$$i_x = \sum_y i_{xy} + i_{vx} \quad \text{for } x \in [a, b, c] \quad (4.6)$$

$$i_y = \sum_x i_{xy} + i_{vy} \quad \text{for } y \in [1, 2, 3] \quad (4.7)$$

To guarantee the validity of the split model, it has to be proven that from the controller point of view, the following equations are verified: (4.4) = (4.6) and (4.5) = (4.7). It is of importance to prove that, from the controller point of view, there is no influencing difference between the model on the RT-HIL and the actual converter circuit. As the high frequencies are filtered out in the control loop, the frequencies that may interfere with the control are the low frequencies close to the nominal operating

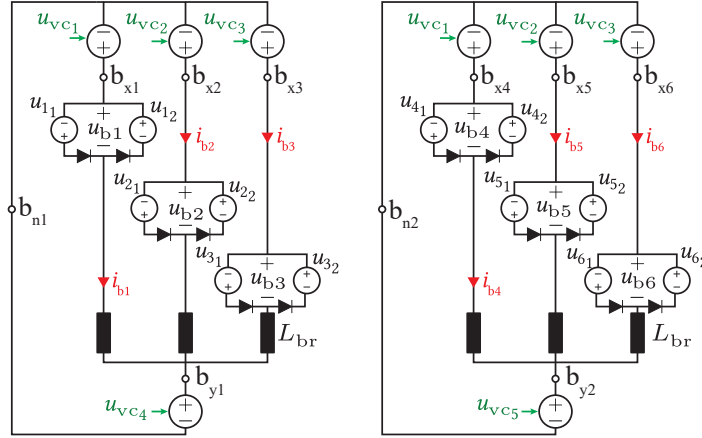


**Fig. 4.9** Separating both subcluster 1, shown on the left side, and subcluster 2, illustrated on the right side, from the initial model of the M3C

frequencies of the model. With a properly tuned virtual circuit, resulting in a very high impedance for low frequencies and thus a current lower than 2% of the nominal current flowing through the virtual circuit, this model can be considered equivalent to the actual converter circuit, at least from the controller verification viewpoint.

With a properly tuned virtual circuit, subclusters 1 and 2 in **Fig. 4.8** can be separated from the model and be represented by **Fig. 4.9**. However, to guarantee Kirchhoff voltage laws to be equal to the initial model, some constraints have to be applied to the voltage sources present in the subcluster model.

- The potential between the points marked by  $b_{x1}$  and  $b_{x2}$  must be equal to the potential between the points A and B in **Fig. 4.8**. The same condition holds for  $b_{x4}$  and  $b_{x5}$ .
- The potential at the points  $b_{n1}$  and  $b_{n2}$  should be equal.
- The potential between the points  $b_{y1}$  and  $b_{y2}$  must be equal to the potential between the points 1 and 2 in **Fig. 4.8**.

With these conditions, following voltages can be defined:

$$u_{vc1,2,3} = u_{a,b,c} - 0.5u_0 \quad (4.8)$$

$$u_{vc4,5,6} = u_{1,2,3} + 0.5u_0 \quad (4.9)$$

With the conditions above, it can be shown that the Kirchhoff current laws from the initial model are verified as well. The expression of the branches from the two separated subclusters 1 and 2 are defined below:

$$L_{br} \frac{\partial i_{b_{1,2,3}}}{\partial t} = u_{vc1,2,3} - u_{b_{1,2,3}} - u_{vc4} = u_{a,b,c} - u_{b_{1,2,3}} - u_1 - u_0 \quad (4.10)$$

$$L_{br} \frac{\partial i_{b_{4,5,6}}}{\partial t} = u_{vc1,2,3} - u_{b_{4,5,6}} - u_{vc5} = u_{1,2,3} - u_{b_{4,5,6}} - u_2 - u_0 \quad (4.11)$$

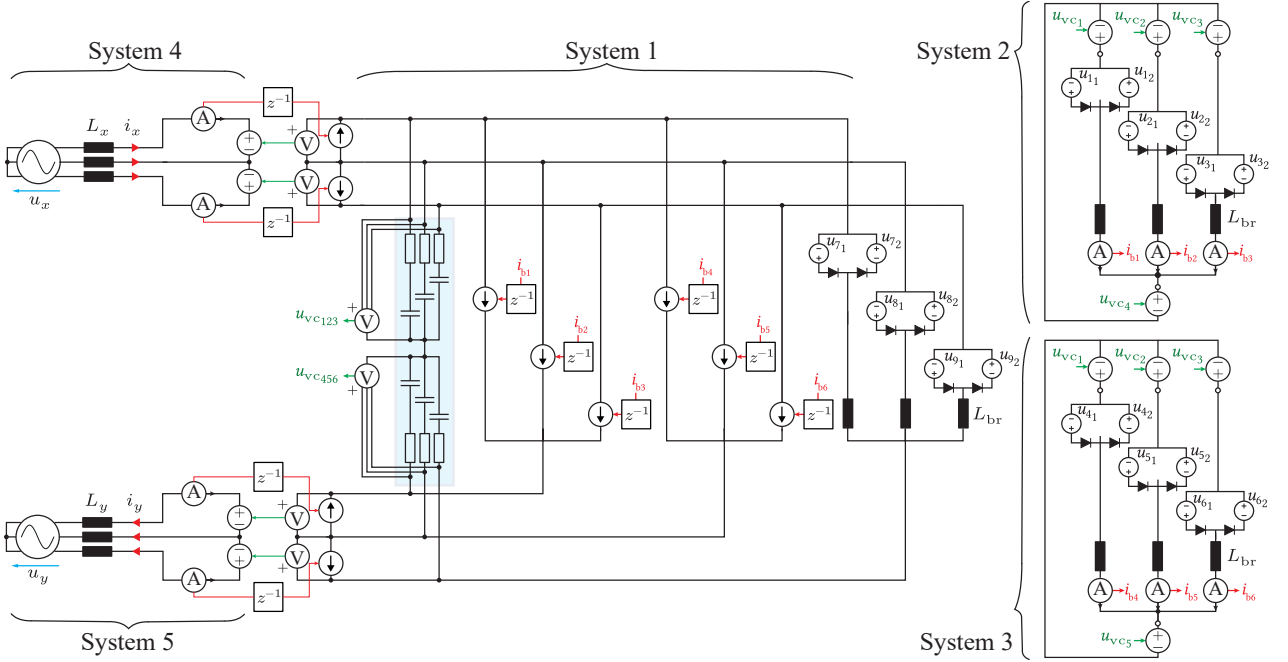


**Fig. 4.10** Final RT suitable model of the M3C divided into five independent circuits. System 1 incorporates the virtual circuit as well as all nine branches, where the first six are replaced with ideal current sources. System 2 and 3 are the separated circuit of the branches 1 to 3 and 4 to 6 respectively. System 4 is the three phase grid input and system 5, while shown as three phase output grid, can also be replaced with a three phase machine, as would be the case for a PHSP.

After both subclusters are modeled separately, as they constitute a series connection of a voltage source with an inductor, they can be replaced by a controlled current source in the initial model. Two additional conditions have to be fulfilled to guarantee proper operation of the split model, namely:

1. The virtual circuit is tuned in a way to constitute a very high impedance for low frequency currents, thus its influence on the model, from a simulation point of view, can be discarded.
2. The simulation time step should be small enough to validate the statement that the variation of two neighboring samples of any quantity, here labeled with  $x$ , can be considered negligible, which is mathematically formulated as:  $x[k] - x[k+1] \approx 0$ . This second condition is necessary as a delay between the current measurement of the split circuit and the main circuit has to be introduced to avoid an algebraic loop. This delay should not influence the behavior of the overall system.

With the previously mentioned conditions fulfilled, the split model shown in **Fig. 4.10** can be defined. The main objective to reduce the number of state space matrices has successfully been achieved as with the splitting, this number was reduced to  $3 \times 2^6$ .

The final model seen in **Fig. 4.10** contains additional splitting where both the AC grids are replaced each by two current sources. This additional splitting is possible because of the addition of the VC, and further simplifies the overall model, further reducing the required computational resources. From **Fig. 4.10**, it can be observed that the initial model is split into five separate instances:

- System 1  $\rightarrow$  Subcluster 3 including VCs and VRs

- System 2 → Subcluster 1
- System 3 → Subcluster 2
- System 4 → Input AC grid
- System 5 → Output AC grid or AC machine

Previously, it was proven that the addition of the virtual circuit, if tuned properly, does not influence the functionality of the basic model. The separation of the two subclusters from the initial model was shown not to change the operation of the converter. With all the circuits together, shown in **Fig. 4.10**, the final verification to prove that the replacement of the two subclusters with current sources, as well as the addition of the VC and VR, does not change the input and output terminal dynamics of the initial model, is presented below. With 21 branches and 9 nodes in the circuit, a total of 13 voltage loops can be defined in the circuit shown in **Fig. 4.10**, from where the expression of the ac input grid voltage is found.

$$u_{g_{a,b,c}} - L_x \frac{\partial i_{a,b,c}}{\partial t} = \frac{u_{b_{7,8,9}}}{3} + \frac{L_{br}}{3} \frac{\partial i_{b_{7,8,9}}}{\partial t} + \frac{2u_{vc_{1,2,3}}}{3} - \frac{u_{vc_4}}{3} - \frac{u_{vc_5}}{3} + u_0 \quad (4.12)$$

Inserting (4.10) and (4.11) leads to the final expression:

$$u_{g_{a,b,c}} - L_x \frac{\partial i_{a,b,c}}{\partial t} = \frac{\overbrace{u_{b_{1,2,3}} + u_{b_{4,5,6}} + u_{b_{7,8,9}}}^{u_{eq_{a,b,c}}}}{3} + u_0 + \frac{L_{br}}{3} \frac{\partial i_{a,b,c}}{\partial t} \quad (4.13)$$

With the same procedure, the expression of the ac output voltage can be developed:

$$u_{g_{1,2,3}} + L_y \frac{\partial i_{1,2,3}}{\partial t} = - \left( \frac{\overbrace{u_{b_{1,4,7}} + u_{b_{2,5,8}} + u_{b_{3,6,9}}}^{u_{eq_{1,2,3}}}}{3} + u_0 \right) - \frac{L_{br}}{3} \frac{\partial i_{1,2,3}}{\partial t} \quad (4.14)$$

With both (4.13) and (4.14), an equivalent model of the analyzed M3C as seen from the input and output ac terminals can be developed. Thereafter, the dynamics of the M3C input and output ac currents can be described and compared to the dynamics of the initial model shown in **Fig. 4.6** in order to validate the usage of the model shown in **Fig. 4.10**.

$$L_{\Sigma_x} \frac{\partial i_a}{\partial t} = \frac{2u_{g_a} - u_{g_b} - u_{g_c}}{3} - \frac{2u_{eq_a} - u_{eq_b} - u_{eq_c}}{3} \quad (4.15a)$$

$$L_{\Sigma_x} \frac{\partial i_b}{\partial t} = \frac{2u_{g_b} - u_{g_a} - u_{g_c}}{3} - \frac{2u_{eq_b} - u_{eq_a} - u_{eq_c}}{3} \quad (4.15b)$$

$$L_{\Sigma_x} \frac{\partial i_c}{\partial t} = \frac{2u_{g_c} - u_{g_a} - u_{g_b}}{3} - \frac{2u_{eq_c} - u_{eq_a} - u_{eq_b}}{3} \quad (4.15c)$$

$$L_{\Sigma_y} \frac{\partial i_1}{\partial t} = \frac{2u_{g_1} - u_{g_2} - u_{g_3}}{3} - \frac{2u_{eq_1} - u_{eq_2} - u_{eq_3}}{3} \quad (4.15d)$$

$$L_{\Sigma_y} \frac{\partial i_2}{\partial t} = \frac{2u_{g_2} - u_{g_1} - u_{g_3}}{3} - \frac{2u_{eq_2} - u_{eq_1} - u_{eq_3}}{3} \quad (4.15e)$$

$$L_{\Sigma_y} \frac{\partial i_3}{\partial t} = \frac{2u_{g_3} - u_{g_1} - u_{g_2}}{3} - \frac{2u_{eq_3} - u_{eq_1} - u_{eq_2}}{3} \quad (4.15f)$$

Where  $L_{\Sigma_x} = L_x + \frac{L_{br}}{3}$  for the equivalent circuit seen from the input ac side, and  $L_{\Sigma_y} = L_y + \frac{L_{br}}{3}$  for the equivalent circuit seen from the output ac side. Equations (4.15a) to (4.15f) are equivalent to the equations from the initial model seen in **Fig. 4.6**, thus this initial model can be interchanged with the one from **Fig. 4.10**, effectively reducing the number of state space matrices to  $3 \times 2^6$ , reducing the step size as to allow the usage of small scale RT Boxes.

The time step achieved on the Application RT Box due to the reduction in state space matrices is  $10.5\mu s$ . Furthermore, the Branch RT Box is run with a simulation time step of  $5\mu s$  and the Machine RT Box with a time step of  $10\mu s$ .

### 4.3.2 Tuning of the VC

To enable the splitting of the model, the addition of the VC is required. Nevertheless, proper sizing of the capacitance is required to ensure its negligible influence on the converter terminal currents. To limit the current flowing through the VC, the smallest possible value of capacitance should be chosen, however this is not the only condition to be fulfilled. The addition of the VC might trigger resonance in the circuit and a thorough analysis of the system is needed to avoid such resonances by proper sizing of the VC. The resonant frequencies of the system can be obtained from the eigenvalues of the state matrix  $A$  for a specific circuit state, and to ensure stability, the discretization time step should be at least ten times higher than the shortest of all resonant periods of the system [81].

Determining the shortest resonant period of the circuit shown in **Fig. 4.10** analytically would require the development of all  $3 \times 2^6$  possible  $A$  state matrices and analyze their eigenvalues. While this method ultimately leads to the optimal solution of the VC value, it requires a high number of iterations to reach it. For this reason, a simplification of the circuit from **Fig. 4.10** is done to reduce the number of state space matrices.

The equivalent capacitance across the terminals of a branch changes with the switching state of each cell. However, as the resonant frequency is orders of magnitude higher than the operating frequency of the converter, these capacitance variation can be considered constant for several discretization steps. Similarly, the fact that the dynamics of the cell voltage is lower than the discretization time step allows for the assumption that the variation of this voltage are negligible between the discretization steps. Additionally, in the model shown in **Fig. 4.10**, the equivalent electrical circuit between the terminals of the branch can be simplified to a single voltage source, as one of the diodes is always in blocking state. For these reasons, the equivalent branch model, which can be considered for the analysis of the resonant frequency, can be simplified to a simple series connection of a voltage source and the branch inductor, which is also referred to as averaged model and shown in **Fig. 4.11**. Although not accurate for the simulation of the M3C, this model allows for an accurate calculation of the VC with the advantage of having only a single state space matrix.

In order for the split model to be valid, the following conditions have to be fulfilled regarding the simplified model described above:

- 1 All the poles of the system must be located in the Left Half-Plane (LHP).
- 2 The low frequency current through the virtual circuit is limited to 2% of the nominal grid current.
- 3 The shortest resonant period is at least ten times bigger than the simulation time step.

**Tab. 4.1** Details of the ac grid, SM and M3C model running on RT-HIL

parameters	Value
Grid Voltage	6.6 kV
Grid Inductance	27.7 mH
Grid Resistance	0.1 m $\Omega$
SM Voltage	6.3 kV
SM Power	500 kW
SM Torque	6088 Nm
SM Speed	750 rpm
Shaft inertia	152 kgm <sup>2</sup>
M3C cell capacitance	1 mF
M3C cell voltage	1500 V
M3C cells per branch	8
M3C branch inductance	2.5 mH
M3C branch resistance	66.4 m $\Omega$

Simply using a VC might not allow to fulfill all the conditions above, thus a VR is added with the aim to damp resonances while keeping a low capacitance value. With the system being of 12<sup>th</sup> order and having two degrees of freedom, namely the value of the VR and the VC, solving the optimization problem analytically seems to be out of reach. For this reason, a simple algorithm is developed, which sweeps numerically values for VC and VR, and for each combination checks all the above mentioned conditions. As multiple sets of VR and VC fulfill all the above mentioned conditions, the set with the highest impedance is chosen, because it has the lowest possible current flowing through the virtual circuit. The positions of the poles for the chosen values of the VC and VR are shown in **Fig. 4.12**. The final result that is used is this work is:

$$C_v = 850 \text{ nF} \quad (4.16)$$

$$R_v = 35 \Omega \quad (4.17)$$

### 4.3.3 RT-HIL simulation verification

The parameters of the M3C model which is running on the Application RT Box are given in **Tab. 4.1**.

A start up procedure of the M3C is shown in **Fig. 4.13** (a), where initially the converter is disconnected from the grid. After the connection to the grid, the cells are charged through passive charging using

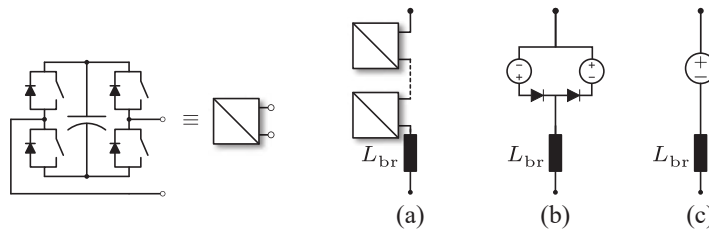


**Fig. 4.11** Equivalent branch model for (a) the real converter using a cascaded connection of FB cells (b) the RT model using two controlled voltage sources and two diodes (c) the tuning of the virtual circuit using a single controlled voltage source.



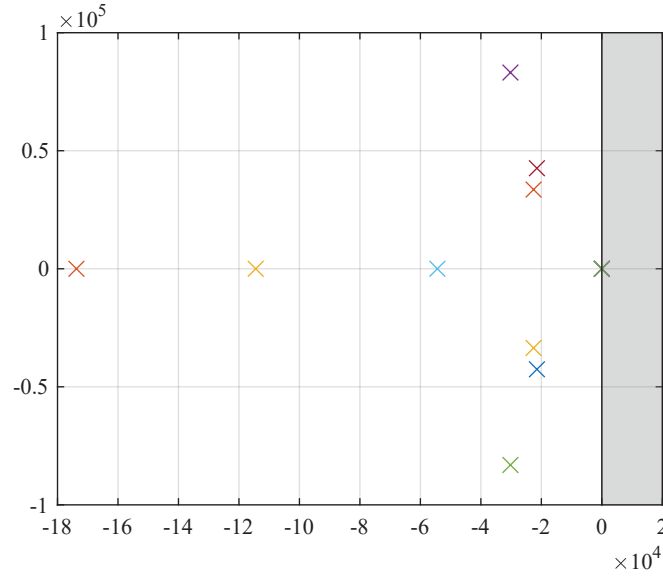


**Fig. 4.12** Position of the poles of the system shown in **Fig. 4.10** using the previously found values for the virtual circuit,  $C_v = 850$  nF and  $R_v = 35$  . All 12 poles are situated in the left half-plane.

a charging resistor to limit the inrush current. This stage allows each of the branches to be charged at the amplitude of the ac grid voltage, thus each cell within this branch has a capacitance voltage of one eighth of the total branch voltage. After passive charging and before starting active charging, a timeout is introduced during which the charging resistors are bypassed. After passive charging, the M3C is able to control the ac currents from the grid, thus enabling the active charging process. During this stage, the ac grid currents are controlled to increase the branch voltages to their nominal set point. When the cells are charged close to their nominal voltage of 1.5 kV, the branch energy balancing control is activated, enabling energy exchange between the branches to guarantee the equal distribution of energy to all branches. Throughout the passive charging, negligible currents are flowing through the virtual network, and once active charging starts, they remain negligible due to their high frequency nature as will be shown in the following simulation result.

**Fig. 4.13** (b) shows the start-up sequence in pumping mode, accelerating the machine to nominal speed, namely 750 rpm and applying the full 6000 Nm load torque. The SM is accelerated with the maximum available torque, whereas the load torque is increased linearly over 3 seconds, simulating the opening of the PDV.

Full load operation of the electrical machine in pumping mode is shown in **Fig. 4.14** (a). The currents flowing through the virtual network are shown in the last plot. To prove that these currents have a negligible influence on the control algorithm, a spectral analysis of the currents flowing through the VC is shown in **Fig. 4.15**. As the high frequencies are filtered out in the control loop, an additional zoom on the frequency components below 200 Hz, which are of interest, is included. The two peaks revealed in the zoomed part of **Fig. 4.15** occur at the nominal input and output frequency of the current operating condition of the M3C. As previously mentioned, to validate the control structure and algorithm, the virtual network should not influence the currents within the frequency range of the ac terminals, as these frequencies are not filtered out in the control loop. As can be seen in **Fig. 4.15**, neither of the peaks of the VC currents at operating frequencies is exceeding the threshold

of 2% of the nominal ac terminal currents.

To validate the use of the M3C model implemented on the RT-HIL to serve the purpose of simulating PHSP scenarios, **Fig. 4.14** (b) shows the speed reversal from pumping to generating of the electrical unit. Theoretically, the transition from full pumping power to full generating power takes less than 2 seconds, as both the load torque and machine torque contribute to this transition. However, due to mechanical and hydraulic limitations, this transition time is increase and highly dependent on the size of the unit. Throughout the whole process, the currents through the virtual network remain of high frequency nature, and the current amplitude within the frequency band of the ac terminals through the VC remain negligible. Balancing of the energy between the branches is provided through a proper implementation of an energy control algorithm, which is covered in **Chap. 5**.

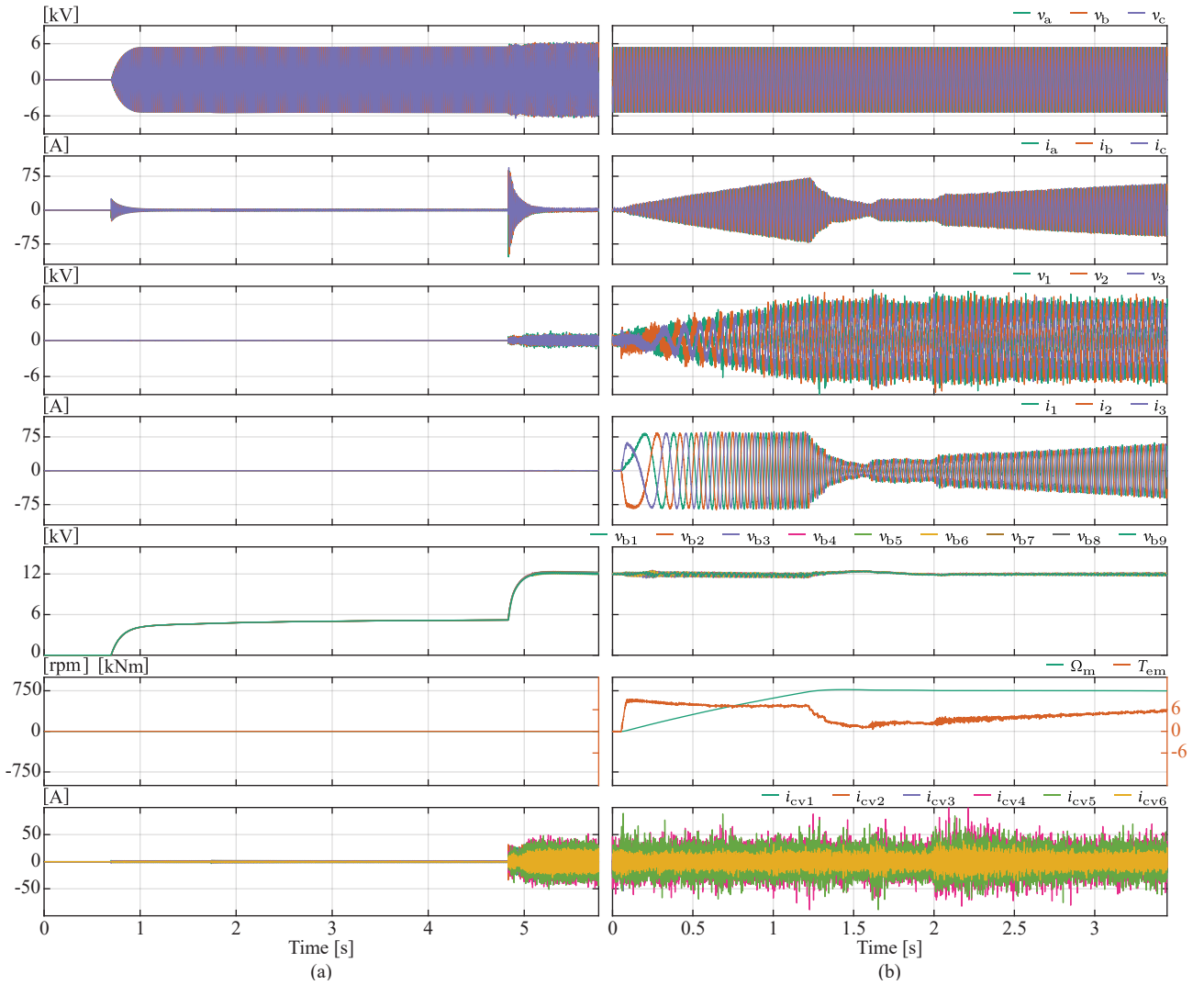


**Fig. 4.13** (a) illustrates the results of the RT-HIL simulation during the start up process of the M3C. (b) illustrates the speed-up and loading process of the SM. The Results of the RT-HIL simulation show input grid voltages and currents, machine voltages, currents, branch voltages, torque and speed as well as the currents through the virtual network.

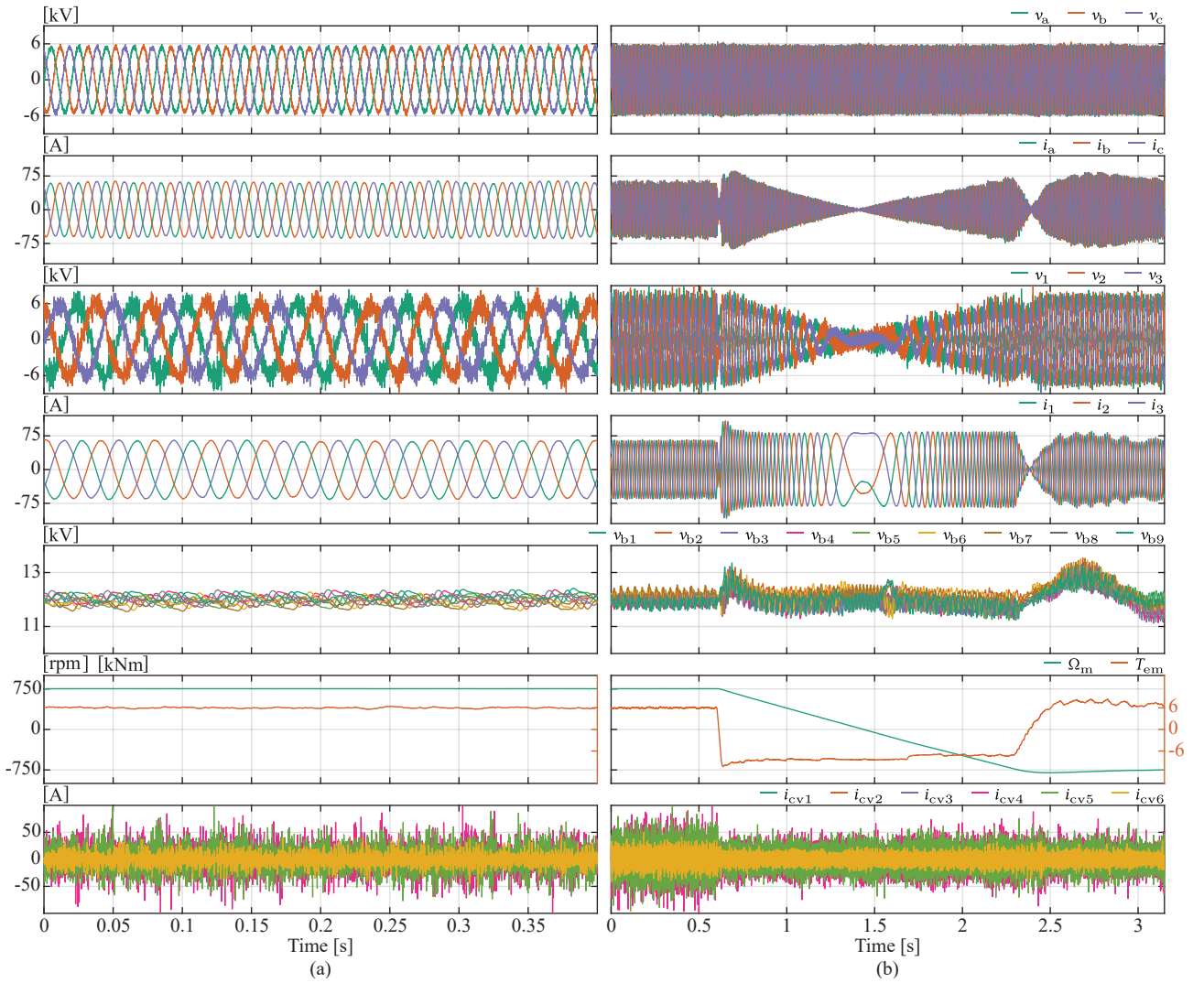


**Fig. 4.14** (a) illustrates the results of the RT-HIL simulation for a full load operation of the SM. (b) illustrates the speed-reversal under load of the SM. The Results of the RT-HIL simulation show input grid voltages and currents, machine voltages, currents, branch voltages, torque and speed as well as the currents through the virtual network.

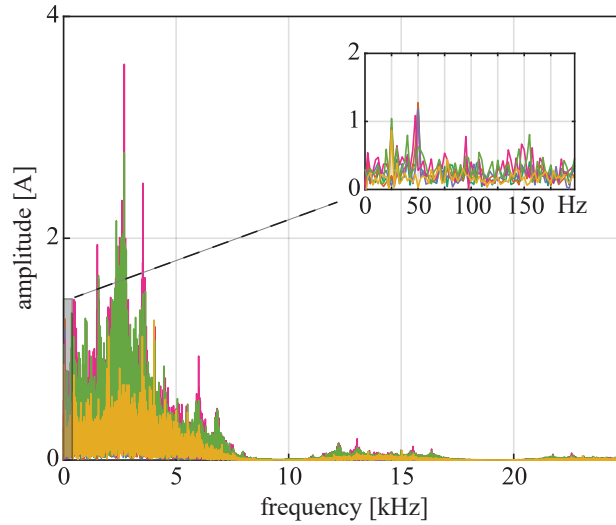


**Fig. 4.15** Spectral analysis of the currents passing through the virtual capacitances in full load mode, including a zoom on the amplitude for the frequency range from 0 Hz to 200 Hz.

## 4.4 Summary

The time step constitutes a major factor in the determination of the quality of RT simulations. For a RT-HIL system with the main purpose of validating the control structure and algorithms, the smallest possible time step is required to guarantee the fidelity of the simulation results. This chapter presents the possibility of a simulation time step reduction through the use of VC and VR, which allows the splitting of a converter into multiple independent subsystems. In this chapter, this splitting process using VC and VR is demonstrated using the M<sub>3</sub>C topology, allowing a reduction in simulation time step through a division into three independent subsystems. Proper tuning of the virtual network ensures negligible influence of the addition of this virtual network to the basic operational principle of the original model. In addition, this chapter includes a mathematical proof as well as simulation results demonstrating the validity of the split M<sub>3</sub>C model for the implementation on a RT-HIL system to validate the control structure and algorithms.

Having the equivalent control structure to the prototype that is being developed in the PEL, the above validated RT-HIL platform is generating high fidelity results for the validation of the control algorithms. Having all power elements simulated on RT Boxes, the RT-HIL enables testing of the most extreme conditions that the M<sub>3</sub>C might encounter without the risk of damaging high value equipment. Thus, the control structure and algorithms can be validated in all the extreme scenarios that could occur either from the grid side, the SM side, or even from within the M<sub>3</sub>C.

The three main control parts for the M<sub>3</sub>C are the grid current control, the SM vector control, as well as the energy balancing control within the M<sub>3</sub>C. These three control loops are verified in the coming chapters, starting with the most essential one, the energy balancing within the branches of the M<sub>3</sub>C.

# 5

## Performance Comparison of Energy Balancing Algorithms for M3C

The main advantage of the matrix modular multilevel converter, which is its series connection of full bridge cells with each having its own energy storage, introduces an additional control challenge to balance the energy among all the cells of the converter. The voltage of each capacitance must be controlled to their respective setpoints to ensure correct operation of the converter. Relying on the use of circulating currents, which are controlled to be unobservable at the converter terminals, the energy can be exchanged among the branches, balancing them. At the point of writing this thesis, the literature counts three different methods of achieving energy balancing among the cells of the matrix modular multilevel converter. These three control principles, resulting in three different implementations are thoroughly explained and their dynamic performances are compared. The results are verified using a hardware-in-the-loop platform simulating a hydro power plant using matrix modular multilevel converter connected between a 6.6 kV grid and a 6 kV synchronous machine.

### 5.1 Energy balancing requirements

In **Chap. 2**, the instantaneous branch power expression for the M3C is developed, and recalled here for convenience:

$$\begin{aligned}
 p_{xy}(t) = & \left( u_x(t) - u_y(t) - u_0(t) \right) \left( \frac{1}{3} i_x(t) + \frac{1}{3} i_y(t) + i_{\text{circ}_{xy}}(t) \right) \\
 = & \frac{1}{3} \underbrace{u_x(t) i_x(t)}_{\substack{\omega_\Sigma = 2\omega_x \\ \omega_\Delta = 0}} - \frac{1}{3} \underbrace{u_y(t) i_x(t)}_{\substack{\omega_\Sigma = \omega_y + \omega_x \\ \omega_\Delta = \omega_y - \omega_x}} - \frac{1}{3} \underbrace{u_0(t) i_x(t)}_{\substack{\omega_\Sigma = \omega_0 + \omega_x \\ \omega_\Delta = \omega_0 - \omega_x}} + \frac{1}{3} \underbrace{u_x(t) i_y(t)}_{\substack{\omega_\Sigma = \omega_x + \omega_y \\ \omega_\Delta = \omega_x - \omega_y}} - \frac{1}{3} \underbrace{u_y(t) i_y(t)}_{\substack{\omega_\Sigma = 2\omega_y \\ \omega_\Delta = 0}} - \frac{1}{3} \underbrace{u_0(t) i_y(t)}_{\substack{\omega_\Sigma = \omega_0 + \omega_y \\ \omega_\Delta = \omega_0 - \omega_y}} \\
 & + \underbrace{u_x(t) i_{\text{circ}_{xy}}(t)}_{\substack{\omega_\Sigma = \omega_x + \omega_{\text{circ}} \\ \omega_\Delta = \omega_x - \omega_{\text{circ}}}} - \underbrace{u_y(t) i_{\text{circ}_{xy}}(t)}_{\substack{\omega_\Sigma = \omega_y + \omega_{\text{circ}} \\ \omega_\Delta = \omega_y - \omega_{\text{circ}}}} - \underbrace{u_0(t) i_{\text{circ}_{xy}}(t)}_{\substack{\omega_\Sigma = \omega_0 + \omega_{\text{circ}} \\ \omega_\Delta = \omega_0 - \omega_{\text{circ}}}}
 \end{aligned} \tag{5.1}$$

In (4.5), the two degrees of freedom are the zero sequence voltage  $u_0(t)$  and the circulating currents  $i_{\text{circ}_{xy}}(t)$ . If chosen carefully, they generate a dc power component, allowing for the balancing of the energy among the branches. The input ac system frequency, which in this case is the grid, has a frequency defined at 50 Hz, and the output ac system frequency is defined by the operating frequency of the electrical machine connected to the converter.

The nominal machine frequency, defined during its design, can be optimized for a given application. This optimization falls out of the scope of this analysis and the assumption of different input and

output frequencies is made, which is logical given that the M3C has been adopted exactly for these application as the best candidate [82], [83]. Thus, neither input nor output frequency are a degree of freedom and the power components depending solely on these frequencies should not generate any dc power offset, leading to the following conditions:

- Input power should be equal to the output power and the losses combined:

$$\frac{1}{3}u_x(t)i_x(t) = \frac{1}{3}u_y(t)i_y(t) + P_{\text{loss}}$$

- Input and output frequencies should not be equal:

$$\omega_x \neq \omega_y$$

Assuming that the total energy controller works properly, thus that input and output power cancel each other out as mentioned in the first condition above, (5.1) takes the following shape:

$$\begin{aligned} p_{xy}(t) = & -\frac{1}{3} \underbrace{u_y(t)i_x(t)}_{\substack{\omega_\Sigma = \omega_y + \omega_x \\ \omega_\Delta = \omega_y - \omega_x}} - \frac{1}{3} \underbrace{u_0(t)i_x(t)}_{\substack{\omega_\Sigma = \omega_0 + \omega_x \\ \omega_\Delta = \omega_0 - \omega_x}} + \frac{1}{3} \underbrace{u_x(t)i_y(t)}_{\substack{\omega_\Sigma = \omega_x + \omega_y \\ \omega_\Delta = \omega_x - \omega_y}} - \frac{1}{3} \underbrace{u_0(t)i_y(t)}_{\substack{\omega_\Sigma = \omega_0 + \omega_y \\ \omega_\Delta = \omega_0 - \omega_y}} + \underbrace{u_x(t)i_{\text{circ}_{xy}}(t)}_{\substack{\omega_\Sigma = \omega_x + \omega_{\text{circ}} \\ \omega_\Delta = \omega_x - \omega_{\text{circ}}}} \\ & - \underbrace{u_y(t)i_{\text{circ}_{xy}}(t)}_{\substack{\omega_\Sigma = \omega_y + \omega_{\text{circ}} \\ \omega_\Delta = \omega_y - \omega_{\text{circ}}}} - \underbrace{u_0(t)i_{\text{circ}_{xy}}(t)}_{\substack{\omega_\Sigma = \omega_0 + \omega_{\text{circ}} \\ \omega_\Delta = \omega_0 - \omega_{\text{circ}}}} \end{aligned} \quad (5.2)$$

To make sure that all the dc components of (5.1), have been eliminated in (5.2), the second condition mentioned above regarding the different input and output frequency needs to be fulfilled. The operating point of equal input and output frequencies generates additional dc branch power components, as shown in **Chap. 2**. This operating point can be achieved by a set of specially defined circulating current references but falls out of the scope of this comparison [65], [84].

Following these considerations, the final expression of the branch power allowing for balancing of the energy between the branches is:

$$p_{xy\text{bal}}(t) = \frac{1}{3}u_x(t)i_{\text{circ}_{xy}}(t) - \frac{1}{3}u_y(t)i_{\text{circ}_{xy}}(t) - \frac{1}{3}u_0(t)i_x(t) - \frac{1}{3}u_0(t)i_y(t) - \frac{1}{3}u_0(t)i_{\text{circ}_{xy}}(t) \quad (5.3)$$

The above expression can be divided into three main parts:

- Power components generated through circulating currents.
- Power components generated through zero sequence voltage.
- Power component generated through both circulating currents and zero sequence voltage.

The aim of the energy balancing algorithm is to use one or more of the above mentioned available degrees of freedom as to achieve its goal. In general, the component with the least impact on the overall operation of the M3C is chosen. In normal operation, the high branch voltage component favors the use of the circulating currents as to generate a dc power component. However, in cases of, for example LVRT, where the branch voltage components are reduced significantly, it would require very high circulating currents to achieve balancing action. In this case, the branch currents are high

due to the injection of reactive power to the grid. Thus, this case favors the use of zero sequence components to achieve balancing of the energy between the branches. The third component relying on both the zero sequence voltage and the circulating currents is generally not used, as the low circulating currents would require a high zero sequence voltage.

When both input and output terminal voltages are present, which is the case for most of the converters operating points, energy balancing between the branches is achieved through the use of circulating currents rather than using the zero sequence voltage. For this reason, the comparison of the three methods is carried out under the assumption that the energy balancing is achieved through the use of circulating currents. Additionally the total energy controller, which is the same for any voltage source converter, is omitted from the analysis and the assumption is made that the overall energy within the converter is following the given setpoint. Thus, with  $u_0(t) = 0$ , (5.3) becomes:

$$p_{xy_{bal}}(t) = \frac{1}{3}u_x(t)i_{circ_{xy}}(t) - \frac{1}{3}u_y(t)i_{circ_{xy}}(t) \quad (5.4)$$

The circulating currents used for energy balancing should not affect the terminal currents, which is mathematically expressed as:

$$\begin{aligned} i_x(t) &= \sum_{y=[1,2,3]} i_{xy}^*(t) && \text{where } x \in [a, b, c] \\ &= i_x^*(t) + \underbrace{\frac{1}{3} \sum_{y=[1,2,3]} i_y^*(t) + \sum_{y=[1,2,3]} i_{circ_{xy}}^*(t)}_{=0} \end{aligned} \quad (5.5)$$

$$\begin{aligned} i_y(t) &= \sum_{x=[a,b,c]} i_{xy}^*(t) && \text{where } y \in [1, 2, 3] \\ &= i_y^*(t) + \underbrace{\frac{1}{3} \sum_{x=[a,b,c]} i_x^*(t) + \sum_{x=[a,b,c]} i_{circ_{xy}}^*(t)}_{=0} \end{aligned} \quad (5.6)$$

With the assumption of balanced terminal currents, in both (5.5) and (5.6), the influence of the opposite terminal currents on the considered current is always equal to 0. Two main concepts are used to ensure the sum of the circulating currents to add up to zero on the converter terminals.

The first one relies on the reference frame change to the so called double- $\alpha\beta 0$  frame, which ensures that the circulating currents generated do sum up to zero at the converter terminals [85]–[88]. This reference frame transformation generates four currents which, independent of their amplitude and phase angle, always sum up to zero on the converter terminals. Converting the initial energy reference to the double- $\alpha\beta 0$  frame and using these four previously mentioned currents to fulfill the energy reference ensures proper energy balancing.

The second concept does not rely on a reference frame change, but modifies the circulating current reference for each branch in a way to ensure the condition above [89], [90]. The nine branch energy references are generated separately, and only the resulting branch current following this reference is modified to sum up to zero on the converter terminals. This concept is used for both the second and

the third method compared in this work. Even though these two methods are said to belong to the same reference modification concept, mapping of the original circulating current references is done in a different way. This affects the converter balancing dynamics as shown in this chapter.

## 5.2 Existing energy balancing control methods

To achieve balancing without interfering with the terminal currents, either of the two previously introduced concepts (working directly in the double- $\alpha\beta 0$  domain or relying on post-processing of references derived for every branch individually) has to be used. This mathematical manipulation of the references aims to find the closest possible circulating current reference that achieves the required balancing action while not acting on the terminal currents. Three mathematical transformations are analyzed in the following sections, namely the double- $\alpha\beta 0$  transformation, the projection on the null space and the direct arm energy control. Through modification of the power references, the first method allows to extract the four circulating currents, which can be controlled individually. The two other methods compute the required branch power for each branch separately and the resulting circulating current references do not necessarily sum up to zero at the terminals, given that energy unbalances can be arbitrarily distributed over the converter. This requires a modification of the branch current references in order to eliminate the influence on the terminal currents.

Hereafter, an illustration of the mathematical transformation applied to the branch power references aiming to balance the energy among the branches is developed. The branch energy controller gains are set to be equal for all three methods and will thus not be further developed in this work. The structure, including the PI-controllers to generate the dc branch power reference for internal balancing, is shown in **Fig. 5.1**. While the nine separate branch energy controllers are used for all three methods, it is noteworthy that for the double- $\alpha\beta 0$ , the control structure could be modified to transform the input to the PI-controllers, rather than the obtained power reference. This would allow different tuning of the PI-controllers for the different energy balancing directions. However, for a fair comparison of the reference modification applied for each method, the structure as seen in **Fig. 5.1** is used for all three methods.

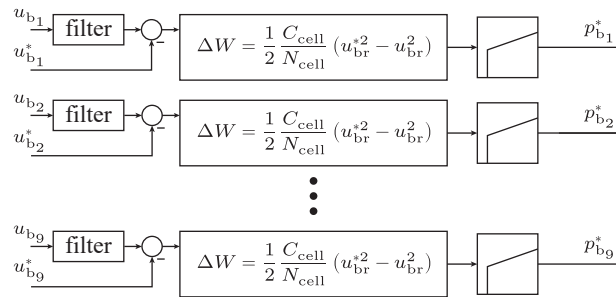


**Fig. 5.1** Implementation of the energy PI controllers used for the energy balancing power reference calculation. Method 1 transforms the obtained power references into the double- $\alpha\beta 0$  frame and generates the current references in this new frame. Methods 2 and 3, however, compute the current reference without modifying the obtained power references and modify only the obtained current references.



### 5.2.1 Method 1: double $\alpha\beta 0$ transformation

The double- $\alpha\beta 0$  transformation relies, as the name suggests, on the use of the Clarke transformation matrix. Applying this transformation twice to the branch powers will lead to:

$$\begin{bmatrix} P_{\alpha\alpha} & P_{\alpha\beta} & P_{\alpha 0} \\ P_{\beta\alpha} & P_{\beta\beta} & P_{\beta 0} \\ P_{0\alpha} & P_{0\beta} & P_{00} \end{bmatrix} = C_{\alpha\beta 0} \left( C_{\alpha\beta 0} \begin{bmatrix} P_{a1} & P_{b1} & P_{c1} \\ P_{a2} & P_{b2} & P_{c2} \\ P_{a3} & P_{b3} & P_{c3} \end{bmatrix} \right)^T \quad \text{where} \quad C_{\alpha\beta 0} = \frac{2}{3} \begin{bmatrix} 1 & \frac{-1}{2} & \frac{-1}{2} \\ 0 & \frac{\sqrt{3}}{2} & \frac{-\sqrt{3}}{2} \\ \frac{1}{2} & \frac{1}{2} & \frac{1}{2} \end{bmatrix} \quad (5.7)$$

To implement the control algorithm as explained in [88], an additional transformation is required:

$$\begin{bmatrix} P_{d1\alpha} \\ P_{d1\beta} \\ P_{d2\alpha} \\ P_{d2\beta} \end{bmatrix} = C_D \begin{bmatrix} P_{\alpha\alpha} \\ P_{\alpha\beta} \\ P_{\beta\alpha} \\ P_{\beta\beta} \end{bmatrix} \quad \text{where} \quad C_D = \frac{1}{2} \begin{bmatrix} 1 & 0 & 0 & 1 \\ 0 & 1 & -1 & 0 \\ 1 & 0 & 0 & -1 \\ 0 & 1 & 1 & 0 \end{bmatrix} \quad (5.8)$$

Based on these transformations, four balancing directions can be differentiated, which are defined as follows:

- Vertical: Energy balancing between the set of branches connected to the same output phase ( $[P_{a1,b1,c1}]$ ,  $[P_{a2,b2,c2}]$ ,  $[P_{a3,b3,c3}]$ ).
- Horizontal: Energy balancing between the set of branches connected to the same input phase ( $[P_{a1,a2,a3}]$ ,  $[P_{b1,b2,b3}]$ ,  $[P_{c1,c2,c3}]$ ).
- Diagonal 1: Energy balancing between the set of branches along the first diagonal ( $[P_{a1,b3,c2}]$ ,  $[P_{a2,b1,c1}]$ ,  $[P_{a3,b2,c1}]$ ).
- Diagonal 2: Energy balancing between the set of branches along the second diagonal ( $[P_{a1,b2,c3}]$ ,  $[P_{a2,b3,c1}]$ ,  $[P_{a3,b1,c2}]$ ).

To generate the given power references, a set of circulating currents in the double- $\alpha\beta 0$  frame needs to be defined. Similar to (5.7), these currents can be defined as:

$$\begin{bmatrix} i_{\alpha\alpha} & i_{\alpha\beta} & i_{\alpha 0} \\ i_{\beta\alpha} & i_{\beta\beta} & i_{\beta 0} \\ i_{0\alpha} & i_{0\beta} & i_{00} \end{bmatrix} = C_{\alpha\beta 0} \left( C_{\alpha\beta 0} \begin{bmatrix} i_{a1} & i_{b1} & i_{c1} \\ i_{a2} & i_{b2} & i_{c2} \\ i_{a3} & i_{b3} & i_{c3} \end{bmatrix} \right)^T \quad (5.9)$$

The currents  $i_{\alpha 0}$ ,  $i_{\beta 0}$ ,  $i_{0\alpha}$  and  $i_{0\beta}$  represent the input and output terminal currents. Assuming balanced input and output terminal currents,  $i_{00} = 0$  holds true. Thus, a total of four currents that are internal to the M3C are used for the balancing of the energy among the branches. Mathematically, the same conclusion can be drawn by analyzing the structure shown in **Fig. 2.12**. With a total of nine branches and six nodes, the number of independent circulating currents is defined to be 4. Using the

transformation matrix  $C_D$  as defined above, these circulating currents are transformed:

$$\begin{bmatrix} i_{d1\alpha} \\ i_{d1\beta} \\ i_{d2\alpha} \\ i_{d2\beta} \end{bmatrix} = C_D \begin{bmatrix} i_{\alpha\alpha} \\ i_{\alpha\beta} \\ i_{\beta\alpha} \\ i_{\beta\beta} \end{bmatrix} \quad (5.10)$$

Using these four circulating currents, the nine power references defined in the double- $\alpha\beta 0$  frame can be achieved without interfering on the terminal currents.

To determine the amplitude, frequency, and phase shift of the above defined circulating currents, the nine branch power expressions have to be defined in the double- $\alpha\beta 0$  frame. This is done in three steps:

1. Express all nine branch voltages and currents in the  $abc$ -frame as a function of the previously developed double- $\alpha\beta 0$  components.
2. Express all nine branch powers in the  $abc$ -frame using the previously developed double- $\alpha\beta 0$  current and voltage expressions.
3. Develop the branch power expressions in the double- $\alpha\beta 0$  frame using the transformation shown in (5.7) and (5.8)

To express the branch voltages and current using double- $\alpha\beta 0$  components, the inverse of the matrices  $C_D$  and  $C_{\alpha\beta 0}$  needs to be defined as:

$$C_D^{-1} = \begin{bmatrix} 1 & 0 & 1 & 0 \\ 0 & 1 & 0 & 1 \\ 0 & -1 & 0 & 1 \\ 1 & 0 & -1 & 0 \end{bmatrix} \quad \text{and} \quad C_{\alpha\beta 0}^{-1} = \begin{bmatrix} 1 & 0 & 1 \\ \frac{-1}{2} & \frac{\sqrt{3}}{2} & 1 \\ \frac{-1}{2} & \frac{-\sqrt{3}}{2} & 1 \end{bmatrix}$$

The following development is demonstrated only for the currents, but holds true for the branch voltages as well.

$$\begin{bmatrix} i_{\alpha\alpha} \\ i_{\alpha\beta} \\ i_{\beta\alpha} \\ i_{\beta\beta} \end{bmatrix} = C_D^{-1} \begin{bmatrix} i_{d1\alpha} \\ i_{d1\beta} \\ i_{d2\alpha} \\ i_{d2\beta} \end{bmatrix} \quad (5.11)$$

$$\begin{bmatrix} i_{a1} & i_{b1} & i_{c1} \\ i_{a2} & i_{b2} & i_{c2} \\ i_{a3} & i_{b3} & i_{c3} \end{bmatrix} = C_{\alpha\beta 0}^{-1} \left( C_{\alpha\beta 0}^{-1} \begin{bmatrix} i_{\alpha\alpha} & i_{\alpha\beta} & i_{\alpha 0} \\ i_{\beta\alpha} & i_{\beta\beta} & i_{\beta 0} \\ i_{0\alpha} & i_{0\beta} & i_{00} \end{bmatrix} \right)^T \quad (5.12)$$

The branch voltages expressed in the double- $\alpha\beta 0$  frame can be simplified. The influence of the diagonal voltage components  $u_{d1\alpha\beta}$  and  $u_{d2\alpha\beta}$  is negligible on the overall branch voltage compared to the magnitude of the input and output voltages. The diagonal voltage components can thus be eliminated from the final expression. Taking this into account leads to the final nine branch power expression in the double- $\alpha\beta 0$  frame:

$$p_{\alpha 0} = \frac{1}{6}(u_{\alpha 0}i_{\alpha 0} - u_{\beta 0}i_{\beta 0}) + \frac{1}{2}(u_{0\alpha}i_{d1\alpha} + u_{0\beta}i_{d1\beta}) + \frac{1}{2}(u_{0\alpha}i_{d2\alpha} + u_{0\beta}i_{d2\beta}) + \frac{1}{3}u_{00}i_{\alpha 0} \quad (5.13)$$

$$p_{\beta 0} = -\frac{1}{6}(u_{\alpha 0}i_{\beta 0} + u_{\beta 0}i_{\alpha 0}) - \frac{1}{2}(u_{0\alpha}i_{d1\beta} + u_{0\beta}i_{d1\alpha}) + \frac{1}{2}(u_{0\alpha}i_{d2\beta} - u_{0\beta}i_{d2\alpha}) + \frac{1}{3}u_{00}i_{\beta 0} \quad (5.14)$$

$$p_{0\alpha} = \frac{1}{6}(u_{0\alpha}i_{0\alpha} - u_{0\beta}i_{0\beta}) + \frac{1}{2}(u_{\alpha 0}i_{d1\alpha} - u_{\beta 0}i_{d1\beta}) + \frac{1}{2}(u_{\alpha 0}i_{d2\alpha} + u_{\beta 0}i_{d2\beta}) + \frac{1}{3}u_{00}i_{0\alpha} \quad (5.15)$$

$$p_{0\beta} = -\frac{1}{6}(u_{0\alpha}i_{0\beta} + u_{0\beta}i_{0\alpha}) + \frac{1}{2}(u_{\alpha 0}i_{d1\beta} + u_{\beta 0}i_{d1\alpha}) + \frac{1}{2}(u_{\alpha 0}i_{d2\beta} - u_{\beta 0}i_{d2\alpha}) + \frac{1}{3}u_{00}i_{0\beta} \quad (5.16)$$

$$p_{d1\alpha} = \frac{1}{6}(u_{\alpha 0}i_{0\alpha} + u_{\beta 0}i_{0\beta}) + \frac{1}{6}(u_{0\alpha}i_{\alpha 0} + u_{0\beta}i_{\beta 0}) + \frac{1}{2}(u_{\alpha 0}i_{d2\alpha} - u_{\beta 0}i_{d2\beta}) + \frac{1}{2}(u_{0\alpha}i_{d2\alpha} - u_{0\beta}i_{d2\beta}) + u_{00}i_{d1\alpha} \quad (5.17)$$

$$p_{d1\beta} = \frac{1}{6}(u_{\alpha 0}i_{0\beta} - u_{\beta 0}i_{0\alpha}) - \frac{1}{6}(u_{0\alpha}i_{\beta 0} - u_{0\beta}i_{\alpha 0}) + \frac{1}{2}(u_{\alpha 0}i_{d2\beta} + u_{\beta 0}i_{d2\alpha}) - \frac{1}{2}(u_{0\alpha}i_{d2\beta} - u_{0\beta}i_{d2\alpha}) + u_{00}i_{d1\beta} \quad (5.18)$$

$$p_{d2\alpha} = \frac{1}{6}(u_{\alpha 0}i_{0\alpha} - u_{\beta 0}i_{0\beta}) + \frac{1}{6}(u_{0\alpha}i_{\alpha 0} - u_{0\beta}i_{\beta 0}) + \frac{1}{2}(u_{\alpha 0}i_{d1\alpha} + u_{\beta 0}i_{d1\beta}) + \frac{1}{2}(u_{0\alpha}i_{d1\alpha} - u_{0\beta}i_{d1\beta}) + u_{00}i_{d2\alpha} \quad (5.19)$$

$$p_{d2\beta} = \frac{1}{6}(u_{\alpha 0}i_{0\beta} + u_{\beta 0}i_{0\alpha}) + \frac{1}{6}(u_{0\alpha}i_{\beta 0} + u_{0\beta}i_{\alpha 0}) + \frac{1}{2}(u_{\alpha 0}i_{d1\beta} - u_{\beta 0}i_{d1\alpha}) - \frac{1}{2}(u_{0\alpha}i_{d1\beta} - u_{0\beta}i_{d1\alpha}) + u_{00}i_{d1\beta} \quad (5.20)$$

Each of the power components developed above includes at least one of the previously defined circulating currents. In order to act on the average energy of the branch, a dc power component must be generated. Taking into account the voltage on which the circulating current acts, these can be defined to generate the required dc power reference. Summing up the resulting circulating current references will lead to the final reference required for a correct balancing of the energy. With this procedure, all internal balancing power references can be achieved.

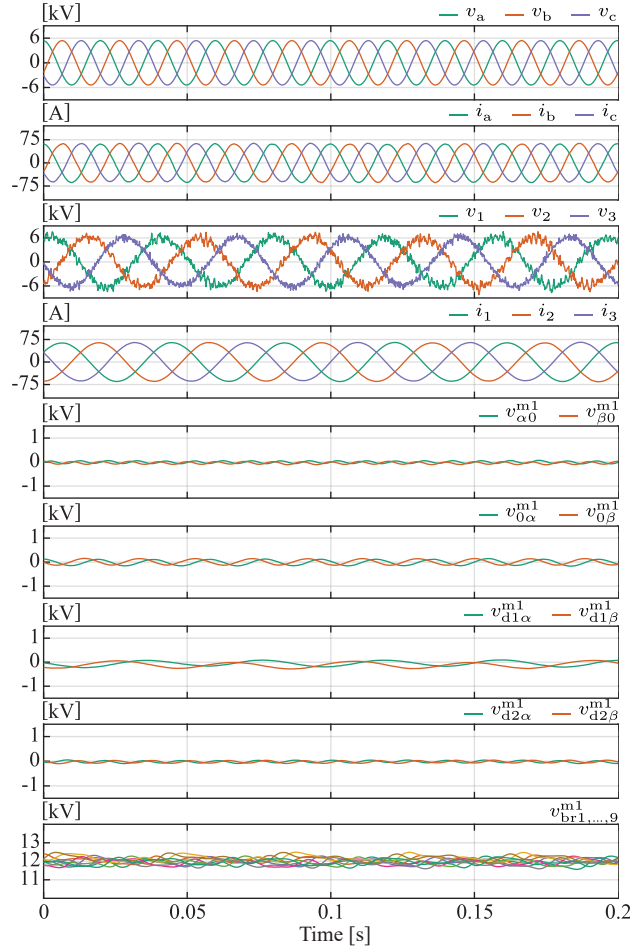


**Fig. 5.2** Full load operation of the M3C using the double- $\alpha\beta 0$  transformation for balancing of the energy among the branches. Input and output terminal ac current waveforms remain uninfluenced by the circulating currents. The branch voltages remain balanced throughout the whole simulation as they all remain centered on 12 kV, defined by the 8 cells charged to 1.5 kV. Their oscillations are defined by the respective branch currents and chosen branch capacitance.

**Fig. 5.2** shows the full load operation of the M3C using the double- $\alpha\beta 0$  transformation method for balancing of the energy among the branches. The voltages of the four previously defined balancing directions are shown and centered around 0 V, meaning that no imbalance in either direction is present. The oscillations of these voltages are a consequence of applying the double- $\alpha\beta 0$  transformation to the branch voltages without filtering. However, as stated above, balancing of the energies takes only the branch average components into account, and to remove the influence of the notch filter on the dynamic responses compared hereafter, the branch voltages are represented in their unfiltered form. The amplitude of these oscillations is defined by the branch current and the cell capacitance and should not be considered for the balancing of the energy between the branches.

### 5.2.2 Method 2: Null space vector projection

Rather than acting on the power reference itself, the energy control method developed in [89] and presented below, modifies the current references. This method is based on the principle of projecting

the nine initial circulating current references onto the null space of the matrix mapping the branch current to the terminal currents. This mapping matrix is denoted by  $T_i$  in the equation below:

$$\begin{bmatrix} i_1 \\ i_2 \\ i_3 \\ i_a \\ i_b \\ i_c \end{bmatrix} = T_i \underbrace{\begin{bmatrix} i_{a1}^* & i_{b1}^* & i_{c1}^* & i_{a2}^* & i_{b2}^* & i_{c2}^* & i_{a3}^* & i_{b3}^* & i_{c3}^* \end{bmatrix}^T}_{\vec{I}_b^*} \quad (5.21)$$

Where the matrix  $T_i$  represents the mapping  $\mathbb{R}^9 \rightarrow \mathbb{R}^6$  and is defined as:

$$T_i = \begin{bmatrix} 1 & 1 & 1 & 0 & 0 & 0 & 0 & 0 & 0 \\ 0 & 0 & 0 & 1 & 1 & 1 & 0 & 0 & 0 \\ 0 & 0 & 0 & 0 & 0 & 0 & 1 & 1 & 1 \\ 1 & 0 & 0 & 1 & 0 & 0 & 1 & 0 & 0 \\ 0 & 1 & 0 & 0 & 1 & 0 & 0 & 1 & 0 \\ 0 & 0 & 1 & 0 & 0 & 1 & 0 & 0 & 1 \end{bmatrix} \quad (5.22)$$

All the vectors  $\vec{I}_b^*$  that are mapped to zero ( $T_i \vec{I}_b^* = 0$ ) represent branch currents which do not impact neither input nor output terminal currents. The vectors with this property represent the null space of  $T_i$ , which is labeled as  $\ker(T_i)$ .

This balancing method relies on projecting the initial branch current references  $\vec{I}_b^*$  for which  $T_i \vec{I}_b^* \neq 0$  onto the null space of  $T_i$ . This projection results in a modified set of branch current references  $\vec{I}_b^{m*}$  for which  $T_i \vec{I}_b^{m*} = 0$ . To allow a projection of  $\vec{I}_b^*$  on  $\ker(T_i)$ , the basis vectors of this space have to be defined. Finding these base vectors constitutes the core of this balancing method. The decomposition of the mapping matrix  $T_i$  using the Singular Value Decomposition (SVD), as explained in [91] and similar to the development for the MMC done in [92], allows the extraction of the required base vectors. This decomposition can be written as:

$$T_i = U \times \Sigma \times V^T \quad (5.23)$$

which can be expressed as:

$$T_i = \begin{bmatrix} U_R & U_N \end{bmatrix} \times \begin{bmatrix} \Sigma_R & 0 \\ 0 & 0 \end{bmatrix} \times \begin{bmatrix} V_R^T \\ V_N^T \end{bmatrix} \quad (5.24)$$

Based on the definition of the SVD and the definition of base vectors representing a space, it can be shown that  $V_N$  constitutes the basis of  $\ker(T_i)$ . Projecting the initial branch current references on this base is done using:

$$\vec{I}_b^{m*} = V_N V_N^T \vec{I}_b^* \quad (5.25)$$

For the mapping matrix defined above, the base vectors are:

$$V_N = \begin{bmatrix} \frac{1}{2} & \frac{1}{2\sqrt{3}} & \frac{1}{2\sqrt{3}} & \frac{1}{6} \\ 0 & -\frac{1}{\sqrt{3}} & 0 & -\frac{1}{3} \\ -\frac{1}{2} & \frac{1}{2\sqrt{3}} & -\frac{1}{2\sqrt{3}} & \frac{1}{6} \\ 0 & 0 & -\frac{1}{\sqrt{3}} & -\frac{1}{3} \\ 0 & 0 & 0 & \frac{2}{3} \\ 0 & 0 & \frac{1}{\sqrt{3}} & -\frac{1}{3} \\ -\frac{1}{2} & -\frac{1}{2\sqrt{3}} & \frac{1}{2\sqrt{3}} & \frac{1}{6} \\ 0 & \frac{1}{\sqrt{3}} & 0 & -\frac{1}{3} \\ \frac{1}{2} & -\frac{1}{2\sqrt{3}} & -\frac{1}{2\sqrt{3}} & \frac{1}{6} \end{bmatrix} \quad (5.26)$$

Applying this matrix to the initial set of branch current references results in the following modified reference:

$$i_{\text{circ}_{xy}}^{m*} = i_{\text{circ}_{xy}}^* - \frac{1}{3} \left( \sum_{k=a,b,c} i_{\text{circ}_{ky}}^* \right) - \frac{1}{3} \left( \sum_{j=1,2,3} i_{\text{circ}_{xj}}^* \right) + \frac{1}{9} \left( \sum_{k=a,b,c} i_{\text{circ}_{kj}}^* \right) \quad (5.27)$$

The initial branch power reference required to achieve branch energy balancing is used to define the initial branch current reference. For each branch, this current reference is divided into two parts, one acting with the grid voltages to achieve horizontal balancing and another one at load frequency to achieve vertical balancing. These initial branch current references are defined as:

$$i_{\text{circ}_{xyh}}^* = \frac{2P_{xy}^*}{\hat{V}_x^2} v_x(t) \quad (5.28)$$

$$i_{\text{circ}_{xyv}}^* = \frac{2P_{xy}^*}{\hat{V}_y^2} v_y(t) \quad (5.29)$$

The implementation includes the initial definition of the branch currents as expressed in (5.28) and (5.29). These references are multiplied by  $V_N V_N^T$ , using the matrix  $V_N$  as defined in (5.26), which corresponds to (5.27).

From (5.3), it is known that the branch energy average is affected by the dc power components within the branch. The above developed horizontal circulating current reference creates a dc power component using only the input terminal voltages. Multiplying (5.27) by the respective input terminal voltage present in the given branch yields the dc power component which enables balancing of the

energy. The resulting dc power which contributes to the horizontal balancing of the energy can be calculated for each branch as:

$$\begin{aligned}\overline{P_{hxy}^{m2}} &= i_{\text{circ}_{xyh}}^{m*} v_x(t) \\ &= \frac{4}{9} P_{xy}^* + \frac{1}{9} \sum_{\substack{k=a,b,c \\ k \neq x}} P_{ky}^* - \frac{2}{9} \sum_{\substack{j=1,2,3 \\ j \neq y}} P_{xj}^* - \frac{1}{18} \sum_{\substack{k=a,b,c \neq x \\ j=1,2,3 \neq y}} P_{kj}^*\end{aligned}\quad (5.30)$$

Similarly, the same development can be done for the vertical energy balancing using the load voltages:

$$\begin{aligned}\overline{P_{vxy}^{m2}} &= i_{\text{circ}_{xyv}}^{m*} v_y(t) \\ &= \frac{4}{9} P_{xy}^* + \frac{1}{9} \sum_{\substack{j=1,2,3 \\ j \neq y}} P_{xj}^* - \frac{2}{9} \sum_{\substack{k=a,b,c \\ k \neq x}} P_{ky}^* - \frac{1}{18} \sum_{\substack{k=a,b,c \neq x \\ j=1,2,3 \neq y}} P_{kj}^*\end{aligned}\quad (5.31)$$

The final branch power acting on the average branch energy is the sum of both the horizontal and the vertical component.

$$\overline{P_{xy}^{m2}} = \overline{P_{hxy}^{m2}} + \overline{P_{vxy}^{m2}} \quad (5.32)$$

**Fig. 5.3** demonstrates the proper operation of this method under full load operation as the overall energy balancing among the converter is achieved.

### 5.2.3 Method 3: Direct arm energy control

Similar to the second method described above, the direct arm energy control modifies the circulating current references rather than the power reference as is the case for the first method. The principle of this method relies on subtracting the average of all circulating currents references from the branches connected to the same input and output phases to the given branch circulating current reference.

As the method is developed in the  $abc$  frame, the same balancing directions, namely the vertical and the horizontal direction, can be defined. While the diagonal direction defined in the double- $\alpha\beta 0$  frame is not explicitly defined in the initial set of current references, they are implicitly included, which is shown when converted to the double- $\alpha\beta 0$  frame, as will be seen later on.

Horizontal balancing is achieved by acting on the input grid voltage component present in the branch voltage expression, and the initial branch current reference for each of the nine branches is equal to the one presented in method 2:

$$i_{\text{circ}_{xyh}} = \frac{2P_{xy}^*}{\hat{V}_x^2} v_x(t) \quad (5.33)$$

As this reference is generated directly from the power reference, while energy unbalances within the converter can be arbitrarily distributed, it cannot be guaranteed that the terminal currents remain

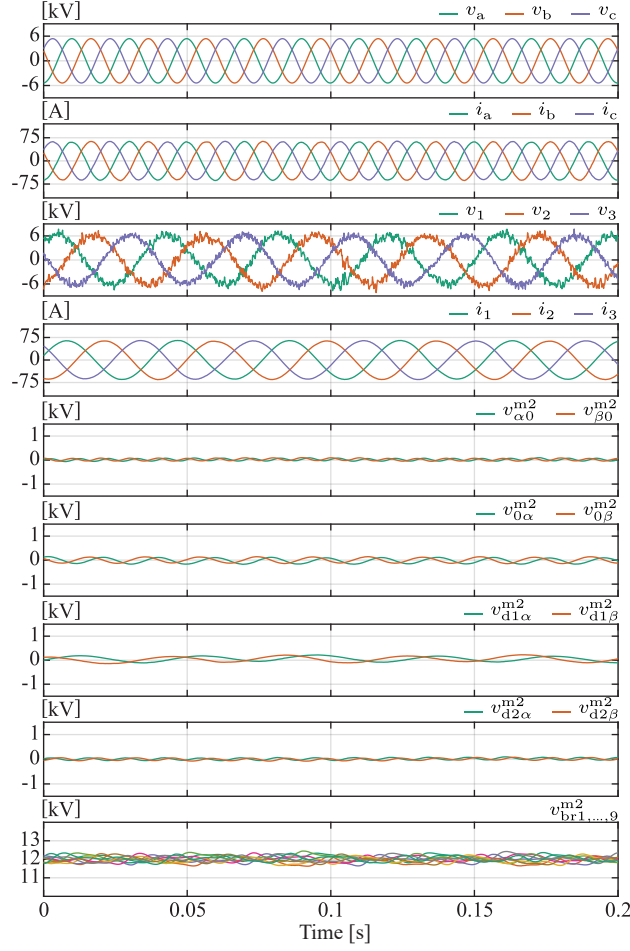


**Fig. 5.3** Full load operation of the M3C using the null space vector projection for balancing of the energy among the branches. Input and output terminal ac current waveforms remain uninfluenced by the circulating currents. The branch voltages remain balanced throughout the whole simulation while their oscillations are defined by the respective branch currents and chosen branch capacitance.

uninfluenced. As shown in [90], the influence on the input grid terminals can be eliminated by modifying the initial circulating current references using:

$$i_{\text{circ}_{xyh}}^{t_1} = i_{\text{circ}_{xyh}} - \frac{1}{3} \left( \sum_{k=a,b,c} i_{\text{circ}_{kyh}} \right) \quad (5.34)$$

While the modification of the initial reference shown above ensures no influence on the input grid terminals, there is no guarantee that the output terminal currents remain uninfluenced. For this reason, an additional modification of the reference is required:

$$i_{\text{circ}_{xyh}}^{t_2} = i_{\text{circ}_{xyh}}^{t_1} - \frac{1}{3} \left( \sum_{j=1,2,3} i_{\text{circ}_{xjh}}^{t_1} \right) \quad (5.35)$$

While this method uses a seemingly different transformation than method 2, when comparing the final references of both methods in the horizontal direction, they lead to the same final expression.



Due to the two modifications illustrated above, the final circulating current reference of the given balancing direction does not alter the terminal currents of the M3C. As the final horizontal branch current reference is equal to the one of the previous method, the resulting dc branch power in the horizontal direction will have the same expression as well:

$$\begin{aligned}\overline{P_{hxy}^{m3}} &= i_{\text{circ}_{xyh}}^{t_2} v_x(t) \\ &= \frac{2}{9} P_{xy}^* + \frac{1}{18} \sum_{\substack{k=a,b,c \\ k \neq x}} P_{ky}^* - \frac{1}{9} \sum_{\substack{j=1,2,3 \\ j \neq y}} P_{xj}^* \\ &\quad - \frac{1}{36} \sum_{\substack{k=a,b,c \neq x \\ j=1,2,3 \neq y}} P_{kj}^*\end{aligned}\tag{5.36}$$

Vertical balancing is achieved through circulating currents acting on the load terminal voltages. Assuming that the total energy control works properly, averaging the power reference of all branches connected to the same input terminal eliminates the influence on the load terminals. This leads to the initial circulating current reference for vertical balancing:

$$i_{\text{circ}_{xyv}} = \frac{v_y(t)}{3\hat{V}_y^2} \sum_{j=1,2,3} P_{xj}\tag{5.37}$$

To eliminate the impact on the input terminals of the M3C, the same procedure as for the horizontal balancing is used. A single modification is enough to eliminate influence on all terminals, due to the initial definition of the circulating current:

$$i_{\text{circ}_{xyv}}^{t_1} = i_{\text{circ}_{xyv}} - \frac{1}{3} \left( \sum_{k=a,b,c} i_{\text{circ}_{kyv}} \right)\tag{5.38}$$

A dc power component is achieved through the multiplication of the vertical circulating currents with the load terminal voltages present in the branches. This multiplication leads to the following dc power expression:

$$\begin{aligned}\overline{P_{vxy}^{m3}} &= i_{\text{circ}_{xyv}}^{t_1} v_y(t) \\ &= \frac{1}{9} \sum_{j=1,2,3} P_{xj}^* - \frac{1}{18} \sum_{\substack{k=a,b,c \neq x \\ j=1,2,3}} P_{kj}^*\end{aligned}\tag{5.39}$$

The final branch power acting on the average branch energy is the sum of both the horizontal and the vertical component as defined for method 2 in (5.31).

$$\overline{P_{xy}^{m3}} = \overline{P_{hxy}^{m3}} + \overline{P_{vxy}^{m3}}\tag{5.40}$$

**Fig. 5.4** shows the full load operation of the M3C using the above described direct arm energy control and demonstrating its proper energy balancing performance.

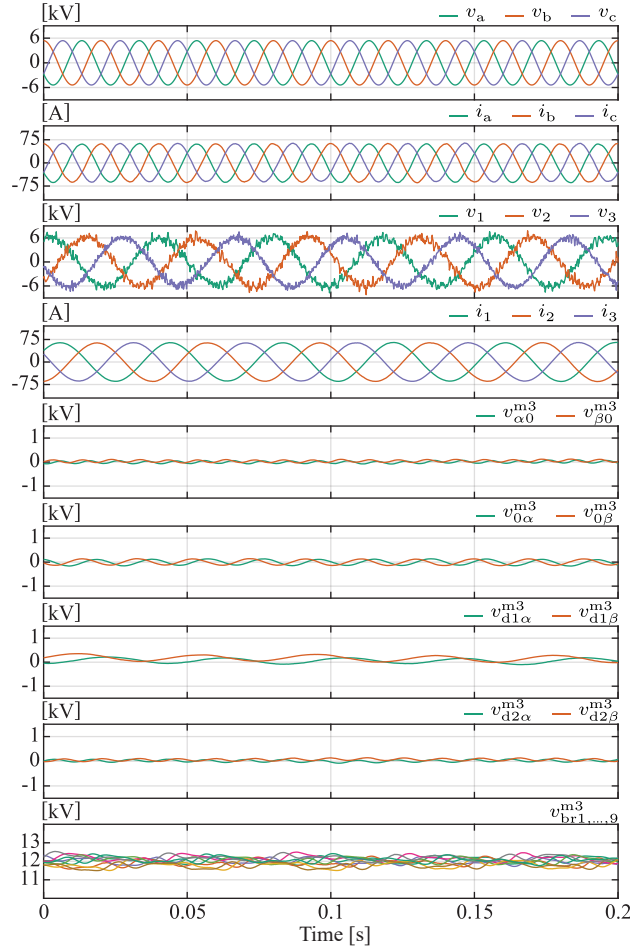


**Fig. 5.4** Full load operation of the M3C using the direct arm energy control for balancing of the energy among the branches. Input and output terminal ac current waveforms remain uninfluenced by the circulating currents. The branch voltages remain balanced throughout the whole simulation while their oscillations are defined by the respective branch currents and chosen branch capacitance.

## 5.3 Performance comparison

The development for each of the methods done above demonstrates that all three achieve the required goal of balancing the energy among the branches of the M3C. While the mathematical development already pointed out a few similarities and differences between the methods, it does not provide any information on the balancing performance in various conditions. This section includes a mathematical comparison of all three methods as well as a comparison on the RT-HIL platform introduced in Chap. 4.

### 5.3.1 Power reference comparison

To enable a comparison between the methods, the frame in which they are analyzed should be the same. In addition, equal controller gains are required to allow a fair comparison. The double- $\alpha\beta 0$  method is developed in the double- $\alpha\beta 0$  frame, whereas the null space projection method and the direct arm energy control are in the  $abc$  frame. Transforming the latter method into the double- $\alpha\beta 0$

requires the development of the equations (5.7) and (5.8).

$$P_{\alpha 0} = \frac{1}{9} \left( 2 \sum_{j=1,2,3} P_{aj} - \sum_{\substack{k=b,c \\ j=1,2,3}} P_{kj} \right) \quad (5.41)$$

$$P_{\beta 0} = \frac{1}{3\sqrt{3}} \left( \sum_{j=1,2,3} P_{bj} - \sum_{j=1,2,3} P_{cj} \right) \quad (5.42)$$

$$P_{0\alpha} = \frac{1}{9} \left( 2 \sum_{k=a,b,c} P_{k1} - \sum_{\substack{k=a,b,c \\ j=2,3}} P_{kj} \right) \quad (5.43)$$

$$P_{0\beta} = \frac{1}{3\sqrt{3}} \left( \sum_{k=a,b,c} P_{k2} - \sum_{k=a,b,c} P_{k3} \right) \quad (5.44)$$

$$P_{d1\alpha} = \frac{1}{9} \left( 3(P_{a1} + P_{b2} + P_{c3}) - \sum_{\substack{k=a,b,c \\ j=1,2,3}} P_{kj} \right) \quad (5.45)$$

$$P_{d1\beta} = \frac{1}{3\sqrt{3}} (P_{a2} + P_{b3} + P_{c1} - P_{a3} - P_{b1} - P_{c2}) \quad (5.46)$$

$$P_{d2\alpha} = \frac{1}{9} \left( 3(P_{a1} + P_{b3} + P_{c1}) - \sum_{\substack{k=a,b,c \\ j=1,2,3}} P_{kj} \right) \quad (5.47)$$

$$P_{d2\beta} = \frac{1}{3\sqrt{3}} (P_{a2} + P_{b1} + P_{c3} - P_{a3} - P_{b2} - P_{c1}) \quad (5.48)$$

The first method, using the double- $\alpha\beta 0$  transformation, fulfills the exact required power reference as explained in the section above using (5.13) to (5.20). For the second method, substituting (5.31) into (5.41) - (5.48) transforms the power references into the double- $\alpha\beta 0$  frame, whereas for the third method, the same procedure is done using (5.40). The resulting power can be expressed as the multiplication of a scaling factor and the power expression of method 1:

$$\begin{bmatrix} P_v^{m2,m3} \\ P_h^{m2,m3} \\ P_{d1}^{m2,m3} \\ P_{d2}^{m2,m3} \end{bmatrix} = \begin{bmatrix} k_v^{m2,m3} & 0 & 0 & 0 \\ 0 & k_h^{m2,m3} & 0 & 0 \\ 0 & 0 & k_{d1}^{m2,m3} & 0 \\ 0 & 0 & 0 & k_{d2}^{m2,m3} \end{bmatrix} \begin{bmatrix} P_v^{m1} \\ P_h^{m1} \\ P_{d1}^{m1} \\ P_{d2}^{m1} \end{bmatrix} \quad (5.49)$$

A scaling factor  $k = 1$  means that both methods have equal performances in the given direction. **Tab. 5.1**, shows the scaling factor for each of the defined balancing directions. Based on the branch energy variation established in the first section, this scaling factor affects the dc power component within the branches to achieve balancing in the given direction. Analyzing **Tab. 5.1** shows that all three methods generate the same dc power component in the vertical as well as in the horizontal direction, demonstrating equal performance of all three methods in these balancing directions.

**Tab. 5.1** Scaling coefficient for the comparison of method 1, method 2 and method 3.

Balancing direction	Scaling coefficients		
	Method 1	Method 2	Method 3
Vertical ( $P_{\alpha 0}, P_{\beta 0}$ )	1	1	1
Horizontal ( $P_{0\alpha}, P_{0\beta}$ )	1	1	1
Diagonal 1 ( $P_{d1\alpha}, P_{d1\beta}$ )	1	1	$1/2$
Diagonal 2 ( $P_{d2\alpha}, P_{d2\beta}$ )	1	1	$1/2$

A closer analysis of the branch power equations of method 2 converted to the double- $\alpha\beta 0$  frame shows that, even without explicitly defining the diagonal directions, it achieves the same performance along these axes compared to method 1. However, method 3, developed similarly to method 2 in  $abc$  frame, shows a reduced dc power component in the diagonal directions. Both methods generate the same horizontal power component as shown in (5.30) and (5.36), thus they differentiate each other only by their vertical power component. This demonstrates that the modification of the circulating currents in the vertical direction for method 2 influences the diagonal balancing directions while the initially defined vertical direction  $\overline{P_{vxy}^{m3}}$  acts only on the vertical direction.

As method 3 defines only the horizontal and vertical balancing directions explicitly, introducing a gain on the current reference to achieve equal diagonal balancing performance will influence the horizontal direction. This leads to an excess in power reference in the horizontal direction. Thus, method 3 cannot achieve equal performance compared to methods 1 and 2, since no gain can be explicitly defined for diagonal directions.

While **Tab. 5.1** compares the dc power references resulting from the three methods in the four directions, it does not reveal any information about the actual amplitude and phase shift of the circulating currents. Methods 1 and 2 achieve equal performance in all four balancing directions, however, the circulating currents achieving this power components are different for these methods, as will be demonstrated in the following section.

### 5.3.2 Circulating currents comparison

In the double- $\alpha\beta 0$  frame, the currents used for balancing of the energy among the branches of the converter are  $i_{d1\alpha, d1\beta}$  and  $i_{d2\alpha, d2\beta}$ . For each of the four previously defined balancing directions, these currents can be defined to generate the required power reference. This leads to the following equations:

$$i_{d1} = k_{i_{d1v}} i_{d1v} + k_{i_{d1h}} i_{d1h} + k_{i_{d1d1}} i_{d1d1} + k_{i_{d1d2}} i_{d1d2} \quad (5.50)$$

$$i_{d2} = k_{i_{d2v}} i_{d2v} + k_{i_{d2h}} i_{d2h} + k_{i_{d2d1}} i_{d2d1} + k_{i_{d2d2}} i_{d2d2} \quad (5.51)$$

Each of the two diagonal currents above includes components of both input and output ac frequencies, and **Tab. 5.2** shows the value of the coefficients for each method. Analyzing the equations (5.13) to (5.20), it can be seen that no power expression includes all four circulating currents. The currents that are not present and thus cannot be used for balancing in a given direction are the same for all three methods and marked by a black cell in **Tab. 5.2**. To achieve an accurate dc power reference in the

**Tab. 5.2** Circulating current scaling coefficient for each of the frequency component of the available circulating currents. Black cells indicate the impossibility of using this component for the given balancing direction and are the same for all three methods. A red cell highlights the impossibility of creating this component for a given method, which is only present for method 3. This table compares the current coefficients for the three methods compared in this chapter.

			Current Scaling Coefficients			
	Curr.	Freq.	Ver	Hor	Dia. 1	Dia 2
Meth 1	$ I_{d1} $	$\omega_x$		$1 - k_{hor}^{m1}$		$1 - k_{d2}^{m1}$
		$\omega_y$	$1 - k_{ver}^{m1}$			$k_{d2}^{m1}$
	$ I_{d2} $	$\omega_x$		$k_{hor}^{m1}$	$1 - k_{d1}^{m1}$	
		$\omega_y$	$k_{ver}^{m1}$		$k_{d1}^{m1}$	
Meth 2	$ I_{d1} $	$\omega_x$		0.5		0.5
		$\omega_y$	0.5			0.5
	$ I_{d2} $	$\omega_x$		0.5	0.5	
		$\omega_y$	0.5		0.5	
Meth 3	$ I_{d1} $	$\omega_x$		0.5		0.5
		$\omega_y$	0.5			0
	$ I_{d2} $	$\omega_x$		0.5	0.5	
		$\omega_y$	0.5		0	

branch for a given balancing direction, all the circulating current coefficients of that given direction should sum up to 1.

Analyzing the table for method 1, it is shown that not only do all the columns of the four directions always sum up to 1, it is also shown that the contribution of the currents for a given direction can be modified. This is a significant advantage considering the LVRT capabilities. In this case, the input ac voltage drops down to nearly 0, thus the voltage component at the frequency  $\omega_x$  is significantly reduced in all the branches. For the vertical direction, the LVRT does not reduce the balancing action, as this balancing direction requires only the presence of load voltage frequencies in the branch. The horizontal direction cannot be controlled with neither of the methods, as the only possibility is to act on the grid frequencies which are not or almost not present in the LVRT. For the first diagonal balancing, the possibility of choosing the frequency component of the circulating current allows to achieve the required dc power component by choosing  $k_{d1}^{m1} = 1$ , in which case only the load frequency is used. Similarly, for the second diagonal,  $k_{d2}^{m1} = 1$  achieves the required power reference using the load frequency. In normal operation, the freedom to choose the frequency component of the circulating currents allows to reduce their amplitude by considering the branch voltage amplitudes at the given frequencies.

Taking the example of method 2 in any of the four defined directions, it can be seen that in all four cases, the sum of the coefficients is equal to 1, thus achieving the required branch power reference to balance in the given directions. In contrast to method 1, however, the method 2 does not have any degree of freedom to chose the frequency of the circulating currents. Consequently, during a loss of the grid voltage, the balancing in both diagonal directions is affected, as only the part acting on the load voltages contributes to generating a dc power reference in the branches, which will thus be reduced by 50%. Furthermore, the missing freedom to choose the frequency of the circulating currents does not allow for any circulating current amplitude optimization as is the case for the first

method.

The third method shows the same reduced freedom to choose the frequency of the circulating currents demonstrated in method 2. However, as shown by the cells marked in red, this method does not include any load frequency component for the diagonal balancing actions. While in normal operation, this translates into only half the required dc power component present in the branch as is shown in **Tab. 5.1**, in LVRT this means a complete loss of balancing in either of the diagonal actions, as no grid frequency voltage component is present in the branches.

## 5.4 HIL simulation results

The dynamic response of these control algorithms can be tested in two different ways. The first one being their ability to reject an imbalance, whereas the second one is their ability to generate an imbalance. As both ways achieve the same goal, the latter one is used in this comparison.

To achieve a representative comparison between the three methods, the instance regarding terminal conditions at which the branch energy reference is modified is the same for all the methods.

The performance regarding the vertical balancing is shown in **Fig. 5.5** (a). In a balanced operating scenario, such as shown in **Fig. 5.4** and **Fig. 5.2**, all the branch voltage components in the double- $\alpha\beta 0$  frame oscillate with a mean value of 0 V, which corresponds to an equivalent branch voltage of 12 kV for all nine branches. A vertical imbalance is generated at 0.1 s, where the reference corresponding to the  $\alpha$  component of this direction is increased to 1 kV. Transforming this imbalance into the  $abc$  frame results in a voltage reference of 13 kV for the branches a1, a2 and a3 whereas the other six branches have a reference of 11.5 kV to keep the overall charge within the converter constant. The response to this reference change is shown in green for method 1, orange for method 2 and violet for method 3. From the plot showing  $v_{\alpha 0}$ , no significant difference in the response of the three methods can be noticed.

**Fig. 5.5** (b) compares the response of the three methods in the horizontal balancing direction. The reference to all the branches connected to the first output phase (a1, b1, c1) is increased by 1 kV whereas the reference for the remaining six branches is reduced to 11.5 kV. In the double- $\alpha\beta 0$  frame this corresponds to a 1 kV reference of the  $v_{0\alpha}$  component, which can be seen in (b). Similar to the observation of the vertical imbalance, all the methods reach the required reference at the same rate.

For part (a) of **Fig. 5.6**, an imbalance along the first diagonal of the branches of the M3C is generated. Regarding the branch references, branches a1, b2 and c3 are increased to 13 kV and to keep the overall energy within the converter constant, the other six branch references are decreased to 11.5 kV. While the first and second methods reach the reference voltage within the same time as for the previous two imbalances shown in (a) and (b), method 3 requires a longer time compared to the vertical and horizontal imbalance. This observation correlates with the conclusion of theoretical development shown in **Tab. 5.1**.

**Fig. 5.6** (b) shows the imbalance along the second diagonal, which is the last of the four defined balancing directions. For the scenario presented here, the branch references of a1, b3 and c2 are increased to 13 kV and the remaining references are decreased to 11.5 kV. For the second diagonal, this transforms into a 1 kV reference, which is achieved by methods 1 and 2 within the same time delay as for all the previous presented imbalances. Similar to the imbalance along the first diagonal,

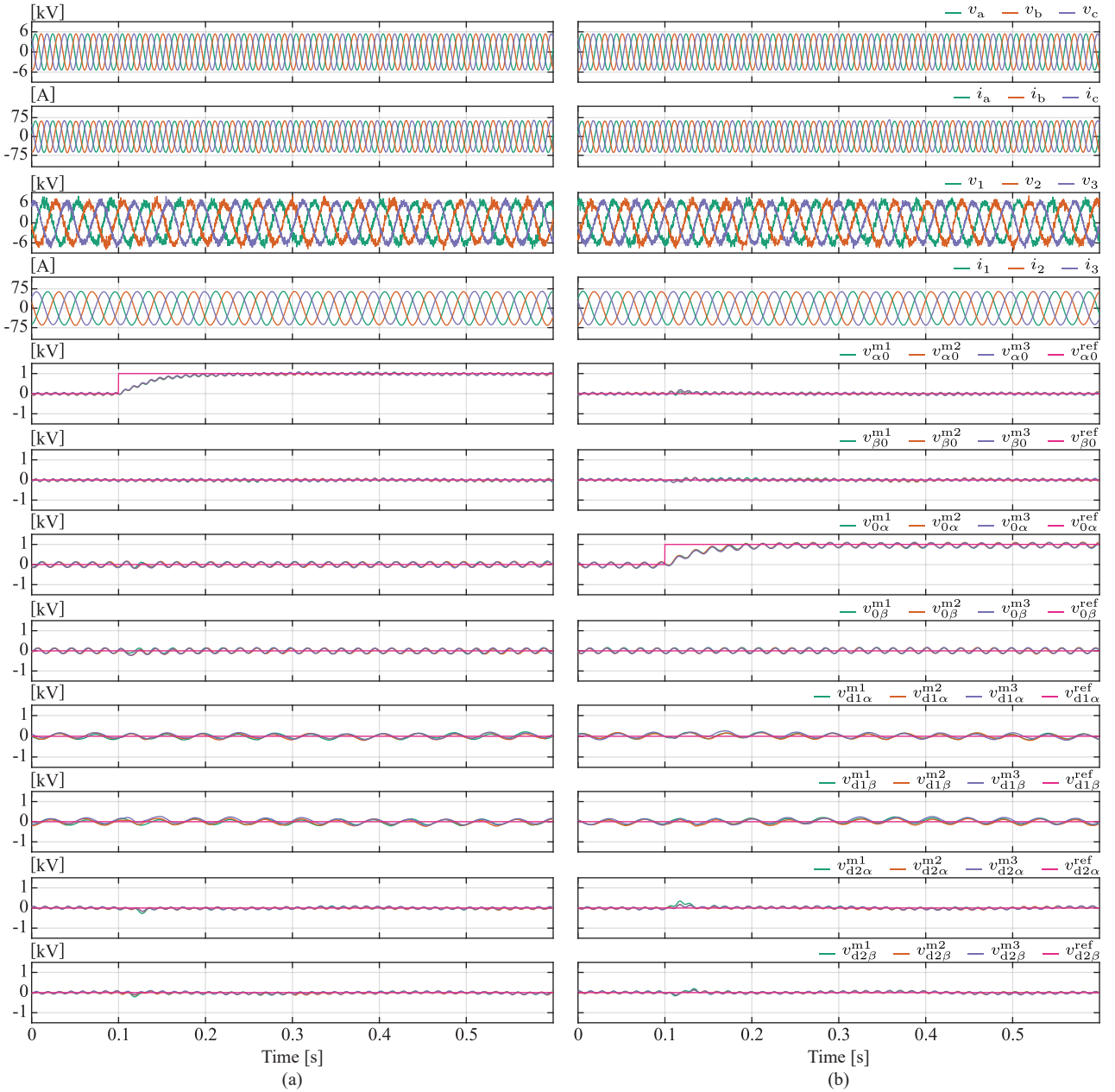


**Fig. 5.5** RT-HIL results showing two different branch energy reference imbalances and the response of the three previously introduced methods. The subfigures show, from top to bottom, the grid voltages and currents, the machine voltages and currents, the vertical  $\alpha$  and  $\beta$  branch voltages, the horizontal  $\alpha$  and  $\beta$  branch voltages, the diagonal 1  $\alpha$  and  $\beta$  branch voltages as well as the diagonal 2  $\alpha$  and  $\beta$  branch voltages. The first four subfigures, showing the terminal currents and voltages, demonstrate unchanged waveforms regardless of the circulating currents. Part (a) shows the response of the algorithm to a vertical imbalance of 1 kV and part (b) illustrates the same for the horizontal direction.

the third method requires also for the second diagonal imbalance more time compared to the other two methods.

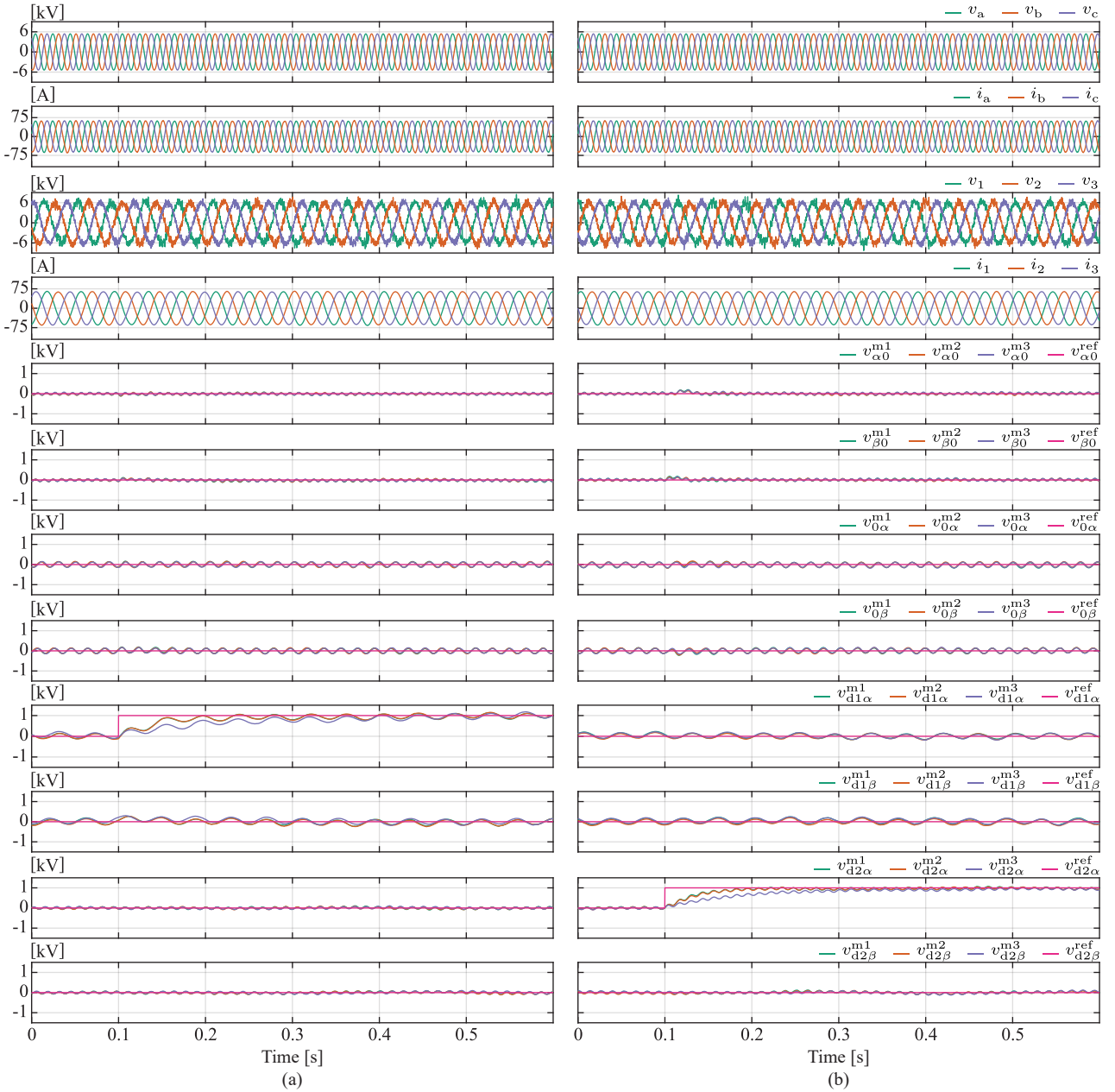


**Fig. 5.6** RT-HIL results showing two different branch energy reference imbalances and the response of the three previously introduced methods. The subfigures show, from top to bottom, the grid voltages and currents, the machine voltages and currents, the vertical  $\alpha$  and  $\beta$  branch voltages, the horizontal  $\alpha$  and  $\beta$  branch voltages, the diagonal 1  $\alpha$  and  $\beta$  branch voltages as well as the diagonal 2  $\alpha$  and  $\beta$  branch voltages. The first four subfigures, showing the terminal currents and voltages, demonstrate unchanged waveforms regardless of the circulating currents. Part (a) shows the response of the algorithm to a imbalance of 1 kV on the first diagonal and part (b) illustrates the same for the second diagonal.

A random imbalance presented in **Fig. 5.7** (a) validates all the previous conclusions drawn for the individual imbalances. Methods 1 and 2 cannot be distinguished in their performance, however, they both outperform the third method in the two diagonal imbalance directions. For both the horizontal



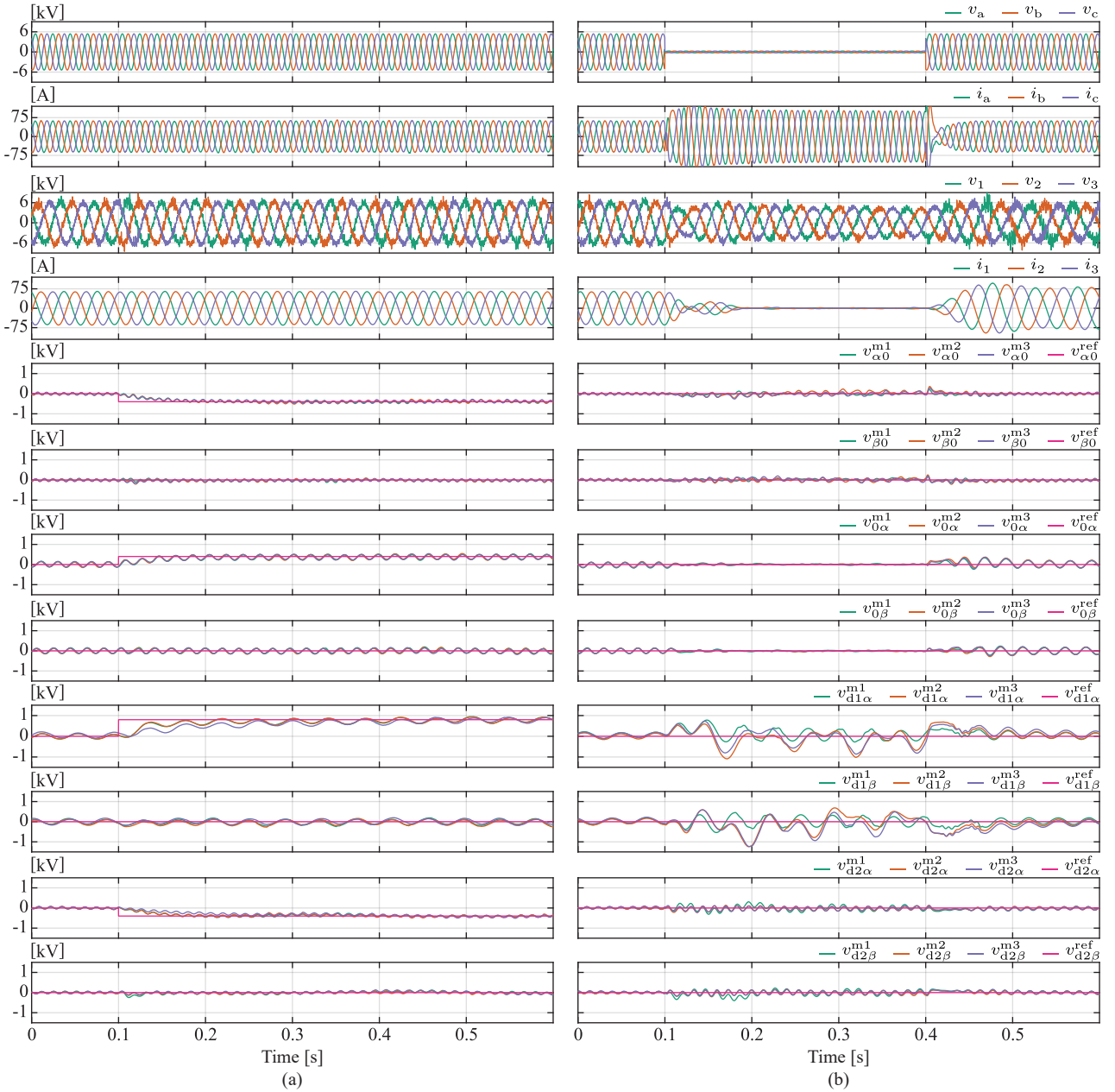


**Fig. 5.7** RT-HIL results showing two different branch energy reference imbalances as well as the LVRT response of the three previously introduced methods. The subfigures show, from top to bottom, the grid voltages and currents, the machine voltages and currents, the vertical  $\alpha$  and  $\beta$  branch voltages, the horizontal  $\alpha$  and  $\beta$  branch voltages, the diagonal 1  $\alpha$  and  $\beta$  branch voltages as well as the diagonal 2  $\alpha$  and  $\beta$  branch voltages. The first four subfigures, showing the terminal currents and voltages, demonstrate unchanged waveforms regardless of the circulating currents. Part (a) shows the response of the algorithm to an arbitrary imbalance along all defined directions and part (b) illustrates the response to a LVRT without generating any imbalances.

and the vertical directions, all three methods reach the required reference within the same time, thus no performance difference can be noticed.

**Fig. 5.7** (b) shows the LVRT performance of all three methods, while the converter complies with the German grid code as defined in [93]. During this scenario, neither load currents nor grid voltages are present in the branch, required for horizontal balancing of all three methods. However, as no imbalance is created in this direction during the transient, as seen on the  $v_{0\alpha}$  and the  $v_{0\beta}$  plots, no balancing action is required. As shown in **Tab. 5.2**, method 1 provides the additional degree of freedom to choose between grid or load voltages to balance in the diagonal directions. As seen in **Fig. 5.7** (b), even without grid voltage components, method 1 manages to balance the energy in the three remaining directions. Neither method 2 nor method 3 have this degree of freedom and rely on the grid voltage to achieve diagonal balancing. Method 3 relies solely on the grid voltage to achieve diagonal balancing, thus during LVRT, no energy balancing in these direction can be achieved. Even if method 2 relies on both input and output components to achieve diagonal balancing and should thus outperform method 2 during LVRT, no significant performance difference can be observed between the two methods.

For all the imbalance scenarios shown in **Fig. 5.5**, **Fig. 5.6** and **Fig. 5.7**, the reference change does not generate a steady state imbalance along any other balancing direction. Even if during the transients, a small variation of the diagonal voltages can be observed, no significant difference between the three methods can be observed.

## 5.5 Summary

Through the mathematical development of the main energy balancing control algorithms, this chapter fills existing theoretical gaps and allows a thorough analytical comparison of all methods. While a similar study on the MMC exists [92], the performance of the methods differs for the M3C topology. In the previous study, the here called method 2 had a reduced dynamic performance compared to method 1, whereas in this work, assuming normal operation, both methods perform similarly.

**Fig. 5.8** illustrates the most important characteristics for each of the three methods. Method 1, shown in green, requires a high implementation effort due to the high amount of transformation blocks as well as the conditions to chose the optimal circulating current references. On the other hand, the implementation in the double- $\alpha\beta 0$  frame, while allowing different control gains for different balancing directions, allows tuning of one control loop for each balancing direction. This method provides a high degree of freedom in choice of the circulating currents to fulfill the energy balancing between the branches. This choice, however, requires a high amount of scenarios to be implemented, as well as multiple conditions choosing among all the possible circulating current components. Method 1, however, achieves the highest dynamic response during normal operating mode, thus leading to an efficient energy balance among the branches. The advantage of the high degrees of freedom of the circulating currents is the good performance during grid scenarios such as LVRT as was shown in the RT-HIL test results.

The second method, shown in blue on **Fig. 5.8**, requires an extensive knowledge of linear algebra as well as vector spaces and might not be intuitive. However, the implementation of this method is the simplest of all three analyzed methods, as it only requires a single gain to get a modified current reference. During normal operation, this method achieves the same high dynamic behavior to the first method. The computation in  $abc$  frame does not allow individual tuning of the energy controllers for the four defined directions. Additionally, the simple implementation does not provide any degrees of freedom in choice of circulating current reference and, as a consequence, has a very low performance

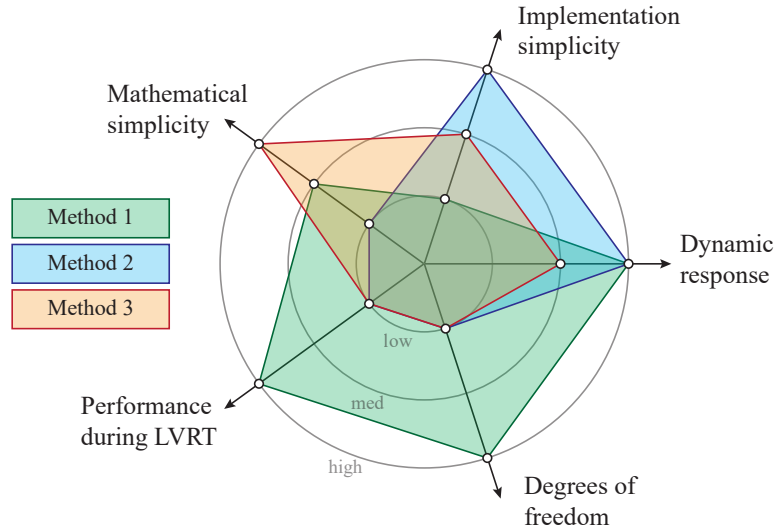


**Fig. 5.8** Overview of the characteristics of each control method. Mathematical simplicity is defined as the ease of understanding the principle of the given method. The implementation simplicity is representative of the complexity and time investment for the implementation. The dynamic response illustrates the energy balancing performance during normal operation of the converter. The degrees of freedom demonstrate the possibility of introducing various gains for the different balancing directions as well as having the possibility of choosing the components of the circulating currents. The LVRT illustrates the energy balancing performance of the various control methods during this grid fault.

during LVRT.

The third method, shown in orange on **Fig. 5.8**, relies on a simple mathematical transformation, which can be easily understood with a relative effort of implementation. However, the reduced diagonal 1 and 2 balancing performance of this method results in a lower dynamic response compared to the two previous methods. Similar to method 2, the implementation in the  $abc$  frame does not allow an individual tuning of the energy controllers of the different directions. Furthermore, this method does not allow any flexibility in choice of circulating currents, which translates into a poor performance during LVRT.

Each of the analyzed methods achieves balancing of the energy within the converter without affecting the terminal currents, for this reason they all fulfill the main requirement of the energy balancing algorithm. Regarding the choice of implementation, it is up to the control engineer to evaluate the trade off between the different implementations, considering the resources at disposal for the given application.

With the energy balancing control covered in this chapter, the two remaining control parts include the grid current control as well as the SM control. Being a grid connected storage, the PHSP is required to comply to a grid code in order to enable a proper power exchange in all possible scenarios. This will be the focus of the following chapter.



# 6

## Grid Code Compliant Behavior of CFSM in PHSP

*As a grid connected storage, a pumped hydro storage power plant has to meet grid code requirements to ensure and contribute to the grid stability as well as to allow a smooth power transfer. This chapter presents a flexible and grid code complying operation of the matrix modular multilevel converter used in variable speed pumped hydro storage power plants. Compliance with the grid code is demonstrated through simulations involving frequency deviations and voltage sags, which are tested on the previously introduced real-time hardware-in-the-loop platform. Furthermore, a detailed description of the control algorithm deployed on the hardware-in-the-loop achieving grid compliance and energy control of the matrix modular multilevel converter is provided.*

### 6.1 M3C control algorithms

**Chap. 2** gave a general overview of the various control elements included in the M3C. Divided into three main categories, namely the grid side current control, the machine side current control and the internal energy balancing control, this chapter aims to further explain the first two, while the energy balancing is elaborated in **Chap. 5**. Furthermore, an optimization of the machine side current control is presented in **Chap. 7**.

From a control perspective, two different operating modes of the PHSP unit are to be considered. First, the so-called power mode, which consists of a power reference provided by the grid operator and followed by the PHSP unit. Second, the so-called speed mode, in which, as the name suggests, the speed of the PHSP unit is controlled without controlling the power exchange towards the grid.

In the power mode, the speed of the PHSP unit is a consequence of the required power reference and the load torque applied to the shaft through the water. In pumping mode, no speed regulation from the hydraulic side can occur as the water flow cannot be changed. At fix speed, the load torque cannot be altered and is defined by the available hydraulic head, thus the power of the unit cannot be regulated in any way. In turbine mode, however, there is the possibility of regulating the applied torque on the turbine through manipulation of the water flow. The dynamics of the power reference change in turbine mode is thus determined by the hydraulic speed regulation, whereas in pump mode, the dynamics of the M3C are determinant.

The speed mode of the PHSP unit is generally used during transients. While in normal operation the main task of the unit is to follow the grid power reference, thus operating in power mode, during the transients, the aim lies in achieving a given operating condition. Thus, the power exchanged with the grid is a consequence of the machine speed and torque reference points.

### 6.1.1 Grid code requirements

The grid code exists to ensure the proper functionality and stability of the grid. Every country has its specific requirements for given plant operators to be followed. Being a grid connected storage facility, the PHSP operator is required to comply to the given grid code. While hereafter the German grid code is considered, similar grid codes are available in different countries, with only small differences between them [93].

From the various scenarios depicted in the German grid code, four are chosen to be examined further within this work. The first one is related to a grid frequency deviation, the second chosen scenario is a Low Voltage Ride Through (LVRT), the third a single phase fault and the last a voltage swell. For the scenarios including a voltage variation, the German grid code requirements, which define the amount of minimum reactive power to inject to or absorb from the grid, are shown in **Fig. 6.1** (a). A grid voltage amplitude variation lower than  $\pm 10\%$  of the nominal voltage does not require any reactive power reference from the converter, and beyond that limit, the reactive power reference is defined by the red line. **Fig. 6.1** (b) shows the LVRT defined by the German grid code throughout which the converter must provide the required amount of reactive power to the grid. For any voltage

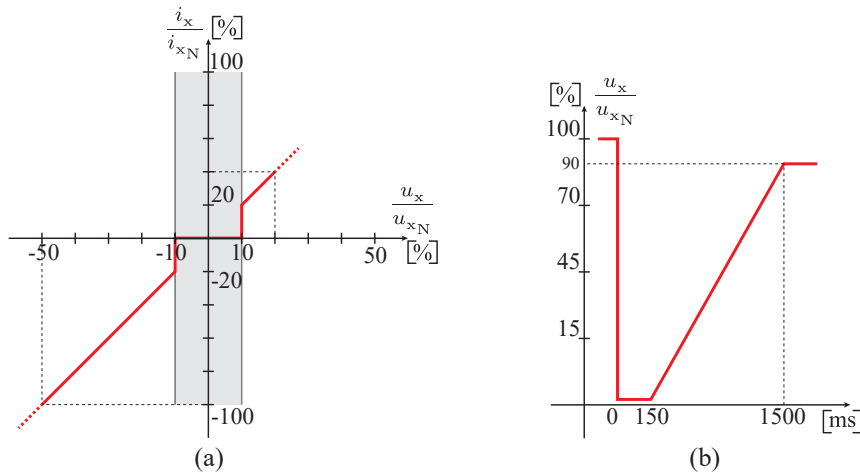


**Fig. 6.1** Grid scenarios as defined by the German grid code. (a) shows the amount of reactive current to inject into or absorb from the grid depending on the voltage sag or swell. (b) shows the limit of a voltage sag above which the converter must remain connected to the grid and provide reactive power.

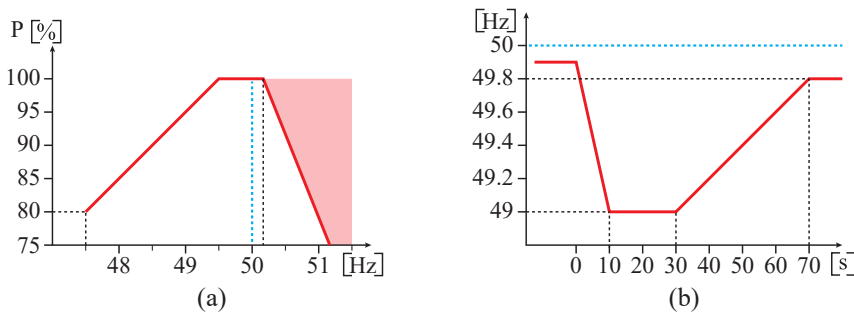


**Fig. 6.2** Grid scenarios as defined by the German grid code. (a) shows the minimum and maximum amount of active power generation depending on the grid frequency. (b) shows the limit of a frequency deviation above which the converter must provide the nominal power to the grid.

variation beyond the line of **Fig. 6.1** (b), the converter is allowed to disconnect from the grid.

**Fig. 6.2** shows the German grid code requirements regarding active power generation during grid frequency deviations. If the grid frequency falls below 49.5 Hz, the minimum required active power generation is defined by the red line in **Fig. 6.2** (a). For a frequency lower than 47.5 Hz, the converter is allowed to disconnect from the grid. Exceeding the value of 50.2 Hz, the active power injection to the grid must be limited to a maximum defined by the red line in **Fig. 6.2** (a). The most extreme scenario during which the full nominal power must be injected to the grid is shown in **Fig. 6.2** (b). Any frequency deviation exceeding the red line allows a reduction in active power generation defined by **Fig. 6.2** (a).

### 6.1.2 Grid side control

The grid terminal voltage of the M3C has to comply with the grid code requirements. The control method chosen in this paper is the Instantaneous Active and Reactive Control (IARC), as introduced in [94].

To allow a power exchange with the grid even under faulty grid conditions, both positive and negative sequence voltage have to be extracted from the measured grid voltages. The usage of a stationary reference frame allows the implementation of the Double Second-Order Generalized Integrator (DSOGI) with Frequency Lock Loop (FLL) as shown in **Fig. 6.3** (a). Depending on the amplitude of the measured positive sequence grid voltage, the grid code requires the injection or absorption of reactive power, which is implemented as shown in **Fig. 6.3** (b). Taking into account the required reactive power reference and the maximum allowed current limit, the maximum possible active power reference can be computed. In case of a grid fault requiring a reactive power exchange with the grid, the priority is given to this reactive power reference in order to support the grid. The active power reference is followed, provided the maximum current limit of the M3C is not exceeded.

Following these power reference calculations, the required grid current references can be computed in the  $\alpha\beta$ -frame as shown in **Fig. 6.3** (c).

$$i_{x_\alpha} = \frac{3}{2\hat{U}_{x_{pos}}^2} (P^* u_{x_\alpha} + Q^* u_{x_\beta}) \quad (6.1)$$

$$i_{x_\beta} = \frac{3}{2\hat{U}_{x_{pos}}^2} (P^* u_{x_\beta} + Q^* u_{x_\alpha}) \quad (6.2)$$

Finally, the grid voltage reference is obtained using a PR controller shown in **Fig. 6.3** (d). The PR controller is centered around the estimated grid frequency generated by the FLL shown in **Fig. 6.3** (a).

### 6.1.3 Machine current control

**Fig. 6.4** shows the implementation of the classical and well established vector control used for the SM. Two different methods of generating the quadrature current reference for the SM, related to the previously mentioned speed and power mode of operation, are shown in **Fig. 6.4** (a) and **Fig. 6.4** (b).

In speed mode, the power exchange with the grid is a consequence of the speed and torque of the SM, and the respective q-current reference is generated as shown in **Fig. 6.4** (a). The aim is to follow a

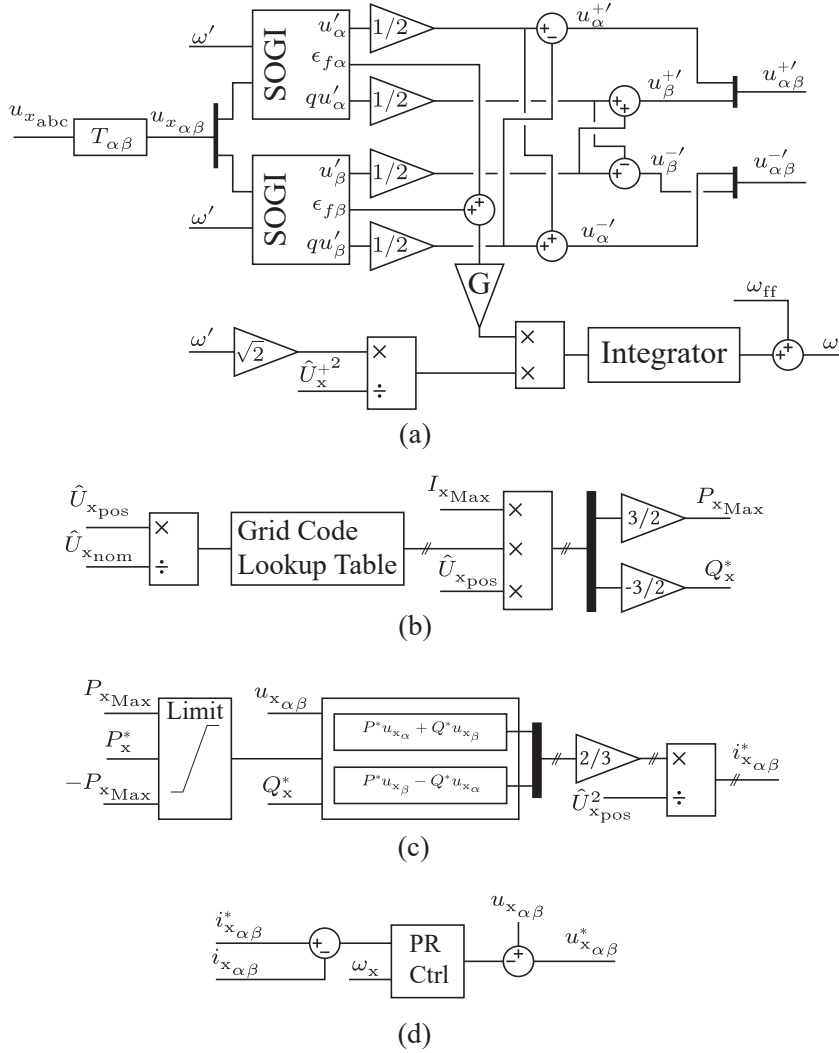


**Fig. 6.3** Grid current control implementation. (a) shows the implementation of the FLL to extract both positive and negative sequence as well as the frequency of the grid voltages. (b) shows the implementation of the active and reactive power reference. (c) shows the computation of the grid current references, which are used in the PR controller shown in (d).

given speed reference, which is achieved through the use of a PI-regulator, generating a given torque reference for the SM. With the torque reference and the magnetizing flux, the respective q-current reference is calculated as shown in **Fig. 6.4** (a). In this case, the active power absorbed or injected into the grid is defined by the total energy controller, keeping the overall energy in the M3C constant. This part of the SM control is usually required during transients, when a certain speed of the pump/turbine is required prior to enabling a power setpoint or a defined speed profile has to be followed.

The depicted control used during operation of the M3C in power mode is shown in **Fig. 6.4** (b). The power reference is coming from the total energy controller, which aims to ensure constant energy within the cells of the M3C, thus the SM power reference has to follow to the required grid power reference. In this operation mode, the speed of the SM is not directly controlled and is defined by the load torque and the power reference imposed by the grid operator to which the losses in the M3C are



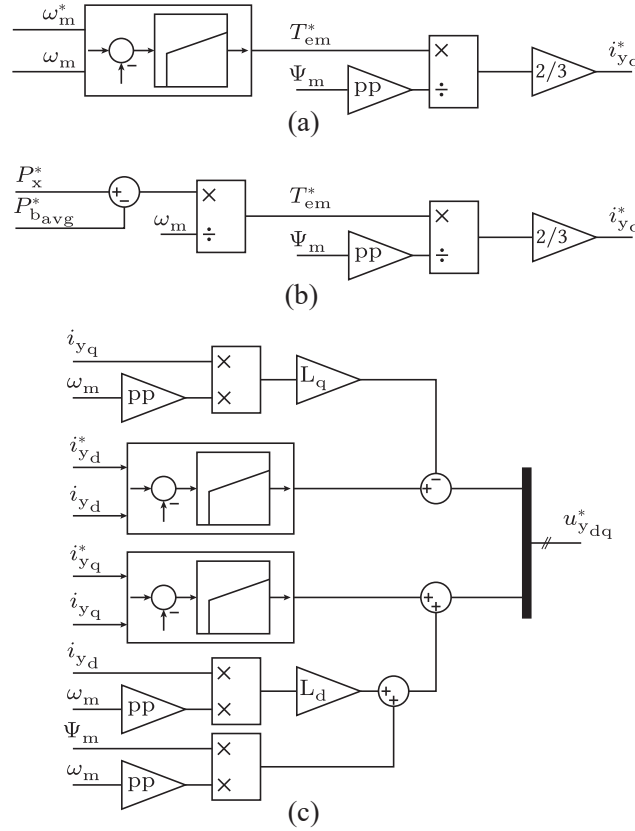


**Fig. 6.4** SM current control implementation. (a) showing the q-current reference calculation using the speed controller. (b) showing the q-current reference calculation using the power reference. (c) showing the vector control implementation.

added.

The implementation of the vector control scheme is shown in **Fig. 6.4** (c). The cross coupling terms are a consequence of the mathematical transformation of the variables into a rotating reference frame. In this chapter, the d-current component of the SM gets a constant 0 reference throughout all the simulations. Later on, in **Chap. 7**, an ideal control of this current component is further discussed and simulated.

#### 6.1.4 M3C energy balancing

From the three energy balancing methods that were analyzed in **Chap. 5**, the direct arm energy control (method 3) is implemented in this chapter.

With the grid current control and the machine vector control, the terminal currents of the M3C are controlled to fulfill both grid and machine requirements. Doing so, a branch current containing both input and output frequencies is created. For a current flowing in the branch connecting the input phase x to the output phase y, the expression is:

$$i_{xy}(t) = \frac{1}{3} (i_x(t) + i_y(t)) \quad (6.3)$$

$$i_{xy}(t) = \frac{1}{3} \left( \hat{I}_x \sin(\omega_x t + \phi_x) + \hat{I}_y \sin(\omega_y t + \phi_y) \right) \quad (6.4)$$

However, to assure proper operation of the M3C, the average energy in all nine branches must be equal, leading to the necessity of an additional control layer, ensuring equal energy distribution among the branches. This energy balancing control of the M3C can be separated in two major categories. The first category is the balancing between the branches of the same subcluster (shown in **Fig. 2.11**), meaning the branches that are connected to the same output phase. The second category of balancing is between branches of different subclusters and connected to the same input phase. While these two balancing actions must be achieved, the resulting balancing currents must neither influence the input nor the output terminal currents.

In addition to these two categories, a total energy controller, regulating the input and output power to be equal and thus ensuring constant average energy in the M3C, has to be added. The output reference of this controller is either transmitted to the grid current control or the SM control, depending on the operating conditions. To enable the tracking of a fast changing variable, the instantaneous power is used as a feed-forward term in this controller.

The total energy control of the M3C, shown in **Fig. 6.5** (a), is done using the average of all nine

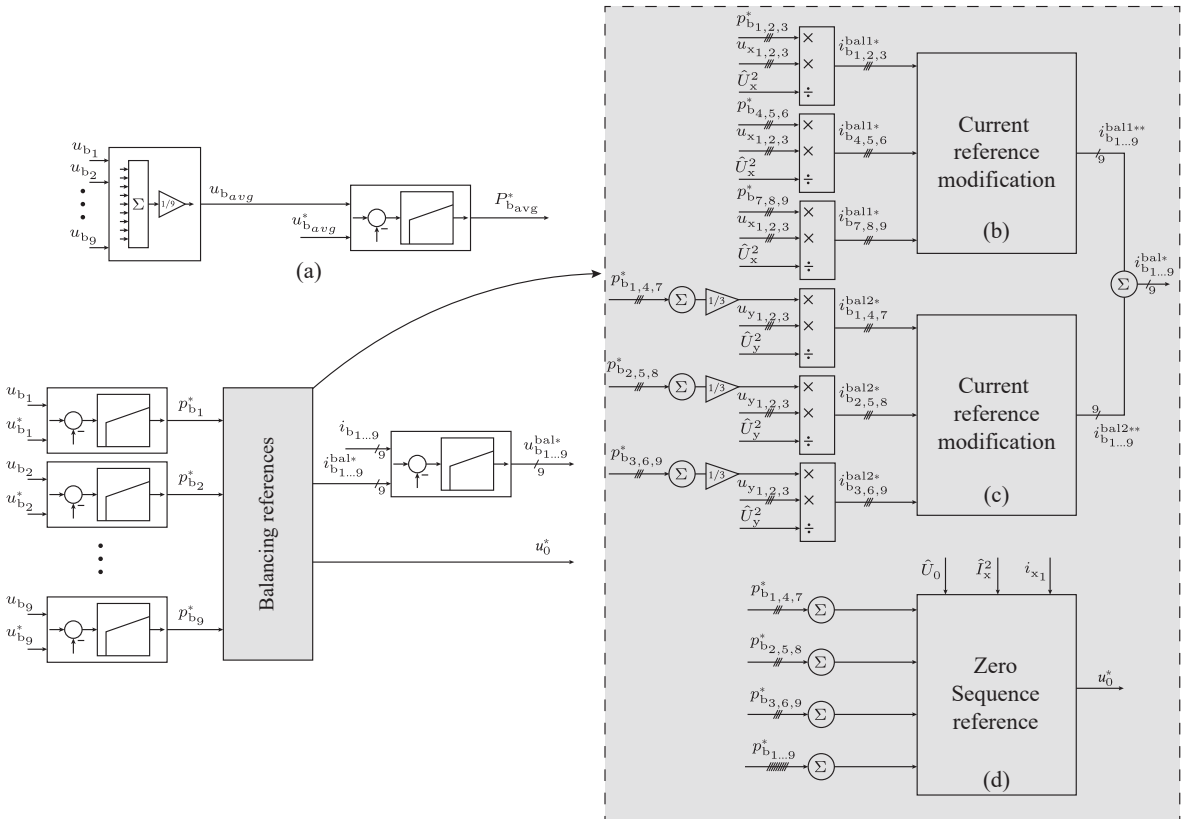


**Fig. 6.5** Structure of the direct arm energy balancing method. (a) shows the total energy control part, keeping the overall energy in the branches constant. (b) shows the reference calculation of the circulating currents acting on the grid voltages. (c) shows the circulating current reference calculation acting on the load voltages. (d) shows the common mode voltage calculation used when no load voltages are available.

branches voltages, to which the reference branch voltage is subtracted and, using a PI controller, the needed power reference can be computed.

To achieve balancing between the branches, each branch voltage is converted to the respective branch energy and compared to its reference, and using a PI controller, the required power reference to achieve balancing for the given branch is computed. However, these power references have to be modified before being transmitted to the branches to make sure that the resulting circulating current does not influence neither the input nor the output terminal currents. In order to create the given circulating power references, the corresponding circulating currents acting on present branch voltages have to be calculated. During operation of the SM, branch voltages consist of the input and output terminal voltages. However, in case no output voltage is present, another degree of freedom, namely the common mode voltage has to be used. Further development of the energy balancing algorithm has been presented in **Chap. 5**.

During normal operation, the balancing of the energy between the branches is achieved through circulating currents acting on the branch voltages, having frequency components of both input voltages, shown in **Fig. 6.5** (b), and output voltages, shown in **Fig. 6.5** (c). To make sure that these circulating currents influence neither of the terminal currents, the modification of the circulating current references as presented in [95] is used. In case of missing load voltages, **Fig. 6.5** (c) is replaced by (d), which generates a common mode voltage component acting on the input currents to allow balancing of the energy between the branches.

The final branch voltage references are:

$$u_{b_{1,2,3}}^* = u_{x_{1,2,3}}^* - u_{y_1}^* + u_{b_{1,2,3}}^{bal*} - u_0^* \quad (6.5)$$

$$u_{b_{4,5,6}}^* = u_{x_{1,2,3}}^* - u_{y_2}^* + u_{b_{4,5,6}}^{bal*} - u_0^* \quad (6.6)$$

$$u_{b_{7,8,9}}^* = u_{x_{1,2,3}}^* - u_{y_3}^* + u_{b_{7,8,9}}^{bal*} - u_0^* \quad (6.7)$$

## 6.2 RT-HIL simulation results

The aforementioned control algorithms are implemented on the industrial controller of the RT-HIL platform. Being a safe testing platform without the risk of damaging high value equipment and generating high fidelity results, as explained in detail in **Chap. 4**, the control algorithms deployed on the ABB control platform are unable to differentiate it from an actual prototype.

### 6.2.1 Power reference change

**Fig. 6.6** shows a power reference change in pumping mode, where in the first part, the power reference is dropped from 500 kW to 300 kW and in the second part, the power reference is increased back to 500 kW. After the power reference drop, the speed of the SM drops from 750 rpm to 450 rpm at a rate defined by the load torque and the shaft inertia. In pumping mode, the pump is entirely submerged in water and the PDV are fully opened. This leaves no freedom in controlling the speed hydraulically; however, there is no need to actively control the speed of the unit as it will automatically end up at a stable operating point. Reducing the power setpoint will decrease the driving torque generated by the SM, thus the load torque generated by the water will start slowing down the unit until an equilibrium is reached. Similarly, when increasing the power reference, the driving torque exceeds the load torque and the speed of the unit is increased until achieving an equilibrium. Thus, as long as

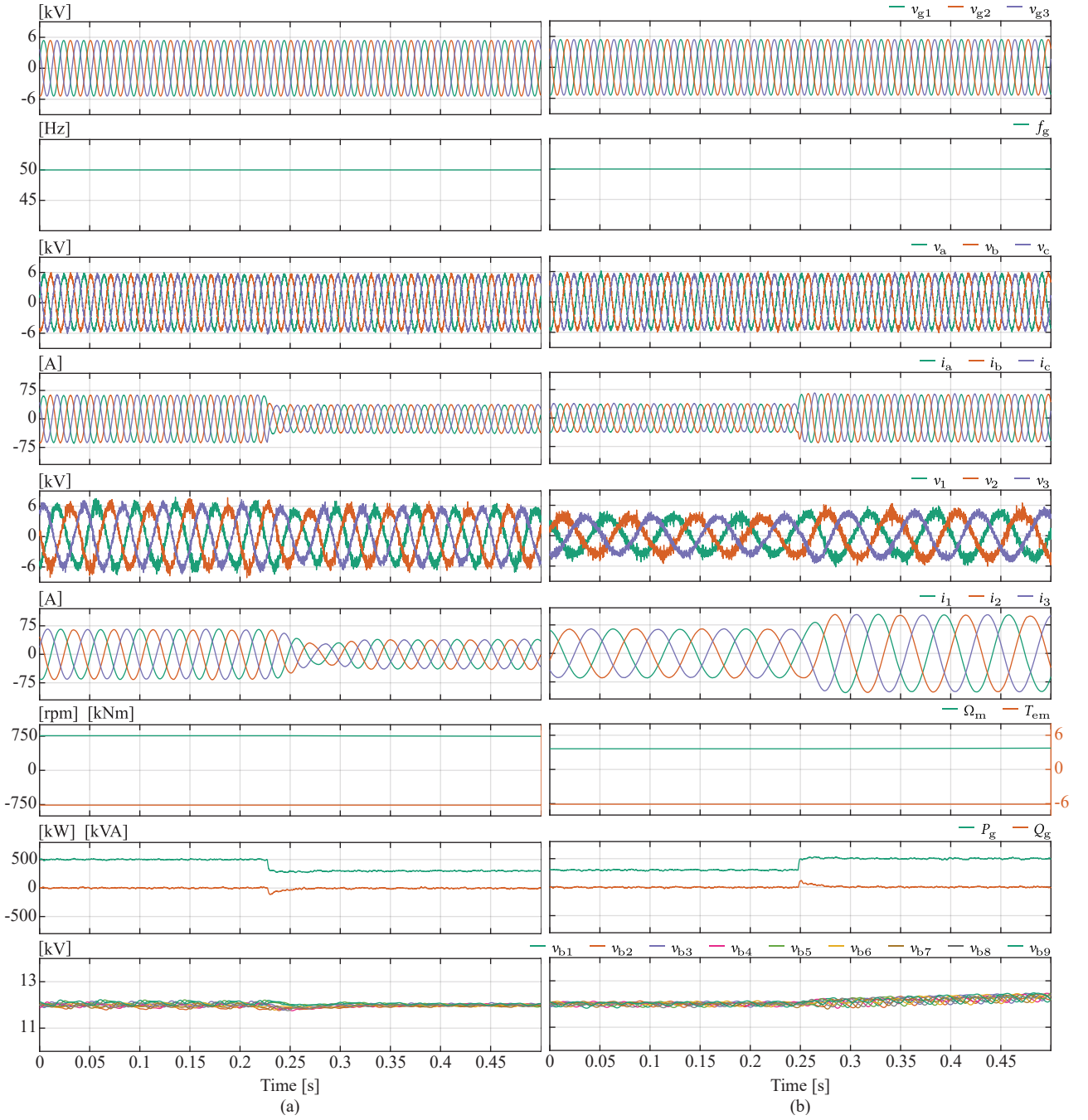


**Fig. 6.6** RT-HIL results illustrating flexible pumping operation of a PHSP with (a) showing a power reference change from 500 kW to 300 kW and (b) showing the rise back to 500 kW.

the resulting SM current reference remains within the imposed limits, the power reference can be tracked within a few milliseconds.

The branch voltages, thus also the cell voltages, which represent the cell energies, remain constant throughout the process of power reference drop as shown by the branch voltage waveform at the

bottom of the **Fig. 6.6**. The reduction in the amplitude of the branch voltage oscillations after the power reference change is explained by the reduced power flowing through the branches.

The right side of **Fig. 6.6** shows the power reference rise from 300 kW to 500 kW, which is achieved by exceeding the nominal stator current during the transient, where the machine is accelerated back to its nominal speed. The excess of current is necessary to achieve the correct power reference considering the lower induced stator voltages of the SM due to its reduced speed. As for the power reference drop, the energy balancing between the branches is achieved and shown on the lower part of **Fig. 6.6**.

While the power reference can be tracked within a few milliseconds for the pumping operation mode, in turbine operation, the speed of the unit is regulated through a mechanical system controlling the water flow towards the turbine. The driving torque is coming from the water and the braking torque from the SM. Taking the example of a power reference reduction, the torque of the SM is reduced, eventually being lower than the driving torque of the turbine, which leads to an increase in rotational speed of the unit. As this results in a non stable operating point, the speed needs to be controlled by a mechanical system, therefore, the power reference tracking is defined by the dynamics of the mechanical system, which is typically a few orders of magnitude slower than the electrical system dynamics.

### 6.2.2 Grid frequency deviation

**Fig. 6.7 (a)** shows the grid code compliant behavior of the M3C regarding a frequency deviation. For this scenario, the PHSP is operated in generating mode, and the power reference following a frequency decrease should not drop below the red line defined in **Fig. 6.2 (a)**. As the grid frequency remains above 47.5 Hz, the converter must remain connected to the grid. To demonstrate the increased capability of the M3C regarding grid compliance, the rate of change of the grid frequency is higher and drops lower than the one defined in **Fig. 6.2 (b)** while ensuring nominal power injection to the grid. In this case, the frequency is changed from 50 Hz to 47.5 Hz within one second, where it remains for one second and is ramped up to 50 Hz with the same rate of change. During the whole process, the active power reference remains unchanged, delivering the full active power to the grid, thus exceeding the requirements of the German grid code.

### 6.2.3 Low voltage ride through

**Fig. 6.7 (b)** shows a voltage sag on the grid following the profile defined in the German grid code, shown in **Fig. 6.1 (b)**. After the voltage sag, the maximum reactive current is injected into the grid, which in this case corresponds to 100 A, and the active power is reduced to zero to use the full current capability of the grid for reactive power, supporting the voltage. During the grid voltage ramp up, the injected reactive current corresponds to the relation shown in **Fig. 6.1 (a)**, and the active power reference is adapted to operate the M3C at maximum power. As a consequence of the active power reference from the grid being zero, the machine stator currents instantly drop to zero in order to keep the total energy in the M3C constant. Once the grid voltage is high enough to enable active power exchange, the SM current and in consequence also the SM speed are ramped up. Following the voltage ramp up defined in **Fig. 6.1 (a)**, the final grid voltage value is fixed at 90% of the nominal voltage and at this operating point, the converter keeps injecting 20% of its maximum current limit as reactive power into the grid.

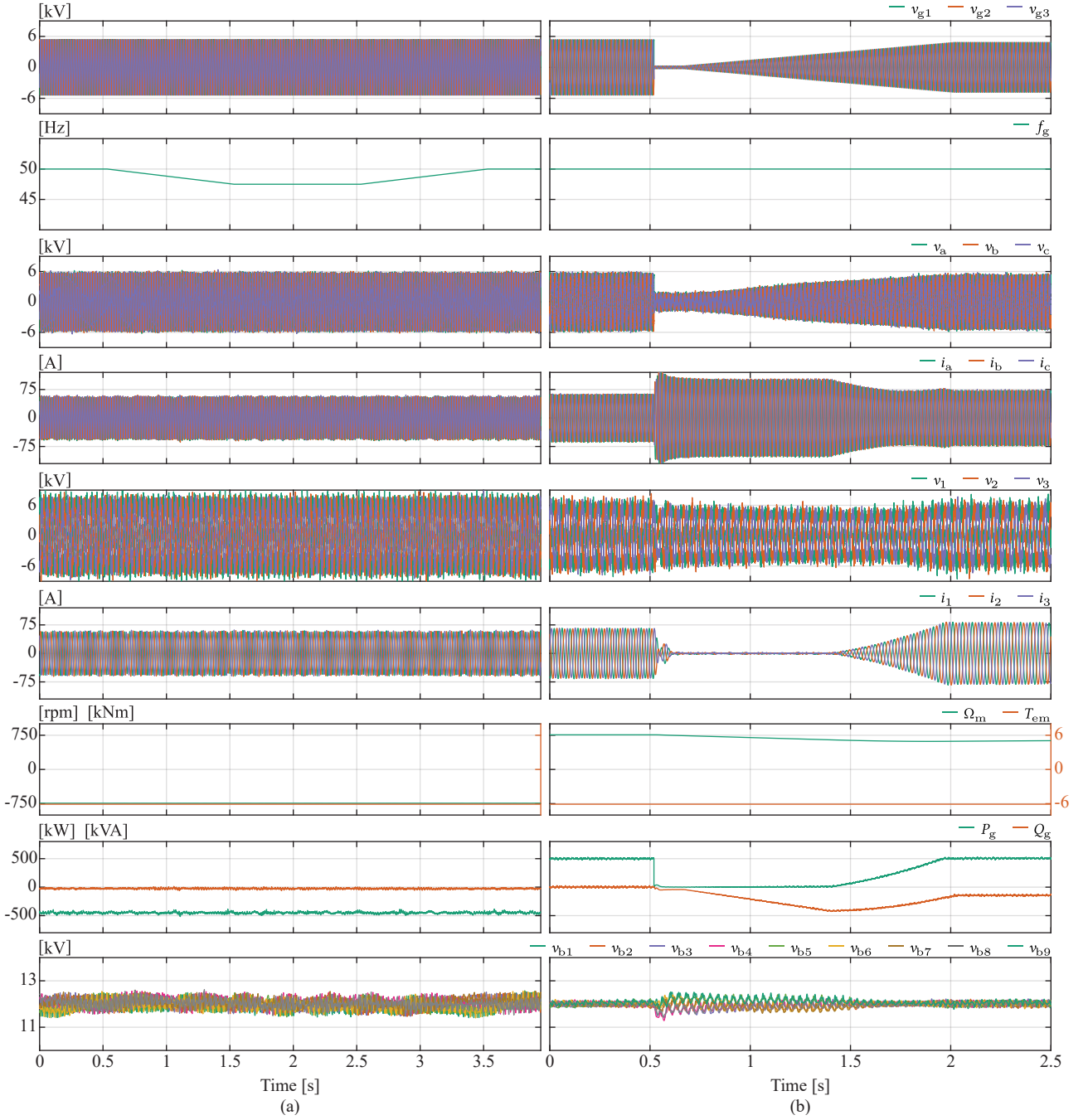


**Fig. 6.7** RT-HIL results showing the performance of the M3C for various grid conditions, (a) illustrates the M3C reaction to a grid frequency deviation and (b) demonstrates the grid compliant behavior during a LVRT.

The balancing of the energy between the branches is achieved throughout the whole scenario, as seen by the branch voltages shown in the bottom graph of **Fig. 6.7** (b). During the LVRT, a slight increase in branch voltage oscillation can be observed, which is explained by the very low grid voltage limiting the balancing action acting on the grid voltage as shown in **Fig. 6.5** (b). Even with a limited energy balancing action, none of the nine branch voltages are exceeding the 10% margin of its nominal value.

This corresponds to the observations made during the LVRT comparison presented in **Chap. 5**.

#### 6.2.4 Single phase to ground fault

The behavior of the M3C during a single-phase-to-ground fault is illustrated in **Fig. 6.8 (a)**. The here implemented version of the power control ensure symmetrical grid current waveforms under all circumstances, thus, during a single-phase-to-ground fault, symmetrical grid currents will lead to oscillations in the power exchange with the grid. However, this control allows maximum load operation throughout the fault, as can be seen by the SM speed and load torque shown in **Fig. 6.8 (a)**.

This operating condition can be withstand for an undefined period of time, as both full load operation remains possible and balancing of the energy among the branches is guaranteed. Voltage oscillations of the branches connected to the faulty phase will increase in amplitude, however, they remain within the 10% limit and are not diverging over time.

#### 6.2.5 Voltage swell

**Fig. 6.8 (b)** illustrates the behavior during a grid voltage swell of 30%. The higher voltage occurring during the voltage swell together with the 100 A phase current limit on the grid side terminals allows for an overall higher power proportionally to the increase in grid voltage. As defined by the grid code, for a voltage swell of 30%, the minimum amount of absorbed reactive current corresponds to 60% of the nominal current as illustrated in **Fig. 6.1 (a)**. While in nominal grid voltage conditions this corresponds to 60% of the maximum power, during a voltage swell, the power is increased proportionally to the increase in grid voltage. For this reason, as observed in **Fig. 6.8 (b)**, the available part of the maximum current enables the active power reference to reach the nominal power setpoint of 500 kW, even with the absorbed reactive power. Throughout the whole process, the branch voltage, shown in the lowest plot of **Fig. 6.8 (b)**, remain balanced, even if a slight increase in their oscillations is observed.

The observations above show that the voltage swell operation, illustrated in **Fig. 6.8 (b)**, could be maintained indefinitely, under the condition that the equivalent branch voltage is high enough to cope with the respective voltage swell. If the voltage swell exceeds the branch limitations, the load side voltage has to be reduced by slowing down the machine, leading to a lower back emf in case of the PHSP operation.

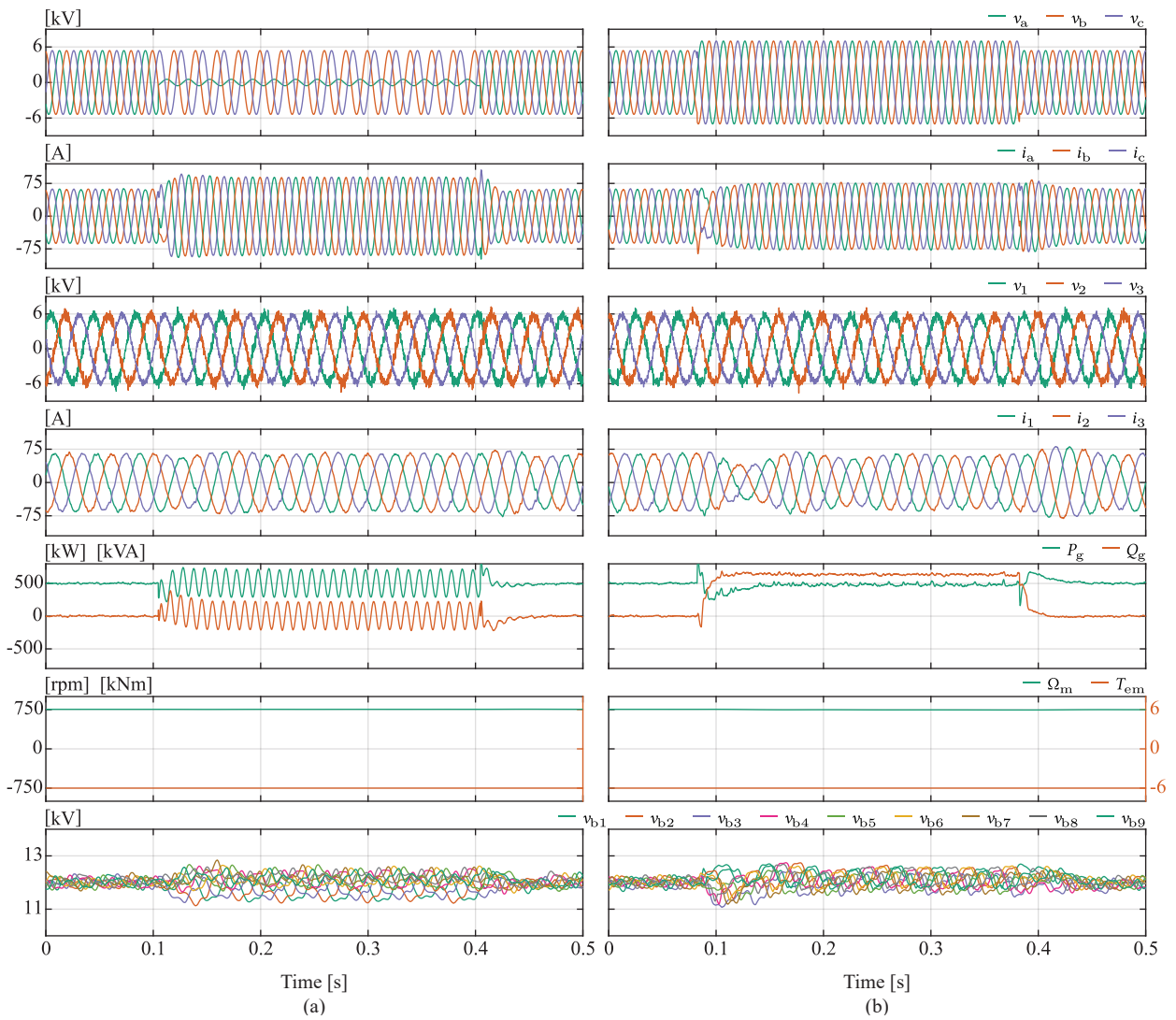


**Fig. 6.8** RT-HIL results showing the performance of the M3C for various grid conditions, (a) illustrates the M3C reaction to a single phase-to-ground fault and (b) demonstrates the grid compliant behavior during a voltage swell.



## 6.3 Summary

This chapter presents the control structure of the M<sub>3</sub>C used for the simulation of a PHSP and demonstrates the gained flexibility through fast power reference changes in pumping mode as well as grid compliant behavior during grid faults such as LVRT, frequency deviations, voltage swells and single-phase faults. As shown in the simulation results, the M<sub>3</sub>C exceeds the grid code requirements during frequency deviations, as it maintains nominal active power injection throughout a significantly more severe scenario than the one defined by the German grid code. The simulations presented in this chapter are carried out on the RT-HIL system introduced in **Chap. 4** and developed to allow a thorough verification of the control structure and algorithms of the M<sub>3</sub>C.

From the three main control parts of the M<sub>3</sub>C, **Chap. 5** covered the energy balancing among the branches of the M<sub>3</sub>C and **Chap. 6** the grid current control as well as the SM vector control. The optimization of the application side remains the last control part to be analyzed and will be in the next chapter.



## PHSP Variable Speed Drive Loss Minimization

*The increase of installed intermittent renewable energy sources, requires flexible grid storage facilities, such as variable speed pumped hydro storage power plants. In this changing energy market, the number of start-stop sequences throughout the day rises significantly, increasing the interest in an efficiency optimization of these transients. Exploiting all possible degrees of freedom in the machine operation in order to maximize efficiency of the overall system allows to increase the profitability of the plant. Doing so in real-time on the same hardware-in-the-loop platform used for the validation of the control algorithm saves time and resources. This chapter presents the most energy efficient steady-state and transient operation of an externally excited synchronous machine driven by a matrix modular multilevel converter. To this end, this chapter includes a real-time compatible converter and machine loss calculation to extract the losses of the electrical system for any operating point including transients such as the start in turbine mode.*

### 7.1 System description

The required flexibility of modern VS PHSPs to follow the fast changing production of the RES, involves a higher number of start-stop transients as well as steady-state operation at various speeds. This rise in occurrence of start-stop sequences increases the interest for an efficiency optimization as to ensure the extraction of the full potential of the overall system. This allows to reduce the losses, thus increasing the profits for the PHSP operator.

The system considered for the efficiency optimization is shown in **Fig. 7.1**. The converter, the M3C, is constituted of eight FB cells per branch with a nominal voltage of 1500 V. The characteristics of the cells correspond to the prototype in the ongoing development at the PEL and can be found in the **Tab. 7.1**. The simulated SM is a separately excited salient pole machine with an apparent power of 526 kVA and a nominal frequency of 25 Hz. The excitation of the SM is controlled through the ABB Unitrol 1020 rectifier. As the hydraulic machinery is disregarded in this system optimization, the pump/turbine is modeled as an additional inertia on the machine shaft, with a controlled torque output modeling the hydrodynamic load. During start-up the load torque reference follows the best hydraulic efficiency curve as presented in [96], whereas for the steady-state operation, constant load torque is applied.

The system loss evaluation is done for a full load pumping operation as well as a start of the unit in turbine mode. The shaft speed and load torque references for the turbine start-up are generated taking into account hydraulic efficiency, which also yields benefits in terms of fatigue damage to the mechanical system. Since more flexibility also implies more frequent start and stop cycles, stresses on the hydro-mechanical system during transient operations must carefully be studied. The synchronization phase required to couple fixed speed turbine units to the grid is known for its harmful

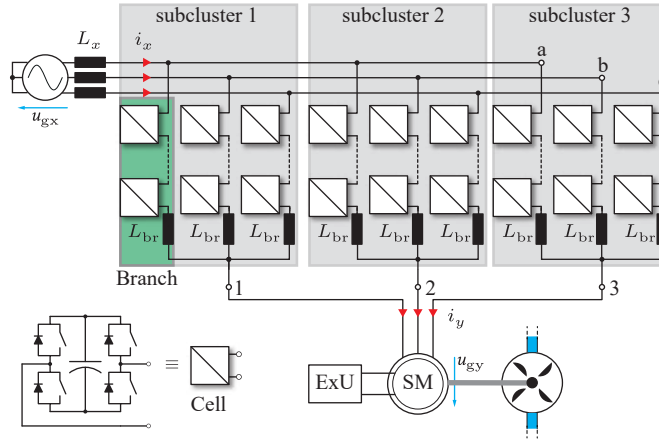


**Fig. 7.1** The M3C with the three subclusters, highlighted in gray, each containing three branches, highlighted in green, and  $N$  cells per branch. The two AC systems connected to the terminals are represented by a grid on the input side and a 3 phase machine on the output side connected to a pump/turbine as is the case in a PHSP.

hydrodynamic conditions [97]. Thanks to the speed control possibilities enabled by the FC, soft starts can be realized by avoiding damaging operating ranges. Based on Computational Fluid Dynamics (CFD) simulations and structural Finite Element Analysis (FEA) performed by [96], a fixed speed turbine start-up sequence is compared to the variable speed start-up sequence with hydraulic Best Efficiency Point (BEP) tracking strategy considered here. In the latter case, important mitigation of fatigue damage of the hydraulic runner is predicted by the numerical models. Moreover, the duration of the start-up is drastically reduced, which yields improvements regarding the Frequency Containment Reserve (FCR) capabilities of the PHSP. The optimal sequence generated under these conditions is shown in **Fig. 7.2**. The large number of start-stop transients for a VS PHSP requires not only the consideration of the hydraulic efficiency and fatigue damage of the hydraulic runner, but also the electric efficiency of both the FC and the SM.

Prior to the optimization of the efficiency of the overall electrical system, the different losses of the various elements have to be defined. This includes converter and machine losses. The losses considered within the M3C include semiconductor conduction and switching losses as well as branch resistive losses and cell capacitor losses. The high amount of switches requires special considerations when evaluating their losses in order to maintain a low computational cost and allow RT simulations. For the SM, the losses include stator and rotor conduction losses, friction and ventilation losses as well as eddy current and hysteresis losses.

The evaluation of the here mentioned losses in RT can be achieved in three different ways. The first one being their offline evaluation and storage into lookup tables implemented in RT. While this

**Tab. 7.1** Cell characteristics considered for simulations and loss considerations. Each cell requires four semiconductor devices in a FB configuration and has 5 series and 4 parallel connected capacitors.

Capacitors	TDK B43630A5108Mo	1000 $\mu$ F, 450 V
Semiconductors	IXYS IXBF55N300	3000 V, 34 A
Cell nominal voltage	$V_{\text{cell}}$	1500 V
Switching Frequency	$f_{\text{sw}}$	1 kHz

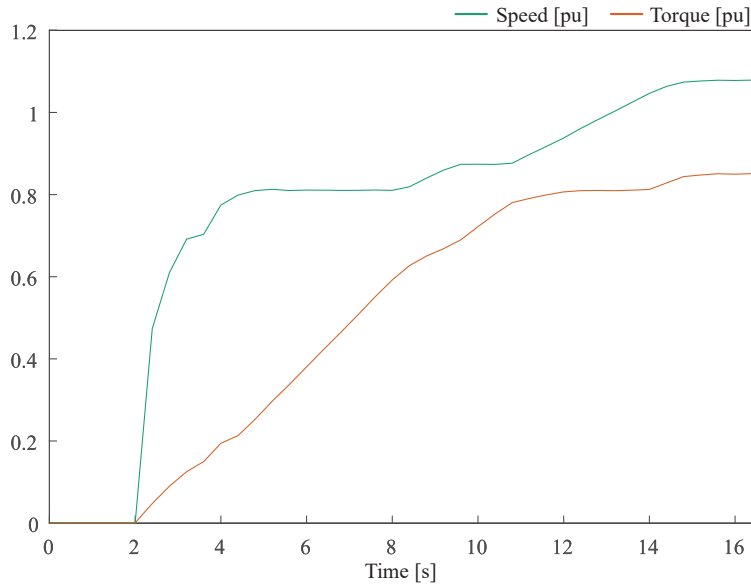


**Fig. 7.2** Optimal trajectory for least damage in turbine mode as presented in [96].

method has a very low computational burden, it requires extensive offline simulations to guarantee the validity of the lookup table for various operating points. The second method requires an offline evaluation as well as an identification of the entities influencing the losses, which allows to determine the parameters of the function and implement this function in RT. The third method computes the losses in RT without prior offline evaluation. While this method generates the most reliable results, it requires the highest computational resources of all three methods. As will be elaborated in the following section, this work relies on both the second and third method for the converter and machine loss computations, respectively.

## 7.2 Loss calculation of the M3C using sub-cycle averaged model

The branch model used on the RT-HIL computers relies on the use of the sub-cycle average model, shown in **Fig. 7.3**. The description of which is given in [98] and the validity of the RT-HIL platform using this modeling approach is shown in [99]. The advantage of the sub-cycle average model is the reduced amount of switches required to model a system such as the M3C, as presented in **Chap. 4**. The reduced number of switches reduces proportionally the number of state spaces, which allows for the use of small RT computers to model a complex system such as the M3C. However, by not modeling all the switches, the evaluation of the losses together with the requirement of low computational cost is more complicated. When using the HIL platform for control validation, the evaluation of the losses is often neglected, as the objective lies in the verification of the control software and hardware. However, the evaluation of the optimal operating point in RT requires a correct implementation of the converter loss calculation.

**Fig. 7.3** illustrates the implementation of a branch of the M3C using the sub-cycle average model. The part highlighted in gray is vectorized, which means that the signals  $S_1, S_2, S_3, S_4, v_1$  and  $v_2$  are vectors of dimension  $N$ . With eight cells per branch on the implemented M3C model, the dimension of the given vectors is eight,  $N = 8$ . As each branch is simulated using two controlled voltage sources,

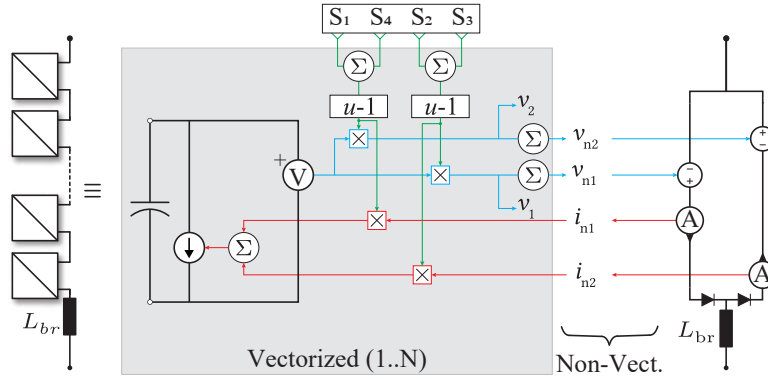


**Fig. 7.3** Modeling of the M3C branch using the sub-cycle average model allowing for accurate simulation result with a lower computational cost. For the simulations, the vectorized parts include eight elements, as the simulated M3C has eight cells per branch.

the elements of the vectors representing the cell voltages are summed up to generate a non-vectorized value representing the equivalent branch voltage.

The computation of the losses from the available signals of **Fig. 7.3** is divided into multiple stages. In the first stage, the inserted voltage of each cell within the branch is computed, which is shown in **Fig. 7.4**. This has to be a vectorized entity as the variation in the cell capacitance voltage results in each cell having a different terminal voltage, which needs to be determined.

In a second stage, depending on the respective cell voltage and the branch current direction, the number of diodes and transistors that are conducting is determined as shown in **Fig. 7.5**. The input signal  $i_{n1}$  is the positive branch current and remains zero whenever the branch current has a negative value. The signal  $i_{n2}$  shows the absolute value of the branch current in case of a negative branch current and remains zero whenever the branch current is positive. With these signals, a square signal of value +1 for a positive branch current and -1 for a negative branch current is generated. Whenever the cell terminal voltage multiplied by the previously mentioned square signal is positive, the given cell has two diodes conducting. On the other hand a negative product of both means that two transistors are conducting. When the cell terminal voltage is zero, independently of the branch current direction, the given cell has one switch and one diode conducting. The outputs  $D_{cell}$  and  $T_{cell}$  are vectors of dimension 8 with each element showing the number of diodes respective transistors that are conducting for that given cell. Summing up the elements of the vectors results in two non-vectorized values  $D_{br}$  and  $T_{br}$ , which represent the number of diodes and transistors that are conducting for a given branch.

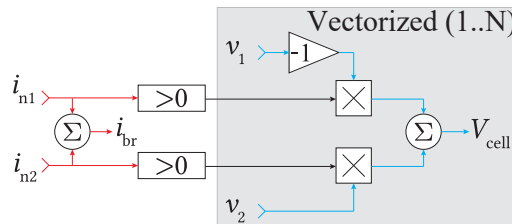


**Fig. 7.4** Determination of the terminal voltage of each cell based on the branch current directions voltages resulting from the sub-cycle averaged model.

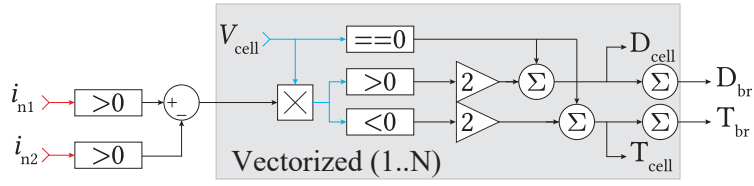


**Fig. 7.5** Calculation of the number of diodes and Insulated Gate Bipolar Transistors (IGBTs) that are conducting within a given branch at a given time instance. The inputs required for this determination is the direction of the branch current as well as the cell terminal voltage.

The conduction losses are determined as shown in **Fig. 7.6**. Using two 2D-lookup tables with the temperature and the branch current as input, the on state voltage drop of the diode and the transistor is determined. These lookup tables are determined using data sheet values of the given diodes and transistors, which usually give the on state voltage drop for two temperatures. Within the model, the values from the lookup table are interpolated or extrapolated depending on the branch current and the operating temperature. Finally, simply multiplying the voltage drop with the branch current and the number of devices that are conducting results in the instantaneous branch conduction losses. Additionally, the losses through the branch resistance,  $P_R(t) = i_{br}^2(t)R_{br}$  and cell capacitor,  $P_C(t) = i_C^2(t)R_{esr}$ , are determined and added to the previously calculated conduction losses. The cell capacitor losses are taking into account only the inserted cells of the branch.

The computation of the switching losses is more challenging, and shown in **Fig. 7.7**. The principle of this computation relies on the detection of a change in the number of transistors that are conducting within a given branch between two simulation time steps. A positive value indicates that not only a transistor turned on, but also a diode turned off, thus the reverse recovery losses should be considered as well. Similarly, if the change is negative, this translates into a turn-off event of a transistor. Multiplying this change detection signals with the measured branch currents and feeding it into a lookup table results in the energy loss of the given switching action. However, as multiple switching events within a given branch can occur simultaneously, this energy is multiplied by the amplitude of the change of the number of conducting transistors which represents the number of transistors that switched at the given time instance. The temperature scaling of the losses is done using the equation  $P_{sw}(T) = P_{sw}(T_0)(1 + K_T(T - T_0))$  as presented in [100].

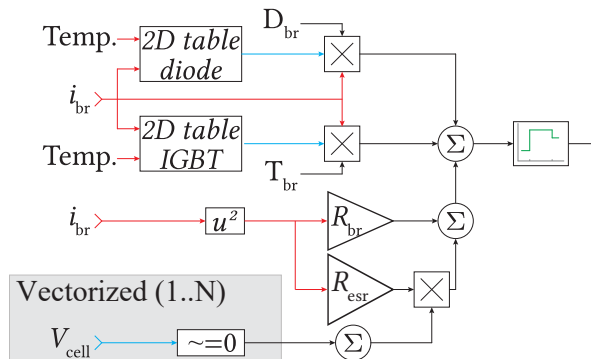


**Fig. 7.6** Calculation of the conduction losses of each branch. The lookup tables provide forward voltages of diodes and IGBTs for the given temperature and branch current. Furthermore, the power loss in the branch resistance and in the cell capacitor is computed.

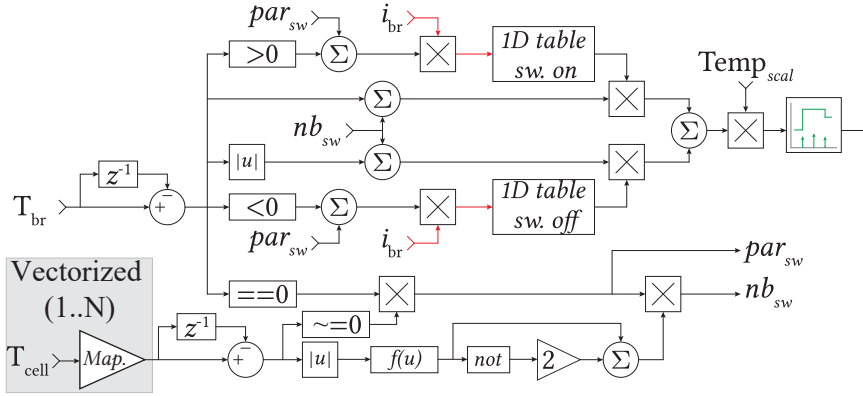


**Fig. 7.7** Calculation of the M3C branch switching losses. Whenever a variation in the total number of conducting IGBTs occurs, the number of switches involved are determined and based on the switched current, the power loss is calculated. The diode reverse recovery losses are included within the switch on lookup table of the IGBTs.

While the description above results in a very good approximation of the losses, it fails to detect whenever two cells of the same branch turn transistors on and off simultaneously, which results in a constant number of transistors conducting. The lower part of **Fig. 7.7** detects these simultaneous switching events. The variable  $par_{sw}$  takes the value 1 whenever such an event occurs, and  $nb_{sw}$  determines the number of transistors that switched simultaneous at that time instance. The vector  $T_{cell}$  includes one element with the number of transistors conducting for each cell. To reduce computational cost and not evaluate each element of the vector for a change, it is multiplied by a mapping vector, which makes sure that any change in the initial  $T_{cell}$  results in a distinctive value after the multiplication with the mapping vector. Analyzing this distinctive value allows to determine if a simultaneous switching event occurred and how many switches are involved.

**Fig. 7.8** illustrates the results of the loss calculation, taking as an example the first branch of the converter. At full power operation, as shown on the left side of **Fig. 7.8**, the average losses through a branch are around 850 W. The following nomenclature is adopted for the various losses,  $P_R$  for the branch resistive losses,  $P_C$  for the cell capacitance losses,  $P_{Con}$  for the semiconductor conduction losses,  $P_{Sw}$  for the semiconductor switching losses, including the reverse recovery losses of the diode.  $P_\Sigma$  is the sum of all branch losses. The capacitor losses are calculated based on the Equivalent Series Resistance (ESR) value extracted from the data sheet, accounting for the cell dc link being made of 5 series and 4 parallel capacitors. The final expression of the losses is:  $P_C(t) = i_C^2(t)R_{esr}$ . The branch parasitic resistance losses generated from the branch inductances are found through measurements on the MMC prototype. For the operating point at full power and unity power factor as shown on the left side of **Fig. 7.8**, the semiconductor conduction losses represent the highest part in the overall branch losses, with an average of 540 W, followed by the switching losses with 190 W. The relatively low switching losses are caused by the low switching frequency of the individual cell. The capacitor losses are on average 90 W and the branch resistive losses account for 30 W. The overall average converter losses at this operating point are at 7.6 kW, resulting in an efficiency of 98.5%. For various active power references and grid side power factors, the different losses are shown on the right side of **Fig. 7.8**.



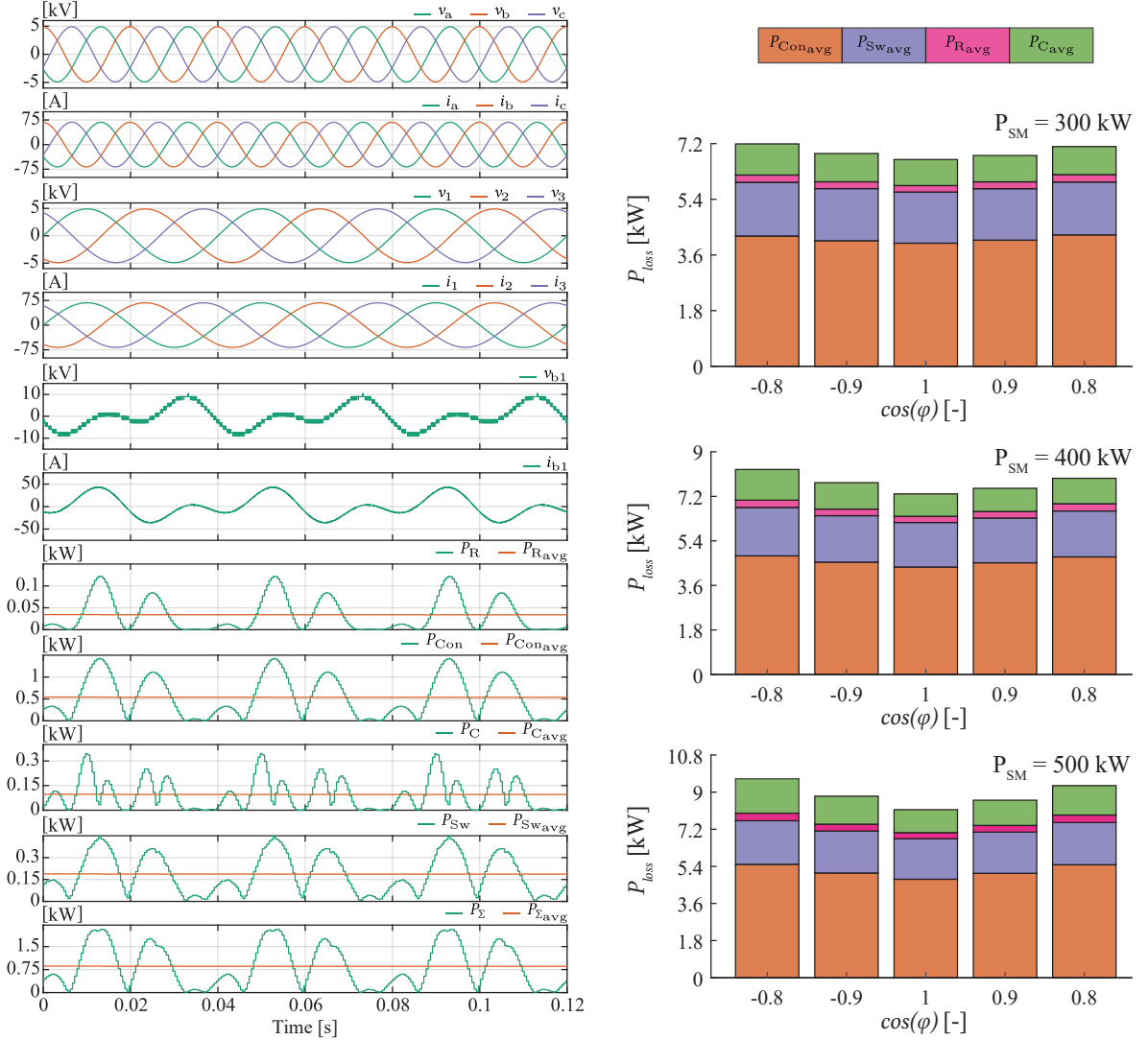


**Fig. 7.8** Results of the introduced M3C loss calculation for an operating point at full power (500 kW) with a detailed illustration of all calculated losses in branch 1 shown on the left side.  $P_R$  represent the branch resistive losses,  $P_{Con}$  the semiconductor conduction losses,  $P_C$  the capacitor losses and  $P_{Sw}$  the semiconductor switching losses. The right side shows the losses of the whole converter for various grid side power factors,  $[-0.8, -0.9, 1, 0.9, 0.8]$  and for various active power references  $[300, 400, 500]$  kW.

### 7.3 Synchronous machine loss determination and implementation

In addition to the M3C switching and conduction losses, the SM is a major source of losses in the system. Four types of losses are characterized and simulated in this work. First, the stator  $P_{S_L}$  and rotor winding losses  $P_{R_L}$ , defined by the respective resistance and the instantaneous current measurement. Second, the rotational speed dependent losses, which, on one hand include the friction and ventilation losses  $P_{fv_L}$  and on the other hand the hysteresis and the eddy current losses  $P_{he_L}$ . The latter ones are dependent not only on the rotational speed of the machine, but also on the magnetic flux.

The estimation of the stator winding losses in the RT simulation is straightforward using the stator current amplitudes calculated from the amplitude invariant Park transformation. With the data sheet value of the stator resistance and the previously calculated stator currents, the power losses can be calculated. A similar approach is used to determine the rotor winding losses.

The evaluation of the other losses mentioned above requires either a Finite Element Modeling (FEM) analysis or experimental measurements on the given SM [101]. For the experimental result evaluation used in this work, the angular momentum laws expressed below are used.

$$M|_{\psi_m} = J \frac{d\omega_m}{dt} \Big|_{\psi_m} \quad (7.1)$$

$$P|_{\psi_m} = \omega_m M|_{\psi_m} \quad (7.2)$$

Where  $J$  is the machine inertia,  $\omega_m$  the mechanical rotational speed in rad/s,  $M$  is the mechanical torque produced on the shaft and  $P$  the mechanical power. With the knowledge of the total shaft inertia and the measurement of the speed variation, the mechanical torque can be determined using (7.1). As both  $P_{fvL}$  and  $P_{heL}$  result in frictional torque acting on the shaft, evaluating this torque while controlling the magnetizing flux  $\psi_m$  to a known value allows to determine these losses.

The SM, which is characterized in this work, is shaft-connected to an IM. For the deceleration measurements, the IM is driving the SM, which has open stator windings and the ABB Unitrol 1020 excitation system controlling the excitation current. A picture of the setup is shown in **Fig. 7.9** with the dark blue being the SM and the light blue the IM. The parameters of the SM are given in **Tab. 7.2**.

The results from the deceleration measurement are shown in **Fig. 7.10**. The excitation current was increased from 0% to 100% of its maximum value in steps of 10%. A total of 12 measurements are conducted, with two measurements done without any excitation current. The reason for the repetition of the first measurement at the end is to evaluate the influence of changing machine conditions throughout the measurement process, i.e. temperature. As both measurement show similar deceleration characteristics, the hypothesis that all measurement were done in similar conditions can

**Tab. 7.2** SM ratings.

Apparent power	$S$	526 kVA
Power	$P$	500 kW
Stator voltage	$V_s$	6.3 kV
Stator current	$I_s$	53 A
Excitation. current (max)	$I_{exc}$	8.8 A (16 A)
Torque	$T_m$	6088 Nm
Speed	$n$	1500 rpm
Pole pairs	$pp$	2
Inertia	$J$	11.2 kg m <sup>2</sup>



**Fig. 7.9** Picture of the MV test bench at PEL. In dark blue the SM and in light blue the IM. Both machines are rated at 500 kW and are connected on the same shaft.

be validated. As expected and can be observed on **Fig. 7.10**, the higher the excitation current, the faster the deceleration, translating into a higher breaking torque due to the increased losses.

The frictional losses are varying linearly with the rotational speed, whereas the ventilation losses have a cubic relation with the speed. With this knowledge, a function with the parameters  $k_f$  and  $k_v$  can be created, considering  $w_{nom} = 1500 \frac{\pi}{30}$ .

$$P_{fvL} = k_v \left( \frac{w_m}{w_{nom}} \right)^3 + k_f \left( \frac{w_m}{w_{nom}} \right) \quad (7.3)$$

The test measurement done without any excitation current allows for the calculation of the torque and power losses generated by the friction and ventilation losses using (7.1) and (7.2). The inertia used in the calculation corresponds to the sum of the SM and IM inertias. Using the power losses from the measurement, the parameters  $k_f$  and  $k_v$  from (7.3) can be derived to match the equation. However, during the measurements, both machines, the IM as well as the SM are connected to the shaft, thus the measurement represent the sum of the frictional and ventilation losses of both the machines. As both machine have similar dimensions, the assumption of equal power loss can be made, thus half of the measured losses are occurring in the SM.

Before extracting the hysteresis and eddy current losses, the influence of the friction and ventilation losses need to be eliminated from the measurements. Similar to the frictional and ventilation losses, an equation representing the variation of the hysteresis and eddy current losses is required for the simulation [102].

$$P_{heL} = k_h(\psi_m) \left( \frac{w_m}{w_{nom}} \right) + k_e(\psi_m) \left( \frac{w_m}{w_{nom}} \right)^2 \quad (7.4)$$

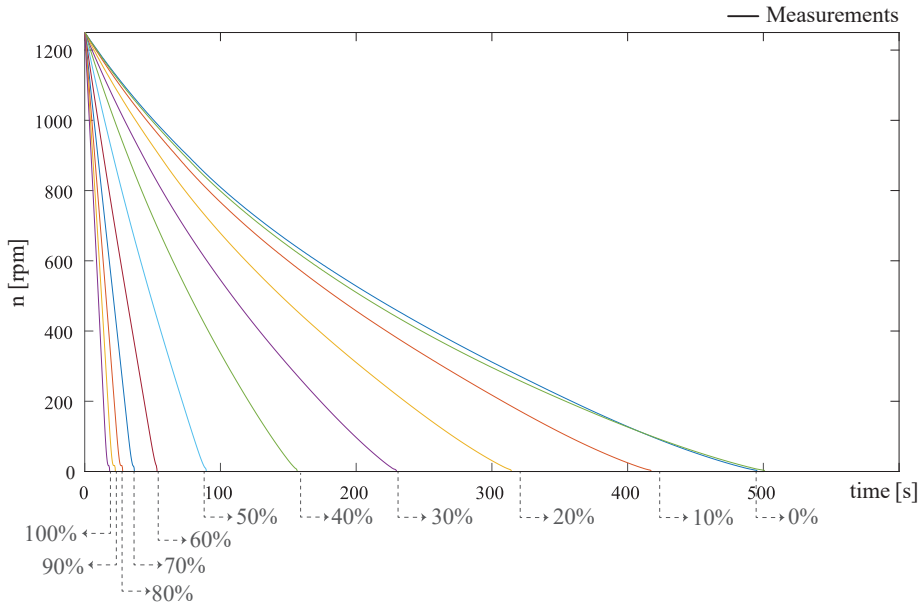


**Fig. 7.10** Measurement result of the deceleration tests of the SM under varying excitation currents. The stator remained in open circuit throughout the measurements.

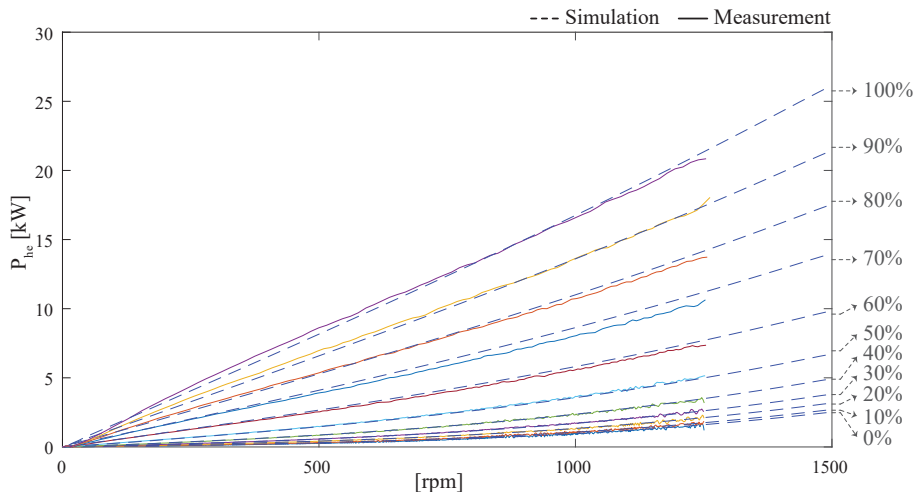


**Fig. 7.11** Illustration of the measured power losses due to eddy currents and hysteresis and comparison to the simulation losses depicted with dotted lines. The comparison is done for the whole range of excitation currents varying from 0% to 100% in steps of 10%.

**Fig. 7.11** illustrates the good match between measurements and simulation using the power loss expression described above for various excitation currents.

Further verification of the frictional torque, representing the friction and ventilation losses as well as the eddy current and hysteresis losses, resulting from the power losses equation divided by the given machine speed are shown in **Fig. 7.12**. For this verification, an offline model with the same parameters as the machines shown in **Fig. 7.9** and the same wiring as done during the experimental

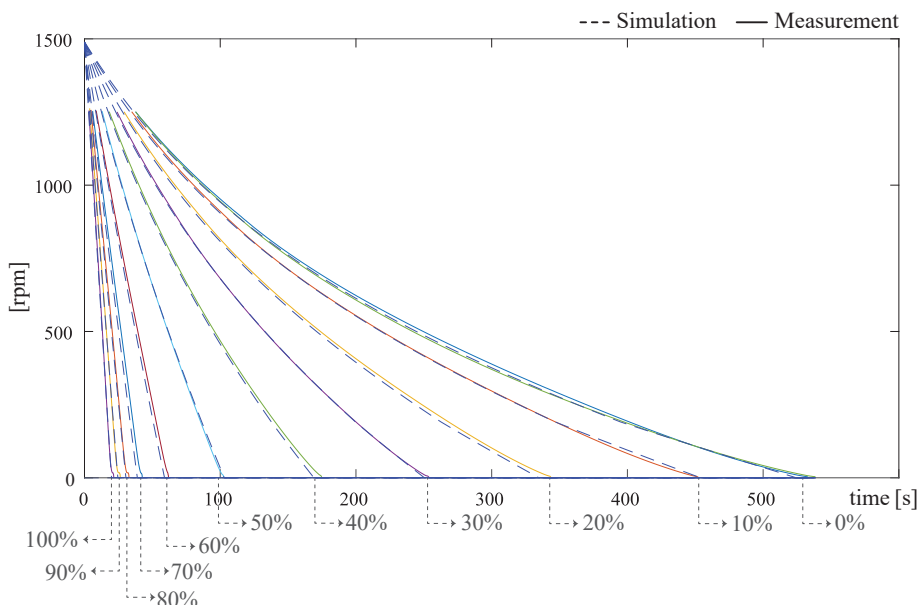


**Fig. 7.12** Illustration of the measured speed variation due to frictional torque created by eddy currents and hysteresis, and comparison to the simulation depicted with dotted lines. The comparison is done for the whole range of excitation currents varying from 0% to 100% in steps of 10%.

measurements is done. The same procedure as for the experimental measurements is repeated in the simulation and the comparison between the measurements and the simulation is matching nicely, as illustrated in **Fig. 7.12**. The dashed lines correspond to the simulations for various excitation currents, whereas the solid lines are the measurement results as presented in **Fig. 7.10**.

## 7.4 Optimal trajectory

The evaluation and implementation of all the losses present in the system allows for an efficiency optimization. The degrees of freedom that are used for the optimization include stator and rotor currents of the SM. While additional efficiency optimization can be achieved by hardware modification of the FC, such as the semiconductor choice or even considering a variation in switching frequency, this chapter is based on the FB cell being build at the PEL, using unipolar modulation with a 1 kHz carrier frequency. For PHSP with a defined hydraulic head and a given power reference issued by the grid operator, speed and torque of the shaft are defined and cannot be used as a degree of freedom. In this optimization, the aim is to achieve the lowest losses within the electrical system by optimizing SM stator and rotor currents. The losses that are considered have been presented in the previous sections.

Analyzing the influence of each degree of freedom on the various losses offers an insight on their impact to reduce the overall system losses. While both direct and quadrature stator currents can be controlled individually, for a given direct and excitation current, the quadrature current has only a single value that fulfills the required shaft torque. For the SM with salient poles presented above, the mechanical torque can be expressed as:

$$M_{SM} = \frac{3}{2} p \left( L_{md}|_{i_m} i'_{ex} i_q + (L_d - L_q)|_{i_m} i_d i_q \right) \quad (7.5)$$

The adapted approach for the modeling of the SM is the single saturation factor approach, introduced in [103], [104]. The saliency factor  $m$  is defined as a constant depending on the unsaturated main direct and quadrature inductances. With this approach, it is assumed that both d- and q-axis inductances saturate to the same level.

$$m = \frac{L_{mq0}}{L_{md0}} \quad (7.6)$$

Using the isotropic equivalent model of the salient pole SM machine, a single magnetization flux, as well as magnetization current, can be defined:

$$\Psi_m = \sqrt{\Psi_{md}^2 + \frac{\Psi_{mq}^2}{m}} \quad (7.7)$$

$$i_{md} = i'_{ex} + i_d \quad \text{and} \quad i_{mq} = i_q \quad (7.8)$$

$$i_m = \sqrt{i_{md}^2 + m i_{mq}^2} \quad (7.9)$$

**Tab. 7.3** illustrates the variation of the losses for a given torque and speed operating point while varying the available degrees of freedom.

**Tab. 7.3** Power loss variation for a given current variation.

Variation:	$P_{M3C}$	$P_{exc}$	$P_{SM_{res}}$	$P_{heL}$
$i_q = cte, i_d \nearrow, \Psi_{md} = cte$	$\nearrow$	$\searrow$	$\nearrow$	$\sim 0$
$i_q = cte, i_d \searrow, \Psi_{md} = cte$	$\searrow$	$\nearrow$	$\searrow$	$\sim 0$
$i_d = cte, i_q \nearrow, \Psi_{md} \searrow$	$\nearrow$	$\searrow$	$\nearrow$	$\searrow$
$i_d = cte, i_q \searrow, \Psi_{md} \nearrow$	$\searrow$	$\nearrow$	$\searrow$	$\nearrow$

Some of the variation shown in **Tab. 7.3** are indirect influences, such as the influence of the stator d-current on the excitation losses. The increased d-current component increases the magnetization field, thus allowing for a lower excitation current, provided the q-current component remains constant. Similarly, increasing the excitation current under the assumption of constant d-current component allows for a reduction in q-current reference to produce equivalent torque.

When controlling the stator currents to have the smallest possible value for the required torque, the  $P_{M3C}$  as well as the  $P_{SM_{res}}$  are minimized, as these power losses are solely determined by the magnitude of the stator currents. However, no consideration is given to the hysteresis and eddy current losses  $P_{heL}$ . Thus this operating point might not correspond to the lowest overall losses. From (7.5), it is intuitive that the reluctance torque and thus also the highest torque per ampere is achieved with a positive d-current. However, the variation of the inductances due to the saturation cannot be neglected in (7.5). An increase in d-current leads to an increase in magnetizing current, which in turn may lead to a decrease of the inductance, thus also a decrease in the produced torque.

**Fig. 7.13** shows the best torque per amp operating point with and without saturation taken into account. Without saturation, the optimal d-current component will always be positive, as this will result in a positive reluctance torque in (7.5). However, saturation created by the increase in d-

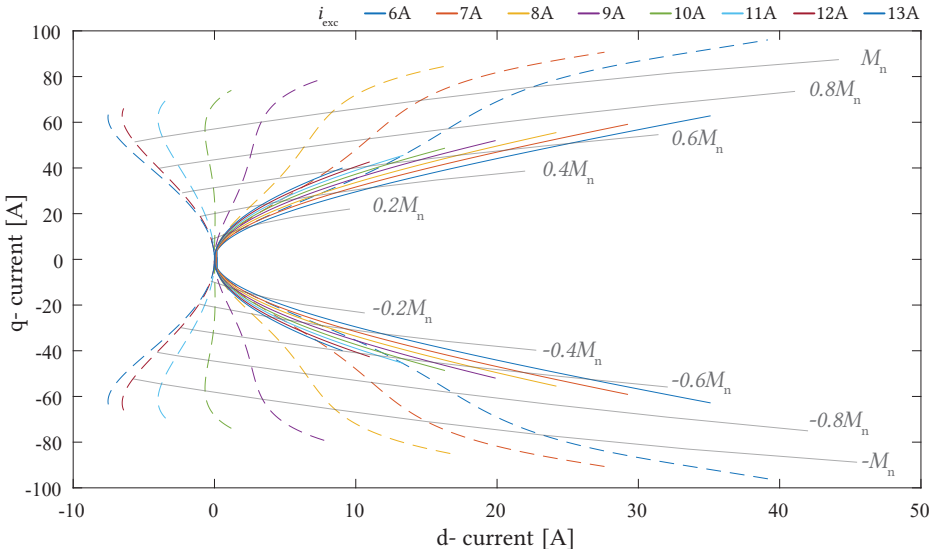


**Fig. 7.13** Highest torque per ampere points for various excitation currents. The continuous lines indicate the result when neglecting the saturation effect and the dotted lines in the same color include saturation effects of the SM. The gray lines illustrate the constant torque curves.

current component leads to a reduction in the inductances  $L_{md}$  and  $L_{mq}$ . This influences not only the reluctance torque, but reduces also the electromotive torque, thus the optimal d-current can be negative as shown in **Fig. 7.13**.

The optimization routine implemented in Matlab that generates **Fig. 7.13** includes all considered machine losses including resistive, friction and ventilation, hysteresis and eddy current losses. The objective function is expressed as the sum of the winding losses in the SM as shown in (7.10). The constraints include a given speed and torque reference which is to be considered. The expression of the electromagnetic torque produced by the SM is a nonlinear constraint due to the saturation effects of the SM. As the other losses present in the SM, such as the friction and ventilation losses as well as the hysteresis and eddy current losses, can be represented as frictional torque, they are included in the nonlinear torque constraint. The problem above is solved using the gradient-based method included in the Matlab toolbox. While this method does not ensure conversion to the absolute minimum for a non convex problem, the result of the minimization function is verified using the RT-HIL.

$$\underset{(i_d, i_q, i_e)}{\text{minimize}} : f(i_d, i_q, i_e) = \frac{3}{2} (i_d^2 + i_q^2) R_s + i_e^2 R_r \quad (7.10)$$

$$\begin{aligned} \text{constraints} : \quad & M_{SM} = M^* + M_{Loss} \\ & \sqrt{i_d^2 + i_q^2} < 100 \\ & |i_d| < 50 \\ & i_e < 16 \end{aligned}$$

To create an optimization function including the exact semiconductor switching and conduction losses results is a very tedious task, as taking the example of the M3C, the branch current frequency

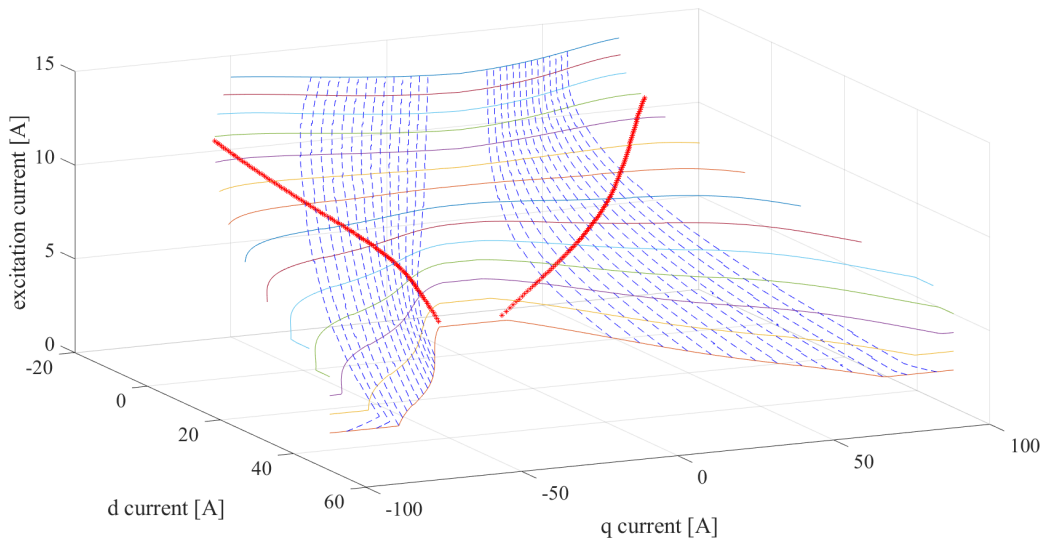


**Fig. 7.14** Best torque per ampere operating points for various excitation currents. The blue dotted lines indicate the constant torque lines and the red dots indicate the optimal current references for a given torque.

and amplitude depends on the amplitudes, frequencies and phase shifts of the input and output ac system. Additionally, including these losses limit the results to a single converter type with specific semiconductor devices.

**Fig. 7.14** illustrates through the red dots the optimal excitation as well as stator d- and q-current components for a given operating torque. The constant torque lines are depicted by the blue dotted lines and the horizontal lines illustrate the d- and q-current references generating the lowest machine losses for a fixed excitation current as already shown in dotted lines on the 2D plot in **Fig. 7.13**. It can be seen that for low torque requirements, a low excitation current combined with a low d-current reference generates the smallest machine losses. With a higher torque reference, the optimal excitation current rises even above the nominal machine excitation current, in order to reduce the stator currents and minimize conduction losses at the expense of higher eddy current and hysteresis losses.

## 7.5 RT-HIL experimental results

Six scenarios are implemented on the RT-HIL platform:

- Run 1: Nominal excitation current (8.8A) without any d-current component.
- Run 2: Nominal excitation current (8.8A) with the previously defined optimal d-current reference.
- Run 3: Previously optimal machine excitation current together with the optimal d-current reference.
- Run 4: Previously optimal machine excitation current offset by 0.5A with optimal d-current reference.
- Run 5: Previously optimal machine excitation current offset by 1A with optimal d-current reference.
- Run 6: Previously optimal machine excitation current offset by 1.5A with optimal d-current reference.

As the instantaneous power losses might not indicate accurately the differences among the various scenarios, the energy loss for a given time span will be used as a reference to determine the best scenario. In the case of the turbine start-up, as shown in **Fig. 7.15**, the total energy loss, of the M3C and SM, for various runs is reduced by up to 4.1% from run 1 to run 5. In run 6, a slight increase in energy loss compared to run 5 is observed. The details of the energy losses for each run are shown at the end of the chapter in **Tab. 7.4**. At the given operating conditions, the d-current reference takes relatively small values and thus has only a reduced impact on the overall losses as illustrated by comparing the first and second run, reducing the energy losses by only half a percent. The impact of the excitation current, however, is significant, considering the saving of up to 4.1%, especially taking into account the high amount of start-stop sequences that a flexible PHSP unit encounters throughout the day.

Similar observations can be done at full load operation, as illustrated on **Fig. 7.16**. While the small difference between no d-current and optimal d-current reference generates a slight decrease in the losses, the impact of the excitation current achieves more than 4.8% off loss reduction compared to



the nominal operating conditions without optimization. Scaling the losses to a 100 MW system, a total of 3400 kWh energy can be saved throughout a full day of pumping operation.

In both operating conditions presented in **Fig. 7.15** and **Fig. 7.16**, the optimal system efficiency is achieved considering the optimal machine excitation current offset by 1 A. This offset is explained by the fact that the previously introduced optimal machine references do not include converter losses. As shown in **Tab. 7.3**, the converter losses are reduced by reducing the overall current flowing through the branches. As this current is reduced by increasing the excitation current on the SM, it is expected that the optimal system efficiency is achieved by increasing the SM excitation current from its optimal

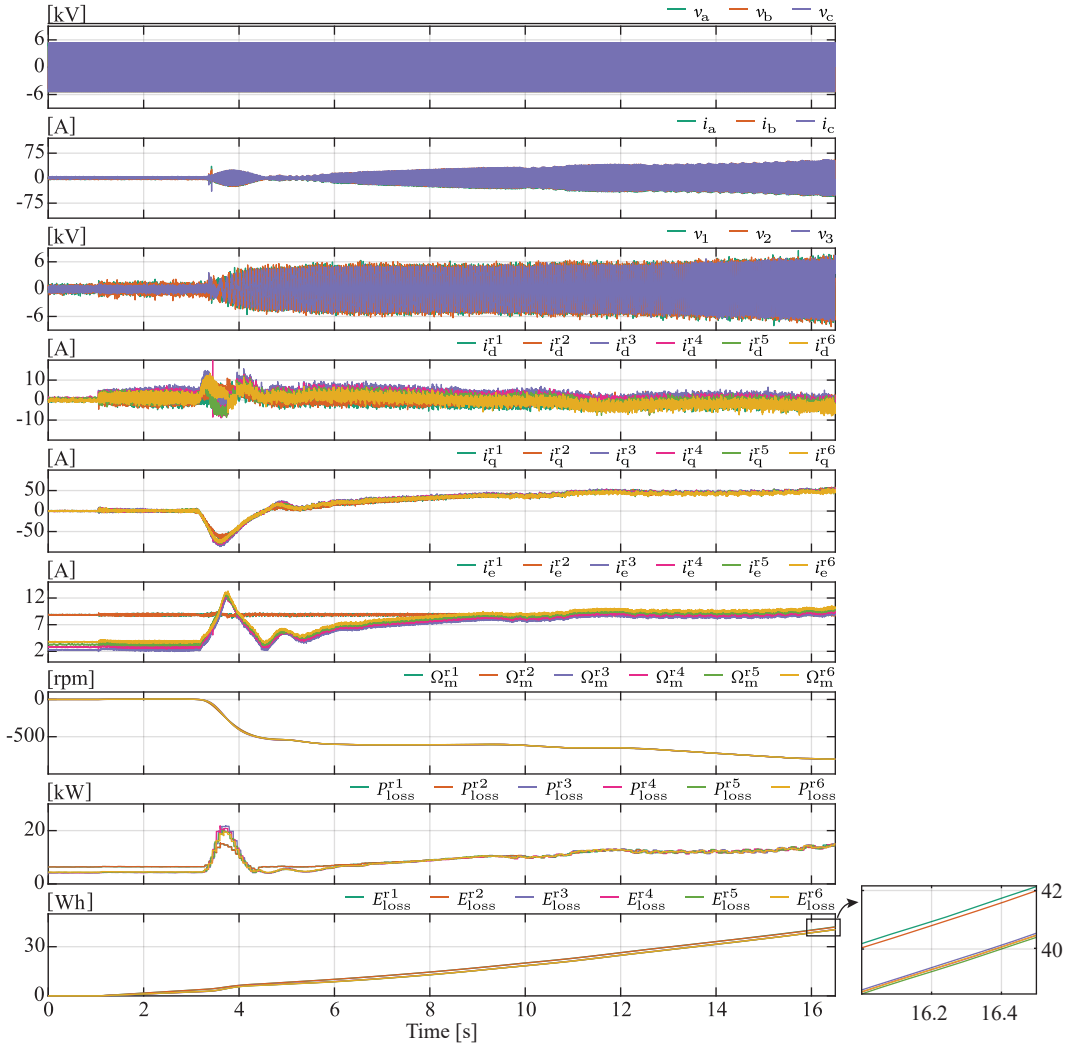


**Fig. 7.15** HIL experimental results showing the various scenarios for the start in turbine mode. The speed and load torque profile correspond to the previously defined lowest damage trajectory. The first three plots from top show, the grid voltages, grid currents and load voltages for the first scenario only as there are only minor changes among the various scenarios. The following three plots show the machine degrees of freedom, namely the d- and q-currents as well as the excitation current. The last two plots illustrate the power loss for the various scenarios and the energy loss over the given time span, including a zoom of the energy losses to observe the differences between the runs.

value.

Increasing the excitation current too high will lead to additional machine losses, which outweighs the reduction in the converter losses, thus increasing again the overall losses of the system. This is illustrated in the sixth run, where the offset from the optimal excitation current is 1.5 A and the overall system losses are higher than for the fifth run, where the excitation current was increased by only 1 A.

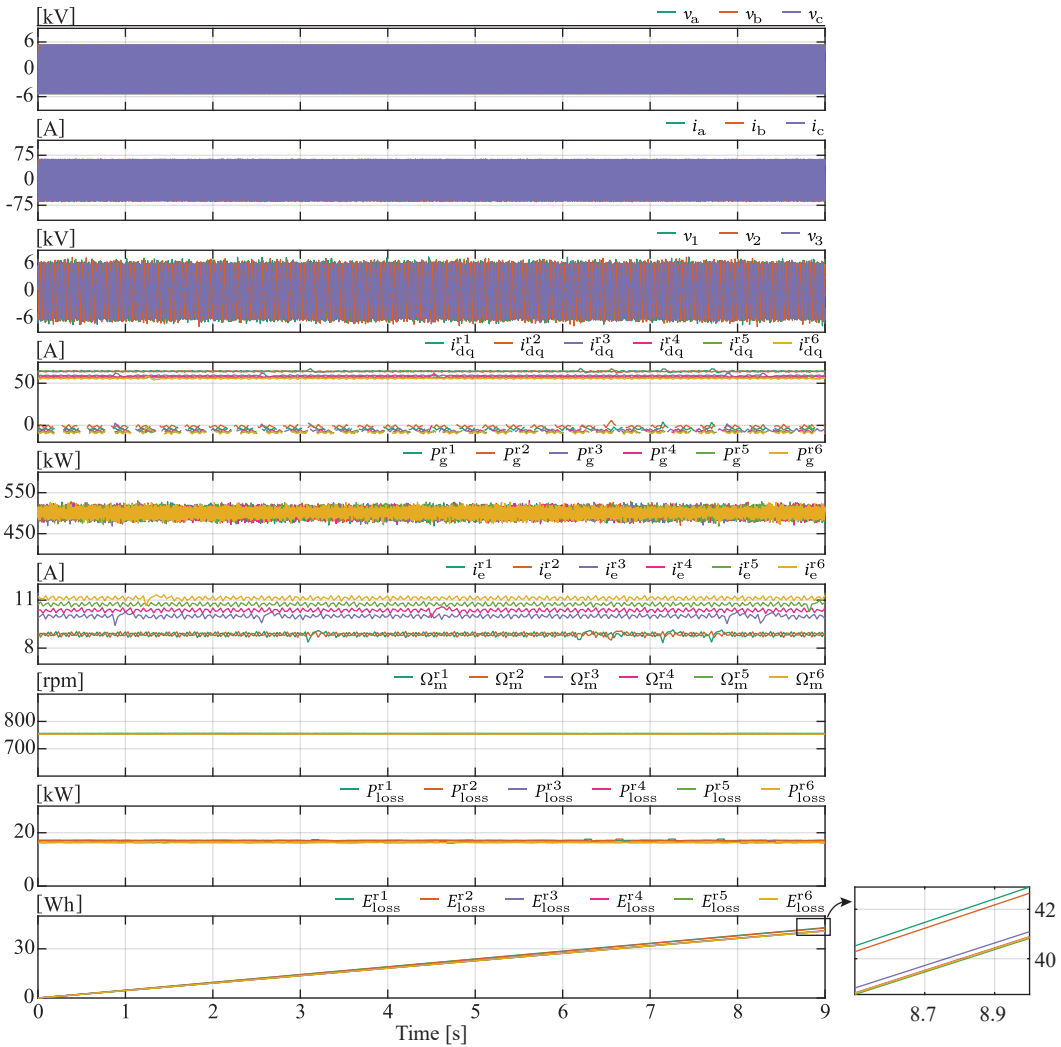


**Fig. 7.16** HIL experimental results showing the various scenarios for the full load operation in pumping mode. The first three plots from the top show the grid voltages, grid currents and load voltages for the first scenario only as there are only minor changes among the various scenarios. The following plot shows the machine d- and q-currents, where the former are depicted in dotted lines and the latter in solid lines of the same color. The fifth plot shows the power absorbed from the grid and the following plot the machine excitation current. The seventh plot shows the speed of the machine, kept constant at the nominal speed throughout the experiments. The last two plots illustrate the power loss for the various runs as well as the energy loss over the given time span, including a zoom of the energy losses to observe the differences between the runs.

**Tab. 7.4** Energy loss for the various runs at both the machine start-up as well as full-load operation.

Energy loss (Wh)	Machine start-up (after 16.5s)	Full load operation (after 9s)
Run 1	42.14 Wh	42.90 Wh
Run 2	41.99 Wh (-0.36%)	42.65 Wh (-0.58%)
Run 3	40.54 Wh (-3.80%)	41.09 Wh (-4.22%)
Run 4	40.47 Wh (-3.96%)	40.89 Wh (-4.68%)
Run 5	40.40 Wh (-4.13%)	40.82 Wh (-4.85%)
Run 6	40.47 Wh (-3.96%)	40.88 Wh (-4.71%)

## 7.6 Summary

Enabling RT loss computation of complex systems, such as a PHSP unit driven by a M3C, allows for fast loss optimization on the same HIL platform used to validate the converter control structure. This chapter presents a method for computing the M3C losses as well as the SM losses to enable a system loss optimization. Both these loss evaluations are done keeping the computational burden low, as to allow implementation on the existing RT-HIL platform used to validate the M3C control structure and algorithms. The here presented loss implementation runs on the RT Box, a small scale RT computer, and enables a loss computation at each time-step of the RT simulator.

As shown by the results presented in this work, the RT loss implementation allows for a low effort optimization of the drive and machine operating conditions. The reduced losses of up to 4.5%, as shown in the results, that can be achieved due to such optimization and considering the high amount of turbine starts throughout the day allow for both water and cost saving for the PHSP owner.



# 8

## Summary, Overall Conclusions and Future Works

*This chapter concludes the thesis by summarizing all the contributions that were brought into the emerging field of variable speed pumped hydro storage power plant relying on the use of the matrix modular multilevel converter for a direct ac-ac conversion. In addition, the future research possibilities resulting from the work done in this thesis are elaborated.*

### 8.1 Summary and contributions

This thesis focused on flexible power electronics solutions for VS PHSP. Considering the power and voltage requirements as well as the ac nature of the application, the M<sub>3</sub>C is considered the most suited converter type. The relevance of the subject chosen for this thesis is proven by the commissioning of the very first VS PHSP using the M<sub>3</sub>C topology in 2021.

**Chap. 2** depicts all the possible VS options for PHSP, for each of which the advantages as well as the physical and technological barriers are presented. Considering its advantages over the other presented options, the focus falls on the CFSM, with its main technological barrier being the high FC ratings. However, due to recent developments in power electronics and with the introduction of the MMC technology, this technological barrier was pushed to enable high power CFSM. Allowing a direct ac-to-ac conversion, the advantages of the M<sub>3</sub>C, which constitutes the focus of the thesis, over the IMMC and other topologies are described. Furthermore, the governing equations and control structure of the M<sub>3</sub>C are detailed. Finally, the two research platforms, namely the P-HIL and the RT-HIL platform, are introduced. Unfortunately, the P-HIL platform was not commissioned during the thesis and results are therefore not included.

**Chap. 3** demonstrates the advantages of VS operation for PHSP for the particular case of CFSM. An in depth analysis of conventional transients such as starting and speed reversal sequences for fixed speed units is done. Following the introduction of the *Z'Mutt* power plant, including the layout and technical characteristics of the various units, the advantages of the installation of a FC is demonstrated through simulations. While not specifically focused on the M<sub>3</sub>C topology, this chapter focuses on demonstrating the resulting benefits of CFSM installations in PHSP irrespective of the converter topology.

**Chap. 4** provides a detailed view of the RT-HIL platform, developed to perform a thorough verification of the control algorithms and control structure. While a similar RT-HIL platform based on the same RT Box 1 already exists for the MMC, the differences in layout of the converter as well as the total number of cells requires significant modifications to both the model as well as the control algorithm

and hardware. The various elements included in the control structure and their functions are described in detail. The complexity of the emulated system together with the usage of small scale simulators, namely the RT Box 1, requires a high number of interconnected RT computers to emulate the system accurately. The concept of VC and VR is introduced within the M3C topology in order to enable splitting into multiple smaller circuits. A detailed view of how the system is divided among the 11 RT Boxes is provided within the chapter.

The M3C model itself, with the high amount of switches resulting in a very large number of state space matrices, requires significant simplifications to enable RT simulations. The validity of the model, as deployed on the here presented RT-HIL platform, is validated both mathematically as well as through simulations. As the RT-HIL platform is thoroughly verified in this chapter, it provides a reliable tool for the all the M3C related simulation provided for the following chapters.

Following the development of the RT-HIL platform with its industrial control platform in **Chap. 4**, the first simulations tackle the main challenge of the M3C, which is its energy balancing algorithm. Being essential for the proper operation of the M3C, various methods with different approaches exist and are presented in depth in **Chap. 5**.

As of today, three main energy control algorithm controlling the circulating currents exist in literature, all of which are thoroughly explained in **Chap. 5**. The differences in their mathematical expression indicate the various performances achieved for different operating conditions. As the task of the circulating currents is to balance the energy among the branches of the M3C, they should remain internal to the converter and not be detectable on either of the terminals. How each of the three methods achieve this is mathematically demonstrated within this chapter. To enable a proper comparison, all the methods are converted into the same reference frame. To further illustrate their performance difference in terms of energy balancing, the three methods are compared using the RT-HIL platform. Various imbalances in normal operating conditions as well as their performance during grid faults is compared. Finally, a spider-chart further illustrates the strengths and weaknesses of each of the balancing methods, enabling application engineers to easily evaluate which method to implement considering the application requirements and restrictions.

With the internal energy balancing algorithms presented in **Chap. 5**, **Chap. 6** focuses on the control of the grid side terminal currents. Being a grid connected storage unit, a PHSP has to comply to grid code requirements. Frequency deviations, LVRT, single phase grid faults as well as grid swelling are only some of the faults that might occur on the grid side. For each possible deviation from normal operation, be it in terms of frequency or amplitude, the grid code provides clear instructions to which power must or can be exchanged. While the power exchanged with the grid is defined, the internal energy balancing of the M3C must be assured throughout the whole grid fault as to guarantee proper operation. **Chap. 6** demonstrates this grid code compliant behavior for all the scenarios listed above, using the RT-HIL platform.

With the internal energy and the grid current control developed in the previous chapter, **Chap. 7** targets the SM control. The aim is to reduce the overall system losses by exploiting all available SM degrees of freedom, namely  $i_d$ ,  $i_q$  and  $i_e$ . The first challenge within this task includes the RT computation of the M3C losses considering the simplified converter model as well as the limited computational power of the RT Box 1. Without the simulation of each separate switching event, the determination of the converter losses in RT relies on the measurement of the branch voltages together with some RT signal analysis. With only very few vectorized calculations, this method enables a fast,

reliable and computationally efficient way to calculate both the switching, reverse recovery as well as the conduction losses of the M<sub>3</sub>C. Additionally parasitic resistive losses from the branch inductance, found through measurements on the MMC prototype, as well as capacitor losses, evaluated using the ESR, are calculated for each branch.

The second major source of losses is found in the SM. The first part of SM losses are the winding losses, which, for the case of the separately excited machine, include both the stator and the rotor windings. Lowering these losses is achieved by lowering the current flowing through the respective winding. The exact calculation of the winding losses can be achieved by winding resistance datasheet values combined with RT current measurements.

The second part of losses of the SM include friction and ventilation losses as well as hysteresis and eddy current losses. Determined either through FEM or experimental measurements, this chapter uses and explains the latter one. The measurements are conducted on the P-HIL that was introduced in **Chap. 2**. Based on the first measurement results without excitation current, the friction and ventilation losses are determined. These are subtracted from all future test to determine solely the eddy current and hysteresis losses. Increasing the excitation current leads to an increase in frictional torque due to the eddy current and hysteresis losses, which allows to determine them. The resulting frictional torque in the RT-HIL model is achieved through a mathematical expression, taking both the speed and magnetic flux as input.

By having a mathematical expression of all the SM losses, a nonlinear optimization using the Matlab toolbox generates the ideal machine current references to minimize the overall machine losses while complying to a given speed and torque reference. Optimal machine operation does not necessarily translate into optimal system efficiency, as the M<sub>3</sub>C losses are not taken into account. Their dependence on current operating conditions of the application, as well as the existence of circulating currents, makes an offline optimization of the M<sub>3</sub>C impossible. **Chap. 7** takes a brute-force approach, starting from the optimal SM operation, to find the optimal system efficiency. As all losses are computed in RT on the RT-HIL platform, this approach constitutes only a small time investment.

## 8.2 Future work

The work presented in this thesis has covered the development of a RT-HIL platform for the M<sub>3</sub>C, which is used for the development and validation of its control methods for PHSP applications. This research platform allowed the development and validation of the entire control structure, including hardware and software parts which is one of the contributions of this thesis. Furthermore, this work includes an in-depth presentation of M<sub>3</sub>C terminal current control as well as circulating current control, thus covering the major control loops for the M<sub>3</sub>C. The computation of the system losses, as presented in this thesis, allows for an efficiency estimation for any scenario that will be simulated on this RT-HIL platform.

### 8.2.1 Operation with one faulty cell or faulty branch

The high amount of cells present within the M<sub>3</sub>C increases the risk of component failure. In general, redundant cells are included within each branch, accounting for a failure within the branch. However, in case no redundant cell is present in the branch, evaluating the possibility of increasing the cell voltage as to account for a bypassed cell can be analyzed.

Similarly, the case of a full branch disconnection, resulting in a limited operation of the M3C, needs to be further examined. In the literature, several papers deal with the control of the M3C under branch fault conditions, however the presented results are limited to either simulations or low voltage prototypes [105]–[108]. The implementation on the here introduced RT-HIL platform could be used to validate given control methods for higher voltage and higher power ratings.

### 8.2.2 M3C design optimization

The development of the RT-HIL platform as shown in **Chap. 4** allows for an evaluation of all possible design optimizations. While this work uses the circulating currents to solely balance the energy among the branches, these currents represent a degree of freedom that can be controlled as to reduce the cell capacitor voltage ripple. This ripple reduction allows for a smaller cell capacitor, which, considering the number of cells, can contribute to a significant cost reduction. Also for the branch inductors, various test can be performed on the RT-HIL platform, aiming to find the optimal branch inductor regarding size, type and potentially also coupling among the branch inductors. In general, the RT-HIL platform allows the validation of all the converter design choices prior to ordering and building the hardware.

The implementation of the losses on the RT-HIL platform as presented in **Chap. 7** enables an additional degree of design optimization that most RT-HIL platforms do not allow, namely the loss optimization. While this work considers a specific cell capacitor and semiconductor, comparing the losses of various possible choices is possible by just a few minor initialization modifications.

### 8.2.3 Building the hardware

The work presented in this thesis includes the industrial control structure and control algorithms which will be found on the final prototype. The rest of the M3C remains simulated on the RT Boxes. The next logical step is the development of a cell, for which the RT-HIL can be used to validate design choices as mentioned previously.

The cell development for the M3C prototype to be build at PEL has started, and the RT-HIL should aid in the design choices. Together with the fully tested control software and hardware structure done in this work on the RT-HIL, this should reduce the overall time to achieve a working M3C prototype.

### 8.2.4 Integration in the P-HIL

The P-HIL research platform as introduced in **Chap. 2** remains to be finalized. From a hardware perspective, the FC of the SM, which should be the M3C, has to be build, tested and integrated into the platform. Some high level protocol needs to be defined to enable the communication with the Speedgoat RT computer, supervising the P-HIL.



# Bibliography

- [1] European Commission. (). “2030 climate & energy framework.” [https://ec.europa.eu/clima/policies/strategies/2030\\_en](https://ec.europa.eu/clima/policies/strategies/2030_en) [Accessed on 17.08.2022].
- [2] European Commission. (). “2050 long-term strategy.” [https://ec.europa.eu/clima/eu-action/climate-strategies-targets/2050-long-term-strategy\\_en](https://ec.europa.eu/clima/eu-action/climate-strategies-targets/2050-long-term-strategy_en) [Accessed on 17.08.2022].
- [3] Eurostat, “Shedding light on energy in the EU,” 2022, <https://ec.europa.eu/eurostat/cache/infographs/energy/index.html?lang=en> [Accessed on 17.08.2022].
- [4] Eurostat, “Electricity production, consumption and market overview,” 2022, [https://ec.europa.eu/eurostat/statistics-explained/index.php?title=File:Net\\_electricity\\_generation,\\_EU,\\_1990-2020\\_\(TWh\).png](https://ec.europa.eu/eurostat/statistics-explained/index.php?title=File:Net_electricity_generation,_EU,_1990-2020_(TWh).png) [Accessed on 19.10.2022].
- [5] European Commission. (). “Paris agreement.” [https://ec.europa.eu/clima/eu-action/international-action-climate-change/climate-negotiations/paris-agreement\\_en](https://ec.europa.eu/clima/eu-action/international-action-climate-change/climate-negotiations/paris-agreement_en) [Accessed on 17.08.2022].
- [6] E. Commission, D.-G. for Energy, C. Andrey, P. Barberi, L. Nuffel, F. Gérard, J. Gorenstein Dedecca, K. Rademaekers, Y. El Idrissi, M. Crenes, and L. Lacombe, *Study on energy storage : contribution to the security of the electricity supply in Europe*. Publications Office, 2007.
- [7] R. Baxter, *Energy Storage: A Nontechnical Guide*. PennWell, 2020.
- [8] S. Rehman, L. M. Al-Hadhrami, and M. M. Alam, “Pumped hydro energy storage system: A technological review,” *Renewable and Sustainable Energy Reviews*, vol. 44, pp. 586–598, 2015.
- [9] V. Koritarov, T. D. Veselka, J. Gasper, B. M. Bethke, A. Botterud, J. Wang, M. Mahalik, Z. Zhou, C. Milostan, J. Feltes, et al., “Modeling and analysis of value of advanced pumped storage hydropower in the united states,” Argonne National Lab.(ANL), Argonne, IL (United States), Tech. Rep., 2014.
- [10] C. J. Yang and R. B. Jackson, “Opportunities and barriers to pumped-hydro energy storage in the United States,” *Renewable and Sustainable Energy Reviews*, vol. 15, no. 1, pp. 839–844, 2011.
- [11] C. Nicolet, A. Beguin, B. Kawkabani, Y. Pannatier, A. Schwery, and F. Avellan, “Variable speed and ternary units to mitigate wind and solar intermittent production,” *Hydro Vision*, 2014.
- [12] M. Valavi and A. Nysveen, “Variable-speed operation of hydropower plants: A look at the past, present, and future,” *IEEE Industry Applications Magazine*, vol. 24, no. 5, pp. 18–27, 2018.
- [13] V. Koritarov, T. D. Veselka, J. Gasper, B. M. Bethke, A. Botterud, J. Wang, M. Mahalik, Z. Zhou, C. Milostan, J. Feltes, Y. Kazachkov, T. Guo, G. Liu, B. Trouille, P. Donalek, K. King, E. Ela, B. Kirby, I. Krad, and V. Gevorgian, “Modeling and analysis of value of advanced pumped storage hydropower in the united states,” Jun. 2014.
- [14] WindEurope, “Wind energy in Europe: 2021 Statistics and the outlook for 2022-2026,” 2021, <https://windeurope.org/intelligence-platform/product/wind-energy-in-europe-2021-statistics-and-the-outlook-for-2022-2026/> [Accessed on 18.08.2022].
- [15] IRENA (2021), *Renewable capacity statistics 2021 International Renewable Energy Agency (IRENA)*, Abu Dhabi. 2021.
- [16] Eurostat, “Cumulative electricity capacity installed in the European Union (EU-27) in 2020, by generation type,” 2022, <https://www.statista.com/statistics/807675/installed-power-capacity-european-union-eu-28/> [Accessed on 19.10.2022].
- [17] European Commission, “Study on energy storage - Contribution to the security of the electricity supply in Europe,” 2020, [https://op.europa.eu/en/publication-detail/-/publication/a6eba083-932e-11ea-aac4-01aa75ed71a1/language-en?WT.mc\\_id=Searchresult&WT.ria\\_c=37085&WT.ria\\_f=3608&WT.ria\\_ev=search](https://op.europa.eu/en/publication-detail/-/publication/a6eba083-932e-11ea-aac4-01aa75ed71a1/language-en?WT.mc_id=Searchresult&WT.ria_c=37085&WT.ria_f=3608&WT.ria_ev=search) [Accessed on 19.08.2022].
- [18] T. Gaal and M. Sallaberger, *Pumped Storage Machines – Hydraulic Short-circuit Operation*. John Wiley and Sons, Ltd, 2022, ch. 16, pp. 289–301.
- [19] R. K. Fisher, J. Koutnik, L. Meier, V. Loose, K. Engels, and T. Beyer, “A comparison of advanced pumped storage equipment drivers in the us and europe,” *Louisville, USA, Hydrovision*, 2012.
- [20] J. Janning and A. Schwery, “Next generation variable speed pump-storage power stations,” in *2009 13th European Conference on Power Electronics and Applications*, Sep. 2009, pp. 1–10.
- [21] E. Nobile, G. Sari, and A. Schwery, “Variable speed hydro pumped storage as flexible enabler of intermittent renewable penetration,” in *2018 IEEE Power Energy Society General Meeting (PESGM)*, Aug. 2018, pp. 1–5.
- [22] K. Scherer, “Recent developments in pumped storage energy,” *Int. council on larg e electric systems, panel session*, 2008.
- [23] J. I. Pérez-Díaz, M. Chazarra, J. García-González, G. Cavazzini, and A. Stoppato, “Trends and challenges in the operation of pumped-storage hydropower plants,” *Renewable and Sustainable Energy Reviews*, vol. 44, pp. 767–784, 2015.

- [24] P. K. Steimer, O. Senturk, S. Aubert, and S. Linder, "Converter-fed synchronous machine for pumped hydro storage plants," in *2014 IEEE Energy Conversion Congress and Exposition (ECCE)*, Sep. 2014, pp. 4561–4567.
- [25] C. Nicolet, Y. Pannatier, B. Kawkabani, A. Schwery, F. Avellan, and J. Simond, "Benefits of variable speed pumped storage units in mixed islanded power network during transient operation," *Proceedings of HYDRO*, pp. 26–28, 2009.
- [26] International hydropower association. (). "2021 hydropower status report: Sector trends and insights." [https://assets-global.website-files.com/5f749e4b9399c80b5e421384/60c37321987070812596e26a\\_IHA20212405-status-report-02\\_LR.pdf](https://assets-global.website-files.com/5f749e4b9399c80b5e421384/60c37321987070812596e26a_IHA20212405-status-report-02_LR.pdf) [Accessed on 18.10.2022].
- [27] T. Hildinger and L. Kodding, "Modern design for variable speed motor-generators-asynchronous (dfim) and synchronous (smfi) electric machinery options for pumped storage powerplants," *Innsbruck, Hydro*, 2013.
- [28] M. Doppelbauer, "The invention of the electric motor 1800-1854," *Philosophical Magazine*, vol. 59, 1822.
- [29] E. Joy and L. Unnikrishnan, "A brief history of power electronics and drives," *International Journal of Engineering Research*, vol. 3, no. 4, 2014.
- [30] N. Holonyak, "The silicon p-n-p-n switch and controlled rectifier (thyristor)," *IEEE Transactions on Power Electronics*, vol. 16, no. 1, pp. 8–16, 2001.
- [31] T. Uzuka, "Faster than a speeding bullet: An overview of japanese high-speed rail technology and electrification," *IEEE Electrification magazine*, vol. 1, no. 1, pp. 11–20, 2013.
- [32] E. Rishavy, W. D. Bond, and T. Zechin, "Electrovair—a battery electric car," *SAE Transactions*, pp. 981–1028, 1968.
- [33] A. Lidow, T. Herman, and H. Collins, "Power mosfet technology," in *1979 international electron devices meeting*, IEEE, 1979, pp. 79–83.
- [34] I. Boldea and S. A. Nasar, *Vector control of AC drives*. CRC press, 1992.
- [35] A. Lesnicar and R. Marquardt, "An innovative modular multilevel converter topology suitable for a wide power range," in *2003 IEEE Bologna Power Tech Conference Proceedings*, vol. 3, 2003, 6 pp. Vol.3-.
- [36] R. Marquardt, "Modular multilevel converter: An universal concept for hvdc-networks and extended dc-bus-applications," in *The 2010 International Power Electronics Conference - ECCE ASIA* -, 2010, pp. 502–507.
- [37] R. Erickson and O. Al-Naseem, "A new family of matrix converters," in *IECON'01. 27th Annual Conference of the IEEE Industrial Electronics Society (Cat. No.37243)*, vol. 2, 2001, 1515–1520 vol.2.
- [38] M. Diaz, R. Cárdenas Dobson, E. Ibaceta, A. Mora, M. Urrutia, M. Espinoza, F. Rojas, and P. Wheeler, "An overview of applications of the modular multilevel matrix converter," *Energies*, vol. 13, no. 21, p. 5546, 2020.
- [39] A. Christe, A. Faulstich, M. Vasiladiotis, and P. Steinmann, "World's first fully-rated direct ac/ac mmc for variable-speed pumped-storage hydropower plants," *IEEE Transactions on Industrial Electronics*, pp. 1–10, 2022.
- [40] V. Koritarov, Q. Ploussard, J. Kwon, and P. Balducci, "A review of technology innovations for pumped storage hydropower," 2022.
- [41] D. Schafer and J.-J. Simond, "Adjustable speed asynchronous machine in hydro power plants and its advantages for the electric grid stability," Jan. 1998.
- [42] A. E. Fitzgerald, C. Kingsley, S. D. Umans, and B. James, *Electric machinery*. McGRAW-hill New York, 2003, vol. 5.
- [43] K. Ikeda, M. Inagaki, K. Niikura, and K. Oshima, "700-m 400-mw class ultrahigh-head pump turbine," *Hitachi Review*, vol. 49, no. 2, pp. 81–87, 2000.
- [44] V. Koritarov, "Modeling and analysis of value of pumped storage hydro," in *NHA Annual Conference*, 2013.
- [45] T. Kuwabara, A. Shibuya, H. Furuta, E. Kita, and K. Mitsuhashi, "Design and dynamic response characteristics of 400 mw adjustable speed pumped storage unit for ohkawachi power station," *IEEE Transactions on Energy Conversion*, vol. 11, no. 2, pp. 376–384, 1996.
- [46] N. Mohan, T. M. Undeland, and W. P. Robbins, *Power electronics: converters, applications, and design*. John wiley and sons, 2003.
- [47] A. Schwery and C. Gentner, "Variable speed pumped storage plants design choices and influencing factors," in *21 International Seminar on Hydropower Plants, Vienna, Austria*, 2022.
- [48] H. Schlunegger and A. Thöni, "100 mw full-size converter in the grimsel 2 pumped-storage plant," *Innsbruck, Hydro*, 2013.
- [49] M. Vasiladiotis. (). "Direct mmc for converter-fed synchronous machines: System design considerations." [https://www.epfl.ch/labs/pel/wp-content/uploads/2021/05/2021.05.11\\_IEEE\\_Webinar\\_Direct\\_MMC\\_System\\_HAPG.pdf](https://www.epfl.ch/labs/pel/wp-content/uploads/2021/05/2021.05.11_IEEE_Webinar_Direct_MMC_System_HAPG.pdf) [Accessed on 19.08.2022].
- [50] A. Christe. (). "Direct mmc for converter-fed synchronous machines: Control requirements and first field results." [https://www.epfl.ch/labs/pel/wp-content/uploads/2021/05/2021.05.11\\_IEEE\\_Webinar\\_Direct-MMC-Control\\_export.pdf](https://www.epfl.ch/labs/pel/wp-content/uploads/2021/05/2021.05.11_IEEE_Webinar_Direct-MMC-Control_export.pdf) [Accessed on 19.08.2022].
- [51] Hitachi ABB Power Grids. (). "Flexible power for hydro pumped storage." <https://search.abb.com/library/Download.aspx?DocumentID=9AKK107992A6965&LanguageCode=en&DocumentPartId=&Action=Launch> [Accessed on 15.02.2023].

- [52] Hitachi Energy. (). "Full converter (sfc light)." <https://www.hitachienergy.com/ch/de/products-and-solutions/facts/static-frequency-converters-sfc/hydro-sfcs/full-converter-sfc-light> [Accessed on 15.02.2023].
- [53] R. Simpson, A. Plumptre, M. Varley, C. Tonner, P. Taylor, and X. Dai, "Press-pack igbts for hvdc and facts," *CSEE Journal of Power and Energy Systems*, vol. 3, no. 3, pp. 302–310, 2017.
- [54] R. Marquardt, A. Lesnicar, J. Hildinger, *et al.*, "Modulares stromrichterkonzept für netzkupplungsanwendung bei hohen spannungen," *ETG-Fachtagung, Bad Nauheim, Germany*, vol. 114, 2002.
- [55] S. Milovanovic and D. Dujic, "On power scalability of modular multilevel converters: Increasing current ratings through branch paralleling," *IEEE Power Electronics Magazine*, vol. 7, no. 2, pp. 53–63, 2020.
- [56] M. Basić and D. Dujic, "Hybrid modular multilevel converter for variable dc link voltage operation," *CPSS Transactions on Power Electronics and Applications*, vol. 6, no. 2, pp. 178–190, 2021.
- [57] M. Basić, M. Utvić, and D. Dujic, "Hybrid modular multilevel converter design and control for variable speed pumped hydro storage plants," *IEEE Access*, vol. 9, pp. 140 050–140 065, 2021.
- [58] R. Hermann, S. Bernet, Y. Suh, and P. K. Steimer, "Parallel connection of integrated gate commutated thyristors (igcts) and diodes," *IEEE Transactions on Power Electronics*, vol. 24, no. 9, pp. 2159–2170, 2009.
- [59] S. Milovanović and D. Dujic, "Modulation considerations for modular multilevel converter operating with parallel branches and phase-shifted carriers," in *2020 IEEE 9th International Power Electronics and Motion Control Conference (IPEMC2020-ECCE Asia)*, 2020, pp. 1285–1292.
- [60] F. Kammerer, "Systemanalyse und Regelung des Modularen Multilevel Matrix Umrichters als Antriebsumrichter," pp. 1–235, 2016.
- [61] A. J. Korn, M. Winkelnkemper, P. Steimer, and J. W. Kolar, "Direct modular multi-level converter for gearless low-speed drives," *Proceedings of the 2011 14th European Conference on Power Electronics and Applications, EPE 2011*, no. direct MMC, pp. 1–7, 2011.
- [62] M. Vasiladiotis, R. Baumann, C. Häderli, and J. Steinke, "Igct-based direct ac/ac modular multilevel converters for pumped hydro storage plants," in *2018 IEEE Energy Conversion Congress and Exposition (ECCE)*, 2018, pp. 4837–4844.
- [63] T. Holzer, A. Muetze, G. Traxler-Samek, M. Lecker, and F. Zerobin, "Generator design possibilities for full-size converter operation of large pumped storage power plants," *IEEE Transactions on Industry Applications*, vol. 56, no. 4, pp. 3644–3655, 2020.
- [64] C. Oates and G. Mondal, "Dc circulating current for capacitor voltage balancing in modular multilevel matrix converter," in *Proceedings of the 2011 14th European Conference on Power Electronics and Applications*, IEEE, 2011, pp. 1–7.
- [65] W. Kawamura, Y. Chiba, M. Hagiwara, and H. Akagi, "Experimental verification of an electrical drive fed by a modular multilevel tsbc converter when the motor frequency gets closer or equal to the supply frequency," *IEEE Transactions on Industry Applications*, vol. 53, no. 3, pp. 2297–2306, 2017.
- [66] W. Kawamura, M. Hagiwara, and H. Akagi, "A broad range of frequency control for the modular multilevel cascade converter based on triple-star bridge-cells (mmcc-tsbc)," in *2013 IEEE Energy Conversion Congress and Exposition*, 2013, pp. 4014–4021.
- [67] F. Kammerer, M. Gommeringer, J. Kolb, and M. Braun, "Energy balancing of the modular multilevel matrix converter based on a new transformed arm power analysis," in *2014 16th European Conference on Power Electronics and Applications*, 2014, pp. 1–10.
- [68] A. Zama, S. A. Mansour, D. Frey, A. Benchaib, S. Bacha, and B. Luscan, "A comparative assessment of different balancing control algorithms for modular multilevel converter (mmc)," in *2016 18th European Conference on Power Electronics and Applications (EPE'16 ECCE Europe)*, IEEE, 2016, pp. 1–10.
- [69] H. A. Pereira, A. F. Cupertino, L. S. Xavier, A. Sangwongwanich, L. Mathe, M. Bongiorno, and R. Teodorescu, "Capacitor voltage balance performance comparison of mmc-statcom using nlc and ps-pwm strategies during negative sequence current injection," in *2016 18th European Conference on Power Electronics and Applications (EPE'16 ECCE Europe)*, IEEE, 2016, pp. 1–9.
- [70] L. Mathe, "Performance comparison of the modulators with balancing capability used in mmc applications," in *2017 IEEE 26th International Symposium on Industrial Electronics (ISIE)*, IEEE, 2017, pp. 815–820.
- [71] E. Alwers, K. Baltisberger, and R. Grabitz, "Asynchronous starting of synchronous machines for pumped storage schemes," *BROWN BOVERI REVIEW*, vol. 59, no. 2-3, pp. 60–67, 1972.
- [72] S. N. Vukosavic, *Electrical machines*. Springer Science & Business Media, 2012.
- [73] S. Milovanovic, I. Polanco, M. Utvic, and D. Dujic, "Flexible and efficient mmc digital twin realized with small-scale real-time simulators," *IEEE Power Electronics Magazine*, vol. 8, no. 2, pp. 24–33, 2021.
- [74] M. Utvic, I. P. Lobos, and D. Dujic, "Low voltage modular multilevel converter submodule for medium voltage applications," in *PCIM Europe 2019; International Exhibition and Conference for Power Electronics, Intelligent Motion, Renewable Energy and Energy Management*, 2019, pp. 1–8.

- [75] PLEXIM, *The simulation platform for power electronics systems*, English, version Version 4-5, 830 pp.
- [76] "Modeling and simulation," in *Design, Control and Application of Modular Multilevel Converters for HVDC Transmission Systems*. John Wiley and Sons, Ltd, 2016, ch. 6, pp. 272–282.
- [77] H. Saad, J. Peralta, S. Denetiere, J. Mahseredjian, J. Jatskevich, J. A. Martinez, A. Davoudi, M. Saeedifard, V. Sood, X. Wang, J. Cano, and A. Mehrizi-Sani, "Dynamic averaged and simplified models for mmc-based hvdc transmission systems," *IEEE Transactions on Power Delivery*, vol. 28, no. 3, pp. 1723–1730, 2013.
- [78] J. Xu, A. M. Gole, and C. Zhao, "The use of averaged-value model of modular multilevel converter in dc grid," *IEEE Transactions on Power Delivery*, vol. 30, no. 2, pp. 519–528, 2015.
- [79] W. Li and J. Bélanger, "An equivalent circuit method for modelling and simulation of modular multilevel converters in real-time hil test bench," *IEEE Transactions on Power Delivery*, vol. 31, no. 5, pp. 2401–2409, 2016.
- [80] J. Allmeling and N. Felderer, "Sub-cycle average models with integrated diodes for real-time simulation of power converters," in *2017 IEEE Southern Power Electronics Conference (SPEC)*, 2017, pp. 1–6.
- [81] Z. Xu, S. Wang, F. Xing, and H. Xiao, "Study on the method for analyzing electric network resonance stability," *Energies*, vol. 11, no. 3, 2018.
- [82] J. Kucka, D. Karwatzki, and A. Mertens, "Ac/ac modular multilevel converters in wind energy applications: Design considerations," in *2016 18th European Conference on Power Electronics and Applications (EPE'16 ECCE Europe)*, 2016, pp. 1–10.
- [83] P. Bontemps and D. Dujic, "Flexible operation of variable speed direct-mmc in hydropower applications," in *PCIM Europe 2022; International Exhibition and Conference for Power Electronics, Intelligent Motion, Renewable Energy and Energy Management*, IEEE, 2022.
- [84] B. Fan, K. Wang, C. Gu, P. Wheeler, and Y. Li, "A branch current reallocation based energy balancing strategy for the modular multilevel matrix converter operating around equal frequency," in *IECON 2016 - 42nd Annual Conference of the IEEE Industrial Electronics Society*, 2016, pp. 3111–3116.
- [85] F. Kammerer, J. Kolb, and M. Braun, "A novel cascaded vector control scheme for the modular multilevel matrix converter," in *IECON 2011-37th Annual Conference of the IEEE Industrial Electronics Society*, IEEE, 2011, pp. 1097–1102.
- [86] F. Kammerer, M. Gommeringer, J. Kolb, and M. Braun, "Energy balancing of the modular multilevel matrix converter based on a new transformed arm power analysis," in *2014 16th European Conference on Power Electronics and Applications*, IEEE, 2014, pp. 1–10.
- [87] F. Kammerer, J. Kolb, and M. Braun, "Fully decoupled current control and energy balancing of the modular multilevel matrix converter," in *2012 15th International Power Electronics and Motion Control Conference (EPE/PEMC)*, IEEE, 2012, LS2a–3.
- [88] F. Kammerer, "Systemanalyse und regelung des modularen multilevel matrix umrichters als antriebsumrichter," 2016.
- [89] A. J. Korn, M. Winkelnkemper, P. Steimer, and J. W. Kolar, "Capacitor voltage balancing in modular multilevel converters," in *6th IET International Conference on Power Electronics, Machines and Drives (PEMD 2012)*, 2012, pp. 1–5.
- [90] M. Utvić and D. Dujić, "Generalized theory on direct arm energy control in modular multilevel converters," *CPSS Transactions on Power Electronics and Applications*, vol. 5, no. 4, pp. 388–399, 2020.
- [91] G. Strang and K. Borre, *Linear algebra, geodesy, and GPS*. Siam, 1997.
- [92] S. Milovanović and D. Dujić, "Comprehensive comparison of modular multilevel converter internal energy balancing methods," *IEEE Transactions on Power Electronics*, vol. 36, no. 8, pp. 8962–8977, 2021.
- [93] E.ON Netz GmbH and Verband Der Netzbetreiber Vnd, *Transmissioncode 2007. network and system rules of the german transmission system operators*, <https://www.vde.com/resource/blob/937766/bfe325518ace878935966b6efbc493e4/transmissioncode-2007--network-and-system-rules-of-the-german-transmission-system-operators-data.pdf> [Accessed on 24.01.2022].
- [94] E. Watanabe, R. Stephan, and M. Aredes, "New concepts of instantaneous active and reactive powers in electrical systems with generic loads," *IEEE Transactions on Power Delivery*, vol. 8, no. 2, pp. 697–703, 1993.
- [95] M. Utvić and D. Dujić, "Generalized theory on direct arm energy control in modular multilevel converters," *CPSS Transactions on Power Electronics and Applications*, vol. 5, no. 4, pp. 388–399, 2020.
- [96] D. Biner, S. Alligné, C. Nicolet, D. Dujic, and C. Münch-Alligné, "Numerical fatigue damage analysis of a variable speed francis pump-turbine during start-up in generating mode," in *IOP Conference Series: Earth and Environmental Science*, IOP Publishing, vol. 1079, 2022, p. 012 079.
- [97] I. Kougiadis, G. Aggidis, F. Avellan, S. Deniz, U. Lundin, A. Moro, S. Muntean, D. Novara, J. I. Pérez-Díaz, E. Quaranta, et al., "Analysis of emerging technologies in the hydropower sector," *Renewable and Sustainable Energy Reviews*, vol. 113, p. 109 257, 2019.
- [98] J. Allmeling and N. Felderer, "Sub-cycle average models with integrated diodes for real-time simulation of power converters," in *2017 IEEE Southern Power Electronics Conference (SPEC)*, 2017, pp. 1–6.

- 
- [99] P. Bontemps, S. Milovanovic, and D. Dujic, "Distributed real-time model of the m3c for hil systems using small-scale simulators," *IEEE Open Journal of Power Electronics*, vol. 2, pp. 603–613, 2021.
  - [100] U. Nicolai and A. Wintrich, "Determining switching losses of semikron igbt modules," *SEMIKRON Application Note, AN*, vol. 1403, 2014.
  - [101] I. E. Commission *et al.*, "Rotating electrical machines—part 2-1: Standard methods for determining losses and efficiency from tests (excluding machines for traction vehicles)," IEC 60034-2-1, Tech. Rep., 2007.
  - [102] R. Grune, "Verlustoptimaler betrieb einer elektrisch erregten synchronmaschine für den einsatz in elektrofahrzeugen," 2013.
  - [103] E. Levi, "Saturation modelling in d-q axis models of salient pole synchronous machines," *IEEE Transactions on Energy Conversion*, vol. 14, no. 1, pp. 44–50, 1999.
  - [104] A. Campeanu and M. Stiebler, "Modeling of saturation in salient pole synchronous machines," in *2010 12th International Conference on Optimization of Electrical and Electronic Equipment*, IEEE, 2010, pp. 258–263.
  - [105] C. Wang, Z. Zheng, K. Wang, B. Yang, P. Zhou, and Y. Li, "Analysis and control of modular multilevel matrix converters under branch fault conditions," *IEEE Transactions on Power Electronics*, vol. 37, no. 2, pp. 1682–1699, 2022.
  - [106] D. Karwatzki, M. von Hofen, L. Baruschka, and A. Mertens, "Operation of modular multilevel matrix converters with failed branches," in *IECON 2014 - 40th Annual Conference of the IEEE Industrial Electronics Society*, 2014, pp. 1650–1656.
  - [107] B. Fan, K. Wang, Z. Zheng, L. Xu, and Y. Li, "Optimized branch current control of modular multilevel matrix converters under branch fault conditions," *IEEE Transactions on Power Electronics*, vol. 33, no. 6, pp. 4578–4583, 2018.
  - [108] J. Yu, Y. Meng, X. Pan, Y. Zou, R. Huang, and M. Zhang, "Fault ride-through of fractional frequency offshore wind power system based on modular multilevel matrix converter," in *2019 IEEE 8th International Conference on Advanced Power System Automation and Protection (APAP)*, 2019, pp. 716–719.



# Bontemps Philippe Alexandre

*PhD candidate in Power Electronics*

✉ [philippe.bontemps@alumni.epfl.ch](mailto:philippe.bontemps@alumni.epfl.ch)

December 8<sup>th</sup> 1993

Luxemburgish, single

## HIGHER EDUCATION

École Polytechnique Fédérale de Lausanne, Lausanne, Switzerland

- 2019 - 2023 PhD candidate, EDEE Electrical Engineering Doctoral School  
Flexible High Power Electronics Solutions for Hydro-Power Applications
- 2017 - 2019 MSc. in Electrical and Electronics Engineering
- 2013 - 2017 BSc. in Electrical and Electronics Engineering

## TEACHING / SUPERVISION EXPERIENCE

- 2021 - 2022 Teaching assistant for the course *Power Electronics*  
Design and prototype of a 50W dc-dc converter
- 2020 Teaching assistant for the course *Industrial Electronics II*  
Modeling and control of power electronics converters and motor drives
- 2020 Teaching assistant for the course *Industrial Electronics I*  
Modeling and control of grid-connected power electronics converters
- 2019 - 2022 Supervision of various BSc. and MSc. student projects

## PROFESSIONAL EXPERIENCE

2019 - 2022	École Polytechnique Fédérale de Lausanne, Switzerland Doctoral assistant
2019	ABB Switzerland, Turgi Intern in the traction team
Summer 2017	Paul Wurth S.A, Luxembourg Intern in the process automation team
Summer 2014	Lotus F1 Team Limited, Enstone, U.K Intern

## LANGUAGES

English	Level C1
German	Level C2
French	Level C2
Luxemburgish	Mother tongue

## COMPUTER TOOLS AND CODING

Simulation	Simulink, Plecs
PCB design	Altium Designer
Coding	Matlab, C, Latex
OS	Windows

## REVIEW

Reviewer for IEEE Transactions on Power Electronics